HZDR-018

DYNAMICS OF THE FREE SURFACE OF STRATIFIED TWO-PHASE FLOWS IN CHANNELS WITH RECTANGULAR CROSS-SECTIONS

Christophe Vallée

Wissenschaftlich-Technische Berichte
HZDR-018 · ISSN 2191-8708

WISSENSCHAFTLICH-
TECHNISCHE BERICHTE

HZDR

HELMHOLTZ
ZENTRUM DRESDEN
ROSSENDORF

Wissenschaftlich-Technische Berichte
HZDR-018

Christophe Vallée

DYNAMICS OF THE FREE SURFACE OF STRATIFIED TWO-PHASE FLOWS IN CHANNELS WITH RECTANGULAR CROSS-SECTIONS

HZDR

HELMHOLTZ
ZENTRUM DRESDEN
ROSSENDORF

Druckausgabe: ISSN 2191-8708

Elektronische Ausgabe: ISSN 2191-8716

Qucosa: http://fzd.qucosa.de/startseite/

Die vorliegende Arbeit wurde sowohl als Dissertation an der Fakultät Maschinenwesen der Technischen Universität Dresden sowie als Wissenschaftlich-Technischer Bericht des Helmholtz-Zentrum Dresden-Rossendorf mit der Berichtsnummer **HZDR-018** veröffentlicht.

2012

Herausgegeben vom

Helmholtz-Zentrum Dresden-Rossendorf e.V.

Postfach 51 01 19

D-01314 Dresden

Bundesrepublik Deutschland/Germany

DYNAMICS OF THE FREE SURFACE OF STRATIFIED TWO-PHASE FLOWS IN CHANNELS WITH RECTANGULAR CROSS-SECTIONS

by

Dipl.-Ing. Christophe Vallée

from Dresden

Ph.D. Thesis

approved by the

Faculty of Mechanical Engineering

of

Technische Universität Dresden

to receive the academic degree of

Doctor of Engineering (Dr.-Ing.)

Submission:	October 6th, 2010
Defence:	Mai 4th, 2011
Chairman:	Prof. Dr.-Ing. habil. Jochen Fröhlich
Referees:	Prof. Dr. rer. nat. Frank-Peter Weiß
	Prof. Dr.-Ing. Akio Tomiyama
	Prof. Dr.-Ing. Horst-Michael Prasser

DYNAMIK DER FREIEN OBERFLÄCHE GESCHICHTETER ZWEIPHASENSTRÖMUNGEN IN RECHTECKIGEN KANÄLEN

von der

Fakultät Maschinenwesen

der

Technische Universität Dresden

zur Erlangung des akademischen Grades

Doktoringenieur (Dr.-Ing.)

angenommene

Dissertation

von

Dipl.-Ing. Christophe Vallée

aus Dresden

Tag der Einreichung:	6. Oktober 2010
Tag der Verteidigung:	4. Mai 2011
Vorsitzender:	Prof. Dr.-Ing. habil. Jochen Fröhlich
Gutachter:	Prof. Dr. rer. nat. Frank-Peter Weiß
	Prof. Dr.-Ing. Akio Tomiyama
	Prof. Dr.-Ing. Horst-Michael Prasser

All I know is that I know nothing

Socrates (c. 469 BC – 399 BC)
reported by Plato (c. 428/427 BC – 348/347 BC)

Donauwasser (IN / 2001)

In memoriam Papi et Papo

ABSTRACT

Stratified two-phase flows were investigated at different test facilities with horizontal test sections in order to provide an experimental database for the development and validation of computational fluid dynamics (CFD) codes. These channels were designed with rectangular cross-sections to enable optimal observation conditions for the application of optical measurement techniques. Consequently, the local flow structure was visualised with a high-speed video camera, delivering data with high-resolution in space and time as needed for CFD code validation.

Generic investigations were performed at atmospheric pressure and room temperature in two air/water channels made of acrylic glass. Divers preliminary experiments were conducted with various measuring systems in a test section mounted between two separators. The second test facility, the **H**orizontal **A**ir/**Wa**ter **C**hannel (HAWAC), is dedicated to co-current flow investigations. The hydraulic jump as the quasi-stationary discontinuous transition between super- and subcritical flow was studied in this closed channel. Moreover, the instable wave growth leading to slug flow was investigated from the test section inlet. For quantitative analysis of the optical measurements, an algorithm was developed to recognise the stratified interface in the camera frames, allowing statistical treatments for comparison with CFD calculation results.

The third test apparatus was installed in the pressure chamber of the TOPFLOW test facility in order to be operated at reactor typical conditions under pressure equilibrium with the vessel atmosphere. The test section representing a flat model of the hot leg of the German *Konvoi* pressurised water reactor (PWR) scaled at 1:3 is equipped with large glass side walls in the region of the elbow and of the steam generator inlet chamber to allow visual observations. The experiments were conducted with air and water at room temperature and maximum pressures of 3 bar as well as with steam and water at boundary conditions of up to 50 bar and 264°C. Four types of experiments were performed, including generic test cases as well as transient validation cases of typical nuclear reactor safety issues. As an example, the co-current flow experiments simulate the two-phase natural circulation in the primary circuit of a PWR. The probability distribution of the water level measured in the reactor pressure vessel simulator was used to characterise the flow in the hot leg. Moreover, the flooding behaviour in this conduit was investigated with dedicated counter-current flow limitation experiments. A comparison of the flooding characteristics with similar experimental data and correlations available in the literature shows that the channel height is the characteristic length to be used in the Wallis parameter for channels with rectangular cross-sections. Furthermore, for the analysis of steam/water experiments, condensation effects had to be taken into account. Finally, the experimental results confirm that the Wallis similarity is appropriate to scale flooding in the hot leg of a PWR over a large range of pressure and temperature conditions.

Not least, different examples of comparison between experiment and simulation demonstrate the possibilities offered by the data to support the development and validation of CFD codes. Besides the comparison of qualitative aspects, it is shown exemplarily how to treat the CFD results in order to enable quantitative comparisons with the experiments.

KURZFASSUNG

Geschichtete Zweiphasenströmungen wurden in verschiedenen Versuchsanlagen mit horizontalen Teststrecken untersucht. Das wesentliche Ziel bestand darin eine experimentelle Datenbank für die Entwicklung und Validierung von CFD-Codes (computational fluid dynamics) bereitzustellen. Diese Kanäle wurden mit rechteckigem Querschnitt konstruiert, um optimale Beobachtungsbedingungen für die Anwendung optischer Messmethoden zu erreichen. So wurde die lokale Strömungsstruktur mit einer Hochgeschwindigkeitskamera visualisiert, welche die für die CFD-Validierung benötigten Daten mit hoher räumlicher sowie zeitlicher Auflösung liefert.

Generische Untersuchungen wurden in zwei Luft/Wasser-Kanälen aus Acrylglas bei Atmosphärendruck und Raumtemperatur durchgeführt. Diverse Vorexperimente wurden mit mehreren Messsystemen in einer zwischen zwei Separatoren eingebauten Testsektion durchgeführt. Der zweite Versuchstand, der Strömungskanal HAWAC (**H**orizontal **A**ir/**Wa**ter **C**hannel), ist eigens für Gleichstromexperimente konstruiert. Der hydraulische Sprung, der den quasistationären diskontinuierlichen Übergang zwischen schießender und Flussströmung darstellt, wurde in diesem geschlossenen Kanal studiert. Zudem wurde das zur Schwallströmung führende instabile Wellenwachstum vom Teststreckeneintritt an untersucht. Für quantitative Analysen der optischen Messungen wurde ein Algorithmus entwickelt, um die stratifizierte Phasengrenze in den Kamerabildern zu erkennen und damit statistische Auswertungen für den Vergleich mit Ergebnissen aus CFD-Rechnungen zu ermöglichen.

In der Druckkammer der TOPFLOW-Anlage wurde der dritte Versuchsaufbau installiert, der somit auch bei reaktortypischen Bedingungen im Druckgleichgewicht mit der Innenatmosphäre des Druckbehälters betrieben werden konnte. Die Teststrecke bildet ein flaches Modell des heißen Strangs eines deutschen *Konvoi* Druckwasserreaktors (DWR) im Maßstab 1:3 nach und ist mit großflächigen Glaswänden im Bereich des Krümmers und der Dampferzeuger-Eintrittskammer ausgestattet, um eine visuelle Beobachtung zu ermöglichen. Die Experimente erfolgten mit Luft und Wasser bei Raumtemperatur und Drücken von maximal 3 bar sowie mit Dampf und Wasser bei bis zu 50 bar und 264°C. Vier Versuchstypen wurden durchgeführt, unter anderem generische Testfälle sowie transiente Validierungsfälle für typische Fragestellungen der Reaktorsicherheit. So zum Beispiel simulieren die Gleichstromexperimente den zweiphasigen Naturumlauf im Primärkreislauf eines DWRs. Die Wahrscheinlichkeitsverteilung des im Reaktordruckbehälter-Simulator gemessenen Wasserstands wurde genutzt, um die Strömung im heißen Strang zu charakterisieren. Darüber hinaus wurde in diesem Modell das Flutverhalten mit speziellen Gegenstrombegrenzungsexperimenten untersucht. Ein Vergleich der Flutkurve mit ähnlichen experimentellen Daten und Korrelationen aus der Literatur zeigt, dass für Kanäle mit rechteckigem Querschnitt die Kanalhöhe die einzusetzende charakteristische Länge im Wallis-Parameter ist. Zudem mussten Kondensationseffekte für die Analyse der Dampf/Wasser-Experimente berücksichtigt werden. Schließlich bestätigten die Versuchsergebnisse, dass die Ähnlichkeit nach Wallis geeignet ist, um die Gegenstrombegrenzung im heißen Strang eines DWRs über einen großen Druck- und Temperaturbereich zu skalieren.

Nicht zuletzt weisen verschiedene Vergleichsbeispiele zwischen Experiment und Simulation nach, welche Möglichkeiten die Daten für die Unterstützung der CFD-Entwicklung und Validierung bieten. Neben dem Vergleich von qualitativen Aspekten wird exemplarisch gezeigt, wie die CFD-Ergebnisse verwertet werden können, um quantitative Vergleiche mit den Experimenten zu ermöglichen.

RÉSUMÉ

Afin de constituer une banque de données expérimentales pour le développement et la validation de codes CFD (computational fluid dynamics), des écoulements diphasiques stratifiés ont été étudiés sur différents bancs d'essai présentant une conduite horizontale. Ces canaux ont été conçus avec une section rectangulaire pour assurer des conditions d'observation optimales à l'application de techniques de mesure optiques. C'est ainsi que la structure locale de l'écoulement fut visualisée à l'aide d'une caméra haute vitesse délivrant les données de haute résolution, spatiale et temporelle, nécessaires à la validation des codes CFD.

Des études génériques furent conduites à pression atmosphérique et température ambiante dans deux canaux de Plexiglas. Différentes expériences préliminaires furent effectuées avec divers systèmes de mesure dans une veine d'essai montée entre deux séparateurs. Le second banc d'essai, le canal HAWAC (**H**orizontal **A**ir/**Wa**ter **C**hannel), est dédié à l'étude des écoulements à co-courant. Le ressaut hydraulique, c'est-à-dire la transition quasi-stationnaire et discontinue se produisant au passage d'un écoulement torrentiel à un écoulement de rivière, fut étudié dans ce canal fermé. De plus, des mesures furent consacrées à la croissance instable de vagues conduisant aux écoulements en bouchons observée depuis l'entrée du canal. Afin de permettre une analyse quantitative des mesures optiques, un algorithme détectant l'interface stratifiée dans les images de la caméra fut développé, ceci autorisant des traitements statistiques pouvant être comparés avec les résultats de calculs CFD.

Le troisième montage expérimental est installé dans l'autoclave du banc d'essai TOPFLOW afin d'effectuer des essais en équilibre de pression avec l'atmosphère de la cuve même dans les conditions opératoires typiques pour un réacteur. La vaine de mesure représentant un modèle aplati de la branche chaude du réacteur à eau pressurisée (REP) allemand *Konvoi* à l'échelle 1/3 est équipée de grandes parois de verre dans la région du coude et de l'entrée du générateur de vapeur afin de permettre une observation visuelle. Les expériences furent conduites en air/eau à température ambiante et une pression maximale de 3 bars ainsi qu'en vapeur/eau jusqu'à 50 bars et 264°C. Quatre types d'expériences furent effectués, incluant des cas de figure génériques ainsi que des cas de validation transitoire concernant des problèmes typiques de sûreté nucléaire. Les essais en écoulement à co-courant simulent par exemple la convection naturelle diphasique dans le circuit primaire d'un REP. La distribution de probabilité du niveau d'eau mesuré dans le simulateur de la cuve réacteur fut utilisée pour caractériser l'écoulement dans la branche chaude. De plus, le comportement d'engorgement de ce modèle fut étudié lors d'expériences dédiées à la limite d'écoulement en contre-courant (CCFL). La caractéristique d'engorgement est comparée avec des données expérimentales et corrélations semblables disponibles dans la littérature. Ceci montre que la hauteur du canal est la longueur caractéristique à utiliser dans le paramètre de Wallis dans le cas de canaux de section rectangulaire. Par ailleurs, des effets de condensation ont dû être pris en compte dans l'analyse des expériences en vapeur/eau. Finalement, les résultats expérimentaux confirment que la similarité de Wallis est appropriée pour dimensionner la limite d'écoulement en contre-courant (CCFL) dans la branche chaude d'un REP sur grande plage de conditions de pressions et températures.

Enfin, divers exemples de comparaison entre expérience et simulation mettent en évidence les possibilités offertes par les données pour aider au développement et à la validation de codes CFD. Outre la comparaison d'aspects qualitatifs, un exemple montre comment traiter les résultats de CFD afin de permettre des comparaisons quantitatives avec l'expérience.

ACKNOWLEDGEMENTS

This thesis is the result of my work as scientific associate at the *Institute of Safety Research* of *Helmholtz-Zentrum Dresden-Rossendorf*. This was mainly carried out in the frame of research projects funded by the *German Federal Ministry of Economics and Technology*, project numbers 150 1265 and 150 1329.

I express my gratitude to Professor Frank-Peter Weiß for inviting me to visit the *HZDR* as I was still a student. Without letting me know what happens in the forest of Rossendorf, I would probably never have tried this way. Thank you in particular for your efforts making my Ph.D. position possible and for accepting to be my "Doktorvater". Furthermore, thank you very much to Professor Horst-Michael Prasser, who gave me the liking for research. Without your contagious enthusiasm for two-phase flows, I may not have chosen to pursue this scientific career. The impulses you gave to my work at the beginning have shaped the Ph.D. till the end. Many thanks also go to Professor Akio Tomiyama for being co-referee of this thesis: it is an honour for me! I hope that our fruitful cooperation will have a long future…

Furthermore, I have to thank my colleagues of the *Institute of Safety Research* who all have their part in this thesis: working on a large scale test facility needs a good team and TOPFLOW has it! My gratitude goes in particular to Dr. Dirk Lucas, Matthias Beyer, Tobias Seidel, Dr. Deendarlianto and Dr. Thomas Höhne for the profitable scientific discussions, helpful comments or legwork for joint papers – especially for the CFD simulations by Thomas Höhne and Deendarlianto shown here. Moreover, I thank my colleagues of the department of *Experimental Thermal Fluid Dynamics* who helped me with more down-to-earth but necessary tasks like for instance the building up of a test facility, the operation of a measuring system or simply with solving daily administrative problems, etc. These are in particular Tobias Sühnel, Dr. Uwe Hampel, Dr. Helmar Carl, Heiko Pietruske, Peter Schütz, Klaus Lindner, Heiko Rußig, Marko Tamme, Steffen Weichelt, Alexandr Zaruba and Claudia Losinski. I am also grateful to the students I had the chance to supervise, among others Katja Scholze and Julia Fiebrandt. This was a great experience for me and your work contributed directly to the thesis. Moreover, thanks to the colleagues of the department of *Reactor Safety* for the helpful discussions on the nuclear background of this work, by name Dr. Frank Schäfer, Polina Tusheva and Dr. Sören Kliem.

A special thank goes to Professor Wallis for the interesting e-mail discussions and for sending me his original poem!

Finally, I am deeply grateful to my family who supported this project over all the years, despite the distance separating us. Not least, thank you so much Andrea for your affection and your patience…

Christophe Vallée

CONTENTS

1. Introduction and motivation 14

1.1. Technical background of stratified two-phase flows 14
1.1.1. Issues in the petroleum industry 14
1.1.2. Issues in the nuclear reactor safety 16

1.2. Objectives of the thesis 19

2. State of the art 20

2.1. Horizontal two-phase flows 20
2.1.1. The horizontal two-phase flow regimes 20
2.1.2. Flow pattern maps for horizontal two-phase flows 21
2.1.2.1. The empirical flow pattern map of Mandhane et al. (1974) 21
2.1.2.2. Flow regime transition model of Taitel & Dukler (1976) 22

2.2. The hydraulic jump phenomenon 26
2.2.1. The hydraulic jump in open channel flows: classical approach 26
2.2.1.1. Historical considerations 26
2.2.1.2. The Bernoulli equation and the specific energy 28
2.2.1.3. The Froude number – characterising the flow conditions 29
2.2.1.4. Calculation of the sequent depths ratio 30
2.2.2. The hydraulic jump in closed conduits 31

2.3. Counter-current two-phase flows and flooding 32
2.3.1. General considerations 32
2.3.2. Flooding characteristics 33
2.3.2.1. Generalities 33
2.3.2.2. The Wallis parameter 34
2.3.2.3. The Kutateladze number 34
2.3.2.4. Range of validity 35
2.3.3. Influence of the fluid properties 35

2.4. Stratified two-phase flow investigations in hot leg typical geometries 37
2.4.1. Overview of the test facilities 37
2.4.2. Co-current flow experiments 39
2.4.3. Investigations on CCFL in hot leg typical geometries 40
2.4.4. Occurrence of the hydraulic jump in hot legs 43

3. Generic investigations in horizontal channels 45

3.1. Preliminary tests in a horizontal channel connected on both ends to separators 45
3.1.1. The horizontal channel for preliminary tests 45
3.1.2. Results obtained by interface capture methods 46
3.1.2.1. Interface capture method 46
3.1.2.2. Water level history during slug flow 47
3.1.3. Dynamic pressure measurements 49
3.1.4. Particle Image Velocimetry (PIV) of a slug 50
3.1.5. Lessons learnt from the preliminary tests 52

3.2. Investigations in the Horizontal Air/Water Channel 52
3.2.1. The **H**orizontal **A**ir/**Wa**ter **C**hannel (HAWAC) 52
3.2.2. Experimental possibilities offered by the HAWAC 53

3.2.2.1. Effects of the inlet blade inclination on the two-phase flow 53
3.2.2.2. Flow regimes and flow pattern map of the HAWAC 54
3.2.2.3. Comparison with the flow pattern transitions of Mandhane et al. (1974) 54
3.2.2.4. Comparison with the flow regime transition model of Taitel & Dukler (1976) 55
3.2.3. Optical measurements on the hydraulic jump 58
3.2.3.1. Water level measurement: methodology 58
3.2.3.2. Example of measurement results 58
3.2.3.3. Probability distribution of the water level 59
3.2.3.4. Study on the influence of the air flow rate on the hydraulic jump 60
3.2.4. Optical measurements during slug flow 63
3.2.4.1. High-speed video observations and interface capture 64
3.2.4.2. Water level measurement 64
3.2.4.3. Statistical treatment of the measured water levels for comparison with CFD 65

4. Applied investigations in a model of the hot leg of a pressurised water reactor 67

4.1. The hot leg model of the TOPFLOW test facility 67
4.1.1. The hot leg test section 67
4.1.2. Specific measures required for the observation of high-pressure steam/water flows 67
4.1.2.1. The pressure chamber for experiments under pressure equilibrium 67
4.1.2.2. Insulation of the test section at high pressure levels 68
4.1.2.3. Special measures needed for the camera observation 69
4.1.2.4. Illumination systems 71
4.1.3. Instrumentation of the hot leg model 72
4.1.3.1. Overview 72
4.1.3.2. Correction of the air flow meter FIC4-10 74

4.2. Overview of the hot leg experiments 75
4.2.1. Type of experiments 75
4.2.2. Boundaries and arrangement of the test matrix 76

4.3. Co-current flow experiments 78
4.3.1. Experimental procedure and test matrix 78
4.3.2. Examples of typical co-current flow experiments 79
4.3.2.1. Experiment with continuous behaviour 79
4.3.2.2. Experiment with periodic behaviour 80
4.3.3. Evolution of the probability distribution of the water level measured in the RPV simulator 81
4.3.4. Comparison with high-speed video observations 84

4.4. Counter-current flow experiments 84
4.4.1. Experimental procedure 84
4.4.2. Example of counter-current flow experiment 85
4.4.3. Qualitative comparison with other counter-current flow experiments 86

4.5. Counter-current flow limitation experiments 87
4.5.1. Experimental procedure and test matrix 87
4.5.2. Typical counter-current flow limitation experiments 88
4.5.2.1. Air/water experiment with a water flow rate of 0.3 kg/s 88
4.5.2.2. Air/water experiment with a water flow rate of 0.9 kg/s 90
4.5.2.3. Flow behaviour observed during a steam/water experiment 91

4.5.3. Data treatment procedures for the arrangement of the flooding curve of the hot leg model 93
4.5.3.1. Principle 93
4.5.3.2. Validation of the processing method 94
4.5.4. The Wallis parameter for channels with rectangular cross-section 95
4.5.4.1. Characteristic length for straight channels: indications from the literature 95
4.5.4.2. Characteristic length for hot leg models with rectangular cross-section – comparison of the air/water flooding characteristics with the results of the Kobe University 97
4.5.4.3. Comparison between the hot leg models with rectangular cross-section and previous investigation in pipes 100
4.5.5. Flooding characteristics of the hot leg model: comparison between air/water and steam/water experiments 103
4.5.5.1. Flooding characteristics in the Wallis parameter diagram 103
4.5.5.2. Flooding characteristics in the Kutateladze number diagram 104
4.5.6. Consideration of steam condensation effects 105
4.5.6.1. Qualitative considerations 105
4.5.6.2. Methodology and analysis of the results 105
4.5.6.3. Plausibility check on the steam condensation rate 107
4.5.6.4. Plausibility check on liquid entrainment from the steam/water separator 109
4.5.7. Comparison with the results obtained at UPTF 110

5. Example of comparisons between experimental results and CFD simulations 112

5.1. CFD simulation with time-dependent inlet boundary conditions for slug generation in a short channel 112
5.1.1. CFD model of the preliminary test channel 112
5.1.2. Qualitative comparison of the CFD results with optical observations 113
5.1.3. Comparison of quantitative data 114
5.1.3.1. Slug propagation across the duct 114
5.1.3.2. Dynamic pressure 115
5.1.4. Pertinence of the comparison with the experiment 116

5.2. CFD model for a self-generation of slug flow 116
5.2.1. CFD model of the HAWAC 116
5.2.2. Qualitative CFD results 117
5.2.3. Interface capture method for the CFD simulation results 118
5.2.3.1. Methodology 118
5.2.3.2. Quantitative results from CFD calculations 119
5.2.4. Quantitative comparison between simulation and experiment 120

5.3. Simulation of the hot leg experiments 120
5.3.1. CFD model of the hot leg test section 121
5.3.2. Simulation results and comparison with the experiment 122

6. Summary and conclusions 124

7. References and credits 126

8. Nomenclature 134

Appendix: Detailed test matrix of the hot leg experiments 137

L'écoulement des fluides diphasiques
Se déguise en régimes spécifiques,
Qui nous rendent perplexes
Et font drôlement complexe
Son dévoilement scientifique.

Pas de deux, G. B. Wallis (1989)

---

1. INTRODUCTION AND MOTIVATION

Most of the time without noticing it, everyone of us is surrounded by gas/liquid multiphase flows in his daily life. This starts already while preparing breakfast, when the tea water boils and steam bubbles rise up or when the coffee machine gurgles due to its heater which uses two-phase flows to elevate the water to the level of the filter. Many other examples may be cited like the impingement of a water jet into a water tank or into a sink, the rising of gas bubbles in a glass of beer or a flute of champagne, the beating of egg whites, etc. Multiphase flow phenomena are encountered in nature as well: falling rain, air entrainment in the flow of mountain torrents, droplet formation from breaking waves, steam production in geysers or volcanic eruptions are some examples.

Furthermore, gas/liquid multiphase flows are of great technical and economic interest as they occur in many industrial fields. However, multiphase flows are still insufficiently understood, and therefore, this domain of fluid mechanics is currently one of the most active in research. In this section, some of the current issues related to stratified two-phase flows in industrial facilities are developed, followed by the objectives of the present work.

1.1. Technical background of stratified two-phase flows

1.1.1. Issues in the petroleum industry

Multiphase flows occur in several major industrial fields and especially in oil and gas extraction facilities. The flow of different immiscible phases together in a single pipe line may be imposed by the local conditions or desired for practical or economic reasons (Biberg, 2005). In fact, in the petroleum fields usually a mixture of liquid and gaseous hydrocarbons (oil and natural gas) is found, which can only be extracted simultaneously. Furthermore, water as a third phase often arises. This is either already present naturally with the hydrocarbons in the reservoir or is injected by the operator to enhance the oil recovery (Hewitt, 2005 ; Berthelsen, 2004). In particular for the extraction of heavy oils, hot water or steam is used to decrease the viscosity of the multiphase mixture (Devold, 2009). Furthermore, in some cases a separation of the phases, although technically possible, may be more expensive than tackling the consequences of the multiphase flow regime. As an example, many offshore platforms or floating production, storage and offloading (FPSO) units are connected to a grid of subsea wells or to the shore with several kilometres long multiphase flow pipelines (see Figure 1.1 and Total, 2008).

In the horizontal or slightly inclined pipes, many different stratified flow regimes can develop depending for instance on the flow rates, the system geometry or fluid properties. Among these flow regimes, especially slug flow has become an important issue for industrial facilities as it exists over a wide range of flow rates and can pose serious operational problems (ABB, 2004). In fact, although the boundary conditions at the pipe line inlet are stationary, the flow develops to an intermittent regime spontaneously. This particular character of slug flow leads to significant variations in time of the instantaneous gas and liquid flow rates as well as to large pressure fluctuations. Consequently, this flow regime hinders a steady-state operation of the facility and, as a result, it can be necessary to severely reduce the production, or in the worst case, to shut the facility down (ABB, 2004). Furthermore, many safety problems arise due to slug flow like, for example, overpressures, especially in separators or at valves and bends, or material fatigue caused by the repetitive stress. In the end,

uncontrolled slugs may lead to a component rupture. The design of the facility and in particular the piping layout can help to reduce the occurrence or the impact of slug flow. Moreover, at the end of a multiphase flow line, a separation of the phases is required before each can be processed, which often necessitate special measures to catch slugs. Therefore, mainly two types of separators are in use: large vessels including internals like baffles, filters and vortex breakers (see Devold, 2009) or special arrangements of interconnected pipes (finger type slug catcher). The buffer volume of such slug catchers should be designed to store the largest expected liquid plugs, which requires knowledge of the flow regime.

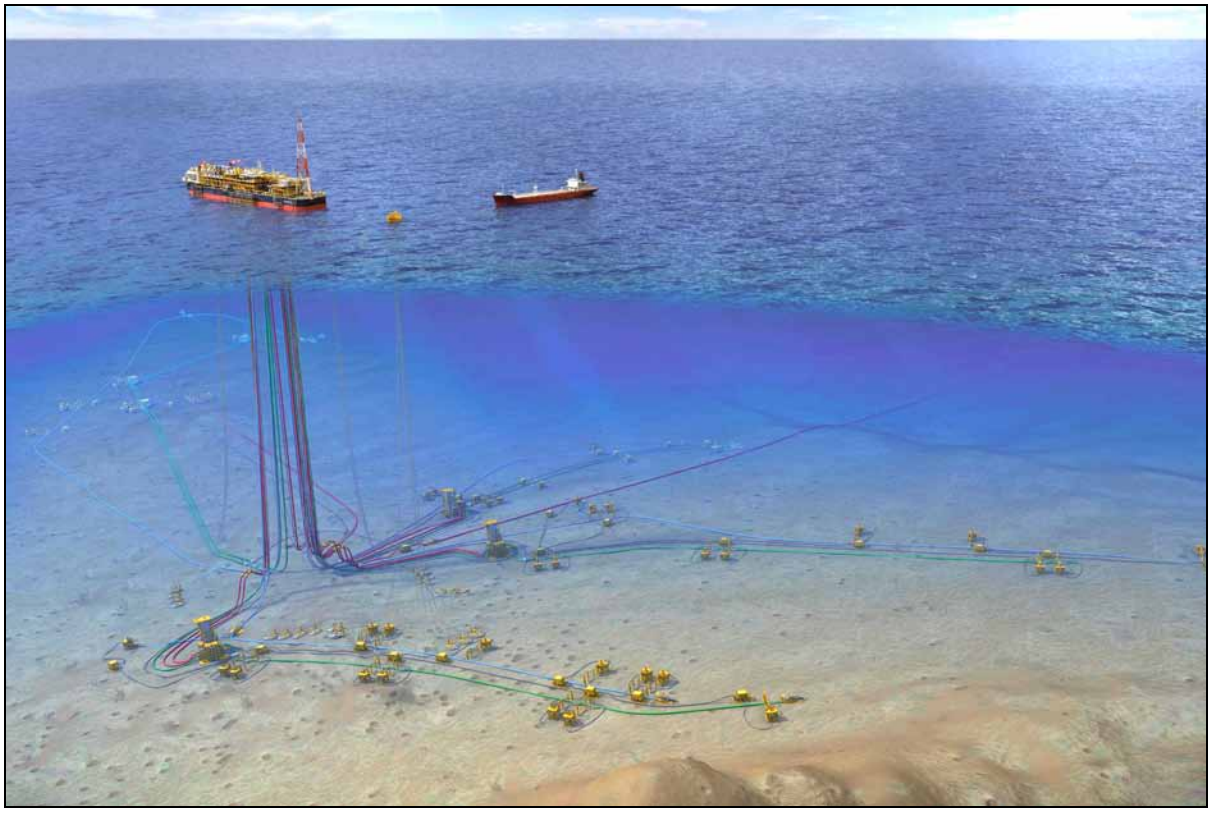

Figure 1.1: Development plan for the offshore field of *Pazflor* (Angola) / source: Total (2008)

Recently, the oil spill in the Gulf of Mexico showed in the news headlines the risks and technical challenges inherent to deepwater offshore oil extraction. During 87 days, gaseous and liquid hydrocarbons were flowing out of the wellbore before the situation could be get under control. Among others, multiphase flow issues may have led to this environmental catastrophe. In fact, in an accident investigation report of BP (2010), eight different events were identified to be possibly involved in the causal chain conducting to the oil spill. According to BP, even though not concerning stratified flows, some of these "key findings" are related to multiphase flows in general:

- One of the physical barriers installed between the wellbore and the reservoir was an annulus of nitrified foam cement slurry. Due for instance to a wrong design of this multiphase material, the cement annulus may have been porous to hydrocarbons, which were consequently not hindered to flow through the wellbore annulus.
- About two hours prior to the ignition on board of the *Deepwater Horizon* platform, the heavy drilling mud contained in the riser was replaced with lighter seawater, underbalancing the well. This operation led to an uncontrolled flow of hydrocarbons in the production casing and later on in the riser. Consequently, at that critical moment, including the unsuspected hydrocarbons, the facility was filled with several fluids of different densities (cf. Figure 1.2). This dangerous blow-out situation was identified only 40 minutes after it can be recognised a posteriori in the records.
- The first well control actions taken by the crew were routing the fluids exiting the riser to a mud gas separator system. This equipment was rapidly overwhelmed and natural gas vented

directly onto the rig, where it ignited. A fire engulfing the drilling platform followed, making it impossible to initiate from the rig further manual actions to prevent an oil spill.

Due to the potential perturbations and hazards, the understanding of the flow phenomena is a key issue for the design and operation of multiphase flow systems. However, the diversity of possible situations and the complexity of the phenomena still do not allow satisfying descriptions of the flow. Therefore, experiments are needed to improve the actual flow regime predictions and simulation tools in order to optimise the design and to guarantee safe operational conditions (called “flow assurance” in the petroleum industry).

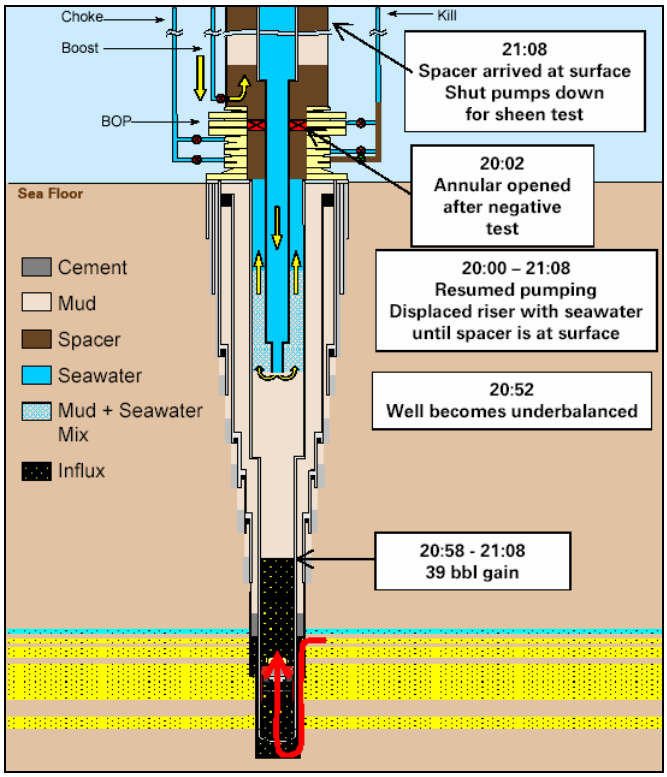

Figure 1.2: Simulated flow conditions in the bore during the injection of seawater underbalancing the well / source: BP p.l.c. (2010)

1.1.2. Issues in the nuclear reactor safety

Two phase flows also occur in all the power plants using a steam/water cycle to drive the turbine in general, and these are an issue for the operation of nuclear reactors in particular. In fact, steam is produced in the core under normal operation conditions in boiling water reactors, but can arise in pressurised water reactors as well during an incident or accident. Consequently, in order to guarantee the highest possible level of safety for these complex and expensive installations over their lifetime, the nuclear community has significantly contributed to the two-phase flow research activities over the past decades.

In a nuclear reactor, emergency strategies have to be mapped out in order to enable the reliable removal of the decay heat from the reactor core under all operational and accidental conditions, as for instance, in the event of a loss of coolant accident (LOCA) in a pressurised water reactor (PWR). During a hypothetical small break LOCA with partial failure of the high pressure emergency core cooling system, because the decay heat cannot be removed by the leak flow, it has to be released to the secondary circuit over the steam generators (SG). Therefore, the primary circuit is designed to favour a natural circulation if the main coolant pumps are not available (D’Auria & Frogheri, 2002). First, a single phase natural circulation arises, even if steam is generated in the core due to the depressurisation of the primary circuit. Later on, when the water level in the reactor pressure vessel (RPV)

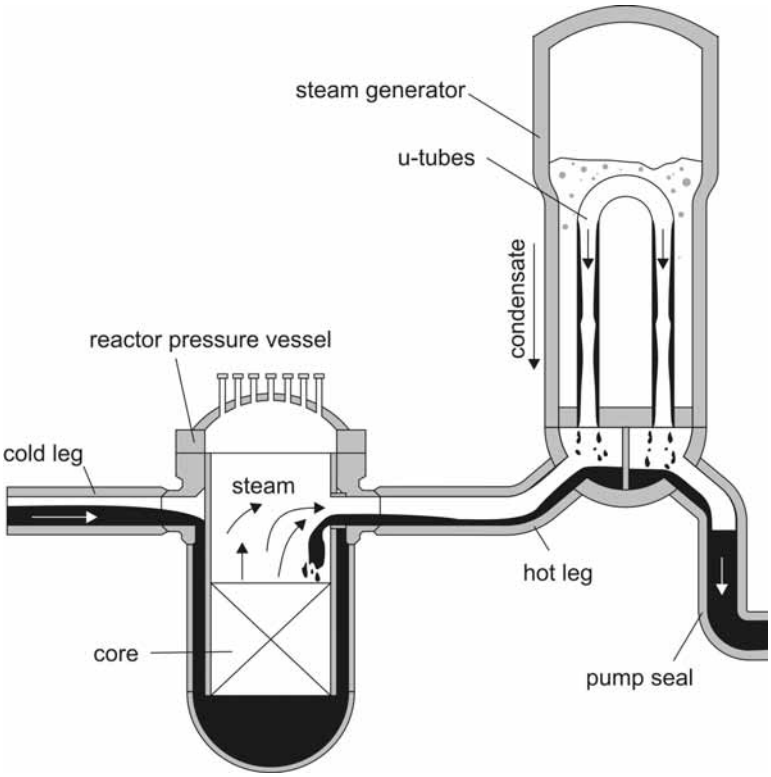

Figure 1.3: Schematic view of the flow in the primary circuit of a PWR during the reflux condenser cooling mode

drops down in the upper plenum to the level of the leg nozzles, the flow evolves to a two-phase natural circulation. In this case, the co-current two-phase flow patterns occurring in the main cooling lines of the PWR influence the heat removal efficiency as well as the duration this regime sustains (Petritsch & Mewes, 1999).

At an advanced stage of a loss of coolant accident (LOCA), when the water level in the RPV falls down below the hot leg nozzle at latest, mainly steam will flow to the steam generator. As a result, when the steam enters the steam generator U-tubes leading to high void fractions, natural circulation breaks down. If, moreover, the coolant temperature is higher in the primary circuit compared to the secondary one, the reflux condenser cooling mode can occur (Wang & Mayinger, 1995). In the reflux condenser mode, the steam coming from the RPV condensates in the vertical U-tubes of the steam generator. In each half of the steam generator, the condensate flows down the tube in which it has been formed. Therefore, about one half of the condensate flows as usual via the pump to the downcomer, whereas the other half flows via the hot leg back to the upper plenum. In the hot leg, the condensate has to flow in counter-current to the steam, as illustrated in Figure 1.3.

However, the counter-current flow of condensate and steam is only stable for a certain range of flow rates. In fact, if the steam flow increases too much, the liquid is carried over by the steam and partially entrained in the opposite direction. This is the beginning of the counter-current flow limitation (CCFL). As a consequence, either the hot leg (Figure 1.4) or the steam generator U-tubes may be flooded (Liu, 2001), which further decreases the water level in the RPV and reduces the core cooling. In case of an additional increase of the steam flow rate, the condensate – but also emergency core cooling water injected in the hot leg if this system is available – may be completely blocked and the cooling of the reactor core from the hot leg would be impossible. Finally, the counter-current flow limitation results in the displacement of the water inventory in the primary system from the RPV to the loops. This causes a further decrease of the water level in the RPV, which may lead to a core uncovering and consequently to a potential failure of the fuel rods. Therefore, the precise prediction of CCFL conditions in the hot legs is an important issue for the nuclear reactor safety (Jeong, 2002).

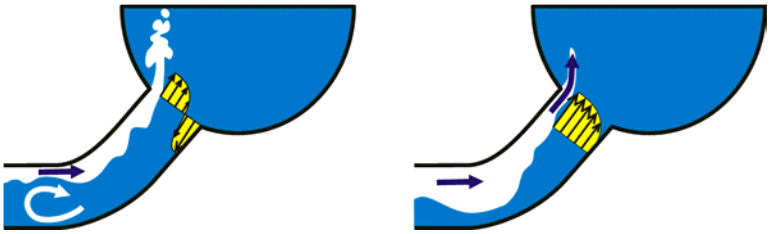

low water inventory high water inventory

Figure 1.4: Possible flow phenomena in the hot leg bend during CCFL
(adapted from Teschendorff et al., 1998)

Moreover, the reflux condenser cooling mode may also appear during the outage of a PWR unit for maintenance or refuelling purposes. During this operational regime, although the heat delivered by the core is very low compared to power operation, the reactor cooling may be problematic because of the particularity of the plant configurations, including the unavailability of many systems. Furthermore, if the core cooling is not assured, the risk of radioactive material release may be high since different confinement barriers can be opened during the outage (e.g. primary circuit or containment building). Moreover, contrary to those defined for power operations, the technical specifications for non-power conditions are based on limited safety analyses. However, in particular the operation at reduced coolant inventory may present unique situations and phenomena not encountered during power operation (cf. U.S.NRC, 1990). Consequently, special care is required for the operation of nuclear reactors during outage.

In an exemplary hypothetic accident scenario, the decay heat power is already low and the primary circuit is cold and at atmospheric pressure. Furthermore, the primary coolant is partially drained and the water level reaches the middle of the main cooling lines, while nitrogen or air fills the remaining volume (Lee et al., 1996). During this phase of the shutdown procedure called mid-loop operation, the decay heat produced by the core is released by a special facility: the residual heat removal (RHR) system. For instance, in case of a station blackout, the pumps of the residual heat removal system may stop (Don Fletcher et al., 1991). If the failure takes place with the primary circuit closed (i.e. before or after the opening of vents, manways or of the reactor pressure vessel upper head), the coolant will be heated up to saturation conditions, leading to vapour production and finally to an increase in the system pressure.

In order to avoid a core uncovering, different counter-measures can be taken to remove the decay heat (Dumont et al., 1994). According to the German guidelines, at least one steam generator should be ready to take over the RHR system, and it consequently has to be filled with water on the secondary side (Schollenberger et al., 2008). In this case, the decay heat would be released to the secondary circuit using the reflux condenser cooling mode as well. If the RHR system cannot be restarted, this is the only way to cool the reactor core indefinitely, nevertheless, feedwater at the secondary side of the active steam generators is needed. Consequently, this hypothetical transient leads to similar flow conditions in the hot leg as described for the LOCA and possibly to counter-current flow limitation. Though, due to the presence of non-condensable gases in the circuit, the behaviour may be different, and in particular, the initiation of reflux cooling may be difficult and require an increase in the system pressure (Don Fletcher et al., 1991).

For the validation and optimisation of accident management strategies, such transient scenarios are reproduced in dedicated test facilities or rather simulated numerically. The use of one-dimensional system codes like *ATHLET*, *CATHARE* or *RELAP5*, which are principally based on empirical correlations, is a common practice. The implemented correlations are adapted to reflect the macroscopic flow characteristics and were extensively validated over the past decades, consequently, they can be used for safety analyses. However, the correlations do not allow to predict the flow conditions from first principles, and therefore, present limitations. In particular for the flow situations dominated by 3D effects, as for instance CCFL, a computational fluid dynamics (CFD) approach is required to evaluate the local behaviour in detail. These simulation methods are state of the art for

single phase flows and are in use for a wide range of industrial applications (e.g. aerodynamic design of cars and aircraft). However, the actual CFD codes applied to two-phase flows do not meet the high level of confidence needed in the field of nuclear reactor safety (Smith & Hassan, 2008). Moreover, the direct numerical simulations (DNS), which are completely based on physics, are currently not practicable for the relevant industrial scale of applications. Therefore, other CFD approaches are followed using models which include closure laws or constants to be determined empirically. As a consequence, the CFD codes must be validated to allow reliable two-phase flow simulations. Therefore, dedicated experimental data is needed with high resolution in space and time, preferably at reactor typical boundary conditions, for comparison with CFD calculations.

1.2. Objectives of the thesis

Due to the technical significance of stratified two-phase flows, many experimental databases and publications are already available. However, most of these are only of limited interest for the development and validation of CFD codes. In fact, ideally the experimental data and the simulation should present similar resolutions in order to catch the same scale of phenomena, and consequently, enable meaningful comparisons. In the past, most experimental investigations were carried out with local measuring systems like thermocouples, optical or conductivity probes, densitometers, etc. The delivered punctual or cross-sectional values were adapted to the development and validation of the previous generation of numerical simulation tools (e.g. system codes). However, the resolution of experimental data has to evolve in parallel to that of computer codes in order to support their theoretical model development and validation. Over the past two decades, this led to the emergence of new high-resolution measuring systems as, for instance, the wire-mesh sensor or particle image velocimetry (PIV). However, there is still a lack of "CFD grade" experimental data, and in particular of high-resolution data at reactor typical boundary conditions as most investigations are conducted with air and water at atmospheric pressure and room temperature. This deficit of existing data is particularly evident for CCFL in hot leg typical geometries, although, according to Damerell & Simons (1993), the reflux condenser mode could appear at primary system pressures of up to 80 bar.

Therefore, in the frame of the present thesis, dedicated experimental investigations were performed in different test channels. For each, a rectangular cross-section was chosen in order to provide optimal observation possibilities for the application of high-resolution optical measuring techniques, like high-speed video observation or PIV. After a state of the art, preliminary investigations performed in a horizontal acrylic glass channel to check the envisaged experimental possibilities are presented. Then, taking advantage of the accumulated experience, a second channel (called HAWAC) was designed for generic investigations of air/water co-current flows at atmospheric pressure and room temperature. The hydraulic jump as the quasi-stationary discontinuous transition between super- and subcritical flow will be analysed in this closed channel. Moreover, the instable wave growth leading to slug flow is investigated. After the application of a self-developed algorithm for the detection of the interface in the camera frames, statistical treatments showing the global structure of the interface will be presented. The main part of this thesis concerns experiments in a flat model of the hot leg of a pressurised water reactor operated in the pressure chamber of the TOPFLOW test facility. This is used to perform air/water and steam/water experiments at pressures of up to 50 bar and temperatures of up to 264°C, but under pressure equilibrium with the inside atmosphere. The investigations focus on the flow regimes observed in the region of the elbow and of the steam generator inlet chamber, which are equipped with glass side walls. An overview of the experimental methodology and of the acquired data will be given. These cover experiments without water circulation, which can be seen as test cases for CFD development, as well as counter-current flow limitation (CCFL) experiments, representing transient validation cases of a typical nuclear reactor safety issue. Detailed data analyses will be presented for the co-current flow and for the CCFL experiments. The influence of the rectangular cross-section geometry on the flooding behaviour and in particular the suited non-dimensional parameter to plot the flooding characteristics will be investigated. Furthermore, the CCFL characteristics measured during the low pressure air/water as well as the high pressure and high temperature steam/water experiments will be compared. Finally, different examples of comparison possibilities offered by the experimental data with CFD simulation results will be presented.

2. STATE OF THE ART

2.1. Horizontal two-phase flows

2.1.1. The horizontal two-phase flow regimes

While flowing co-currently through a pipe, observations show that a gas and a liquid distribute differently depending on the boundary conditions. According to characteristic properties, the different topologies are commonly classified in flow patterns (also flow regimes). In contrast to the vertical flow patterns, which are symmetrical, the influence of gravity leads to a stratification in the case of horizontal flows. The main flow regimes commonly considered in the literature (e.g. Huhn & Wolf, 1975 or Hetsroni, 2010), illustrated in Figure 2.1, are:

- Smooth stratified flow: both phases are completely separated, the gas and the liquid flowing at the top and the bottom of the pipe, respectively. The fluid velocities are rather low so that the interface remains undisturbed.
- Stratified wavy flow: at higher gas velocities, small waves travelling in flow direction are generated at the interface, like the ripples created by the wind on the surface of a lake. However, in this case, the wave crests do not reach the top of the pipe.
- Elongated bubble flow (or plug flow): at higher liquid velocities compared to smooth stratified flow, waves also form at the interface, but reach the top of the tube generating liquid plugs. These plugs are separated by elongated gas bubbles flowing on top of the pipe with the liquid.
- Slug flow: at higher gas velocities compared to elongated bubble flow, the gas becomes the governing phase: the formed liquid plugs are pushed forwards by the gas pockets. The slug front is characterised by a rolling-over structure often leading to droplet entrainment downstream of the slug as well as to bubble capture inside of the slug. At very high gas velocities, the slug may not completely close the tube because the gas flows through a small gap left free on top of the slug. The slug flow regime is characterised by a high pressure drop and large pressure fluctuations.

N.B.: elongated bubble flow and slug flow together are designated as intermittent flow. In both cases, the generation of the liquid plugs are commonly attributed to the Kelvin-Helmholtz instability (cf. Wallis & Dobson, 1973 or Taitel & Dukler, 1976). One considers a disturbance like for instance a solitary wave propagating in a two-phase flow conduit. On top of this wave, the free cross-section for the gas flow is reduced, and consequently, the gas velocity increases. According to the Bernoulli equation, this causes a reduction of the static pressure (like on top of an airfoil) which counteracts the force of gravity and, if dominating, leads to an instable wave growth.

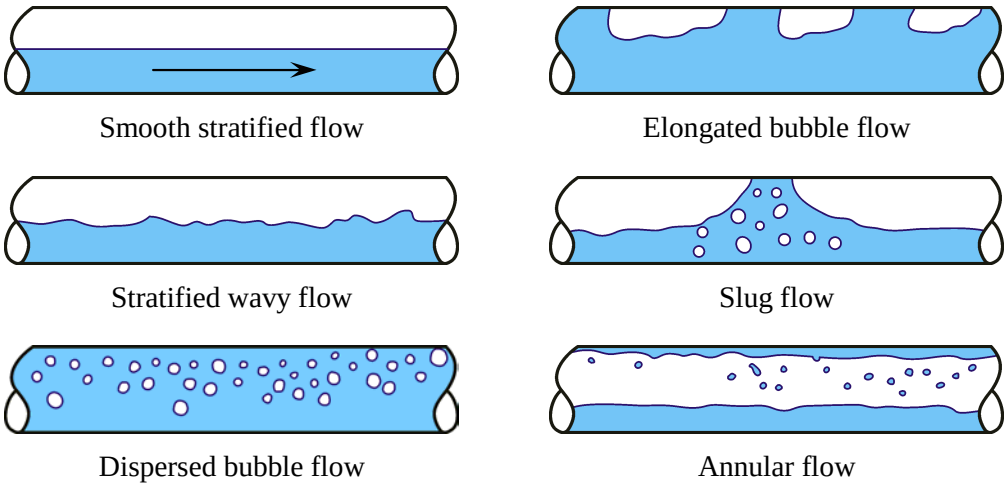

Figure 2.1: Schematic view of the main horizontal two-phase flow regimes (adapted from Hetsroni, 2010)

- Dispersed bubble flow: small gas bubbles are dispersed in the continuous liquid phase. Due to the gravity, the highest gas concentration is found in the upper part of the pipe. This flow regime is observed at very high liquid velocities and relatively low gas flow rates.
- Annular flow: at very high gas velocities and relatively low liquid flow rates, the liquid phase forms a film at the surface of the tube and the gas flows in the central region. The film is usually thicker at the bottom of the pipe and may be continuous or not. Furthermore, droplets often detach from the liquid film and are entrained by the gas to flow in the core.

The variety of observed flow regimes illustrates itself the difficulty to describe or model two-phase flows.

2.1.2. Flow pattern maps for horizontal two-phase flows

The prediction of the flow regime in function of the boundary conditions is very important because this influences many flow parameters like pressure drop or liquid hold-up. Consequently, models of these parameters can not be developed for all flow regimes together. Therefore, the optimal design of facilities depends on the choice of the right model and finally on the accurate prediction of the flow regime. Therefore, many different methods have been proposed in the literature over the last decades. Probably due to its descriptive character, but also to its accuracy, two-dimensional maps of the flow pattern regions have become a widespread tool (see overview in Table 2.1 of Corradini, 1997). In the following sections, two of the most used approaches are presented.

2.1.2.1. The empirical flow pattern map of Mandhane et al. (1974)

The most established flow pattern map for horizontal two-phase flows based on experimental observations is probably the one by Mandhane et al. (1974). According to the authors, one of the main lacks of previous maps was their limited range of applicability, which led to large discrepancies. Consequently, they regroup in a single data bank about 1200 experimental points obtained for horizontal air/water flows and published previously by various authors. The overall range of parameters was as follows:

- pipe diameter: 12.7 … 152.4 mm
- superficial velocities: $j_L = 10^{-3}$ … 7.3 m/s
  $j_G = 0.04$ … 170 m/s

In the past, many different parameters were proposed in the literature for the coordinate axes of the flow pattern map, some of them being rather complex to calculate and therefore difficult to interpret. Following the conclusions of Govier & Aziz (1972), Mandhane et al. choose the fluid superficial velocities for their own flow pattern map (see Figure 2.2). As a result, they found out that this simple parameter takes adequately into account the effect of the pipe diameter. Furthermore, Mandhane et al. studied the influence of the fluid properties on the flow regime transitions with an extended version of the data bank including about 6000 experimental points. Therefore, they compared the results obtained with the fluid property dependent parameters proposed so far in the literature with the points of the data bank. Mandhane et al. found out that none of the methods leads to a significant improvement of the flow regime prediction compared to their flow pattern map for air/water flows.

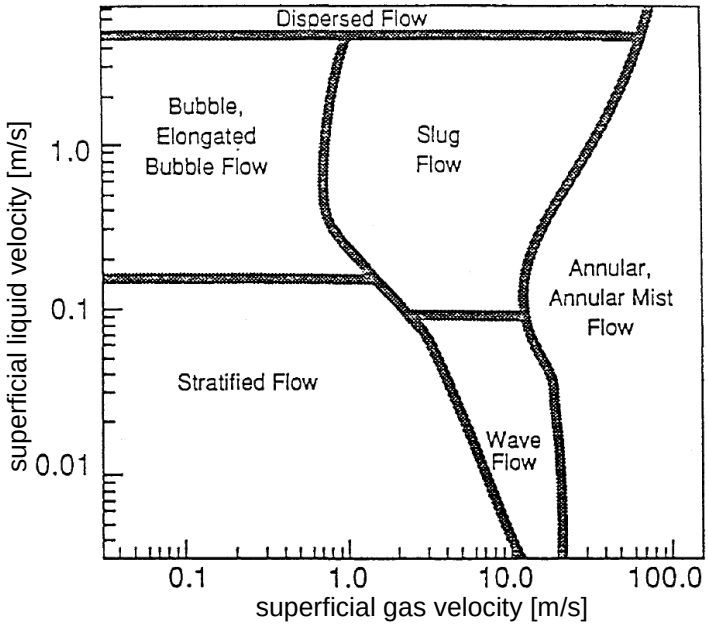

Figure 2.2: Flow pattern map for horizontal gas/liquid flows / source: Mandhane et al. (1974)

2.1.2.2. Flow regime transition model of Taitel & Dukler (1976)

According to Taitel & Dukler, the empirical flow regime maps (e.g. Mandhane et al., 1974) have several limitations: extensive series of experiments are needed, the choice of the map coordinates is arbitrary, an extrapolation of the results to other boundary conditions is uncertain. Therefore, in order to overcome these limitations, Taitel & Dukler (1976) were the first to develop a theoretical model predicting the flow regime transitions in function of the fluid properties and flow rates, of the pipe diameter and its inclination to the horizontal. The proposed transition criteria are based on physical concepts only and have no need of experimental data.

a) Theory of equilibrium stratified flow

The model developed by Taitel & Dukler first needs the calculation of the equilibrium liquid level for stratified flow. As shown in Figure 2.3, this is a hypothetic liquid level, observed if smooth stratified flow would establish in the conduit independently of the boundary conditions. Under this assumption, a momentum balance on each phase (noted with *L* for the liquid and *G* for the gas) leads to:

$$\begin{cases} -A_L \cdot \left(\frac{dp}{dx}\right) - \tau_{WL} \cdot S_L - \tau_i \cdot S_i + \rho_L \cdot A_L \cdot g \cdot \sin\alpha = 0 \\ -A_G \cdot \left(\frac{dp}{dx}\right) - \tau_{WG} \cdot S_G - \tau_i \cdot S_i + \rho_G \cdot A_G \cdot g \cdot \sin\alpha = 0 \end{cases} \quad (2.1)$$

with *A* the cross-sectional area of the flow for the corresponding phase, *S* the part of the conduit perimeter in contact with the phase and α the conduit inclination to the horizontal, as illustrated in Figure 2.3. Furthermore, *p* is the pressure, *x* the coordinate in flow direction, τ the shear stress, ρ the fluid density and *g* the acceleration of gravity. The index *i* designate interfacial parameters.

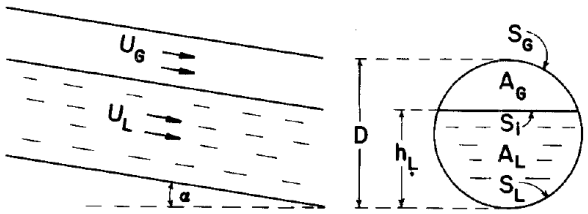

Figure 2.3: Equilibrium stratified gas/liquid flow / source: Taitel & Dukler (1976)

Under equilibrium conditions, the pressure drop should be equal for both phases. Consequently, we obtain the following equation:

$$\frac{dp}{dx} = -\tau_{WL} \cdot \frac{S_L}{A_L} - \tau_i \cdot \frac{S_i}{A_L} + \rho_L \cdot g \cdot \sin\alpha = -\tau_{WG} \cdot \frac{S_G}{A_G} - \tau_i \cdot \frac{S_i}{A_G} + \rho_G \cdot g \cdot \sin\alpha \qquad (2.2)$$

Taitel & Dukler used the following expression for the wall shear stress of phase *k* in function of the flow velocity u:

$$\tau_{Wk} = f_k \cdot \frac{\rho_k \cdot u_k^{\,2}}{2} \qquad (2.3)$$

The friction factor *f* is evaluated for both phases with:

$$f_k = C \cdot \left(\frac{D_{h,k} \cdot u_k}{\nu_k} \right)^{-n} \qquad (2.4)$$

Here, *v* is the kinematic viscosity and $D_{h,k}$ is a phase specific hydraulic diameter calculated as follows:

$$D_{h,L} = \frac{4 \cdot A_L}{S_L} \;;\; D_{h,G} = \frac{4 \cdot A_G}{S_G + S_i} \qquad (2.5)$$

Furthermore, the coefficients *C* and *n* depend on the flow character:

- for laminar flow: $C = 16$ $n = 1$
- for turbulent flow: $C = 0.046$ $n = 0.2$

In general, the shear stress at the interface is obtained with:

$$\tau_i = f_i \cdot \frac{\rho_G \cdot (u_G - u_i)^2}{2} \qquad (2.6)$$

In their paper, Taitel & Dukler consider that the shear stress at the interface can be approximated by the wall shear for the gaseous phase, as defined in equation (2.3).

Furthermore, in order to simplify the expressions, the following terms are non-dimensionlised (and noted with a tilde: $\tilde{X}$) according to the following reference variables:

- lengths: $\tilde{L} = L/D$ (2.7)
- surfaces: $\tilde{A} = A/D^2$ (2.8)
- velocities: $\tilde{u}_k = \frac{u_k}{j_k} = \frac{u_k}{u_k \cdot \frac{A_k}{A}} = \frac{A}{A_k}$ (2.9)

Here, the length term *D* is the pipe diameter, or in the case of non-circular cross-sections the classical hydraulic diameter given by:

$$D_h = \frac{4 \cdot A}{S} \qquad (2.10)$$

Finally, after substitution of the shear stress terms in equation (2.2) according to the expressions given above and non-dimensionalisation, one obtains the following equation:

$$X^2 \cdot \left[\left(\tilde{u}_L \cdot \tilde{D}_{h,L} \right)^{-n} \cdot \tilde{u}_L^{\,2} \cdot \frac{\tilde{S}_L}{\tilde{A}_L} \right] - \left[\left(\tilde{u}_G \cdot \tilde{D}_{h,G} \right)^{-n} \cdot \tilde{u}_G^{\,2} \cdot \left(\frac{\tilde{S}_G + \tilde{S}_i}{\tilde{A}_G} + \frac{\tilde{S}_i}{\tilde{A}_L} \right) \right] - 4 \cdot Y = 0 \qquad (2.11)$$

with *X*, the Lockhart-Martinelli parameter, defined as follows:

$$X^2 = \frac{\left|(dp/dx)_L\right|}{\left|(dp/dx)_G\right|} = \frac{\frac{4 \cdot C}{D} \cdot \left(\frac{j_L \cdot D}{\nu_L}\right)^{-n} \cdot \frac{\rho_L \cdot {j_L}^2}{2}}{\frac{4 \cdot C}{D} \cdot \left(\frac{j_G \cdot D}{\nu_G}\right)^{-n} \cdot \frac{\rho_G \cdot {j_G}^2}{2}} \tag{2.12}$$

and *Y* a parameter given by:

$$Y = \frac{(\rho_L - \rho_G) \cdot g \cdot \sin\alpha}{\left|(dp/dx)_G\right|} = \frac{(\rho_L - \rho_G) \cdot g \cdot \sin\alpha}{\frac{4 \cdot C}{D} \cdot \left(\frac{j_G \cdot D}{\nu_G}\right)^{-n} \cdot \frac{\rho_G \cdot {j_G}^2}{2}} \tag{2.13}$$

For given flow rates, fluid properties, cross-sectional dimensions and inclination, the value of the parameters *X* and *Y* can be determined directly. Furthermore, the other non-dimensional terms in equation (2.11) can be either calculated directly or expressed in function of the non-dimensional liquid level h_L/D (for pipes please see equations 10 to 16 in the paper of Taitel & Dukler). Afterwards, equation (2.11) can be solved iteratively while varying the value of h_L/D. As an example, the variation of the non-dimensional liquid level with the Lockhart-Martinelli parameter plotted by Taitel & Dukler for pipes of various inclinations is shown in Figure 2.4.

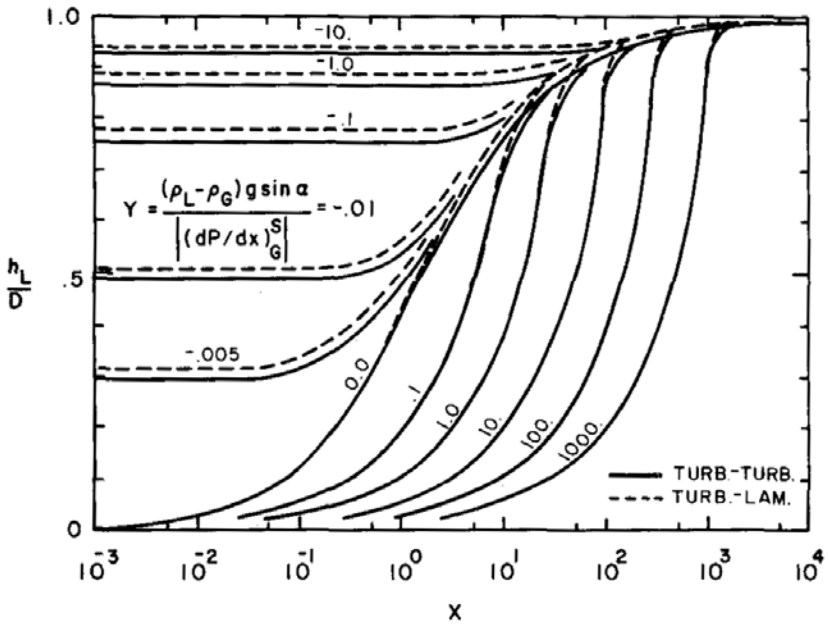

Figure 2.4: Equilibrium stratified liquid level for pipes / source: Taitel & Dukler (1976)

b) Transition models

For the transition between stratified and intermittent (i.e. elongated bubble and slug flow) or annular dispersed flows, Taitel & Dukler (1976) used a stability criterion based on the Kelvin-Helmholtz theory. After a review of the approaches proposed so far in the literature, they choose the following non-dimensional criterion:

$$F^2 \cdot \left(\frac{1}{\left(1-\tilde{h}_L\right)^2} \cdot \frac{{\tilde{u}_G}^2}{\tilde{A}_G} \cdot \frac{d\tilde{A}_L}{d\tilde{h}_L}\right) \geq 1 \tag{2.14}$$

with *F* a modified Froude number defined as follows:

$$F = j_G \cdot \sqrt{\frac{1}{g \cdot D \cdot \cos\alpha} \cdot \frac{\rho_G}{\rho_L - \rho_G}} \tag{2.15}$$

The transition between intermittent and annular dispersed flows is described according to the idea that if the liquid flow rate is too low, the instable growing waves can not reach the top of the pipe, and consequently, plugs or slugs can not appear. Ideally, the water level can be represented by a sinusoid, because waves are taking the liquid of the surroundings while growing, which leads to the trough. Consequently, below a certain liquid level, the conduit dries up at the wave trough before the crest reaches the top of the pipe, and slugging is impossible. In this case, the liquid is swept around the pipe wall and annular flow is obtained. The liquid level delimiting both flow regimes chosen by Taitel & Dukler is simply the centre line, leading to the following criterion:

$$\frac{h_L}{D} = 0.5 \tag{2.16}$$

It should be noticed that this corresponds to a single value of the Lockhart-Martinelli parameter *X* as shown in Figure 2.4.

In order to model the transition between stratified smooth and stratified wavy flows, Taitel & Dukler consider that the gas velocity, which causes wave generation, should be large enough so that pressure and shear work overcome viscous dissipation. Using a condition introduced by Jeffreys (1925, 1926), which is adapted and simplified according to recent findings, Taitel & Dukler proposed the following dimensionless criterion:

$$K > \frac{2}{\tilde{u}_G \cdot \sqrt{\tilde{u}_L \cdot s}} \tag{2.17}$$

with:

$$K = F \cdot \sqrt{Re_L} = \left(j_G \cdot \sqrt{\frac{\rho_G}{(\rho_L - \rho_G) \cdot D \cdot g}} \right) \cdot \sqrt{\frac{D \cdot j_L}{\nu_L}} \tag{2.18}$$

For the calculation of the sheltering coefficient *s*, Taitel & Dukler recommend to use the value of 0.01, which is in agreement with the experiments of Benjamin (1959).

The transition from intermittent to dispersed bubble flow is considered to take place when the turbulent fluctuations at the interface overcome the buoyancy forces which keep the large gas bubbles formed between two plugs on top of the pipe. Consequently, the following non-dimensional equation is used to model the flow regime transition:

$$T^2 \geq \frac{8 \cdot \tilde{A}_G}{\tilde{S}_i \cdot \tilde{u}_L^{\,2} \cdot \left(\tilde{u}_L \cdot \tilde{D}_L\right)^{-n}} \tag{2.19}$$

with *T* defined as follows:

$$T = \sqrt{\frac{\frac{4 \cdot C}{D} \cdot \left(\frac{j_L \cdot D}{\nu_L} \right)^{-n} \cdot \frac{\rho_L \cdot j_L^{\,2}}{2}}{(\rho_L - \rho_G) \cdot g \cdot \cos\alpha}} = \sqrt{\frac{\left|(dp/dx)_L\right|}{(\rho_L - \rho_G) \cdot g \cdot \cos\alpha}} \tag{2.20}$$

c) Flow regime map for pipes

All non-dimensional transition criteria are function of a dimensionless parameter (*F*, *K* or *T*) and of h_L/D, which depends itself on the parameters *X* and *Y*. Consequently, the flow regime transition is a function of three non-dimensional parameters: *X*, *Y* and (*F*, *K* or *T*). Furthermore, each transition satisfies simultaneously the corresponding criterion as well as the equilibrium stratified liquid level equation. Finally, for a given value of *Y*, the coordinates of the transitions can be calculated in function of the Lockhart-Martinelli parameter *X* and of the corresponding parameter (*F*, *K* or *T*). As a result, the transitions can be plotted in a two-dimensional flow regime map, as shown in Figure 2.5 for horizontal pipes.

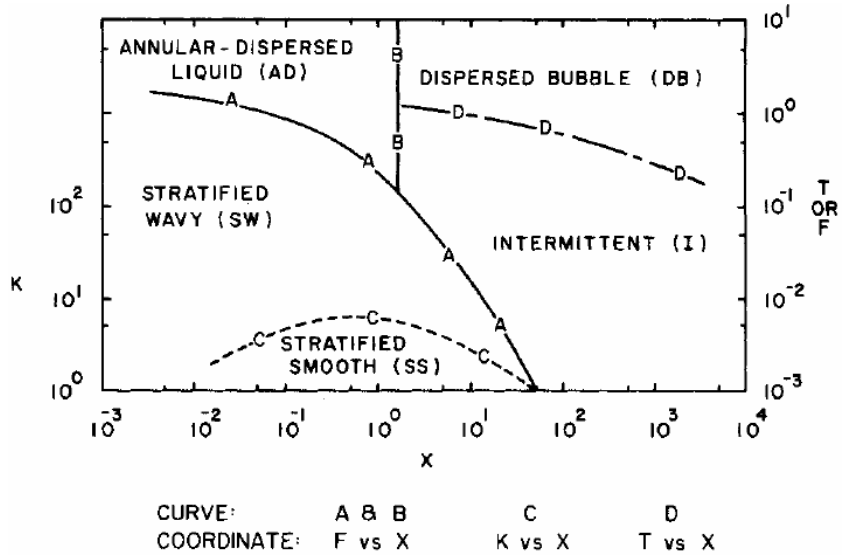

Figure 2.5: Flow regime map for horizontal two-phase flows in pipes / source: Taitel & Dukler (1976)

Moreover, in their paper, Taitel & Dukler (1976) compared the results obtained with their theoretical approach and the empirical flow regime map of Mandhane et al. (1974). They applied the model to air and water at atmospheric pressure and room temperature flowing in a horizontal pipe of 2.5 cm inner diameter. For this relatively small pipe diameter corresponding to the most data of Mandhane et al., Taitel & Dukler found a good agreement of the flow regime transitions obtained with both methods. However, for large diameter pipes, the paper shows that the transitions predicted by the model are sensibly different in a map plotted in function of the superficial velocities. Furthermore, in a parametric study, Taitel & Dukler demonstrate the high sensitivity of the transition lines to the pipe inclination.

2.2. The hydraulic jump phenomenon

The hydraulic jump is the discontinuous transition between super- and subcritical flow, and is characterised by a steep rising of the water surface with a high turbulence zone as well as possible gas entrainment. Hydraulic jumps are common in the every day life, like for instance its circular form encountered when the water jet flowing downwards out of the tap hits the sink. The hydraulic jump occurs also frequently in nature, for example when a mountain torrent flows into a lake or when the torrent current is hindered by an obstacle found in the river bed. The phenomenon is well-known by hydraulic engineers, who use it in particular to protect natural or artificial structures from erosion caused by high velocity flows. In fact, the hydraulic jump can easily be forced in channels, downstream of dam spillways or hydroelectric power stations (called stilling basins) and leads to a very efficient dissipation of the excess kinetic energy. Furthermore, the tidal bore created by the incoming tide in the estuary of some rivers and travelling against the current is actually a moving hydraulic jump.

2.2.1. The hydraulic jump in open channel flows: classical approach

2.2.1.1. Historical considerations

Observations of hydraulic jumps can be established back to the XVth century and the first are commonly attributed to Leonardo da Vinci (1452-1519) (cf. Chanson, 1995). However, the first scientific investigations on the hydraulic jump in open channels were conducted in the early XIXth century by Bidone (1820), who gave his name to the phenomenon in Italian ("salto di Bidone"). For his investigations, Bidone chose two straight channels with rectangular cross-sections, opened at the top and slightly inclined to the horizontal. He installed wooden dams of different heights in the channel bed, perpendicularly to the channel walls, in order to force the apparition of a noticeable jump. Furthermore, the water flow rate was varied. Bidone described in details the phenomenon and found out that the hydraulic jump moves to the dam if the water flow rate (i.e. the velocity) is increased. He

also remarked that the measured water levels upstream of the jump are the same with and without dam in the channel.

A few years later, Bélanger (1828) considered the hydraulic jump in a theoretical essay about the permanent flow regime in open channels. He noticed that the gradually varied flow equation (or backwater equation) can not be applied across the jump. Consequently, he proposed to describe the phenomenon mathematically using the momentum equation applied to fluid particles as formulated by Navier. Bélanger performed a balance before and after the hydraulic jump, which allowed him to determine the water level difference over the jump. The obtained equation (article 59, p. 35 in the original paper) was found to predict well the measurements of Bidone. However, as shown by Chanson (2009), his theoretical treatment was incorrect as it neglects energy dissipation. The good agreement with the data of Bidone was due to the relatively low Froude number of the experiments, where energy losses in the jump are small.

Later on, Darcy & Bazin (1865) published their own research results based on 7 years of work and including 5 years of experiments. Therefore, an approximately 600 m long test channel with a width of 2 m and a depth 0.95 m was built between the canal of Bourgogne and the river Ouche. This open channel declined of 2.7 m over his total length, presenting three different slopes (from 0.0020 to 0.0084 m/m). The channel was used for a considerable amount of experimental investigations (cf. Figure 2.6) including uniform flow regimes, distribution of the velocities in currents, flow discontinuities ("mouvement varié") and wave propagation. In their memoir, Darcy & Bazin described the two possible categories of water accumulation observed upstream of dams depending on the sub- or supercritical character of the incoming flow. In order to characterise the flow behaviour, they identified the importance of a non-dimensional parameter today known as the *Froude number* (including an additional correction coefficient α, estimated to nearly 1). Furthermore, Darcy & Bazin pointed out an analogy between the denominator of this parameter and the propagation velocity of solitary waves as determined by J. Scott Russell in 1845. This comparison was used to provide a physical analysis of the hydraulic jump, which was reinforced by their own experimental observations. Darcy & Bazin described systematically and in detail the shape of hydraulic jumps in function of the upstream Froude number. Moreover, they indicated that two types of pressure loss affect the water level across a hydraulic jump: the wall friction, dominating at Froude numbers slightly larger than 1, and the pressure loss due to "tumultuous movements" inside of the jump (i.e. turbulence), which are preponderant at high Froude numbers.

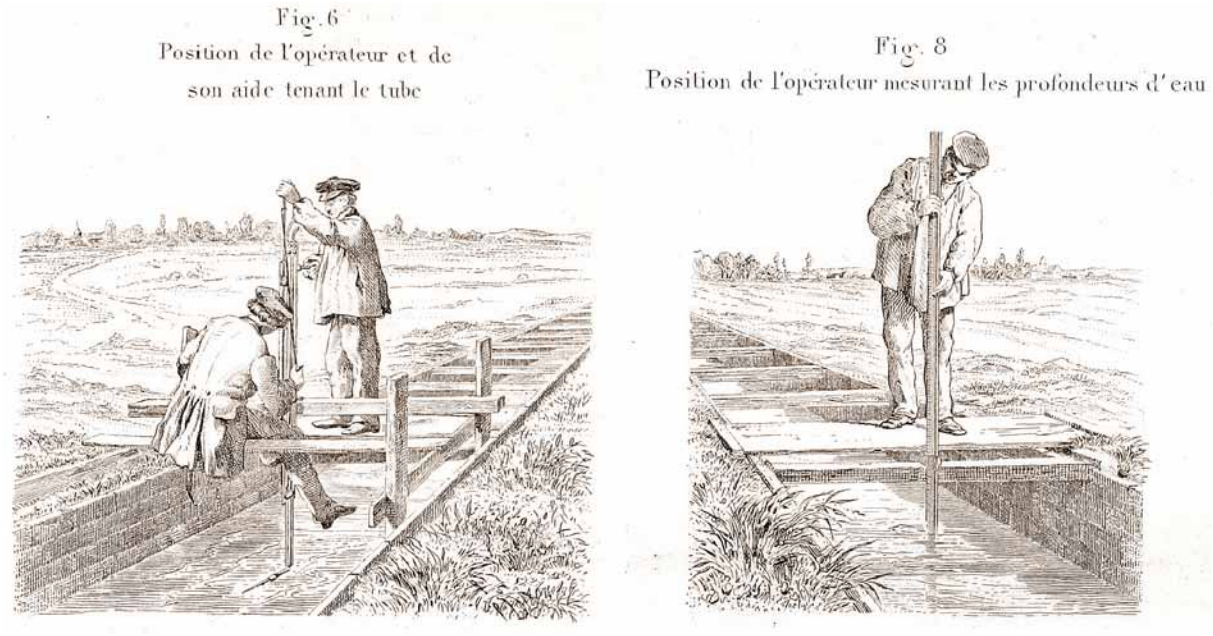

Figure 2.6: Original illustration of the measurements of Darcy & Bazin (1865)

From the beginning of the XXth century, the main characteristics of the hydraulic jump are known and therefore the phenomenon is a standard in university hydraulics (e.g. Flamant, 1900; Henderson, 1966).

2.2.1.2. The Bernoulli equation and the specific energy

According to Henderson (1966) as well as Chanson (1995), the concept of specific energy was introduced by B. A. Bakhmeteff in 1912. Considering that the flow is stationary and is derived from a potential (i.e. irrotational), we can write the Bernoulli equation at each point *A* of the flow (Figure 2.7):

$$\frac{1}{2}\cdot\rho\cdot v^2+\rho\cdot g\cdot z+p=\text{cste} \qquad (2.21)$$

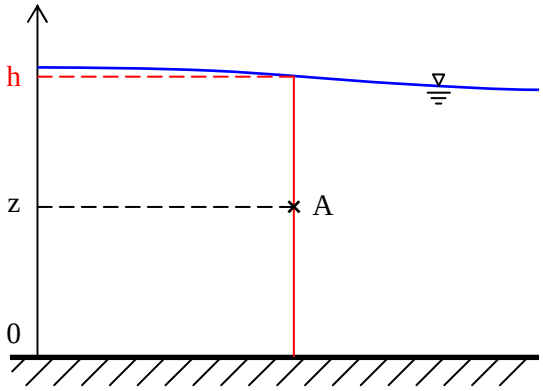

Figure 2.7: Application of the Bernoulli equation to open channel flows

If the slope of the channel bed is close to the horizontal, the pressure term can be expressed according to the hydrostatic pressure distribution:

$$p=p_{atm}+\rho\cdot g\cdot(h-z) \qquad (2.22)$$

The substitution of *p* in the Bernoulli equation and the integration of the value of the atmospheric pressure in the constant delivers:

$$\frac{1}{2}\cdot\rho\cdot v^2+\rho\cdot g\cdot h=\text{cste} \qquad (2.23)$$

Dividing this equation by ρ, the terms are homogeneous to an energy per unit of weight and the constant is called the specific energy *e*:

$$e=\frac{v^2}{2}+g\cdot h \qquad (2.24)$$

Assuming that the velocity distribution is uniform in each channel cross-section of width *W*, the velocity *v* is equal to:

$$v=\frac{\dot{V}}{W\cdot h} \qquad (2.25)$$

Therefore, the specific energy can be expressed in function of constant boundary conditions and of the water level *h* in the cross-section:

$$e=\frac{1}{2}\cdot\left(\frac{\dot{V}}{W\cdot h}\right)^2+g\cdot h \qquad (2.26)$$

For the given channel width *W* and volume flow rate $\dot{V}$, the specific energy can be plot in function of water levels $h \in \mathbf{R}^+$ (negative water levels are not physical), as shown in Figure 2.8. The sum of a hyperbolic function and of a linear function leads to a first decreasing and then increasing specific energy. This means that a specific energy (strictly higher than the minimum possible specific energy at the given flow rate and width) has two preimage water levels, named sequent depths. From the conservation of the mass flow rate applied to an incompressible fluid, a low water level implies a higher velocity. Therefore, the flow regime corresponding to low water levels is called supercritical and this of high water levels is subcritical.

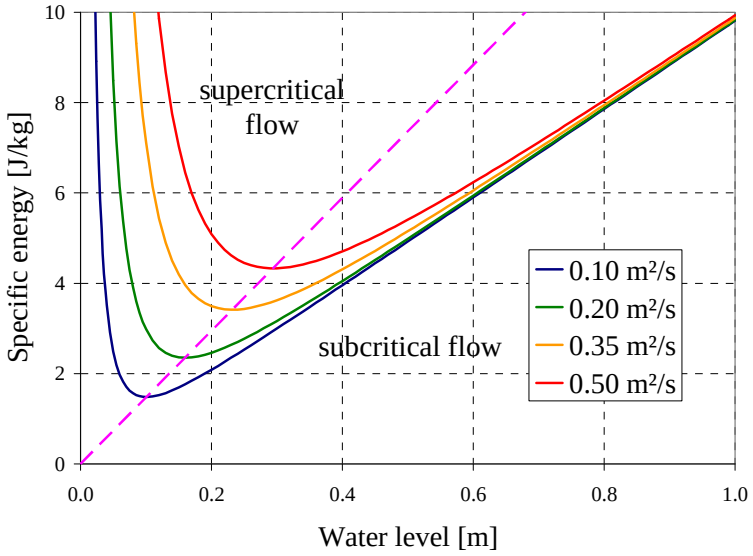

Figure 2.8: Specific energy in function of the water level for given volume flow rates per unit of width

In a hydraulic jump, the flow passes discontinuously from super- to subcritical conditions. The change in water level in the jump indicates that the kinetic energy of the flow upstream of the jump is converted into potential energy, leading to the characteristic sudden rising of the water level. However, the experience shows that this process includes a decrease of the specific energy, which is lost in form of heat over the turbulent energy dissipation.

2.2.1.3. The Froude number – characterising the flow conditions

In order to locate the minimum of the specific energy, we calculate the partial derivative of *e* with respect to *h*:

$$\frac{\partial e}{\partial h} = -\left(\frac{\dot{V}}{W}\right)^2 \cdot \frac{1}{h^3} + g \tag{2.27}$$

The location of the minimum separating the two flow regimes is obtained when the derivative is equal to zero, i.e.:

$$\left(\frac{\dot{V}}{W}\right)^2 \cdot \frac{1}{g \cdot h^3} = \left(\frac{\dot{V}}{W \cdot h}\right)^2 \cdot \frac{1}{g \cdot h} = \frac{v^2}{g \cdot h} = Fr^2 = 1 \tag{2.28}$$

We recognise the Froude number *Fr*, commonly used in open channel hydraulics to characterise the flow conditions in a cross-section (Hager, 1992). This forms the quotient of the flow velocity to the wave propagation celerity in shallow water, as shown hereafter.

According to Ardhuin (2007), the simplest (and at the same time valid) model to describe the motion of surface gravity waves was developed by G. B. Airy in 1841. This theory assumes that:

- the fluid is incompressible;
- the effect of viscosity can be neglected;
- the flow is irrotational (i.e. the velocity vector field is derived from a potential);
- the bottom of the channel is plane;
- the velocity potential varies in space according to a sinusoid.

Ardhuin shows that if all these assumptions are satisfied, the propagation velocity *c* of a wave of wavenumber *k* and angular frequency ω can be expressed in the form of a Laplace equation, which has the following general solution:

$$c^2 = \left(\frac{\omega}{k}\right)^2 = \frac{g}{k} \cdot \tanh(k \cdot h) \tag{2.29}$$

The wavenumber is defined as function of the wavelength λ by:

$$k = \frac{2 \cdot \pi}{\lambda} \tag{2.30}$$

In shallow water flows, the water level *h* can be considered small in comparison to the wavelength, and consequently, the hyperbolic tangent function can be approximated by:

$$\tanh\left(\frac{2 \cdot \pi}{\lambda} \cdot h\right) \xrightarrow[h/\lambda \to 0]{} \frac{2 \cdot \pi}{\lambda} \cdot h \tag{2.31}$$

Finally, the celerity of shallow water surface waves is independent of the wavelength and is equal to:

$$c = \sqrt{g \cdot h} \tag{2.32}$$

According to Equation (2.28) and to Figure 2.8, for a Froude number of unity, the flow is critical. The subcritical flow is defined by $Fr < 1$, which means that waves can propagate downstream as well as upstream. Furthermore, the supercritical flow is characterised by $Fr > 1$ and implies that waves can only propagate downstream. Consequently, a perturbation cannot influence the flow in the upstream direction: the supercritical flow is said upstream controlled.

2.2.1.4. Calculation of the sequent depths ratio

For the calculation of the sequent depths, the Euler equation applied to a control volume enclosing the hydraulic jump can be used (Fermigier, 2004). Its general expression for steady flows is:

$$\sum_i \vec{F}_i = \sum_i \dot{m}_i \cdot \vec{v}_i \tag{2.33}$$

Written for the case of the hydraulic jump as illustrated in Figure 2.9, one gets:

$$\sum_i \vec{F}_i = -\dot{m}_1 \cdot \vec{v}_1 + \dot{m}_2 \cdot \vec{v}_2 \tag{2.34}$$

According to the mass conservation, and assuming that sufficiently far away from the jump the velocity field is unidirectional, this is equivalent to:

$$\sum_i \vec{F}_i = \dot{m} \cdot (v_2 - v_1) \cdot \vec{x} \tag{2.35}$$

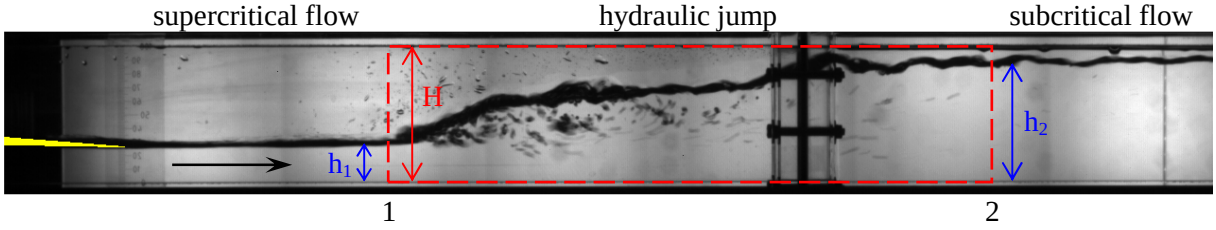

Figure 2.9: Side view of a hydraulic jump in a horizontal channel

Considering that the pressure loss on the walls are negligible compared to turbulent dissipation, the only forces to take into account are the hydrostatic pressure forces applied to the side surfaces of the control volume. This is expressed by the surface integral of the pressure as follows:

$$F_i = \int_S p \cdot dS = \int_{y=0}^{W} \int_{z=0}^{H} p(z) \cdot dy \cdot dz = W \cdot \int_0^{h_i} \left(p_{atm} + \rho \cdot g \cdot (h_i - z)\right) \cdot dz + W \cdot \int_{h_i}^{H} p_{atm} \cdot dz \tag{2.36}$$

The integration leads to:

$$F_i = W \cdot \left[p_{atm} \cdot z + \rho \cdot g \cdot h_i \cdot z - \rho \cdot g \cdot \frac{z^2}{2} \right]_0^{h_i} + W \cdot \left[p_{atm} \cdot z \right]_{h_i}^{H} \tag{2.37}$$

After the evident simplifications, one gets:

$$F_i = W \cdot \left(p_{atm} \cdot H + \rho \cdot g \cdot \frac{h_i^{\,2}}{2} \right) \tag{2.38}$$

In vector form this leads finally to:

$$\sum_i \vec{F}_i = \vec{F}_1 + \vec{F}_2 = W \cdot \left(p_{atm} \cdot H + \rho \cdot g \cdot \frac{h_1^{\,2}}{2} \right) \cdot \vec{x} - W \cdot \left(p_{atm} \cdot H + \rho \cdot g \cdot \frac{h_2^{\,2}}{2} \right) \cdot \vec{x} \tag{2.39}$$

$$\sum_i \vec{F}_i = \frac{1}{2} \cdot W \cdot \rho \cdot g \cdot \left(h_1^{\,2} - h_2^{\,2} \right) \cdot \vec{x} \tag{2.40}$$

According to the Euler equation, equalising this with equation (2.35), both projected on the *x*-axis, one obtains:

$$\dot{m} \cdot (v_2 - v_1) = \frac{1}{2} \cdot W \cdot \rho \cdot g \cdot \left(h_1^{\,2} - h_2^{\,2} \right) \tag{2.41}$$

The mass flow rate can be expressed in function of the density and volume flow rate, which depends itself on the water level and flow velocity upstream of the jump (assuming an uniform velocity distribution):

$$\dot{m} = \rho \cdot \dot{V} = \rho \cdot W \cdot h_1 \cdot v_1 \tag{2.42}$$

Furthermore, from the volume flow rate conservation in a channel with constant width, we have:

$$v_2 = \frac{h_1}{h_2} \cdot v_1 \tag{2.43}$$

Introduced in the above equation, we can write:

$$\rho \cdot W \cdot h_1 \cdot v_1 \cdot \left(\frac{h_1}{h_2} \cdot v_1 - v_1 \right) = \frac{1}{2} \cdot \rho \cdot g \cdot W \cdot h_1^{\,2} \cdot \left(1 - \left(\frac{h_2}{h_1} \right)^2 \right) \tag{2.44}$$

By dividing the equation by $(\rho \cdot W \cdot h_1)$ and expanding the binomial number, we obtain:

$$v_1^{\,2} \cdot \left(\frac{h_1}{h_2} - 1 \right) = \frac{1}{2} \cdot g \cdot h_1 \cdot \left(1 - \frac{h_2}{h_1} \right) \cdot \left(1 + \frac{h_2}{h_1} \right) \tag{2.45}$$

Grouping all the terms in h_2/h_1 on the right and the others on the left lead to:

$$2 \cdot Fr_1^{\,2} = 2 \cdot \frac{v_1^{\,2}}{g \cdot h_1} = \frac{h_2}{h_1} \cdot \left(1 + \frac{h_2}{h_1} \right) \tag{2.46}$$

This is a polynomial equation of the second degree in h_2/h_1, which has one single positive solution:

$$\frac{h_2}{h_1} = \frac{1}{2} \left(-1 + \sqrt{1 + 8 \cdot Fr_1^{\,2}} \right) \tag{2.47}$$

Knowing the water volume flow rate and the water level just before the hydraulic jump, the water level occurring after the jump in open channels can be calculated analytically with this equation.

2.2.2. The hydraulic jump in closed conduits

Contrary to the hydraulic jump in open channel flow, the jump is here limited in size by the conduit height. Moreover, an air flow in the conduit possibly influences the jump over interfacial momentum transfer. In contrast with the extensive literature available for open channel flows and despite occurrence in tunnel spillways, drainage and sewer engineering, the hydraulic jump has received poor attention in closed conduits (Stahl & Hager, 1999).

The hydraulic jump as the transition between free surface flow and discharge single-phase flow in conduits was considered by Hager (1989). This state of the art article is focused on conduit hydraulics applications, principally in inclined lines. The work of Lane & Kindsvater (1938), of Kalinske &

Robertson (1943), of Kalinske & Bliss (1943), of Ahmed et al. (1984), among others, is summarised. The overview given by Hager (1989) concentrates on the following aspects:

- the hydraulic jump characteristics (sequent depth ratio and length);
- the air entrainment in the jump and its ability to transport gas through the conduit.

More recently, Stahl & Hager (1999) reported on hydraulic jump experiments with a free surface flow performed in a nearly horizontal pipe. The jumps were forced by inserting a perforated plate at the pipe outlet. Pictures show the appearance of the hydraulic jump at different Froude numbers. Furthermore, a relation is proposed for the calculation of the sequent depth ratio in this particular case.

Furthermore, Gargallo et al. (2005) investigated the occurrence of hydraulic jumps in a two-phase counter-current flow. In the WENKA test facility, a closed channel with rectangular cross-section, a super-critical water flow was injected in counter-current to a constant air flow. This simulates the injection of emergency core cooling water through the "*Hutze*" in the hot leg of German pressurised water reactors. By reducing the water flow rate, a hydraulic jump occurs in the test section, which was found to be the initiator for a water flow reversal.

2.3. Counter-current two-phase flows and flooding

2.3.1. General considerations

The counter-current flow of a gas and a liquid in the same conduit is possible due to the gravity, which drives the fluid of higher density downwards, while the lighter fluid flows upwards (Figure 2.10-a). However, both phases interact over the friction at the interface. Consequently, for given geometry and fluids, the counter-current flow is only stable up to a maximum relative velocity, known as onset of flooding (Figure 2.10-b). At higher gas or liquid flow rates, the liquid discharge at the bottom of the section is reduced compared to the injected amount. During this flow regime called counter-current flow limitation (CCFL), a part of the downwards flowing liquid is carried over by the gas and entrained in the opposite direction (Figure 2.10-c and d). CCFL is mainly characterised by:

- a sudden increase of the pressure drop over the conduit,
- the generation of large waves and slugs,
- the entrainment of liquid droplets by the gas flow.

At even higher gas flow rates, the liquid can be completely carried over by the gas and the zero penetration is achieved (Figure 2.10-e). In this case as well as at higher gas flow rates, one obtains a co-current flow upstream of the liquid injection point (Figure 2.10-f).

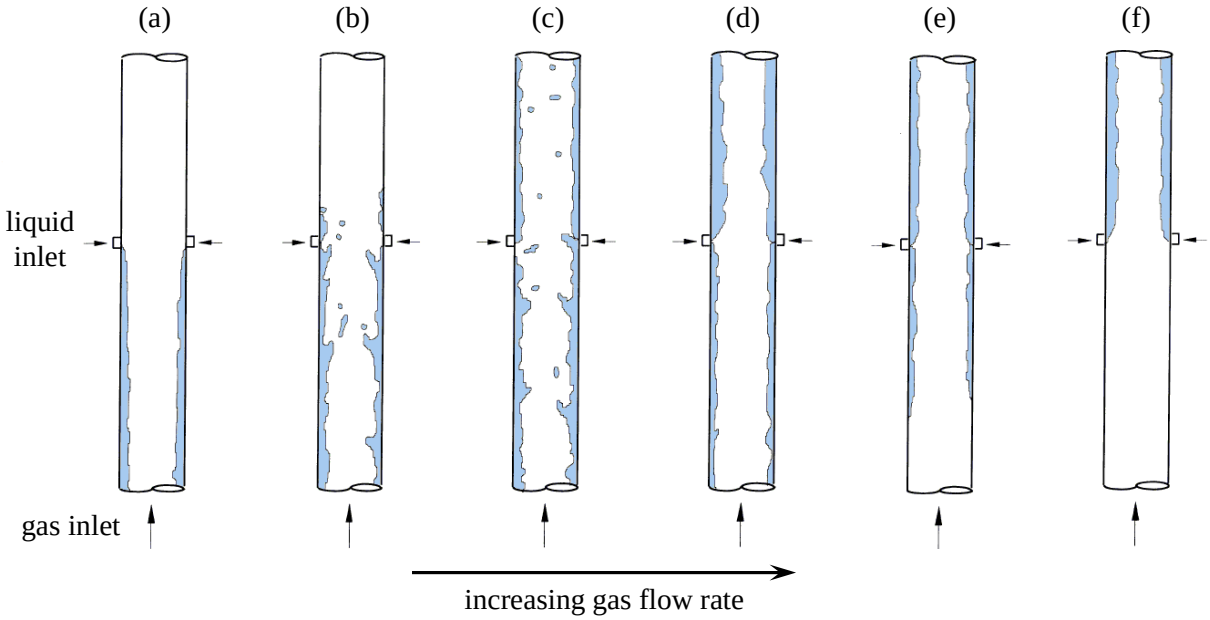

Figure 2.10: Two-phase counter-current flow in vertical pipes (adapted from Zapke & Kröger, 2000-I)

Counter-current flow is of interest in the chemical process industry as it occurs for instance in packed towers and in distillation columns during reflux condensation processes (Levy, 1999). Furthermore, in wickless heat pipes or thermosyphons, used for example in flat plate solar collectors, the evaporated vapour rises to the top end while a condensate film flows in counter-current at the pipe inner wall (cf. Hussein et al., 2006). Not least, flooding is an important issue in the nuclear reactor safety in particular, as described in details in section 1.1.2. Beyond that, CCFL is encountered inconspicuously in the every day life: for instance, a counter-current two-phase flow of wine and air occurs while pouring out a bottle, which limits naturally the maximum outflow.

Consequently, counter-current flows are handled in every book concerning two-phase flows. Among this specific literature, two references of particular interest should be cited here. First, Wallis summarised his results published in the beginning of the 60's in the book "One dimensional two-phase flow" (1969). Later on, Bankoff & Lee (1986) published "A critical review of the flooding literature" resuming all the major work until then. This extensive paper concentrates on CCFL in vertical and inclined conduits and covers all the main aspects like fundamentals, analytical models and experimental investigations.

2.3.2. Flooding characteristics

2.3.2.1. Generalities

In order to quantify the intensity of the counter-current flow limitation, experimental results are usually presented in a flooding diagram. The characteristics are obtained from the plot of the gas flow rate versus the discharge liquid flow rate (i.e. amount of liquid flowing out of the lower test section end). The flooding curve (cf. Figure 2.11) indicates the maximum liquid flow rate for a given gas flow rate, and therefore, delimits the possible combinations of flow rates from the impossible ones. Furthermore, this representation allows to determine an empirical correlation for the general prediction of CCFL conditions as well as of the resulting discharge liquid flow. The correlation depends in general on the section geometry and on the fluid properties. Different parameters like volume or mass flow rate can be used to plot the flooding characteristics, however, non-dimensional parameters have become common as shown in the following sections.

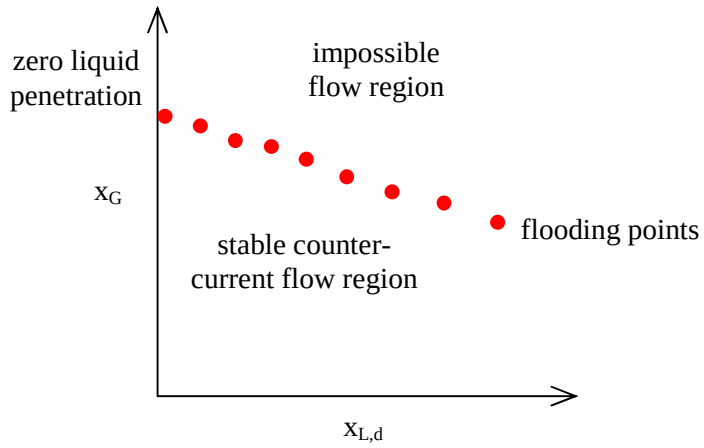

Figure 2.11: Example of empirical flooding characteristics

The CCFL characteristics are often found to be different while the flow rate is increased (flooding) or decreased (deflooding) during the experiment (cf. Wallis, 1969). In fact, as flooding has already been induced, the flow rate has to be significantly reduced to re-establish stable counter-current flow conditions compared to the flow rate necessary to reach the onset of flooding. This phenomenon is commonly described as hysteresis between flooding and deflooding. Dedicated investigations concerning this topic were performed for instance by Celata et al. (1991) with air and water in vertical pipes. This experimental study focuses on the hysteresis effect resulting of a variation of the water flow rate, while the gas flow rate was kept constant.

2.3.2.2. The Wallis parameter

Fundamental investigations on two-phase counter-current flow limitation were performed by Wallis (1961). He conducted experiments with air and water in vertical acrylic glass pipes connected to two tanks. The air was injected in the lower tank, while the upper tank was used for the water injection as well as for the separation of the fluids. A clear head of water was maintained in this reservoir during the experiments. This study includes a variation of the pipe diameter from 1/2 to 2 inches (i.e. 12.7 to 61 mm). Furthermore, Wallis has also investigated the influence of the tube end geometry on the CCFL. Inspired by the work of previous investigators on flooding in packed columns, Wallis proposed to correlate experimental CCFL data using the following general expression:

$$\sqrt{J^*_G} + m \cdot \sqrt{J^*_L} = C \tag{2.48}$$

where C and m are constants determined using experimental results. J^*_G and J^*_L are the non-dimensional superficial velocities (also known as *modified Froude number* or *Wallis parameter*) for gas and liquid, respectively. For the phase i, this is given by:

$$J^*_i = j_i \cdot \sqrt{\frac{1}{g \cdot D} \cdot \frac{\rho_i}{\rho_L - \rho_G}} \tag{2.49}$$

where j is the superficial velocity and ρ the density of the fluid, g the gravitational acceleration and D the inner pipe diameter.

From the dimensional point of view, the Wallis parameter is analogue to the Froude number as defined in equation (2.28). However, the additional density ratio term allows to consider the effect of the fluid densities on the CCFL. Furthermore, this non-dimensional parameter is found to take adequately the effect of the pipe diameter into account, while in general the constants m and C in equation (2.48) depend on the system geometry. In fact, the Wallis type correlation is commonly used for various system geometries, ranging from horizontal or inclined straight pipes to 3 dimensional pipe systems with bends (like the hot leg of a pressurised water reactor, cf. section 2.4.3) as well as perforated plates (cf. Hawighorst et al., 1984). In case of vertical pipes, Wallis (1969) reported that the value of m is equal to unity for turbulent flows. Furthermore, the constant C was found to depend on the geometry of the tube ends: it varies between 0.725 for sharp edges and 1 when end effects are minimised.

2.3.2.3. The Kutateladze number

Another non-dimensional parameter commonly encountered in the flooding literature is the Kutateladze number. According to Sorokin et al. (1965), this parameter was defined in a Russian contribution of 1961 as follows:

$$K_i = j_i \cdot \left(\frac{\rho_i^{\,2}}{g \cdot \sigma \cdot (\rho_L - \rho_G)} \right)^{1/4} \tag{2.50}$$

The Kutateladze number includes the surface tension σ and therefore one essential physical property of the fluids. The Kutateladze number and Wallis parameter are related by the Laplace capillary length λ as the characteristic length in the Wallis parameter. This critical length is defined by:

$$\lambda = \sqrt{\frac{\sigma}{g \cdot (\rho_L - \rho_G)}} \tag{2.51}$$

Consequently, in contrast to the Wallis parameter, the Kutateladze number assumes that the phenomena governing the counter-current flow limitation are independent of the tube diameter. Glaeser (1992) shows that the Kutateladze number is obtained considering that flooding is due to instabilities at the interface. In fact, if the pressure forces at the crest of a wave are higher than the stabilising effect of surface tension, the wave will grow unstably, leading to droplet detachment. The droplets formed in this way are entrained with the gas, and consequently, reduce the discharge water flow. According to Vierow et al. (2008), the Kutateladze type correlation was put forth by Pushkina & Sorokin in 1969 and its most used form (analogous to the Wallis type correlation, see equation (2.48)) was proposed by Tien in 1977. This non-dimensional number is commonly used to correlate flooding experiments in vertical pipes (cf. Levy, 1999) or through perforated plates (cf. Hawighorst et al., 1984

and No et al., 2005). Furthermore, the Kutateladze number is useful in case of geometries where it is difficult to define a characteristic length, like the rod bundles of nuclear reactors.

2.3.2.4. Range of validity

The Wallis parameter and Kutateladze number are convenient for all types of comparisons because of their non-dimensional character, explaining their wide use. Nevertheless, depending on the predominance of surface tension effects or of system scale effects, one of the two parameters is more appropriate to plot the flooding characteristics. For vertical counter-current flow both parameters can be used, however, according to Richter (1981) or Levy (1999) amongst others, the Wallis parameter is better suited for small pipe diameters ($D \leq 50$ mm) and the Kutateladze number for large ones. In order to obtain a smooth variation between both non-dimensional parameters with the pipe diameter, Bankhoff et al. (1981) introduced a special interpolation parameter.

While focusing on stratified flows in inclined or horizontal conduits, it is noticeable that the Wallis parameter has been applied by almost all authors. Furthermore, in a theoretical derivation of the classic flooding correlations, Glaeser (1992) has shown that among the two non-dimensional parameters only the Wallis parameter is applicable to horizontal counter-current flows.

2.3.3. Influence of the fluid properties

Moreover, Wallis (1962) investigated the influence of the liquid viscosity on flooding. The experiments were performed in the same test facility than in the report of 1961 with a vertical pipe of 0.75 inches (i.e. 19 mm) inner diameter. The fluids used were air and different liquids of various viscosities according to Table 2.1. The temperature of the fluids was 10°C ±5°C.

As shown in Figure 2.12, Wallis found out that the flooding characteristics plotted in terms of the non-dimensional superficial velocities are a function of the liquid viscosity. The lower the dynamic viscosity μ, the lower is the zero penetration (interception of the flooding curve with the ordinate axis) and the steeper is the flooding characteristics. Making a parallel with his recent findings about the rise velocity of a cylindrical bubble in a vertical pipe, which depends also on the viscosity, Wallis proposed to use a similar approach. As a consequence, the following non-dimensional inverse viscosity parameter was introduced:

$$N = \frac{1}{\nu_L} \cdot \sqrt{g \cdot D^3 \cdot \frac{\rho_L - \rho_G}{\rho_L}} \tag{2.52}$$

Wallis proposed to express the constants of the flooding characteristics *m* and *C* in the general CCFL equation (2.48) as functions of *N*. For values of *N* greater than 300 (i.e. low viscosities), *m* is equal to unity, whereas for values smaller than 2, the following asymptote is proposed:

$$m = \frac{5.6}{\sqrt{N}} \tag{2.53}$$

The value of the zero penetration constant *C* is equal to 0.7 for small *N* and increases gradually up to 0.88 (or even 1) for values greater that 160 (cf. Figure 3 of the report).

Table 2.1: Fluids used by Wallis (1962) and their properties

Fluid	[-]	water	ethylene	glycerol								
Concentration	[%]	100	100	33	50	60	70	75	80	90	95	99
μ @ 10°C	[Pa·s]	0.0013	0.030	0.004	0.009	0.017	0.039	0.060	0.116	0.498	1.27	3.00
N	[-]	8200	300	2200	1000	560	250	160	90	21	8.2	3.4

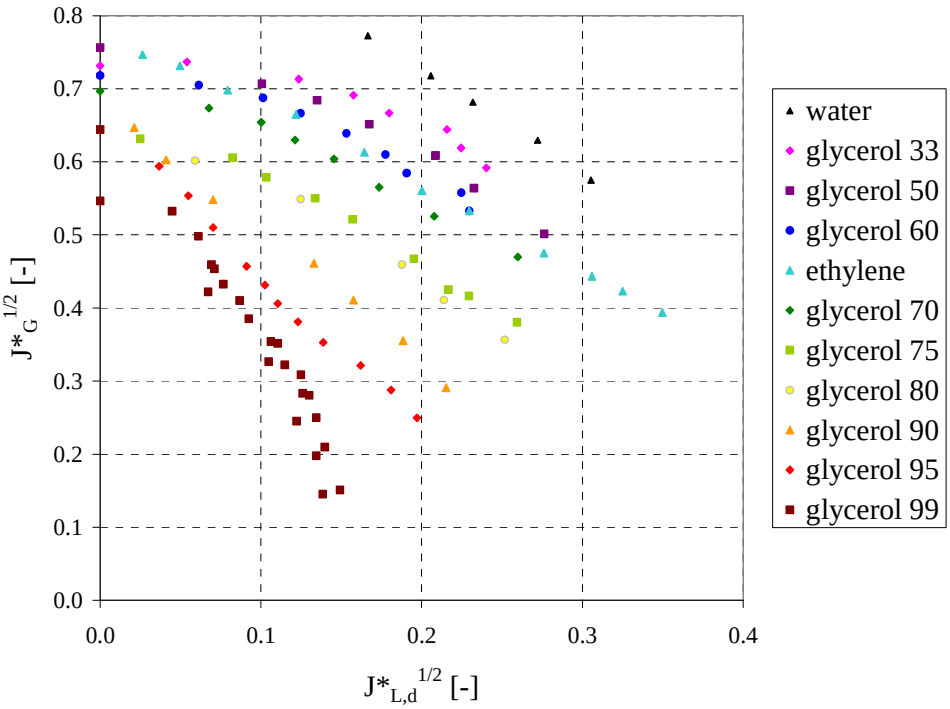

Figure 2.12: Flooding characteristics for counter-current flows of air and various liquids in a vertical pipe obtained by Wallis (1962)

Many years later, Zapke & Kröger performed investigations on counter-current flow limitation in vertical and inclined straight test sections which were published in different papers in 1996 and 2000. First, Zapke & Kröger (1996) studied flooding in a 2 m long transparent acrylic glass tube with 30 mm inner diameter. In order to check the influence of the fluid properties, the experiments were performed with different gases (air, argon, helium and hydrogen) and liquids (water, methanol, isopropanol and aqueous methanol solutions). Before being injected into the test section, the gas was tempered to room temperature in a special heat exchanger in order to compensate the cooling down of the gas due to the expansion from pressurised bottles. The gaseous phase entered the lower separator of the test facility over a honeycomb structure and the liquid phase was introduced into the test section through a 180 mm long sintered section. Zapke & Kröger found that flooding is more sensible to the liquid viscosity than to the surface tension and that the gas viscosity has no effect on CCFL.

Based on their experimental results, Zapke & Kröger (1996) proposed a new flooding correlation for vertical pipes:

$$\sqrt{J_G^*} + \sqrt{J_L^*} = 0.52 \cdot Oh_L^{-0.05} \tag{2.54}$$

The influence of the fluid properties is taken into account in the non-dimensional Ohnesorge number defined as follows:

$$Oh_i = \frac{\mu_i}{\sqrt{\sigma \cdot \rho_i \cdot D}} \tag{2.55}$$

Furthermore, as a result of experiments in inclined pipes with various inlet geometries, Zapke & Kröger proposed a more general formulation of flooding correlation:

$$\sqrt{J_G^*} \cdot (Oh_L)^b + m \cdot \sqrt{J_L^*} \cdot (Oh_L)^b = C \tag{2.56}$$

b, *m* and *C* are empirical constants which depend on the pipe inclination and end geometry. Moreover, the form of the correlation was checked against previous data found in the literature.

A few years later, Zapke & Kröger (2000-II) published a critical discussion on the validity of different dimensionless groups used in the past to correlate CCFL data. They concluded that the Kutateladze-

type equation is not valid for flooding in vertical tubes with a diameter of about 30 mm. Furthermore, Zapke & Kröger proposed to correlate flooding data with 2 different parameters: the Wallis parameter on one hand for the gaseous phase and a product of the Wallis parameter and Ohnesorge number for the liquid phase on the other hand. The product was defined as follows:

$$\left(J_L^*\right)^{0.2} \cdot \left(Oh_L\right)^{0.3} \tag{2.57}$$

The proposed parameters were validated against the own data of 1996 as well as against 2 previous investigations in vertical pipes with 31.8 mm diameter.

The effect of surface tension on flooding was recently investigated by Ousaka et al. (2006) in small diameter inclined pipes. The used test section is a 1.1 m long pipe of 16 mm inner diameter which was inclined at 30, 45 and 60° to the horizontal. The experiments were performed at atmospheric pressure and room temperature with air and aqueous oleic acid sodium solutions of different concentrations. Oleic acid sodium is a surfactant which allows to vary the surface tension from 0.072 to 0.031 N/m without affecting other liquid properties, when used at low concentrations. The experimental results of Ousaka et al. obtained at 0.034, 0.051 and 0.072 N/m demonstrate that the flooding gas velocity increases with the surface tension for all the tested pipe inclinations. Furthermore, optical observations of the flow show that the surface tension affects the interfacial structure, and consequently, the flooding behaviour. Finally, Ousaka et al. proposed an empirical correlation for the flooding gas velocity in inclined pipes taking into account the effects of pipe inclination, pipe length, pipe diameter and surface tension. This correlation is based on the phase specific Reynolds numbers, on the Weber number and on a modified Froude number.

2.4. Stratified two-phase flow investigations in hot leg typical geometries

Because of the particular shape of the hot leg of pressurised water reactors, dedicated experimental investigations on the specific flow behaviour in this geometry are inevitable. In this section, hot leg typical geometries designate as a generalisation a horizontal conduit connected over a bend and an inclined section to a separator.

2.4.1. Overview of the test facilities

In order to investigate experimentally the flow behaviour in hot legs, several different test facilities were built up over the past decades. Due to the different designs chosen for the hot leg by each PWR vendor, to the relative scale of the test facility, or furthermore, to variations in the dimensions motivated by a parametric study, each of the past investigations was performed in a particular geometry. Moreover, the experiments were performed with different fluids and at various pressure and temperature boundary conditions. Therefore, to enable simple comparisons of the previous work mentioned in this thesis (cf. details in the next sections), an overview of the main characteristics is given in Table 2.2. This shows that the majority of investigations were done with:

- a pipe cross-section;
- a noticeably reduced scale test section (D < 100 mm);
- an acrylic glass test section allowing visual observations;
- air and water as fluids at atmospheric pressure and room temperature.

Furthermore, Table 2.2 points out the importance of the experiments achieved during the international 2D/3D Program in the Upper Plenum Test Facility (UPTF) of *Siemens/KWU* (cf. Damerell & Simons, 1993). In fact, these are the only available data in a full scale PWR primary circuit reproducing the multidimensional thermal-hydraulic phenomena with steam and water at increased pressure conditions.

Authors (year)	Cross-section		Bend angle	Test section material	Fluids		Boundary conditions		Experiment type
	Type	Dimensions			Gas	Liquid	Pressure	Temp.	
Richter et al. (1978)	pipe	D = 203.2	45°	acrylic glass	air	water	atmospheric	38-60°C	CCFL
Krolewski (1980)	pipe	D = 50.8	45-90°	acrylic glass	air	water	atmospheric	ambient	CCFL
Ohnuki (1986)	pipe	D = 25.4...76	40-45°	acrylic glass, steal	air, steam	water	atmospheric	amb./sat.	CCFL
Siddiqui et al. (1986) Ardron & Banerjee. (1986)	pipe	D = 36.5...47	90°	acrylic glass	air	water	atmospheric	ambient	CCFL
Wan & Krishnan (1986)	pipe	D = 51	90°	n.s.	air	water	atmospheric	n.s.	CCFL
Wan (1986)	pipe	D = 51	90°	n.s.	steam	water	atmospheric	sat / sub_L: 0-6 K	CCFL
Siemens/KWU (1987)	pipe	D = 750	50°	steal	steam	water	3 ; 15 bar	saturation	CCFL
Ohnuki et al. (1988)	pipe	D = 25.4	50°	acrylic glass	air	water	atmospheric	ambient	CCFL
Geffraye et al. (1995)	pipe	D = 75...351	50-90°	acrylic glass	air	water	atmospheric	ambient	CCFL
Wongwises (1996-a/b)	pipe	D = 64	50-90°	acrylic glass	air	water	1.30 bar	ambient	CCFL
Kang et al. (1999)	pipe	D = 40 ; 80	35°	acrylic glass	air	water	atmospheric	ambient	CCFL
Navarro (2005)	pipe	D = 36...54	30-90°	acrylic glass	air	water	atmospheric	ambient	CCFL
Minami et al. (2008)	rectang. channel	H = 150; W = 10	50°	acrylic glass	air	water	atmospheric	ambient	CCFL
Minami et al. (2010)	pipe	D = 50	50°	acrylic glass	air	water	atmospheric	ambient	CCFL
Gardner (1989)	pipe	D = 84	50°	acrylic glass	air	water	atmospheric	ambient	co-current
Kukita et al. (1989) Asaka & Kukita (1996)	pipe	D = 207	50°	steal	steam	water	70 bar	saturation	co-current
Siemens/KWU (1992)	pipe	D = 750	50°	steal	steam	water	3 ; 5 ; 15 bar	saturation	co-current
Petritsch & Mewes (1997) Petritsch & Mewes (1999)	pipe	D = 441	50°	acrylic glass	air	water	atmospheric	ambient	co-current

Table 2.2: Overview of the experimental work published in the past on two-phase flows in models of the hot leg of a PWR (n.s.: not specified)

2.4.2. Co-current flow experiments

Several experimental investigations of co-current flows in hot legs, simulating the two-phase natural circulation, were performed in dedicated test facilities over the last decades. Basically, among the western types of pressurised water reactors, two different steam generator designs exist: once-through steam generators (*Babcock & Wilcox* design, e.g. reactor TMI-2) and vertical U-tube steam generators (reactors of other vendors: e.g. *Siemens/KWU*, *Westinghouse*, *Framatome*). The once-through SG system is basically a vertical counter-current flow heat exchanger, in which the primary coolant flows downwards. In the secondary circuit, the steam generator is fed with water from the bottom, which is heated up while flowing upwards and evaporates. Consequently, in the *Babcock & Wilcox* reactors, the hot leg presents after the horizontal part a long vertical section, followed by a 180° bend connected to the primary system inlet of the steam generator (cf. U.S.NRC, 2009). The main advantage of the once-through SG design is the possibility to produce superheated steam, whereas the other PWR designs can only heat the steam to saturation conditions. However, the thermal-hydraulic behaviour of the primary system during loss of coolant accident transients, and especially during natural circulation, depends sensibly on the design. In this work, the focus is made on the design of German PWRs with vertical U-tube steam generators, which is the most widespread design of western reactors. However, the experimental investigations for the *Babcock & Wilcox* design made around Ishii are mentioned here. Experiments performed with nitrogen and water in a scaled down test facility with a hot leg piping of 102 mm inner diameter and 5.5 m height were reported by Tan et al. (1988) and Hibiki & Ishii (2000). Lee & Ishii (1990) made experimental investigations in a Freon-113 flow visualisation loop with a 50 mm hot leg pipe over an elevation of about 5 m. Further investigations were performed by Hsu et al. (1998) with nitrogen and water in a test facility with the same dimensions.

For the PWR design with vertical U-tube steam generators, Gardner (1989) for example performed experiments with air and water at atmospheric pressure conditions. The used acrylic-glass test facility reproduces the hot leg and a part of the steam generator of the British “Sizewell B” nuclear power station (design based on the *Westinghouse* 4-loop PWR) at a scale of 1:8.8 (i.e. inner diameter of the hot leg of 84 mm). From visual observations of the two-phase flow in the hot leg, a flow regime map was arranged in terms of the non-dimensional Wallis parameter. The flow map includes the transition from stratified to intermittent flow regimes, the presence of a hydraulic jump in the test section as well as the onset of spray formation. Furthermore, the water level measured in the reactor pressure vessel was compared with the results obtained using a model developed previously by Gardner (1988) for the two-phase discharge through a horizontal break. This model was found to be also adapted to the co-current flow conditions through a hot leg geometry.

Furthermore, natural circulation experiments were performed at the ROSA-IV Large Scale Test Facility (LSTF), a full-pressure and full-height model of the Tsugura-2 *Westinghouse* 4-loop PWR. The test facility was built with a volumetric scale of 1:48 and includes two symmetric primary loops with active steam generators and main coolant pumps. The hot and cold legs are dimensioned to conserve the volumetric scale of 1:24 as well as the ratio of length to square root of the diameter ($L/\sqrt{D}$) in order reproduce accurately the two-phase flow regime transitions (cf. design details in the report by ROSA-IV Group, 1985). Kukita et al. (1989) and Asaka & Kukita (1996) reported about results focused on the main characteristics of the two-phase flow in the hot leg during natural circulation at pressures of about 7 MPa. They observed a stratified flow pattern in the horizontal part of the hot leg which turns into intermittent flow regimes in the riser. At high water flow rates, a hydraulic jump as the discontinuous transition between super- and subcritical flow was noticed at the connection to the riser. It was found that the transition to supercritical flow dependents on the steam flow rate. Furthermore, Asaka & Kukita (1996) extended the model developed by Gardner (1988) in order to predict the transition from sub- to supercritical flow conditions as well as the water level in the hot leg under supercritical conditions.

Moreover, extensive steam/water experiments under increased pressure conditions were performed in the Upper Plenum Test Facility (UPTF), which simulates the primary circuit of a PWR at the original power plant scale. From 1991 to 1997, transient small break LOCA scenarios and accident

management measures were investigated in the frame of the UPTF TRAM (TRansient Accident Management) program. The flow regimes in the hot leg during two-phase natural circulation were examined during the TRAM-A2 experimental series (Siemens/KWU, 1992). Different combination of steam and water flow rates were injected in the core simulator at system pressures of 3, 5 and 15 bar in order to show the development of stratified two-phase flows in the hot leg. It was found that the flow regime in the hot leg as well as in the riser changes with the water flow rate. The sub- and supercritical flow regimes as defined by Gardner (1989) were observed. However, the results show that the generic flow regime maps for horizontal channels are not adapted for the particular geometry of the hot leg. In fact, during stationary experiments, only stratified flow regimes were observed, whereas intermittent flow regimes were also predicted by these maps. Therefore, a qualitative flow regime map was developed for the hot leg geometry.

In order to precise the observations made previously in particular at UPTF, Petritsch & Mewes (1997 and 1999) built a large scale acrylic-glass test facility for air/water experiments at atmospheric pressure and room temperature. In a first series of experiments, the flow map of the facility was determined for a horizontal pipe only, with an inner diameter of 0.441 m. Petritsch & Mewes found similar results compared to the classical flow regime maps for horizontal two-phase flows, although these were obtained in systems with significantly smaller pipe diameter and higher length. In a second stage, the experiments were repeated with a hot leg geometry (i.e. with a riser and steam generator simulator) of the same inner diameter, corresponding to a scale of 1:1.7. The obtained results were very different to those for horizontal pipes, pointing out the important influence of the riser and steam generator on the flow in the hot leg. Consequently, a specific flow regime map was proposed for this geometry.

2.4.3. Investigations on CCFL in hot leg typical geometries

The first detailed investigations on counter-current flow limitation in a hot leg typical geometry (i.e. a horizontal conduit connected to a riser) date back to the late seventies. Richter et al. (1978) performed air/water experiments in a scaled down model of the hot leg of a PWR with 203 mm inner pipe diameter and 45° bend angle. The test section was made of acrylic glass in order to allow visual observation of the two-phase flow. The authors proposed to correlate the obtained flooding data with the non-dimensional superficial velocity introduced by Wallis in 1961 for vertical counter-current flows in pipes (cf. section 2.3.2.2 and equation (2.49)). They tested typical values of the constants *m* and *C* originally determined for vertical pipes against the flooding data obtained in the hot leg test facility. This approach was successful, and consequently, Richter et al. proposed the following correlation:

$$\sqrt{J^*_G} + \sqrt{J^*_L} = 0.7 \tag{2.58}$$

In 1980, Krolewski established the experimental flooding characteristics of five different hot leg geometries with air and water. All the test sections were built with acrylic glass pipes of 2” in diameter (i.e. 50.8 mm) and a length of 23” (i.e. 584.2 mm) for the horizontal part. The angle and length of the riser were varied from 45 to 90° and 10 to 12” (i.e. 254 to 304.8 mm), respectively. Furthermore, two different inlet and two outlet geometries were tested. In her thesis, Krolewski shows that the flooding limits depend significantly on the hot leg geometry, and especially on the angle of the riser. Furthermore, it was found that the hysterisis between flooding and deflooding is particularly high for the hot leg models with 45° bend angle, compared to those with a 90° elbow. Dedicated experiments were performed to determine the Froude number of the stratified liquid layer for the upper and lower air flow flooding limits. As a result, Krolewski suggests that the high hysteresis is associated with a change of the flow regime from subcritical to supercritical.

Later on, Ohnuki (1986) performed counter-current flow limitation experiments in a horizontal pipe connected to an inclined riser with air/water and saturated steam/water, both at atmospheric pressure conditions. From his results, Ohnuki concluded that the flooding characteristics is independent on the fluid combination. Furthermore, he varied the most important geometrical aspects of the hot leg: the conduit diameter (from 25.4 to 76 mm), the length of the straight pipes (from 0 to 0.4 m) and the angle

of the riser (from 40 to 45°). As a result of the investigations on a series of 19 configurations, Ohnuki proposed an empirical correlation to predict the onset of flooding by using the Wallis correlation. For the common outlet of a hot leg (with circular cross-section), he proposed a value of 0.75 for the constant *m* and the following function for the y-intercept constant *C*:

$$C = 0.88 + \ln\left(\frac{L_H}{D} \cdot \frac{1}{L_R}\right)^{-0.066} \tag{2.59}$$

where L_H/D is the length to diameter ratio of the horizontal pipe and L_R the length of the inclined riser. However, it should be noticed that Ohnuki defined these lengths in a particular manner: both lengths are prolonged in the bend to the intersection of the pipe axes (cf. Figure 4 of the paper).

At the same time, Wan investigated the CCFL in a horizontal pipe connected with a 90° elbow to a vertical one, which reproduces the geometry of the coolant inlet and outlet lines of a CANDU reactor. Experiments were performed at atmospheric pressure with air and water (Wan & Krishnan, 1986) as well as with steam and slightly subcooled water (Wan, 1986). In order to investigate the influence of condensation effects, the water subcooling was varied during the steam experiments between 0 and 6 K. However, the results obtained with each fluid combination were published separately and never compared together.

Furthermore, steam/water CCFL experiments at increased pressure conditions were performed in the Upper Plenum Test Facility (UPTF), which simulates the primary circuit of a PWR at full scale. The experiments related in the Siemens/KWU report (1987) simulate the reflux condenser mode after a small break LOCA. These were conducted at pressures of 3 and 15 bar and saturation conditions. A comparison of the results with the correlations of Richter et al. (1978) and Ohnuki (1986) confirmed that the Wallis parameter allows a proper geometrical scaling of the effects of counter-current flow limitation. However, the correlation of Richter et al. was found to be in better agreement with the experimental points determined at UPTF.

Subsequently, scale effects on the CCFL in a hot leg were reported in Ohnuki et al. (1988). Therefore, a test section reproducing the hot leg of the UPTF test facility at the scale of 1:29.5 (i.e. inner pipe diameter of 25.4 mm) was build up and experiments were performed with air and water. Furthermore, similar tests were conducted in a second test section of the same scale but without *Hutze* in order to investigate the influence of this particular ECC nozzle on the CCFL characteristics. As a result, Ohnuki et al. (1988) recommend to consider where applicable the *Hutze* for the calculation of the Wallis parameter: in this case, the flow cross-section and hydraulic diameter have to be taken in the region of the *Hutze*. In this article, the experimental data is principally used to assess a new analytical model based on the two-fluid approach.

Moreover, reflux condenser experiments were performed in the German integral test facility PKL at a pressure of 40 bar (Schmidt & Limprecht, 1991). The power of the reactor core simulator was increased stepwise to reach CCFL in the hot leg or steam generator. As a result, the distribution of the coolant in the primary circuit was measured in function of the core power. However, the flooding characteristics was not determined.

Furthermore, Lopez-De-Bertodano (1994) proposed a correlation based on a theoretical analysis. He used a one-dimensional two-fluid model and the onset of slug flow criteria of Mishima & Ishii to determine the flooding point. Because of the complexity of the developed model, a simple flooding correlation was proposed for the classical hot leg geometry to be implemented in one-dimensional system codes. Derived from a fit of the equation system to the UPTF steam/water flooding points, the following correlation was recommended:

$$\sqrt{J^*_G} + 0.798 \cdot \sqrt{J^*_L} = 0.619 \tag{2.60}$$

Geffraye et al. (1995) performed a study on counter-current flow limitation predictions for hot legs and steam generators in integral test facilities and pressurised water reactors. Experimental

investigations were carried out at the MHYRESA test facility with air and water, focussing on geometrical and scale effects on the flooding behaviour. In fact, in the MHYRESA test facility 4 different test sections were compared:

- 2 test sections are geometrical reproductions of the hot leg of French PWRs at the volumetric scale of 1:100 and 22.7:100, leading to inner diameters of 0.075 and 0.351 m, respectively.
- 2 test sections are designed like the hot leg of integral test facilities: in order to scale down the volume while preserving the elevations, the hot leg is composed of a horizontal part connected via 2 bends and a vertical pipe to the steam generator. In the case of the MHYRESA experiments, the geometry reproduces the hot leg of the BETHSY loop (Boucle d'Études Thermohydrauliques Systeme), which is composed first of a 90° bend and a vertical pipe, followed by another bend and an inclined straight pipe connected to the steam generator. Two different diameters were tested: 0.118 m for the Froude similarity and 0.075 m corresponding to the geometrical similarity.

All the test sections preserve the original NPP elevation between the hot leg axis and the top of the steam generator inlet chamber (i.e. inlet to the U-tubes). Consequently, only the test section of 0.351 mm in diameter reproduces realistically the shape of a PWR hot leg.

The visual observations at MHYRESA show that flooding was located in the bend in the case of small scale test sections (D = 0.075 and 0.118 m) and in the hot leg in the large scale test section (22.7:100), but never in the SG inlet chamber. It was found that the flooding characteristics plotted in the Wallis parameter diagram depends on the pipe system geometry. In fact, CCFL was obtained at lower gas superficial velocities in the test sections reproducing the hot leg geometry of the integral test facility, compared to the original PWR geometry. Furthermore, the flooding characteristics slightly decreases in smaller scale pipes. Moreover, Geffraye et al. evaluated CCFL data published previously by various authors for hot leg test facilities with diameters of 0.0254 to 0.750 m. They showed that the scatter of the measured zero liquid penetration point is significantly higher while using the Kutateladze similarity compared to the Wallis one (300% versus 50%, respectively). Nevertheless, the resulting scatter of the Wallis zero liquid penetration points is found to be high, probably due to many different test parameters: scale, geometry (bends, lengths), fluids (air/water, steam/water), experimental procedures or test facility system effects. Moreover, the possibilities offered by the system code *CATHARE* to model CCFL are discussed and a method is proposed to minimise the user effect.

Furthermore, Kang et al. (1999) performed air/water counter-current flow limitation experiments at atmospheric pressure and room temperature in 8 different acrylic glass test sections. One of the test sections was a horizontal pipe of 80 mm inner diameter and 3388 mm length, whereas the others were models of the hot leg of a PWR. In their hot leg investigations, Kang et al. tested two pipe diameters of 40 and 80 mm and varied the length of the horizontal pipe between 700 and 3388 mm. Furthermore, the bend was connected to a riser with an inclination of 35° to the horizontal and a length of 648 and 623 mm for the 40 and 80 mm test sections, respectively. One of the 80 mm test sections was directly connected after the bend to the steam generator separator (i.e. without riser).

A total of 118 experiments were performed investigating the onset of flooding, the partial delivery region as well as the zero penetration over a wide range of flow rates. Kang et al. found a non monotone behaviour of the onset of flooding curve plotted in terms of the Wallis parameter. Consequently, they divided the curve in 3 regions and explained the different behaviours with the characteristics of the flow (sub- or supercritical) observed in the test section. For the low water flow rates ($0 < J^*_L{}^{1/2} < 0.2$), Kang et al. proposed an empirical flooding correlation depending on the length to diameter ratio of the horizontal pipe:

$$\sqrt{J^*_G} + 0.397 \cdot \sqrt{J^*_L} = 0.603 - 0.00234 \cdot \left(\frac{L_H}{D} \right) \tag{2.61}$$

More recently, Kim & No (2002) have merged in one database the experimental results obtained by eight different research groups, which were published between 1986 and 1999. The database includes cold air/water as well as steam/water experiments. By the regression through a total of 356 data points,

Kim & No proposed the flooding correlation as function of the length to diameter ratio of the horizontal part of the hot leg:

$$\sqrt{J^*_G} + 0.614 \cdot \sqrt{J^*_L} = 0.635 - 0.00254 \cdot \frac{L_H}{D} \tag{2.62}$$

The prediction error of the correlation was evaluated against the considered database to 8.7%.

Navarro (2005) carried out experiments with air and water in different small scale hot leg geometries. The experimental work covered the effect of the following geometrical parameters on flooding: the inner pipe diameter (36 to 54 mm), the length of the horizontal part (0.1 to 0.8 m), the length as well as the inclination of the riser (0.1 to 0.5 m and 30 to 90° to the horizontal, respectively). As a result, he proposed a non-linear experimental correlation to predict the CCFL in the hot leg of a PWR (equation 8 in the paper):

$$\sqrt{J^*_G} + 0.2452 \cdot \sqrt{J^*_L} + 1.17 \cdot J^*_L = 0.5963 \tag{2.63}$$

Furthermore, the test facility of Navarro was equipped with a spillway in the upper separation tank in order to define the level of the accumulated water. Thanks to this feature, he found out that the water level in the steam generator inlet chamber has a slight influence on the flooding characteristics. In fact, an increase of the accumulated water level decreases the zero liquid penetration point and, consequently, the complete flooding curve.

Recently, Minami et al. (2008) performed experiments in a model of the hot leg of a pressurised water reactor with rectangular cross-section. The test section is made of acrylic glass and the fluids used were air and water at atmospheric pressure and room temperature. The study of Minami et al. focuses on the flow patterns observed in the hot leg and the results were compared with the flooding characteristics of the test section. The proposed empirical flooding correlation is based on the Wallis parameters, calculated with the hydraulic diameter D_h of the rectangular channel cross-section. The proposed correlation is:

$$\sqrt{J^*_G} + 0.63 \cdot \sqrt{J^*_L} = 0.93 \tag{2.64}$$

Furthermore, this year Minami et al. (2010) published an experimental study conducted in a 1:15-scale model of a hot leg, leading to 50 mm inner pipe diameter. The test facility is made of acrylic glass in order to allow visual observations of the two-phase flow. As a result of the experiments, flow pattern maps were arranged for both increasing and decreasing air flow rates. It was found that the flow regimes in the elbow and in the riser are strongly affected by those in the horizontal part of the hot leg. Furthermore, a hysteresis effect was observed as the flow pattern transitions obtained by increasing or decreasing the air flow rates differ from each other. Moreover, a similar hysteresis was noticed for the CCFL characteristics, while only the characteristics obtained from decreasing air flow rate was found to be independent of the injected liquid flow rate. Finally, a comparison with the flow pattern map reveals that the CCFL characteristics corresponds to a flow regime transition in the horizontal section (boundary between “negative wavy flow” and “stratified flow”).

2.4.4. Occurrence of the hydraulic jump in hot legs

As noticed in section 2.2.2, the hydraulic jump in closed conduits has not been investigated particularly extensively in the past. However, this classical hydraulic phenomenon has been observed and reported in many studies performed in hot leg typical geometries. This has been already mentioned if applicable in section 2.4.2 for co-current flows during two-phase natural circulation. This concerns in particular the flow map of Gardner (1989) and the analysis of LSTF investigations by Kukita et al. (1989) and Asaka & Kukita (1996).

Furthermore, the hydraulic jump was also observed in hot leg test facilities during counter-current flow limitation experiments. In fact, the water is accelerated by the gravity while flowing down the inclined part of the hot leg and the flow becomes supercritical. If the pressure losses along the horizontal pipe are high enough, the water flow changes to the subcritical regime and a hydraulic jump occurs. This flow regime transition in hot legs was first mentioned by Krolewski (1980) to be a

possible explanation for the large hysteresis observed between flooding and deflooding in the test sections with 45° bend angle. However, in this thesis there is no mention of hydraulic jump observations.

The first to report in details about hydraulic jumps was probably Wongwises (1996-a/b). He performed experiments in an acrylic glass test section of 64 mm inner diameter with air and water at a pressure of 130 kPa. The length of the horizontal pipe was 1300 mm and the bend angle was varied between 50 and 90°. At relatively low water flow rates, a hydraulic jump was observed in the horizontal pipe (cf. Figure 4 and 5 in his paper). Its position was found to depend on the fluid flow rates: the hydraulic jump was moving in the direction of the bend while decreasing the water flow rate or increasing the air flow rate. At the onset of flooding, a large roll wave was observed to be generated from the hydraulic jump. Furthermore, at high water flow rates, the flow was supercritical throughout the horizontal pipe. Under these boundary conditions, the water level increased at the outlet of the horizontal pipe just before CCFL initiates (cf. Figure 6 in his paper).

The observations of Kang et al. (1999) are very similar, and consequently, confirm the results of Wongwises. Additionally, Kang et al. observed that at low water flow rates CCFL begins when the hydraulic jump was located near the bend. Furthermore, Minami et al. (2008) also reported the occurrence of a hydraulic in their model of the hot leg with rectangular cross-section. They noted the same variation of the hydraulic jump position with the fluid flow rates. However, according to the flow pattern map arranged for the horizontal section, at low air flow rates a hydraulic jump was always observed, independently of the inlet water flow rate.

3. GENERIC INVESTIGATIONS IN HORIZONTAL CHANNELS

3.1. Preliminary tests in a horizontal channel connected on both ends to separators

3.1.1. The horizontal channel for preliminary tests

Experiments were carried out at a horizontal duct mounted between two separators (cf. Figure 3.1 and Figure 3.2). This configuration allows both co-current and counter-current flow experiments. The two-meter long acrylic glass test section has a rectangular cross-section (height x width: 250 x 50 mm²).

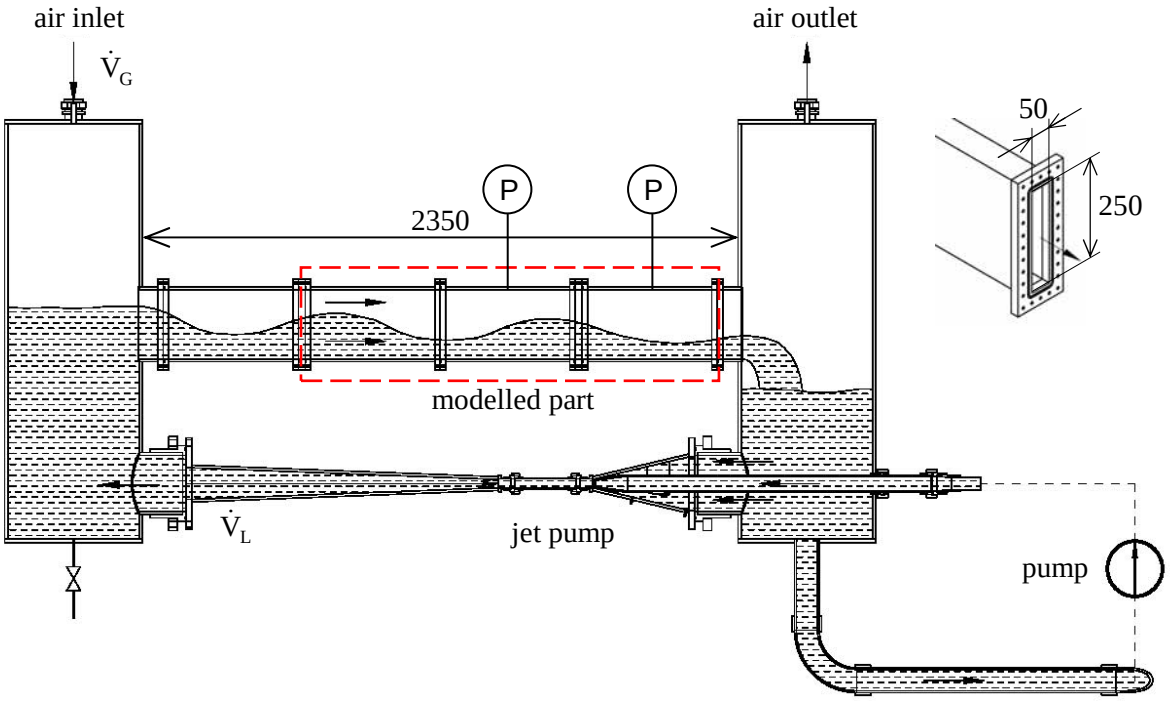

Figure 3.1: Schematic view of the horizontal channel of preliminary tests

The flow rates for both air and water are controlled separately by:

- an air flow controller in a range of up to 1650 l/min (i.e. 2.2 m/s superficial velocity in the test section);
- a frequency transformer for the pump motor to control the water flow rate.

A jet pump is driving the water flow, while the air is being injected at the top of one of the separators depending on the type of experiment (co-current or counter-current flow). The directly pumped water flow rate is measured by an ultrasonic flow meter, which is based on the sound wave propagation time measurement. A jet pump is used to amplify the water flow rate in order to enhance the operation range of the facility. The increase of the water flow rate in the jet pump is calculated from the dynamic pressure difference measured at two positions within the convergent part of the jet pump. The best-achieved amplification factor of the jet pump (i.e. the total water flow divided by the directly pumped water flow) was about 1.8. The maximum total water flow rate reaches about 10 l/s (i.e. 0.8 m/s superficial velocity), whereas the measurement accuracy is about ±10%.

First tests have shown that in co-current mode the flow rates are sufficient to establish the following flow regimes: stratified flow (smooth and wavy flows), slug flow and elongated bubble flow. Due to the rectangular cross-section, the flow can be observed very well from the side of the duct. So, optical techniques, like high-speed video observation and particle image velocimetry (PIV), can be applied to record the flow pattern and to extract quantitative information. For dynamic pressure measurements,

piezoelectric transducers were mounted on top of the duct. Their data acquisition system was synchronised with the high-speed video camera.

Figure 3.2: The horizontal channel for preliminary tests

3.1.2. Results obtained by interface capture methods

3.1.2.1. Interface capture method

In order to make quantitative observations, the flow was filmed with a high-speed video camera from the side of the duct (see Figure 3.3-a, corresponding to the modelled region of Figure 3.1). To capture the gas-liquid interface in the camera frames, an image processing algorithm was developed. The capture method – illustrated in Figure 3.3 – consists in the following steps (cf. details of the developed method in Vallée et al., 2007-b):

1. taking a background picture with fully filled duct (Figure 3.3-b);
2. subtracting the background picture taken in step 1 from the original picture of the flow (Figure 3.3-c);
3. the detection in each vertical line of:
   - the darkest pixel;
   - the minimum of a grey-level time variation;
4. picking out of the pixels detected in step 3, the one which fits best into a continuous interface line (Figure 3.3-d).

Finally, the interface is represented by a water level as function of the duct length x and the time t: $h(x, t)$. The spatial resolution of the pictures is about 1.1 mm/pixel. The accuracy of the interface detection algorithm depends on the thickness of the interface in the images, which is less than 6 pixels for most of the observed stratified flows. Therefore, the accuracy of the water level measurement is about ±3 pixels (i.e. ±3.4 mm).

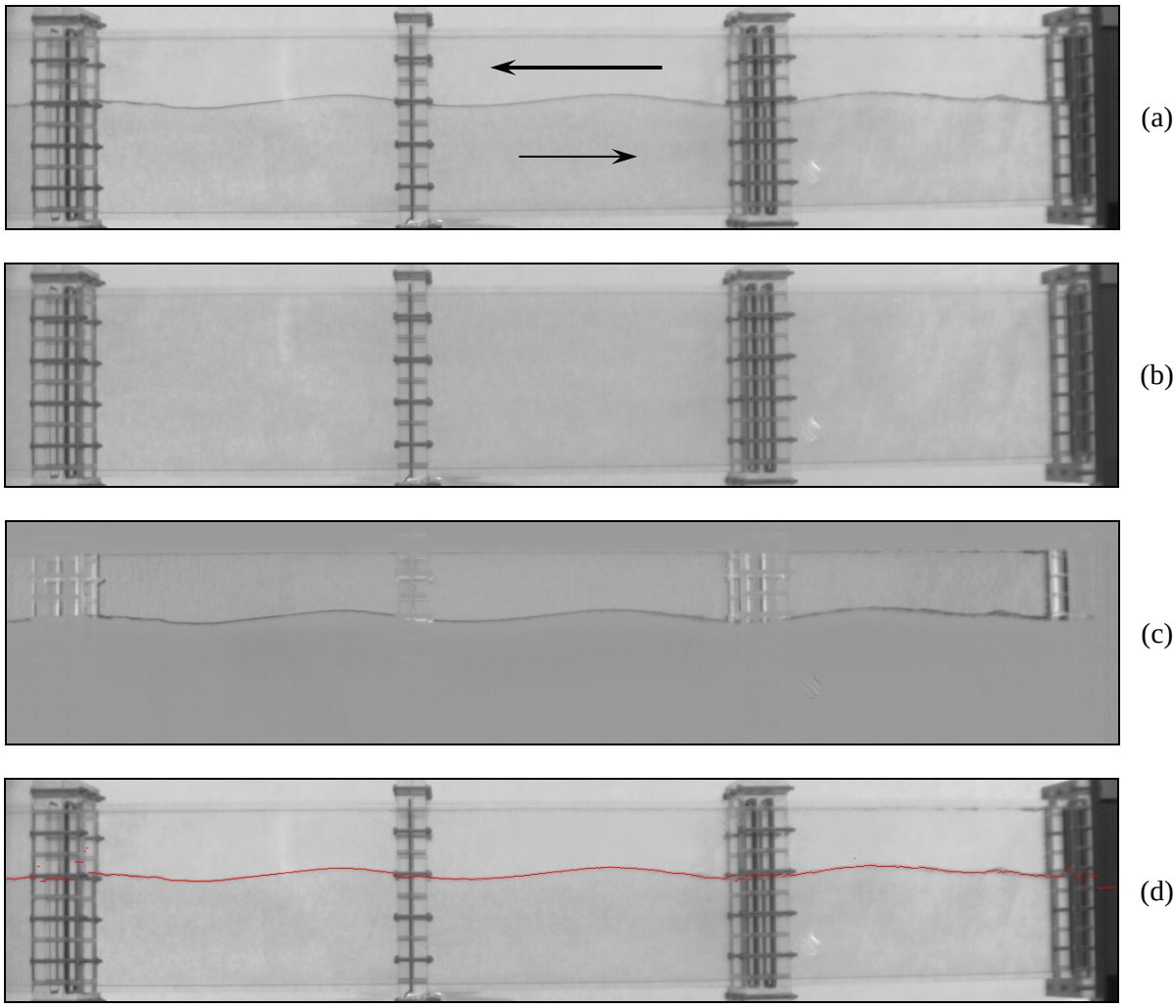

Figure 3.3: Example of picture taken with the high-speed camera during counter-current stratified wavy flow (j_L = 0.14 m/s ; j_G = -2.2 m/s): original picture (a), background picture (b), picture with subtracted background (c) and detected interface (red pixels) over original picture (d)

3.1.2.2. Water level history during slug flow

The superficial velocities during this experiment were as follows: 0.69 m/s for the water flow (i.e. 8.68 l/s) and 2.2 m/s for the air flow (i.e. 1650 l/min). As shown in the sequence of high-speed camera pictures (Figure 3.4), at these boundary conditions slug flow develops in the channel.

The water level in a cross-section as a function of time can be extracted from the function $h(x, t)$ by keeping x constant. The accuracy of the water level detection is in the range mentioned above except in the region of the slug front, where the definition of a water level is difficult due to the generated two-phase mixture. Figure 3.6 shows the resulting water level history for the two cross-sections indicated in Figure 3.5, whose axial positions are as follows:

- at x = 0.75 m, after the first flange (left line in Figure 3.5);
- just before the duct outlet, at x = 2.17 m (right line in Figure 3.5).

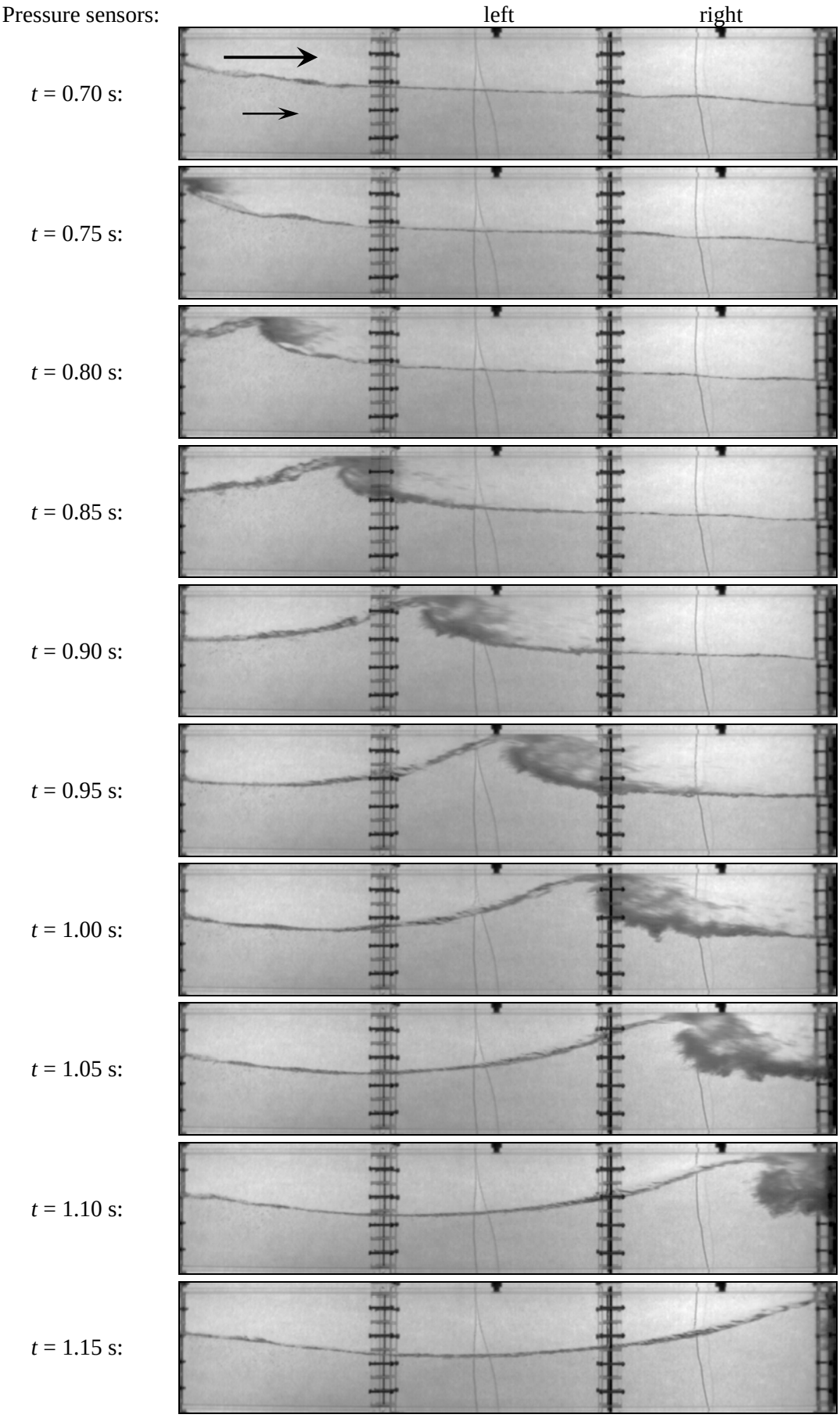

Figure 3.4: Picture sequence during slug flow (superficial velocities: j_L = 0.69 m/s; j_G = 2.2 m/s)

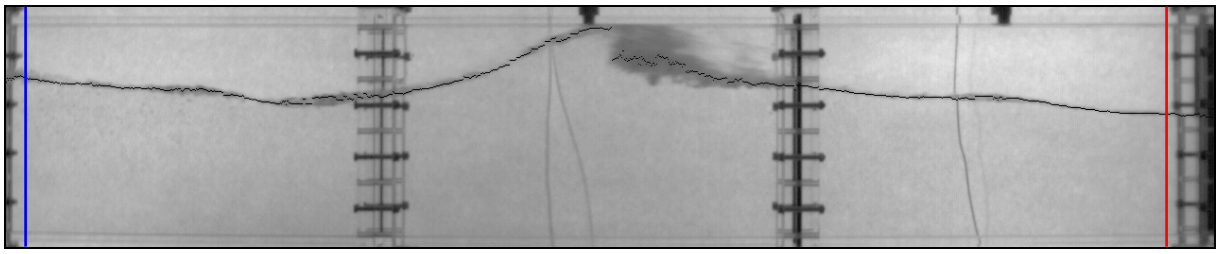

Figure 3.5: Slug flow – chosen inlet and outlet cross-sections (blue and red)

The water level was measured with a frequency of 100 Hz, which corresponds to the frame rate of the high-speed camera. From Figure 3.6 can be seen that the average water level decreases in flow direction because of the pressure drop of approximately 500 Pa. Each slug passing the cross-sections is recognised by a significant peak marked by the boxes. After the passage of the slug, the water level decreases by about 50 mm compared to the level in front of the slug. Then it is increasing slowly until it reaches the critical level and the next slug appears. This phenomenon also shows that a slug expels a significant amount of water from the duct to the second separator.

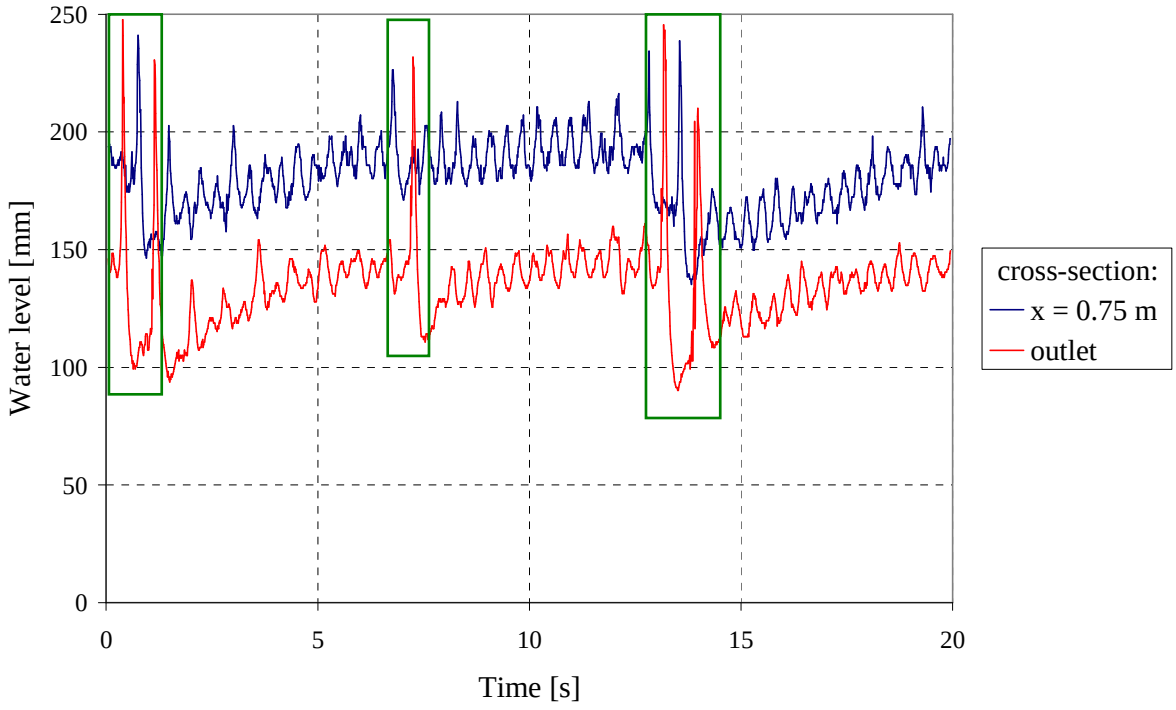

Figure 3.6: Time-dependent water level during slug flow (measuring frequency: 100 Hz)

3.1.3. Dynamic pressure measurements

Since slug flow is a transient phenomenon, suitable pressure sensors have to be fast. That is why existing piezoelectric pressure transducers with a rise time of 2 µs were chosen. They were mounted on top of the last two sections of the duct (i.e. at x = 1.45 m and 1.95 m, cf. Figure 3.1). Moreover, the pressure measurements were synchronised with the high-speed video camera system. A disadvantage of the piezoelectric transducers is the drift due to the discharge time of the quartz crystals. This causes a static error of about 20%. Unfortunately, alternatives were not available for the present studies.

A typical pressure measurement of a slug flow is shown in Figure 3.7. The maximum pressure level behind a slug varies from slug to slug, but it is typically in the order of kilopascals. The zoom in on the first slug passage shows that the pressure increases rapidly: typical rise times are 2 ms (left sensor) and 10 ms (right sensor). An analysis of the camera pictures taken during the pressure measurements could

explain the large spectrum of rise times. They are in fact an indicator of the slug length: the longer the slug, the longer the rise time. This means that in the presented measurement (Figure 3.7), the slug has grown between the two sensors. The pressure decreases simultaneously on both measuring positions. The time of about 20 ms needed to reach atmospheric pressure again, is longer than the rise time. The pictures taken by the camera show that the pressure decreases when the slug leaves the duct towards the outlet separator.

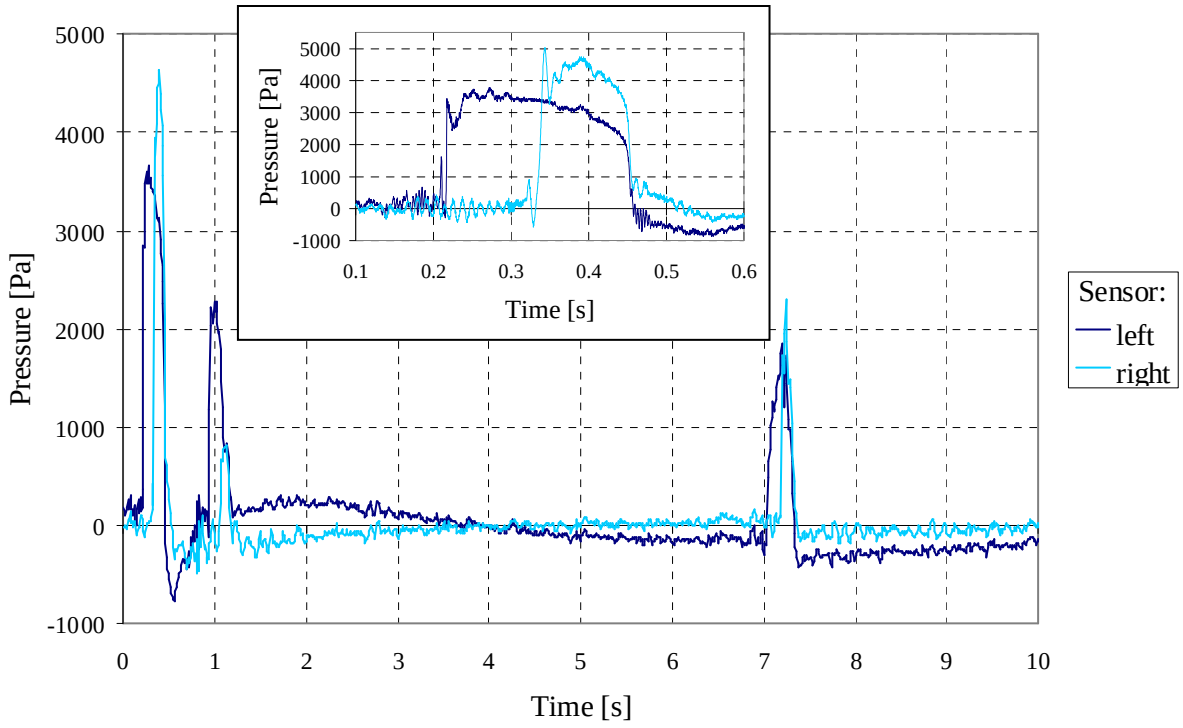

Figure 3.7: Typical pressure measurement by slug flow and zoom in on the first pressure increase

3.1.4. Particle Image Velocimetry (PIV) of a slug

To show the inner structure of the velocity field of a slug, a particle image velocimetry (PIV) system was used. The laser light sheet was focused to the vertical mid-plane of the test section. The PIV camera was directed from the side to the upper part of the duct, in the region of the first pressure sensor (x = 1.45 m). The limited size of the observation area (140 x 105 mm²) did not allow to cover the entire height of the channel of 250 mm.

Figure 3.8 shows a PIV picture of a slug with the calculated velocity field. The absolute vector field (top picture) shows that the entrained air flow on top of the slug accelerates the water to absolute local velocities of about 6 m/s. A slug propagation velocity of 3.8 m/s was measured at the front (horizontal component of the vector in the red circle). The vector direction and length of the lower picture show the relative velocities after subtraction of this slug propagation velocity, which reveals the secondary flow pattern inside of the slug. At the slug front, the water streams upwards. On top, it is accelerated in direction of the slug movement and becomes faster than the slug itself. Due to gravity, the portions that roll over fall down again. In this way, the roll-over vortex structure of the slug is formed.

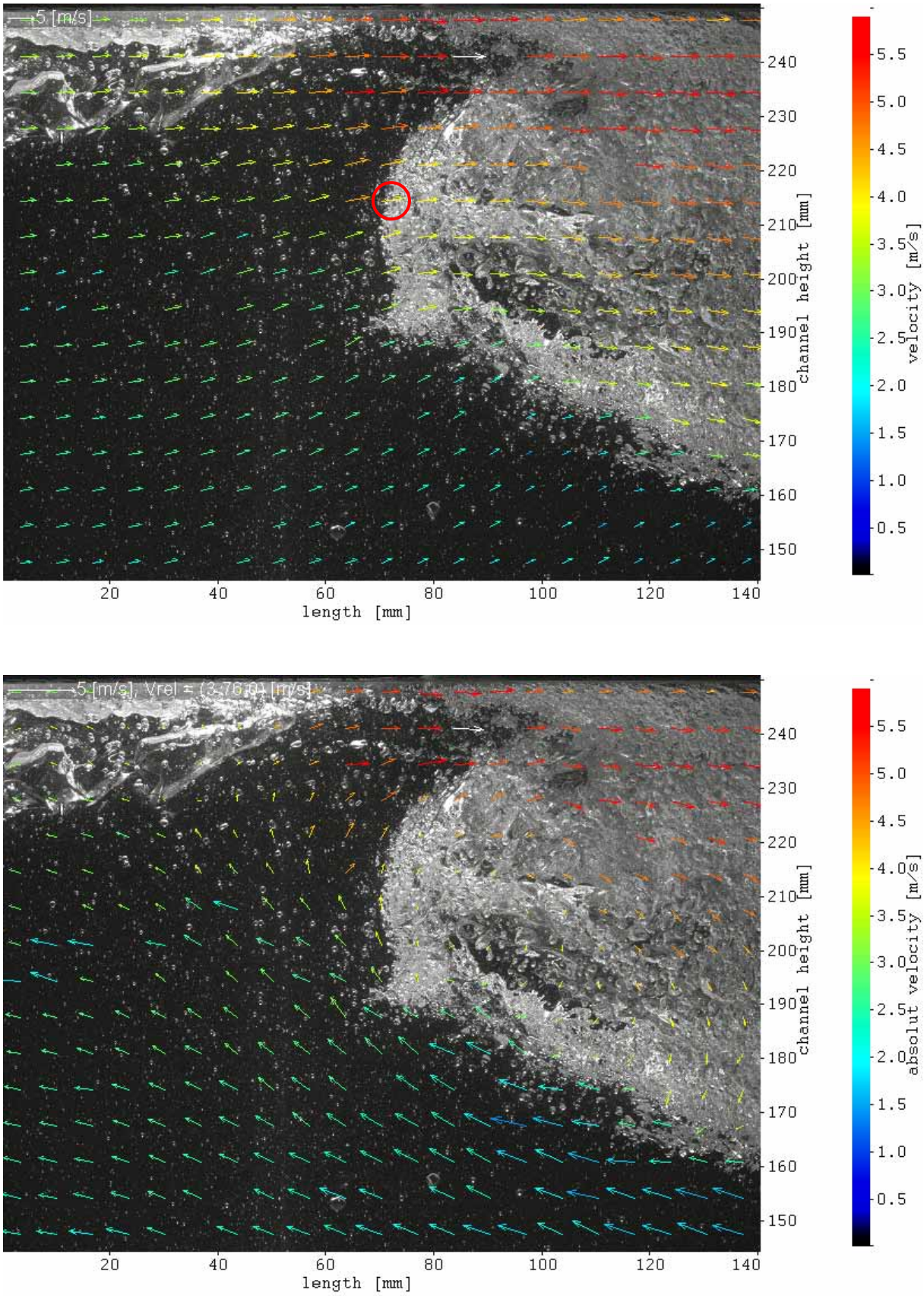

Figure 3.8: Velocity field inside of a slug: absolute velocities on top and secondary flow at the bottom (the vector colour shows the absolute velocity; the vector length and direction show the relative velocity after subtracting the propagation velocity of the slug)

3.1.5. Lessons learnt from the preliminary tests

The experimental results obtained in the test channel presented in this section were preliminary investigations. Basically, this low-cost test facility was built in order to gain experience in the field of stratified two-phase flows as well as to qualify and optimise the design of future test facilities. In fact, apart from the missing bend and steam generator inlet chamber, this channel reproduces the hot leg model build up later on in the pressure chamber of the TOPFLOW test facility (cf. section 4). The preliminary experiments have shown that the jet pump only allows a limited amplification of the water flow rate. Consequently, this solution, potentially optimising pipe connections through the pressure vessel, was not taken into consideration for the final design of the test facility. Moreover, the size of the air inlet pipe was found to be too small, the resulting air jet affecting the interface in the inlet separator at high flow rates. It was also noticed that the outlet separator is undersized as a not negligible amount of water is carried out with the exhaust air flow. Therefore, larger tanks with a flow straightener or a demister at the top are necessary for the hot leg test facility.

Furthermore, this preliminary study shows exemplary some experimental possibilities to generate a database for CFD validation of stratified two-phase flows. In particular, the investigations have demonstrated that a rectangular test section cross-section allows an optimal access for high-resolution optical measuring techniques (camera observations from the side and PIV). Furthermore, the image processing methods applied to the high-speed camera images in order to capture the interface allow to provide reliable and valuable results. However, in order to perform reasonable quantitative comparisons with CFD simulations, the experimental boundary conditions at the channel inlet have to be constant and well defined. Because of the separator at the test section inlet, important inlet parameters such as water level and velocity profiles cannot be controlled properly and are not stationary in the present test facility. Therefore, detailed investigations require the following improvements:

- if possible, the inlet geometry of the test channel should allow constant and well defined boundary conditions. This was realised in a new test facility (HAWAC), which is described in the next section.
- if not possible, like in the case of the hot leg tests, the CFD model should imperatively include the separators. This makes the CDF calculations even more expensive, but this is the only solution to obtain comparable results.

3.2. Investigations in the Horizontal Air/Water Channel

3.2.1. The **H**orizontal **A**ir/**Wa**ter **C**hannel (HAWAC)

Experiments were carried out at the Horizontal Air/Water Channel (Figure 3.9), witch is devoted to co-current flow experiments. A special inlet device provides defined inlet boundary conditions by a separate injection of water and air into the test section. The test section is 8 m long and its cross-section dimensions are 100 x 30 mm² (height x width). Therefore, the length-to-height ratio L/H is 80. Alternatively, related to the hydraulic diameter, the dimensionless length of the channel is L/D_h = 173.

The inlet device (Figure 3.10) is designed for a separate injection of water and air into the channel. The air flows through the upper part and the water through the lower part of this device. Because the inlet geometry produces perturbations in the flow (bends, transition from pipes to rectangular cross-section), 4 wire mesh filters are mounted in each part of the inlet device. The filters are made of stainless steel wires with a diameter of 0.63 mm and have a mesh size of 1.06 mm. They aim at providing homogenous velocity profiles at the test section inlet. Moreover, the filters produce a pressure drop that attenuate the effect of the pressure surge created by slug flow on the fluid supply systems. Air and water come in contact at the final edge of a 500 mm long blade that divides both phases downstream of the filter segment. The free inlet cross-section for each phase can be controlled by inclining this blade up and down. The inclination of the blade is measured over the cross-section opening for the water (see red graduation in Figure 3.10). Both, filters and inclinable blade, provide well-defined inlet boundary conditions for the CFD model and therefore offer very good validation possibilities.

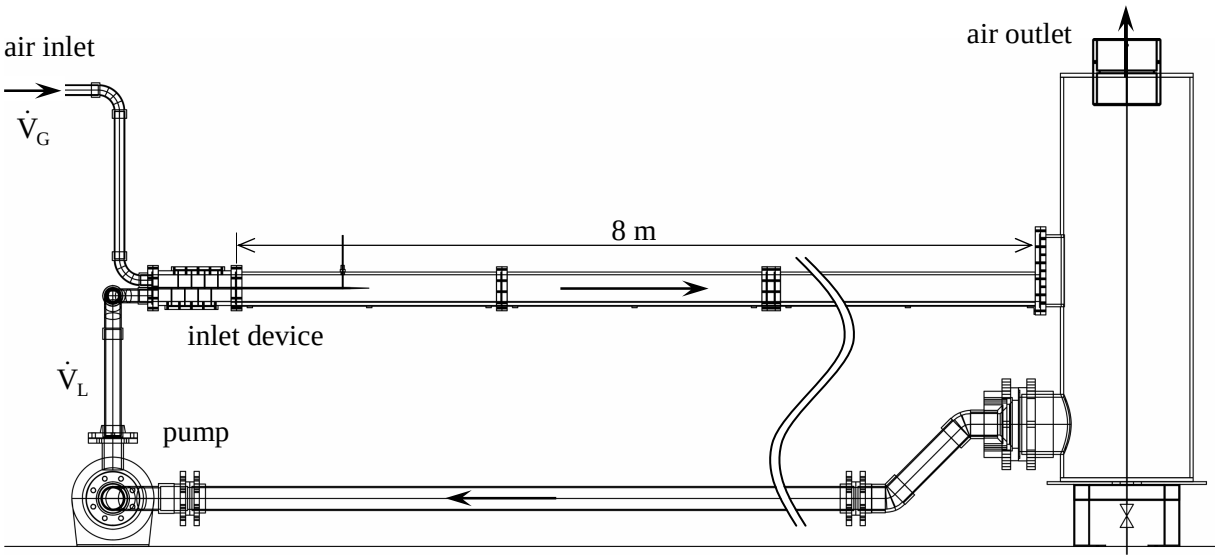

Figure 3.9: Schematic view of the **H**orizontal **A**ir/**Wa**ter **C**hannel (HAWAC)

The water flow rate is measured with a paddle-wheel flow transmitter and is adjusted via the frequency inverter of the pump motor. The air flow rate is measured and controlled with the thermal mass flow meters of the TOPFLOW-facility. These are mounted in parallel in order to ensure a high precision over a large measuring range. The flow rates are measured with an accuracy of ±0.2 l/s for the water and ±1.5% for the air. The maximum superficial velocities achieved in the test section are 2 m/s for the water and 8 m/s for the air.

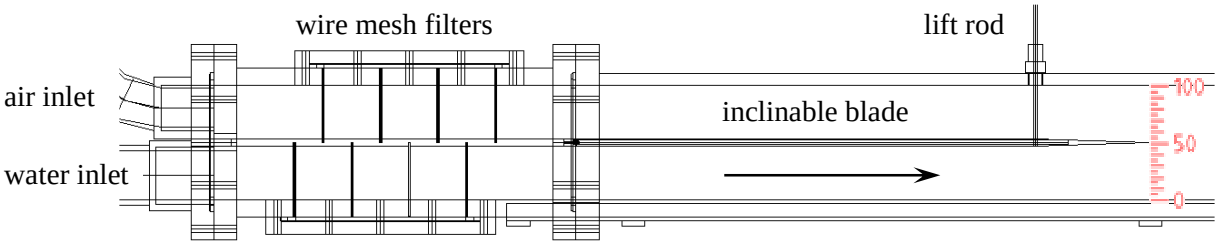

Figure 3.10: Inlet device of the HAWAC channel

3.2.2. Experimental possibilities offered by the HAWAC

3.2.2.1. Effects of the inlet blade inclination on the two-phase flow

The adjustable inclination of the inlet blade separating the phases allows to influence the generation of the two-phase flow regime. The first contact between gas and liquid can be modified with the blade position: if the velocities at the end of the blade are similar, a smooth come together will be managed, else a perturbation can be introduced in the channel. For example, observations have shown that the inlet length needed for slug generation can vary from 0.5 to 3 m just by changing the blade inclination from an opening ration of 80/20 (water/air) to 20/80. Nevertheless, and despite a short channel length, the flow regime established at the end of the channel is not significantly affected by the blade inclination.

Furthermore, at high water flow rates, especially when the inlet blade is inclined down, a hydraulic jump can be realised in the test section. In the supercritical region, the flow is always stratified, whereas after the hydraulic jump (i.e. in the subcritical region) the typical two-phase flow regimes were observed (e.g. elongated bubble flow, slug flow). The position of the hydraulic jump in the channel depends on both flow rates and on the inlet blade inclination. When a hydraulic jump is formed, its position strongly influences the inlet length needed for the generation of slug flow.

It was observed that the position of the inlet blade not always defines the water level at the channel inlet. For example when the inlet blade is inclined upwards and the water flow rate is very low, the water flow separates from the lower surface of the blade. In this case, the initial water level is lower than the height of the outlet edge of the blade. To create proper inlet boundary conditions at these flow rates, the blade has to be inclined down.

3.2.2.2. Flow regimes and flow pattern map of the HAWAC

A flow pattern map (Figure 3.11) was arranged on the basis of visual observations of the flow structure at different combinations of the gas and liquid superficial velocities. According to the terminology used by Mandhane et al. (1974), the observed flow regimes are:

1. smooth stratified flow
2. stratified wavy flow
3. elongated bubble flow
4. slug flow

Further, sub-categories were defined to consider the generation frequency of the intermittent flow structures (designated as plugs, for both slugs or elongated bubbles) in the channel:

a. stratified flow most of the time, but sporadic formation of plugs (i.e. flow regime transition);
b. periodic formation of plugs, but only one plug visible in the channel at the same time (i.e. this plug disappears before the next one develops);
c. periodic formation of plugs and several structures simultaneously present in the test section.

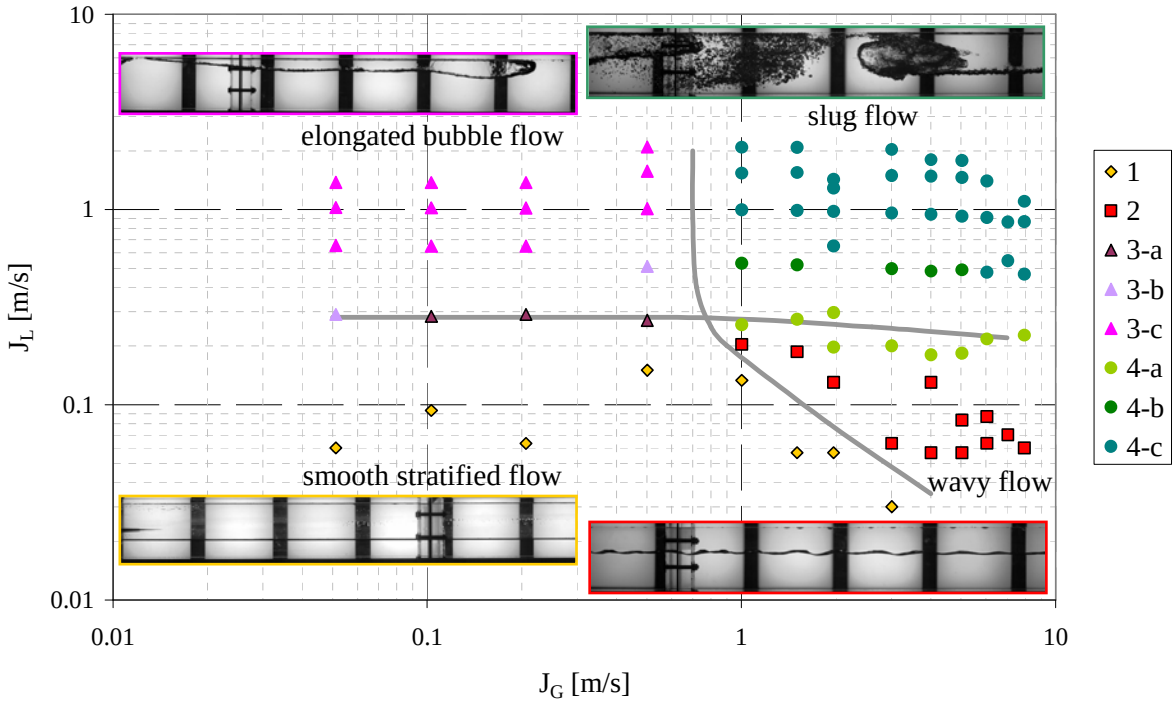

Figure 3.11: Flow pattern map of the HAWAC channel

3.2.2.3. Comparison with the flow pattern transitions of Mandhane et al. (1974)

As shown in Figure 3.12, the flow map determined for the HAWAC channel is in good qualitative agreement with the one of Mandhane et al. (1974). However, the transitions from stratified (smooth or wavy) to intermittent (elongated bubble and slug flow) flow regimes were observed at higher liquid superficial velocities than in their study. This can be attributed to the shorter channel length and would indicate that the flow regime is not fully established at the end of the test section. Another source of discrepancy could be the cross-section geometry since the results from Mandhane are based on pipe measurements. For water levels higher than the middle of the conduit, the instable wave growth leading to the intermittent flow regimes may be reached earlier in pipes compared to rectangular channels. In fact, with each increase of the water level, the gas flow area is faster reduced in pipes due

to their vaulted shape. This may amplify the wave growth, and consequently, make the pipe flow more sensible to the generation of plugs.

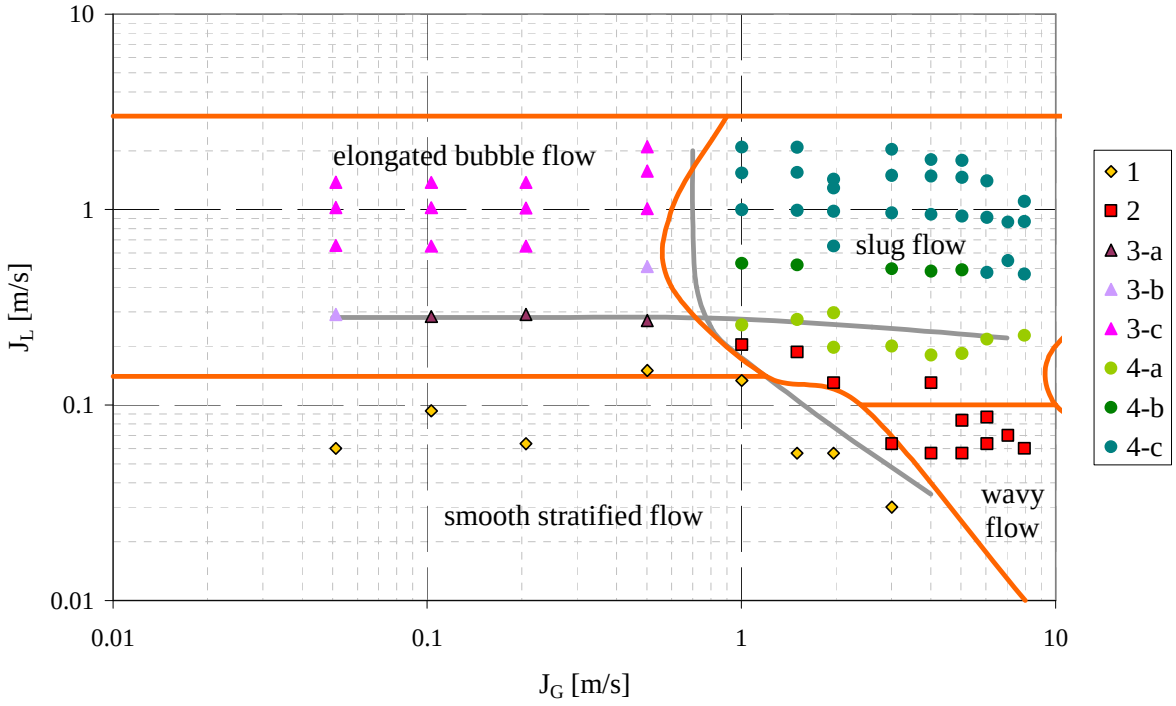

Figure 3.12: Comparison of the flow pattern map of the HAWAC with the results of Mandhane et al. (1974) (orange lines)

3.2.2.4. Comparison with the flow regime transition model of Taitel & Dukler (1976)

In contrast to the flow pattern map of Mandhane et al., the flow regime transition model of Taitel & Dukler (1976) depends on the channel geometry. In fact, the equilibrium stratified liquid level calculated in the first step is specific to the conduit cross-section and inclination (cf. section 2.1.2.2). In general, this theoretical level is a function of A_k, the cross-sectional area of the flow for the phase k, of the part of the conduit perimeter in contact with each phase S_k as well as of the interfacial length S_i, and of α, the conduit inclination to the horizontal. For a channel with rectangular cross-section of height H and width W, these parameters are given by:

$$A_G = W \cdot (H - h_L) \tag{3.1}$$

$$A_L = W \cdot h_L \tag{3.2}$$

$$S_G = W + 2 \cdot (H - h_L) \tag{3.3}$$

$$S_L = W + 2 \cdot h_L \tag{3.4}$$

$$S_i = W \tag{3.5}$$

Furthermore, according to Landman (1991), the characteristic length to use for non-dimensionalisation in case of horizontal or slightly inclined rectangular channels is the height. Consequently, one obtains for:

- lengths: $\tilde{L} = L/H$ (3.6)
- surfaces: $\tilde{A} = A/H^2$ (3.7)

The application of the method described in section 2.1.2.2 using the cross-sectional dimensions of the HAWAC channel (H x W = 100 x 30 mm²) and a null inclination angle leads to the equilibrium stratified liquid level plotted in Figure 3.13 in function of the Lockhart-Martinelli parameter X. In comparison to horizontal flows in pipes, the model predicts a similar trend for the HAWAC, while the transition from low to high equilibrium liquid levels in function of X occurs faster. The higher gradient

of the curve around the middle of the rectangular channel compared to the pipe is due to the absence of width expansion.

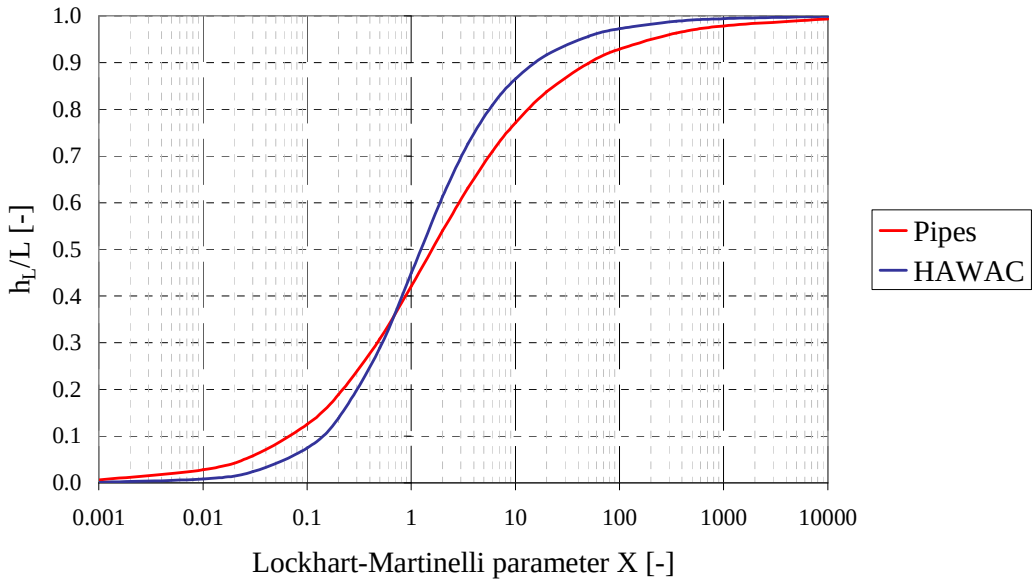

Figure 3.13: Relative equilibrium stratified liquid level calculated according to Taitel & Dukler (1976) for horizontal pipes and for the rectangular channel HAWAC

In order to compare the experimental flow pattern map of the HAWAC with the results obtained by applying the method of Taitel & Dukler, the flow transition boundaries were calculated according to the criteria given in section 2.1.2.2 (equations (2.14) to (2.20)). The criterion describing the transition between stratified and intermittent flows includes the derivative of the cross-sectional area of the flow for the liquid phase A_L with respect to the water level h_L (cf. equation (2.14)). For a channel with rectangular cross-section, this is given by:

$$\frac{d\tilde{A}_L}{d\tilde{h}_L} = \frac{d}{d\tilde{h}_L}\left(\frac{W \cdot h_L}{H^2}\right) = \frac{W}{H} \tag{3.8}$$

A comparison of the results is plotted in non-dimensional form in Figure 3.14 for the transition between the stratified and the intermittent (i.e. elongated bubble and slug) flow regimes. The model proposed by Taitel & Dukler predicts this flow regime transition at lower Lockhart-Martinelli parameters for the HAWAC test section than for pipes. This trend is opposite to the one obtained empirically in the comparison with the flow pattern map of Mandhane et al. (cf. previous section). Furthermore, surprisingly, the comparison with the experimental points shows that the theory gives better agreement applied to pipes than to the special cross-section of the channel. In fact, while the trend of the transition is well described, the transition boundary is quantitatively underpredicted by the model when calculated for the rectangular cross-section. However, these discrepancies are limited in regard to the relatively simple assumptions made by the model. Furthermore, the results obtained for the transition from stratified smooth to stratified wavy flow are presented in Figure 3.15. This shows that the transition is well reflected by the model. Moreover, it is noticeable that in this case the difference between the predictions for pipes and rectangular channel is relatively small.

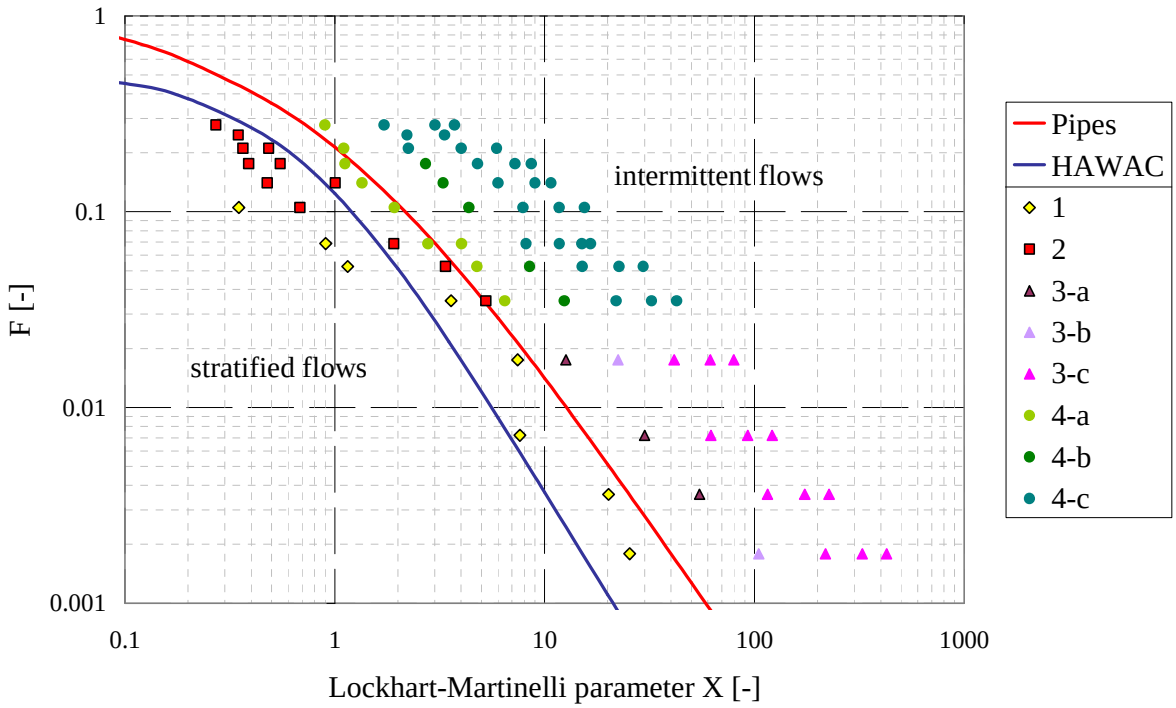

Figure 3.14: Comparison of the transition lines between stratified and intermittent flows predicted by the model of Taitel & Dukler (1976) with the flow patterns observed in the HAWAC (points)

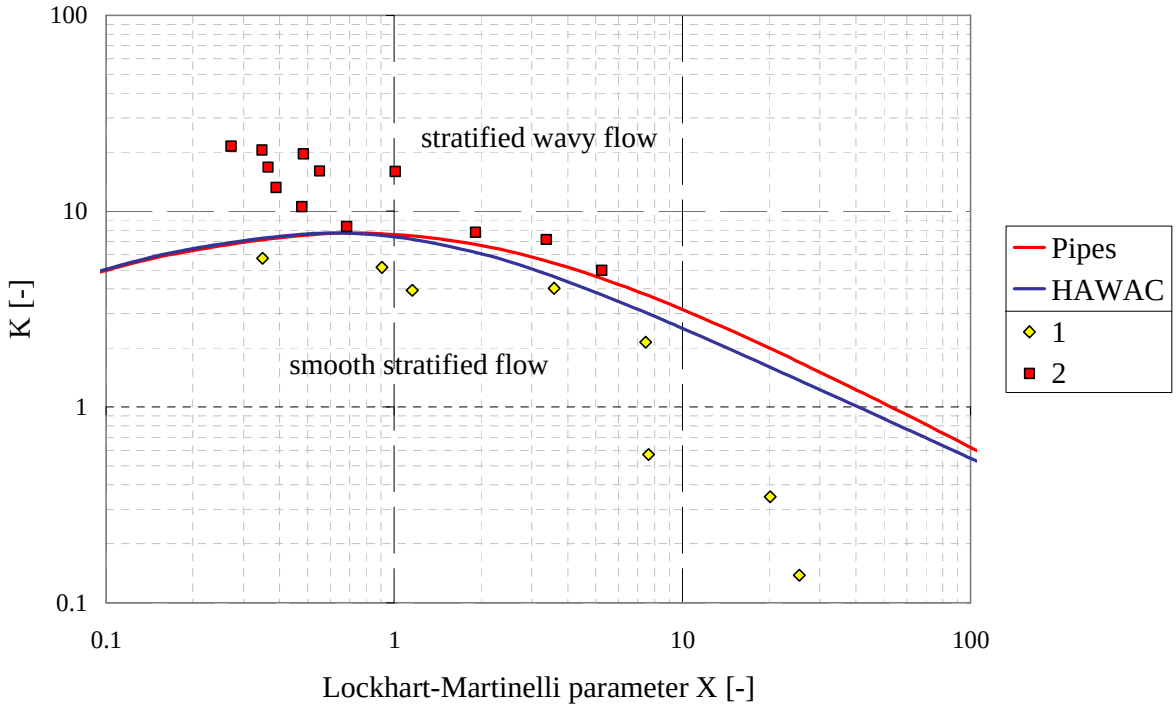

Figure 3.15: Comparison of the transition lines between stratified smooth and stratified wavy flows predicted by the model of Taitel & Dukler (1976) with the flow patterns observed in the HAWAC (points)

3.2.3. Optical measurements on the hydraulic jump

3.2.3.1. Water level measurement: methodology

Optical measurements were performed with a high-speed video camera. As an example, one of the experiments was chosen to explain the methodology used to analyse the camera frames. This run was performed at following boundary conditions:

- water flow rate: 1.4 l/s (i.e. j_L = 0.47 m/s)
- air flow rate: 1.55 l/s (i.e. j_G = 0.516 m/s)

The inlet blade was inclined down to an inlet height of 26 mm for the water and consequently 74 mm for the air.

The flow was filmed from the side of the channel with a high-speed video camera at 60 frames per second. The developed image processing algorithm (cf. section 3.1.2.1) was applied to the camera frames in order to capture the gas-liquid interface (cf. example of result in Figure 3.16). The accuracy of the interface detection algorithm depends on the thickness of the interface in the images. In the stratified flow regions, the interface thickness is quite thin with at most 10 pixels. Therefore, the accuracy of the water level measurement is there about ±5 pixels. This corresponds to ±3.7 mm for a picture resolution of about 0.75 mm/pixel in these experiments. The accuracy is worse in the turbulent region of the hydraulic jump, in particular when bubbles are entrained in the liquid phase. In such cases, the interface may be more than 20 pixels thick, which sometimes induces higher fluctuations in the detected interface.

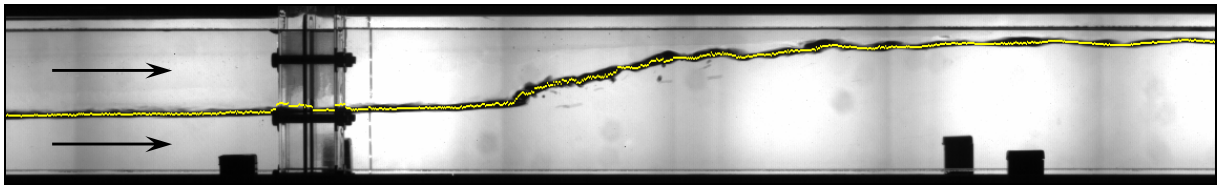

Figure 3.16: Detected interface (yellow pixels) over original picture

3.2.3.2. Example of measurement results

The water level in a cross-section as a function of time was extracted from the data delivered by the interface detection algorithm. The water level was measured with a frequency of 60 Hz, which corresponds to the frame rate of the high-speed camera. As an example, the water level in function of time was plotted in 6 chosen cross-sections identified by colours in Figure 3.17. The indicated axial positions are taken from the final edge of the inlet blade.

Figure 3.17 shows basically two types of time dependent water level behaviours:

1. at 1.40 and 1.55 m, the water level is rather constant with small fluctuations over the measuring time. This is typical of supercritical flow conditions: the interface is very stable because the flow is upstream controlled.
2. from 1.70 to 2.11 m, the water level is instable: fast fluctuations are overlapped to a long period water level variation. This is characteristic for the transitional flow in the hydraulic jump and for the subcritical flow: in the jump, the high turbulence leads to an instable interface generating waves, which propagate along the channel.

The water level measured at 1.62 m shows both behaviours. During the first two seconds the flow is clearly supercritical, and then fast fluctuations start as well as a variation of the water level, typical of the subcritical flow. This point out that despite of constant boundary conditions, the jump position is not constant: this is located downstream of the 1.62 m cross-section before t = 2.0 s and upstream later on.

The water level measured at 2.11 m helps to explain the fluctuating jump position: at about t = 7.5 s, the water level is increasing rapidly to the upper wall, followed by a steep decrease of about 10 mm compared to the mean water level of about 90 mm measured before this event. This behaviour is

characteristic for a slug passing the cross-section (cf. section 3.1.2.2). The slug carrying a certain amount of water from the test section to the outlet separator, the water level is then decreasing in the channel. As a result, the slug coincides with the maximum of the water level in all cross-sections. Especially at x = 1.62 m, the water level decrease measured after t = 7.5 s indicates that the hydraulic jump moves back to the outlet. This indicates that the downstream flow has an influence on the jump position, in particular the water level and the flow regime and therefore the pressure drop.

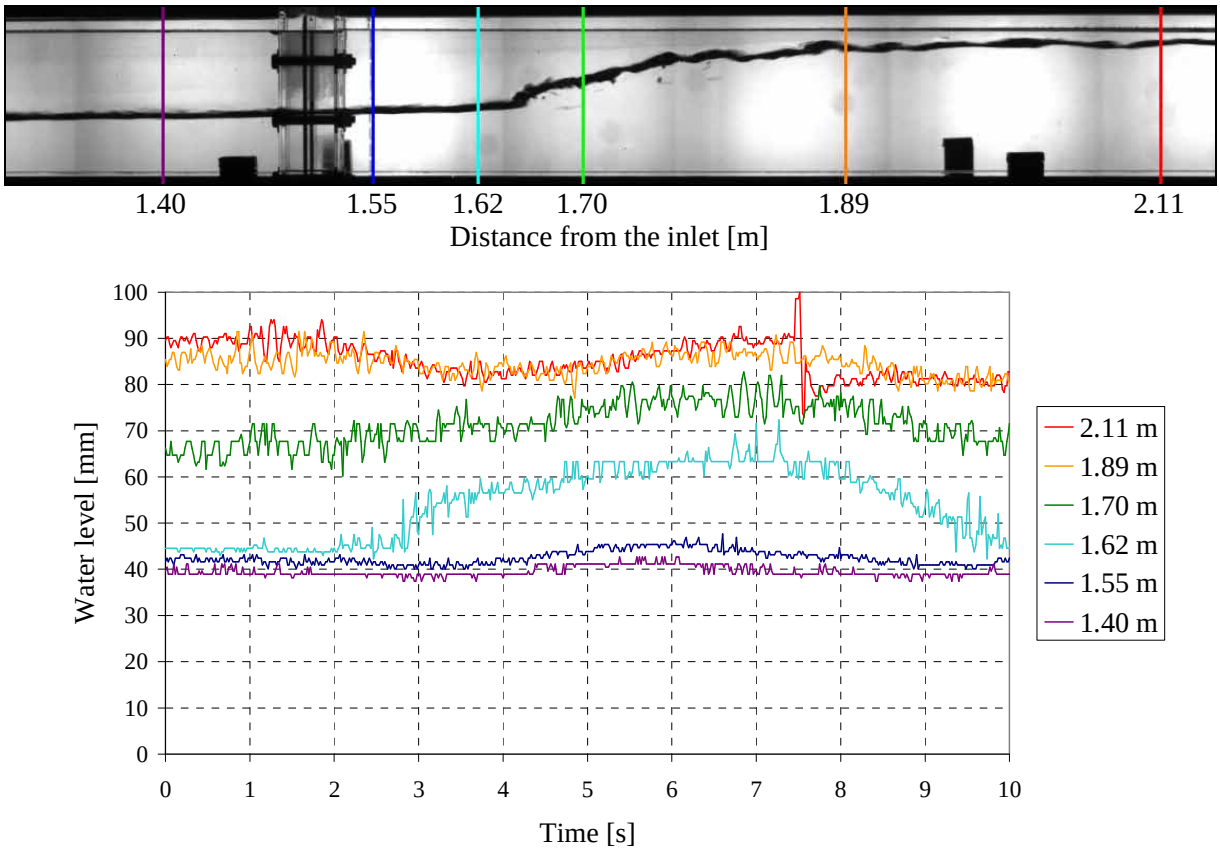

Figure 3.17: Time-dependent water level in 6 chosen cross-sections (measuring frequency: 60 Hz)

3.2.3.3. Probability distribution of the water level

The hydraulic jump realised in the HAWAC test section is a stationary phenomenon. However, as shown in the previous section, the interface is very dynamic because of the high turbulence in the jump. Therefore, a statistical approach is proposed in order to reflect the structure of the interface over the time. The probability distribution of the water levels was calculated in each vertical cross-section for the complete measuring time (N = 672 frames, i.e. 11.2 s). The number $n(x, y)$ of water levels measured at the pixel with the coordinates (x, y) were summed up over the measuring time and the probability p was calculated as follows:

$$p(x,y) = \frac{n(x,y)}{N} \tag{3.9}$$

Since for each frame, one single water level is detected in each vertical line, the sum of the probabilities in a cross-section x is equal to unity:

$$\forall x = \text{const} \quad \sum_{y=0}^{y=H} p(x,y) = 1 \tag{3.10}$$

The calculated probability distributions were represented according to a coloured scale and were superposed to the background picture in Figure 3.18. This shows thin distributions with high probabilities in the supercritical flow region. The beginning of the hydraulic jump is smeared and the probability decreases accordingly. In the second part of the flow transition, the distributions become

thinner and the probability higher. These behaviours were expected from the analysis of the time dependent water levels (cf. previous section).

In the subcritical flow region, on the right hand side of Figure 3.18, the probability distribution becomes bimodal, which can be attributed to the varying water level inherent to the slug flow regime. However, this result requires further investigations. In fact, the flow regime observed during this run corresponds to the transition between elongated bubble flow and slug flow. This means that at these boundary conditions the slug period is quite long. Therefore, this bimodal behaviour has to be confirmed by new measurements with increased statistics (higher number of frames).

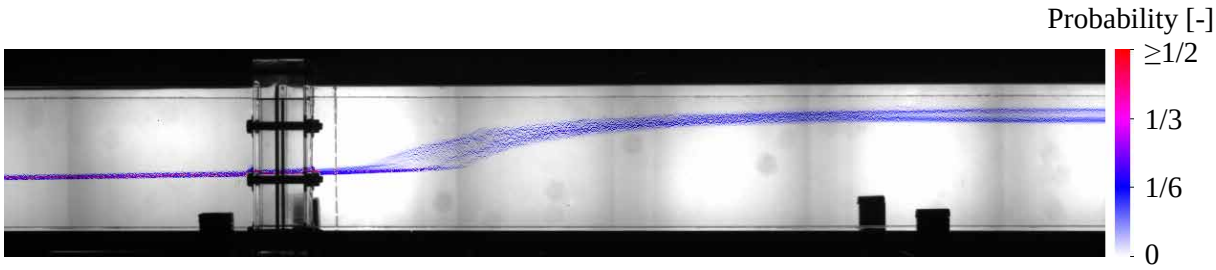

Figure 3.18: Representation of the probability distribution of the water level measured in a hydraulic jump (colours) over the background picture (black and white)

In order to validate qualitatively the final result obtained with the developed image processing method as well as the visualisation of the probability distribution, an average picture of the acquired sequence, shown in Figure 3.19, was calculated. This simple procedure gives very good results in the case of the hydraulic jump measurements due to the high contrast of the raw pictures and to the relatively constant position of the interface over time. Figure 3.19 shows a very similar distribution of the interface, compared to the probability distribution represented in Figure 3.18. In particular, a bimodal distribution is also observed in the subcritical flow region, confirming the results obtained with the interface capturing method.

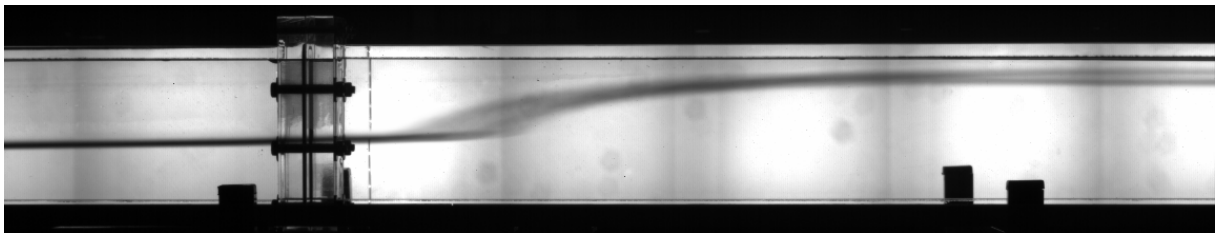

Figure 3.19: Average picture of the flow (over 672 frames, i.e. 11.2 s)

3.2.3.4. Study on the influence of the air flow rate on the hydraulic jump

The presented experiments were focused on the influence of the air flow rate on the hydraulic jump. Therefore, the tests were performed at constant inlet boundary conditions for the water: the water flow rate was 1.4 l/s (i.e. superficial velocity in the test section j_L = 0.47 m/s) and the inlet blade was inclined down to an inlet height of 26 mm for the water. At these conditions, a Froude number of about 3.6 is achieved in the inlet cross-section, which indicates a clear supercritical flow. Moreover, the cross-section opening for the air was 74 mm. Optical measurements were performed by variation of the air flow rate and were processed using the methodology presented in the previous section.

The probability distributions of the water level were calculated for each run and are presented in Figure 3.20. Because the camera had to be moved during the experiments, the pictures show different parts of the test section. For a simple comparison between the runs, the pictures were arranged in Figure 3.20 according to their relative position (reference flange at x = 1.50 m).

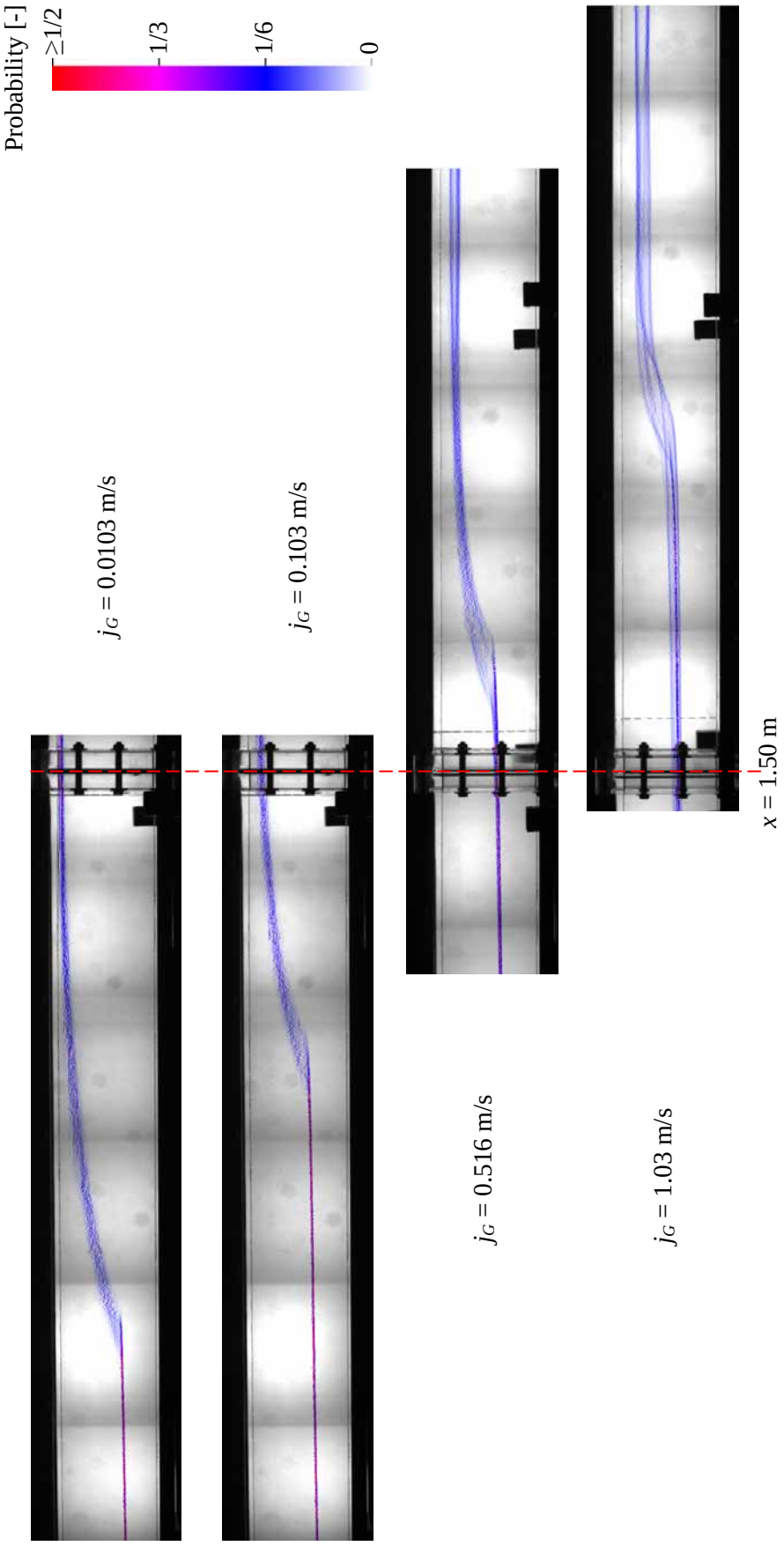

Figure 3.20: Influence of the air flow rate on the probability distribution of the water level measured for hydraulic jumps in a closed channel

At first, Figure 3.20 shows the strong dependence of the hydraulic jump axial position on the air flow rate. The hydraulic jump distance from the inlet was read out of the single pictures representing the probability distribution. As remarked in previous section, this distance varies during the measuring time. Therefore, the minimum and maximum axial positions were plotted in function of the air superficial velocity (cf. Figure 3.21-a). This shows the increase of the hydraulic jump distance from the inlet with the air flow rate, pointing out the influence of the momentum exchange between the phases on the jump position. Furthermore, the increasing distance between minimum and maximum positions reflects the increasing smearing of the area where the jump begins with higher air flow rate.

Moreover, Figure 3.20 shows an increase of the water level immediately upstream of the hydraulic jump with higher air flow rate. This is due to the frictional pressure drop, which increases the water level in flow direction in supercritical flows. The variation of the water level immediately before the jump induces a variation of the Froude number, which characterises the jump. As for the jump axial position, the minimum and maximum water levels were measured in the pictures of probability distribution. From these levels, the corresponding Froude numbers were calculated according to equation (2.28) and were plotted in function of the air superficial velocity in Figure 3.21-b. As a consequence of the increasing water level, the Froude number upstream of the jump decreases with higher air flow rates. The decreasing Froude number results in a change of the jump appearance: the jump becomes flatter and its front smoother. This trend is qualitatively in agreement with studies conducted in open channel flows (Henderson, 1966) and with the experiments made by Stahl & Hager (1999) in a pipe.

As for the jump axial position, the difference between minimum and maximum Froude numbers increases with the air flow rate, which indicates that the supercritical interface oscillates more. This smearing of the probability distribution in a cross-section can be attributed to the flow regime downstream of the hydraulic jump: according to the flow map established for the HAWAC (cf. section 3.2.2.2), at j_L = 0.47 m/s the transition from elongated bubble flow to slug flow occurs for $0.5 \leq j_G \leq 1.0$ m/s. Therefore, the experiments include the transition to slug flow. As indicated in previous section, slug flow induces fluctuations on the hydraulic jump position and water levels.

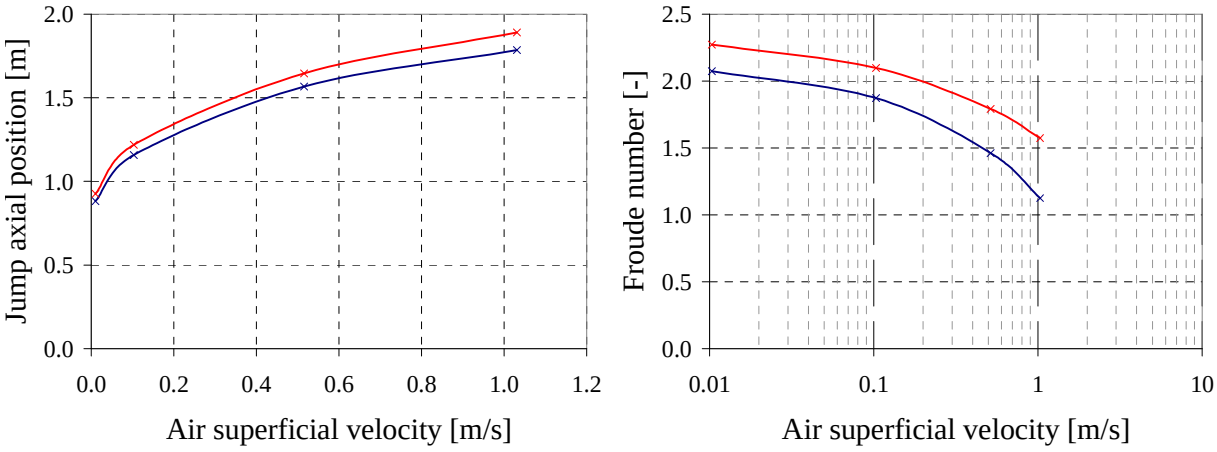

(a) Variation of the jump position (min/max)

(b) Variation of the Froude number immediately before the jump (min/max)

Figure 3.21: Variation of the main characteristics of the hydraulic jump with the air superficial velocity

Moreover, Figure 3.20 points out a logic consequence of the increasing air flow rate: the decreasing water level downstream of the jump. As shown in the state of the art, this water level can be calculated from the water level and the Froude number upstream of the jump for open channel flows (cf. section 2.2.1.4). In order to clarify if this classical relation between the sequent depths is also valid in case of closed channels, equation (2.47) has been applied to the minimum and maximum water levels determined for Figure 3.21-b. The comparison of this prediction with the water levels measured

graphically in the pictures of probability distribution (Figure 3.20) is shown in Figure 3.22. It should be first mentioned that, unfortunately, the field of view chosen for the images of the experiment with j_G = 0.103 m/s did not allow to visualise the fully established flow downstream of the jump. This explains why the corresponding points (in grey in the diagram) do not fit the trend given by the other measurements. Figure 3.22 shows that the minimum of the water level measured downstream of the jump is well predicted by the theory for open channels, especially at low air flow rates. At higher air flow rates, the measurements deviate slightly from the minimum prediction, but are well bounded by the extrema given by the theory.

Nevertheless, the maximum water level is always underestimated by the theory for open channels. In fact, compared to open channel flow, more water accumulates in the test section downstream of the jump, leading to a higher water level in the subcritical region. This is probably due to the pressure drop along the channel, which is higher in case of two-phase flow compared to single phase flow.

The equality of the pressure drop in a conduit for both phases is the fundamental idea of the theory of equilibrium stratified flow (cf. section 2.1.2.2). Consequently, the water level predicted using this approach was calculated for the corresponding experimental boundary conditions. Therefore, fluid densities and viscosities were taken at the measured pressure and temperature conditions of 0.981 bar and 22°C, respectively. The Lockhart-Martinelli parameter corresponding to the measured flow rates was determined according to equation (2.12) with the coefficients *C* and *n* for turbulent flows. Finally, the equilibrium water level was calculated iteratively by applying the method described in section 2.1.2.2 to the geometry of the HAWAC channel (cf. "ESF-Th" curve of Figure 3.22). It is noticeable that the equilibrium water level as function of the air superficial velocity agrees well with the maximum of the measured water level. This result suggests that in a closed channel the water level downstream of the jump is not only dominated by the classical hydraulic mechanisms but also by the two-phase flow behaviour.

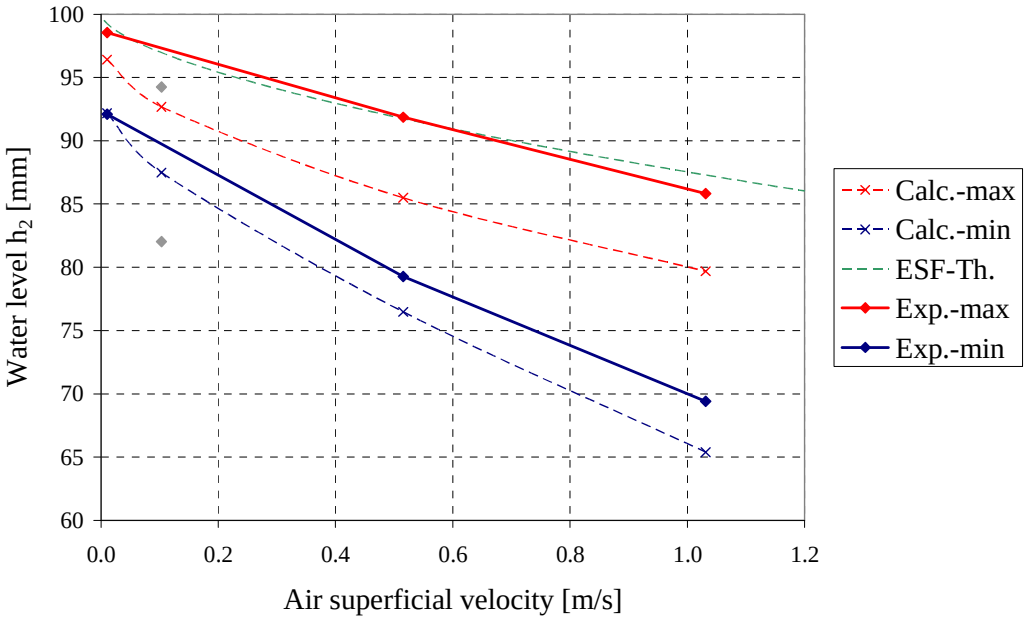

Figure 3.22: Influence of the air flow rate on the water level downstream of the hydraulic jump

3.2.4. Optical measurements during slug flow

The presented experiment was focused on the generation of slug flow. It was performed at following superficial velocities in the test section: j_L = 1.0 m/s for the water flow (i.e. 3.0 L/s) and j_G = 5.0 m/s for the air flow (i.e. 15.0 L/s). Further, the inlet blade was horizontal, and consequently, the cross-section opening at vertex of the inlet blade was 50 mm for each phase. Optical measurements were performed at the channel inlet with a high-speed video camera.

3.2.4.1. High-speed video observations and interface capture

The flow was filmed from the side of the duct with a high-speed video camera at 400 frames per second. The following picture sequence (Figure 3.23) shows an example of camera frames during slug generation.

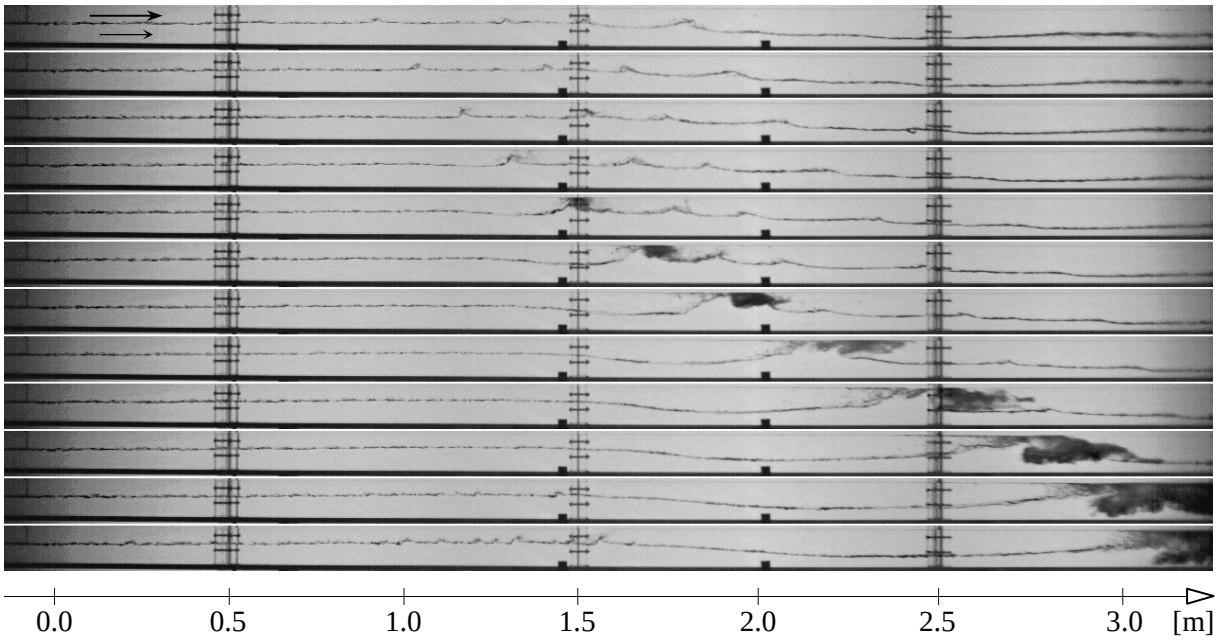

Figure 3.23: Measured picture sequence at j_L = 1.0 m/s and j_G = 5.0 m/s with Δt = 50 ms

Again, the interface capture algorithm (cf. details in section 3.1.2.1) was applied to the camera frames (cf. result in Figure 3.24). As the accuracy of the algorithm depends on the thickness of the interface in the images, this is specific to the flow situation. In the stratified flow regions, the interface thickness is quite thin with at most 3 pixels. Therefore, the accuracy of the water level measurement is there about ±1.5 pixels. This corresponds to ±3.9 mm for a picture resolution of about 2.6 mm/pixel in this experiment. The accuracy is worse in the region of the slug front, where a two-phase mixture is generated (blue circle in Figure 3.24). This makes a definition of the water level difficult and induces sometimes unphysical fluctuations in the detected interface. In particular at the end of the visualised region (farther than 2.5 m from the inlet), where the slugs are developed, the interpretation of the water level measurement is delicate.

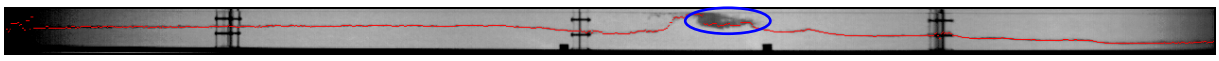

Figure 3.24: Detected interface (red pixels) over original picture

3.2.4.2. Water level measurement

The water level was measured with a frequency of 400 Hz, which corresponds to the frame rate of the high-speed camera. As an example, Figure 3.25 shows the resulting water level history for six chosen cross-sections identified by a colour on the picture above. The indicated axial positions are taken from the final edge of the inlet blade. Close to the inlet, Figure 3.25 shows a rather constant water level which develops into a clear wavy flow at a distance of around 1.0 m. Downstream of 1.5 m, slugs are irregularly generated. With higher inlet length, the number of water level peaks decreases, pointing out that some slugs merge together and some others collapse.

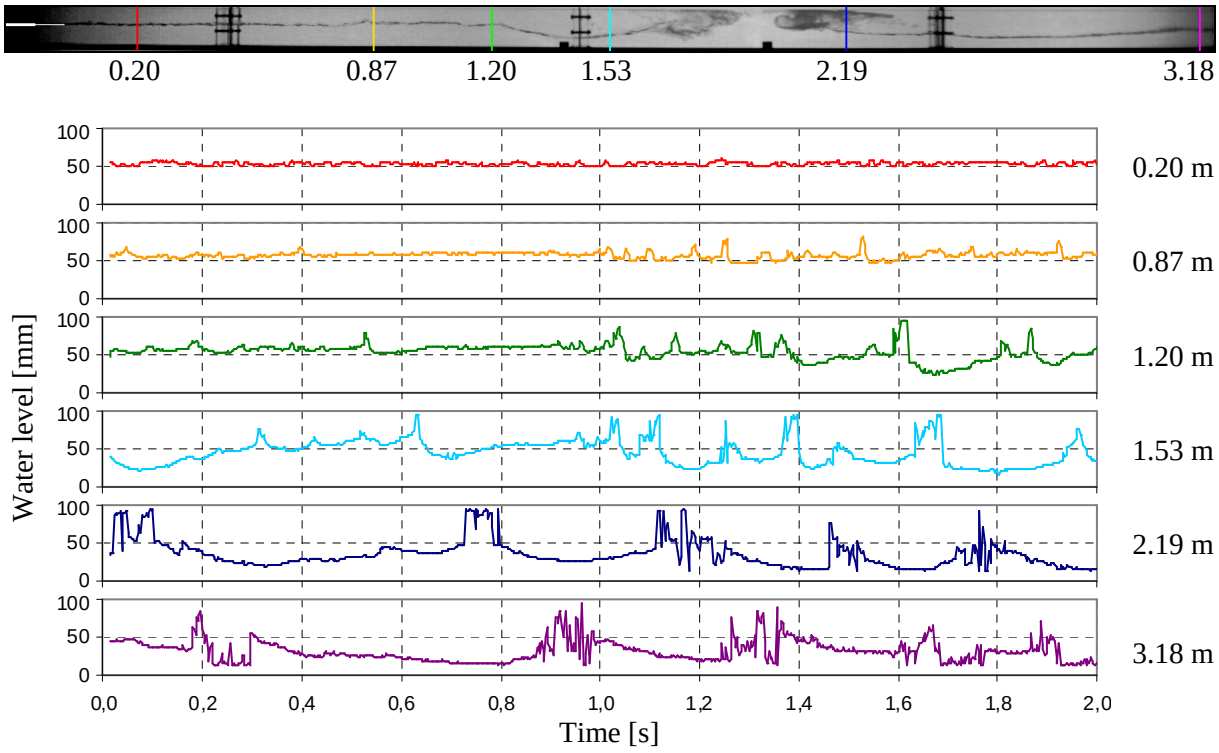

Figure 3.25: Time-dependent water level in chosen cross-sections during slug flow (measuring frequency: 400 Hz)

3.2.4.3. Statistical treatment of the measured water levels for comparison with CFD

Since a direct comparison of the measured water levels with CFD results is difficult (how to synchronise both?), a statistical approach is proposed. First, a time averaged water level was calculated and bounded by the standard deviation in each cross-section (Figure 3.26). This results in a mean water level profile along the channel which reflects the structure of the interface. Further, the standard deviation σ quantifies the spread of the measured values which originates in the dynamic of the free surface.

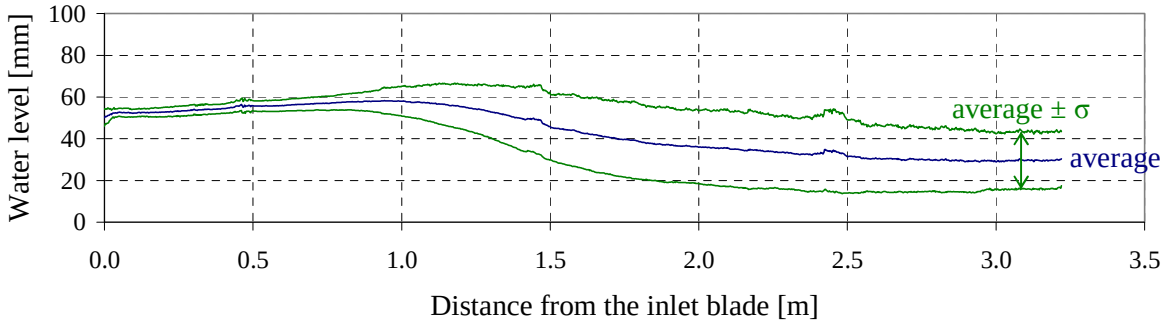

Figure 3.26: Time averaged water level bounded by the standard deviation

In the first part of Figure 3.26, a slight increase of the mean water level from 50 mm at the inlet to 58 mm is observed as well as a low standard deviation. Both are characteristic for the supercritical flow ($Fr \geq 1$) obtained at the test section inlet. In fact, in a supercritical flow the pressure drop due to wall friction results in an increase of the water level. Furthermore, only small supercritical waves can propagate in such a flow. Around the maximum of the mean water level reached at about 0.9 m from the inlet, the standard deviation increases quickly up to about 18 mm. This points out the rapid wave growth induced by the high air velocity in this zone. In the downstream region, where the slugs are generated and propagate, the mean water level decreases to an asymptotic value of about 30 mm. This

shows an acceleration of the water flow, which can be attributed to the momentum exchange between the phases.

Another possibility is to calculate the probability distribution of the water levels according to the method indicated in section 3.2.3.3. Figure 3.27 shows an example of such probability distributions for the same cross-sections chosen for Figure 3.25. Close to the inlet, the distribution is characterised by a quite sharp peak. The distribution then spreads out to form two massifs (for example 2.19 m downstream of the inlet): one small peak near the upper wall due to the slugs and a flat massif below the centre line coming from the low water level measured in between the slugs. The spatial representation of the probability distribution is shown in Figure 3.28 according to the coloured scale. The global trend corresponds to the observations made previously. However, additional details can be observed in comparison to the plot of the averaged water level (Figure 3.26). In fact, one sees likewise that about 1 m downstream of the inlet the water level distribution starts to spread out, but this occurs only to the bottom. Furthermore, from about 2 m of the inlet the vertical probability distribution ends abruptly to the bottom at water levels between 10 and 15 mm (cf. Figure 3.27). This value keeps constant over the rest of the observed part of the test section, indicating that the absolute minimum of the water level is a relatively stable and probable value under this flow regime.

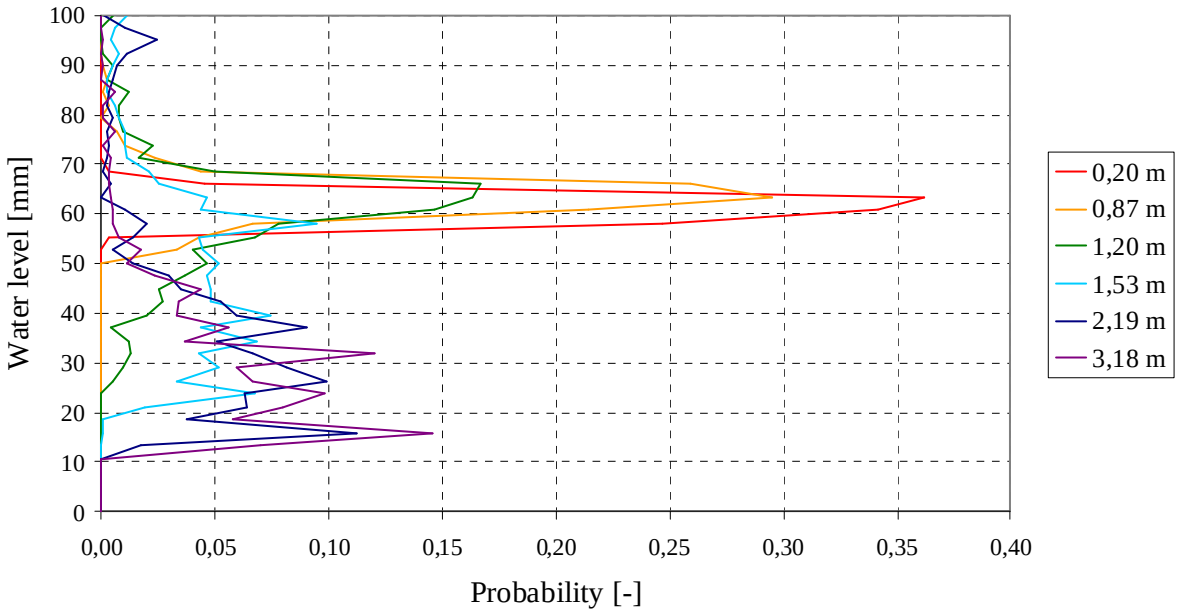

Figure 3.27: Probability distribution of the water levels in chosen cross-sections

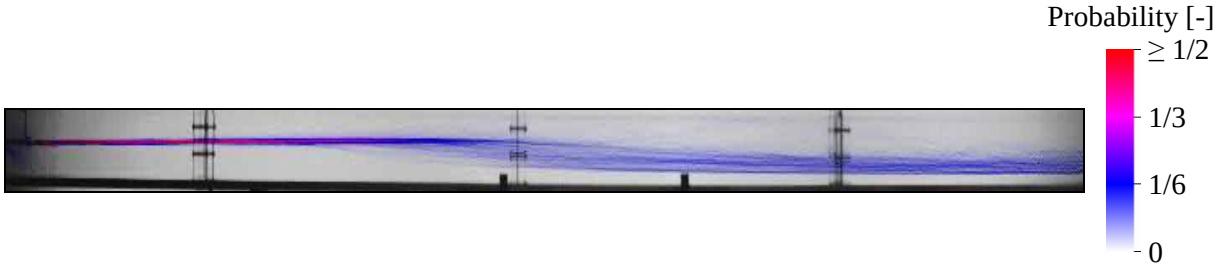

Figure 3.28: Representation of the probability distribution of the water level measured during slug flow (colours) over the background picture (black and white)
N.B.: vertical scale is twice the horizontal one

4. APPLIED INVESTIGATIONS IN A MODEL OF THE HOT LEG OF A PRESSURISED WATER REACTOR

4.1. The hot leg model of the TOPFLOW test facility

4.1.1. The hot leg test section

The test section of the hot leg model is schematically shown in Figure 4.1. The main components consist of the test section itself, the reactor pressure vessel (RPV) simulator located at the lower end of the horizontal channel and the steam generator (SG) separator connected to the SG inlet chamber. The test section reproduces the hot leg of a pressurised water reactor from the German *Konvoi* type at a scale of 1:3. In order to provide optimal observation possibilities, the test section is not composed of pipes like in the original power plant, it is a 50 mm thick channel representing a cut through the vertical mid-plane of the hot leg and of the steam generator inlet chamber. Consequently, the test section is composed of a horizontal rectangular channel, a bend that connects it to an upward inclined and expended channel, and a quarter of a circle representing the steam generator inlet chamber. The horizontal part of test section is 2.12 m long and has a rectangular cross-section of 0.05 x 0.25 m². The SG and RPV simulators are identical vessels with 0.8 x 0.5 x 1.55 m³ (*D* x *W* x *H*) cubic shape.

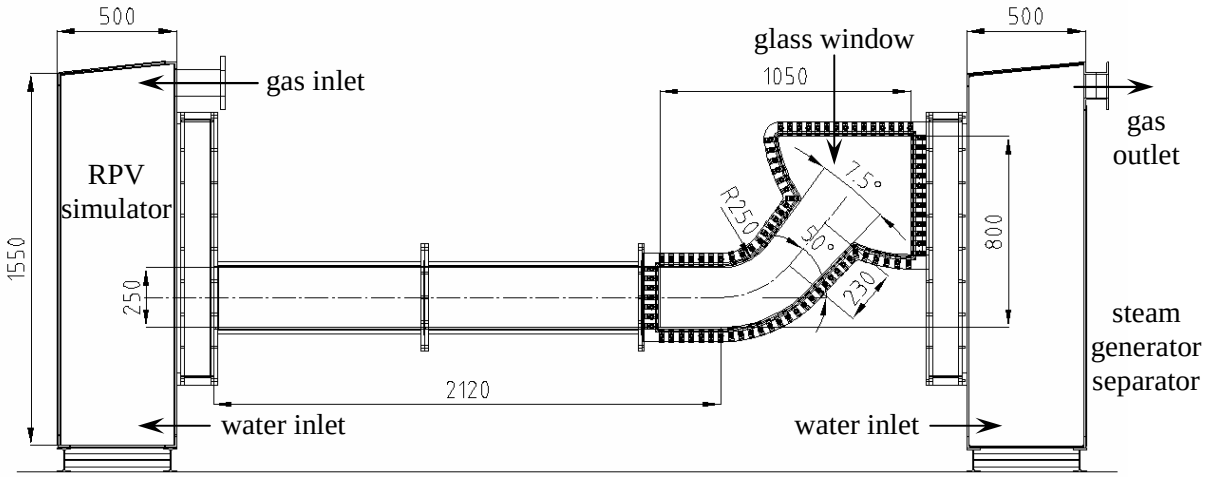

Figure 4.1: Schematic view of the hot leg model test section (dimension in mm)

4.1.2. Specific measures required for the observation of high-pressure steam/water flows

4.1.2.1. The pressure chamber for experiments under pressure equilibrium

Usually, experiments with steam and water at power plant typical boundary conditions implicate to deal with two main constraints: the high pressure and the high temperature. These harsh boundary conditions limit strongly the measuring techniques to be considered and consequently the experimental investigation possibilities. In order to reduce somewhat the requirements to the instrumentation and consequently to open new ways, a special operation technique was developed at HZDR which makes it possible to perform high-pressure steam/water experiments under pressure equilibrium.

Therefore, the test section is installed in the pressure chamber of the TOPFLOW test facility of HZDR (Figure 4.2). For steam/water experiments, a special heat exchanger condenses the exhaust steam from the test section directly in the pressure chamber. This heat exchanger is designed with vertical tubes and two openings connecting the test section to the pressure chamber. As a consequence, the condenser unit is operated with two gases: the steam to condense and a non condensable gas (air or nitrogen) which fills the pressure chamber. Both gases stratify because of the density difference: the lighter steam is injected from the top and the heavier non condensable gas stays at the bottom. The stratification layer in the condenser unit allows a self-regulation of the cooling power of the heat

exchanger according to the arriving steam flow rate. In fact, by displacing the stratification layer up and down, the steam uncovers exactly the heat exchanger surface needed for its full condensation. In order to allow the free movement of the stratification layer inside the condenser unit while changing the steam flow rate, the cold end of the heat exchanger is permanently connected to the inner atmosphere of the chamber over large pipes (see Figure 4.2), which guarantees the full pressure equilibrium at all times. The chamber can be pressurised with compressors up to 50 bar either with air for cold experiments or with nitrogen for steam experiments. Thanks to this experimental method, the test section does not have to support overpressures and can be designed with thin materials. Furthermore, this allows for example to equip the test section with large windows for optical observations of the flow.

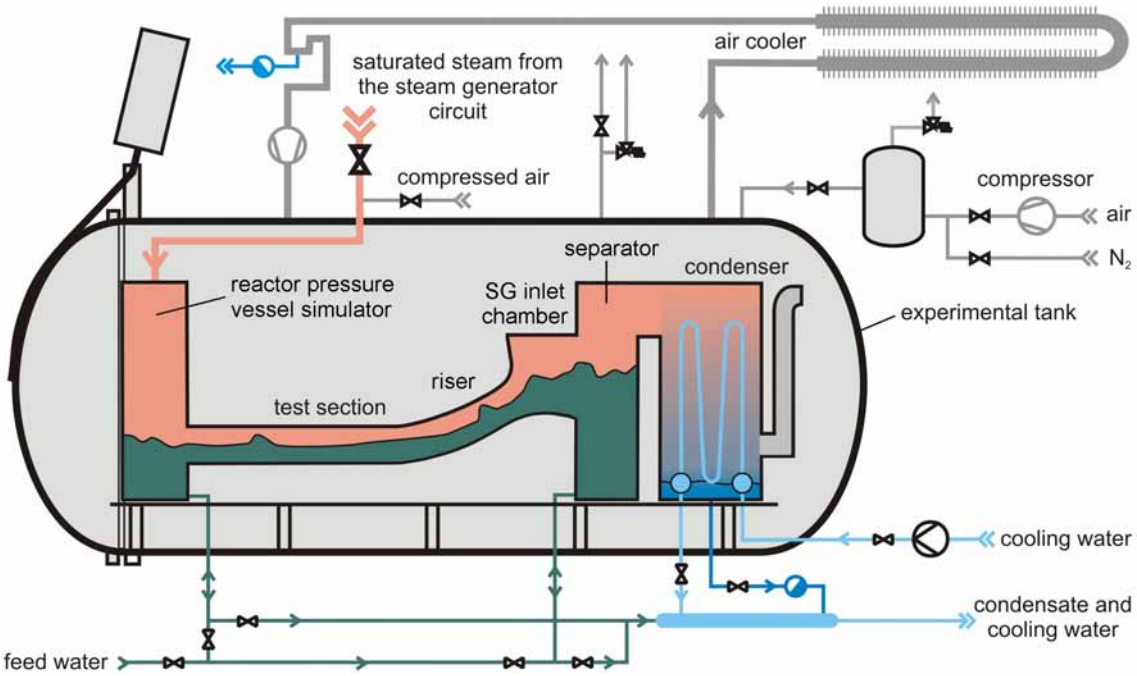

Figure 4.2: Schematic view of the experimental apparatus in the pressure chamber

4.1.2.2. Insulation of the test section at high pressure levels

During steam/water experiments, all the components of the test section are heated up to the saturation temperature of water, i.e. to a maximum of 264°C at 50 bar. Because it is intended to put standard electronic measuring devices (e.g. high-speed video camera) inside the pressure chamber, the temperature of the atmosphere should be kept below their common maximum operation temperature of 50°C. Therefore, the hot components must be insulated and the inevitable heat losses removed to the outside.

First of all, conventional insulation materials like glass wool and mineral wool were used. During commissioning tests, these materials were found to present worse insulation properties with increasing pressure conditions and became insufficient at higher pressure levels. Due to the increasing gas density as well as to the increasing temperature of the components, the density difference between the cold and warm gas increases rapidly with the pressure. As a result, natural convection starts within the fibre packages of the material and reduces strongly its insulation properties. Many different commercial materials were tested under high pressure conditions in house because of the lack of technical information delivered for our application by the manufacturers. Finally, compact micro glass-fibre materials were found to be suitable and were applied very carefully to the hot components. These materials were successfully tested in the pressure chamber (cf. picture of the insulated experimental setup in Figure 4.3) up to the nominal pressure of 50 bar and showed good insulation properties.

Furthermore, the heat inevitably loosed through the insulation material is removed by an air/air heat exchanger installed on the roof of an auxiliary wing of the building. A forced convection of the gas

inside the chamber is established by a pressure-proof electrical fan mounted in the circulation pipe (see Figure 4.2).

Figure 4.3: Complete experimental setup: the insulated hot leg test section in front of the pressure chamber of the TOPFLOW test facility

4.1.2.3. Special measures needed for the camera observation

One additional issue was to enable the observation of the hot steam/water flow without inducing substantial heat losses. For this, the high density difference between the hot and cold gas observed at high pressures was used as an advantage. In fact, the transparent part of the test section was surrounded with an insulation cap (cf. Figure 4.3 and Figure 4.7) where the hot gas forms a stable stratification and stays like in a hot-air balloon. In order to reduce the heat losses to a minimum, the insulation cap is only open to the bottom. This allows to place the camera capturing the flow conditions outside of the hot regions, but implies to place the camera vertically.

Consequently, the observation of the test section from the side is only possible over a 45° inclined mirror placed under the insulation cap, which deflects the light from the test section to the camera. Due to this configuration, the mirror must be designed to withstand temperatures of up to 264°C at which it could be exposed in this region. Furthermore, a front surface mirror should be used in order to avoid ghost images. Therefore, a glass plate was coated to mirror with a 100 nm aluminium layer, which was protected from oxidation by an additional 100 nm SiO_2 coat. Such samples were successfully tested in an air atmosphere at 50 bar and 280°C, which is more than the expected conditions under the insulation cap.

For the evaluation of the position and dimensions of the mirror, a 3D CAD model of the test apparatus was arranged. The optical path was simulated from the camera objective over the mirror to the main outer edges of the transparent part of the test section (Figure 4.4). From the model, the minimum mirror dimensions were estimated to about 745 x 760 mm (L x H). For an easier adjustment as well as for safety margins, a mirror with a reflecting surface of 825 x 825 mm (i.e. after subtraction of the borders for the support) was planned.

After the manufacturing and assembling of the components, the position of the high-speed camera and mirror were adjusted in order to best visualise the test section. The result is shown in a test picture of the high-speed video camera (Figure 4.5). The border between mirror and its support frame was marked in red in the figure, which shows that the adjustment latitude in the vertical direction is really

limited. However, this test proves that the 3D CAD model was a good way for the global design the optical system and in particular for the dimensioning of the mirror.

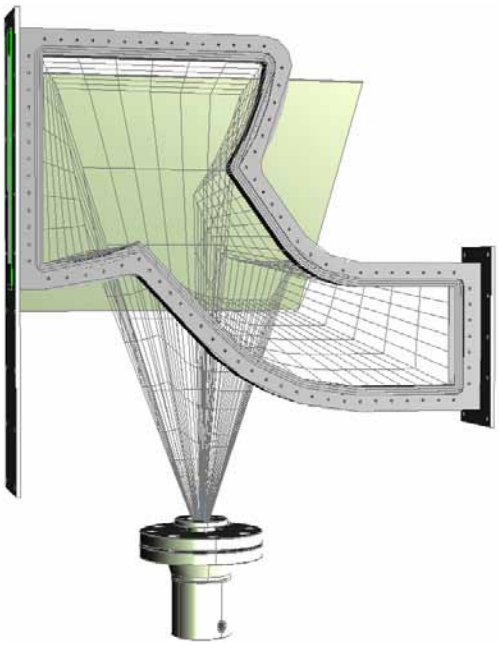

Figure 4.4: 3D model of the optical path for observation of the test section over the mirror

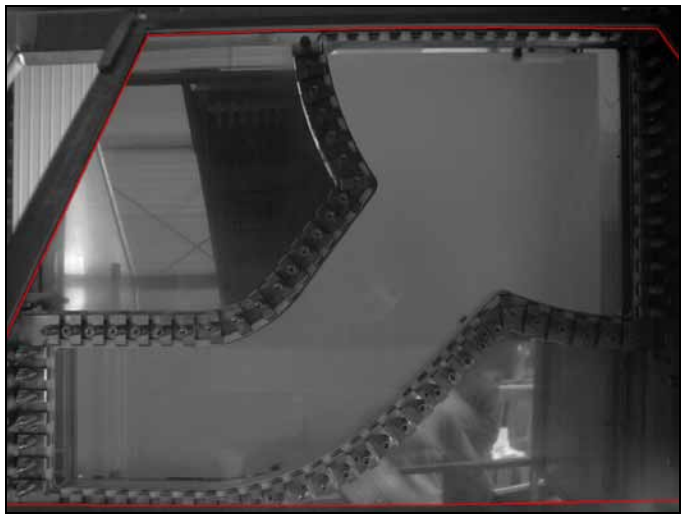

Figure 4.5: Picture of the test section after positioning of the high-speed camera and adjustment of the mirror frame (inner edge in red)

The different cameras (i.e. the CCTV camera used for monitoring purposes and the high-speed video camera serving for the measurements) installed in the pressure chamber were mounted in pressure proof containers (cf. example in Figure 4.6) connected to the outside with special corrugated hoses withstanding external pressure loads (in blue in Figure 4.7).

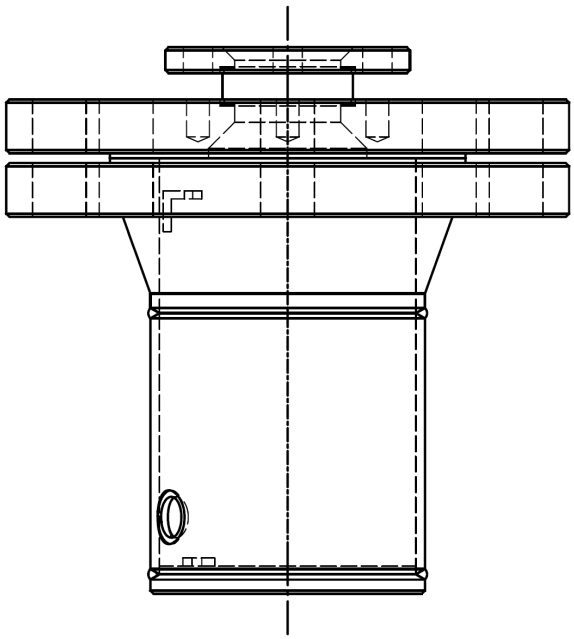

Figure 4.6: pressure proof container for the high-speed video camera: detail of the design drawings

Figure 4.7: insulated test section mounted in the pressure chamber

4.1.2.4. Illumination systems

For the cold air/water experiments, a LED illumination system was chosen. LED array modules of the type *seelectorLUX A150* manufactured by *hema electronic GmbH* were used, which contain 100 ultra bright LEDs each. The advantages of this kind of LED illumination are:

- pressure proof design (tested in house);
- low voltage power supply: according to the technical rules, the power line can be transmitted through the wall of the pressure chamber and consequently the LED modules can be operated directly in the pressure chamber;
- high-power illumination;
- high number and well distributed light sources (i.e. best preconditions to achieve homogenous illumination).

17 single LED array modules were disposed in front of the tests section (see Figure 4.8). Due to ventilation slots designed on the side of the LED modules for their active air-cooling, a space of about 20 mm had to be left free between the modules. In order to achieve a homogeneous background illumination, a diffuser plate was mounted between the LED modules and the test section. For the diffuser, a 5 mm thick glass plate sandblasted on both sides was chosen and was fixed on the steal frame of the test section. The distance between LED modules and diffuser plate was about 0.4 m. The power of the single LED modules was adjusted via output voltage of the power supply units in order to achieve the best possible background uniformity. Moreover, steel sheets were mounted around the transparent part of the test section in order to restrict the illuminated area to the domain of interest.

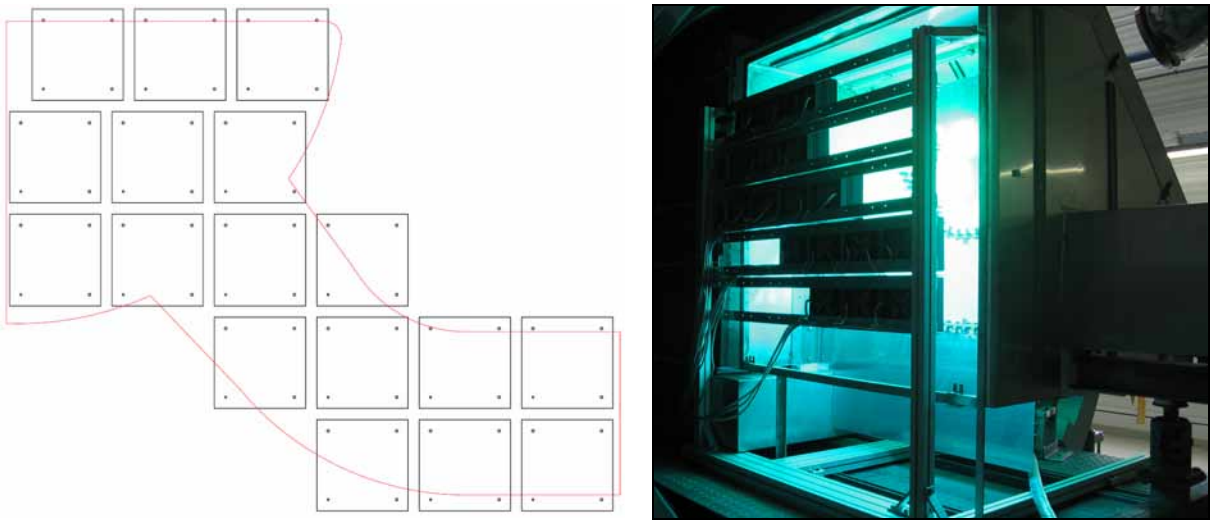

(a) disposition of the LED modules (in black) in front of the diffuser plate (in red)

(b) mounted LED modules and the test section

Figure 4.8: LED illumination for the air/water experiments

Unfortunately, the LED illumination system could not also be used for the steam/water experiments, because the operation of the LED modules is limited to low surrounding temperatures. Therefore, a second illumination system was build up for the hot steam/water experiments. Apart from the LED illumination, no other powerful light source was found which could be installed in the pressure chamber. Therefore, the light had to be generated outside of the pressure chamber, transmitted through a sight glass and guided via fibre optics to the test section.

A high power gas-discharge lamp (see Figure 4.9-a) was used as light source. The power supply of the gas-discharge lamp was chosen with a flicker free mode for high-speed observations up to 1.0 kHz. The beam of parallel light enters the pressure chamber through one of its sight glasses DN125. Afterwards, the light beam is collected with a lens in order to penetrate transversely the inlet of a dedicated fibre optics bundle. Special glass fibres withstanding high temperature gradients were

chosen, because the other end of the fibre optics is exposed to the high temperatures below the insulation cap. The fibre optics bundle was designed with one inlet and multiple outlets in order to distribute the light uniformly over the complete observed area and consequently to achieve a homogeneous illumination of the test section background. Therefore, each of the seven outlets of the fibre optics bundle was connected to wide angle optical systems (Figure 4.9-c) disposed behind the diffuser plate (Figure 4.9-b). Contrary to the LED modules, the wide-angle modules were not placed perpendicularly to the diffuser plate, but were directed to the high-speed camera. Therefore, the ideal room position of the modules has been determined in 3D in function of their angle to the optical axis of the camera. Accordingly, a target was arranged and placed on the test section in order to correctly position the modules with a laser beam.

(a) high power gas-discharge lamp (b) overview of the lightening system (c) wide angle module

Figure 4.9: Lightening system for the steam/water experiments

4.1.3. Instrumentation of the hot leg model

4.1.3.1. Overview

The boundary conditions (e.g. inlet flow rates, pressures, temperatures, or water levels in the separators) were measured at 1 Hz with the data acquisition system of the TOPFLOW test facility. An overview of the position of the measuring devices is shown schematically in Figure 4.10. Furthermore, the general characteristics of each device is indicated in Table 4.1 according to the TOPFLOW nomenclature. For detailed information, including calibration protocols, the reader is referred to the technical report by Seidel et al. (2010).

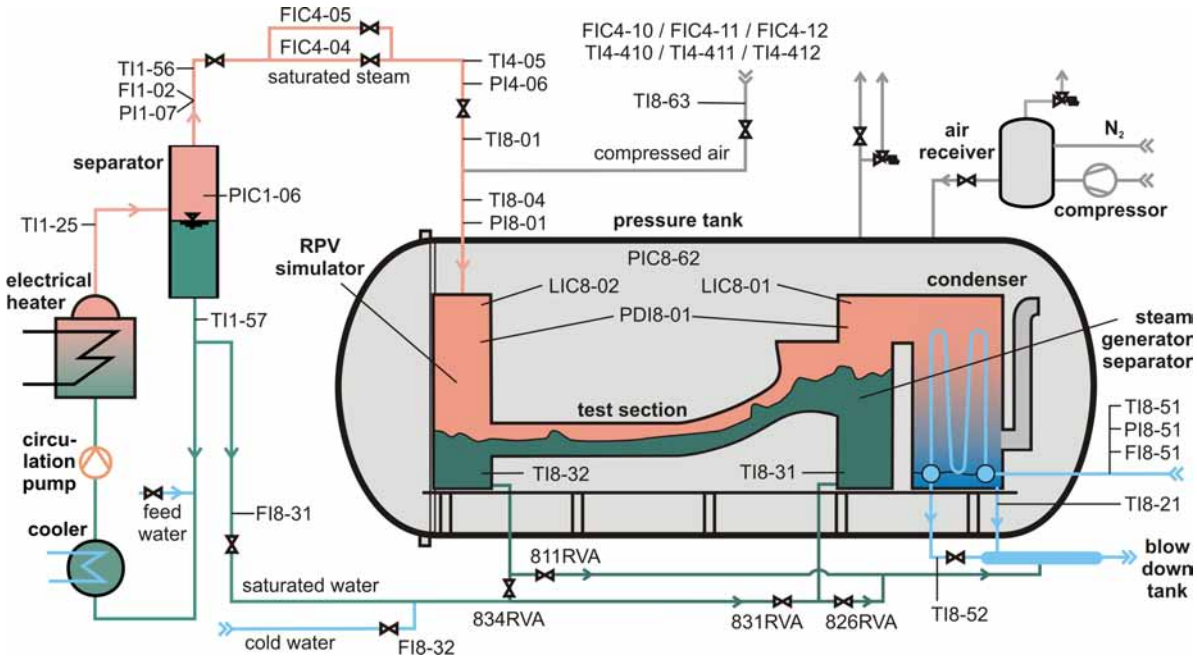

Figure 4.10: Scheme of the instrumentation of the test facility

Table 4.1: Instrumentation of the hot leg model

Device	Description	Measuring range	Unit
FI1-02	steam flow rate out of heater separator	0.27 - 2.7	kg/s
FIC4-04	steam flow rate to test section (high)	0.25 - 2.7	kg/s
FIC4-05	steam flow rate to test section (low)	0.013 - 0.26	kg/s
FIC4-10	air flow rate to test section (high)	400 - 950	Nm^3/s
FIC4-11	air flow rate to test section (medium)	50 - 450	Nm^3/s
FIC4-12	air flow rate to test section (low)	5 - 50	Nm^3/s
FI8-31	flow rate of saturated water to test section	0.4 - 4	kg/s
FI8-32	flow rate of cold water to test section	0.4 - 4	kg/s
FI8-51	flow rate of cooling water to condenser	4 - 38	kg/s
PIC1-06	pressure in heater separator	0 - 10	MPa
PI1-07	pressure in steam line at outlet of heater separator	0 - 7.1	MPa
PI4-06	pressure in steam line after flow meters	0 - 10	MPa
PI8-01	pressure in gas line before test section inlet	0.001 - 5.4	MPa
PIC8-62	pressure in pressure chamber	0.001 - 5.4	MPa
PI8-51	pressure in cooling water line of condenser	100 - 700	kPa
PDI8-01	pressure difference over test section	0 - 50	kPa
TI1-25	temperature in outlet line of electrical heater	0 - 500	°C
TI1-56	temperature in steam line at outlet of heater separator	-270 - 1300	°C
TI4-05	temperature in steam line after flow meters	-270 - 1300	°C
TI8-01	temperature in steam line (intermediate position)	0 - 270	°C
TI8-04	temperature in gas line before test section inlet	50 - 300	°C
TI4-410	temperature in air line after flow meter	35 - 50	°C
TI4-411	temperature in air line after flow meter	35 - 50	°C
TI4-412	temperature in air line after flow meter	35 - 50	°C
TI8-63	temperature in air line (intermediate position)	0 - 100	°C
TI1-57	temperature saturated water after heater separator	50 - 300	°C
TI8-31	temperature at bottom of SG separator	50 - 300	°C
TI8-32	temperature at bottom of RPV simulator	50 - 300	°C
TI8-51	temperature of cooling water at inlet of condenser	0 - 400	°C
TI8-52	temperature of cooling water at outlet of condenser	0 - 400	°C
TI8-21	temperature of condensate outflow	0 - 270	°C
LIC8-01	water level in SG separator		m
LIC8-02	water level in RPV simulator		m
811RVA	opening outlet valve of RPV simulator	0 - 100	%
826RVA	opening outlet valve of SG separator	0 - 100	%
831RVA	opening inlet valve of SG separator	0 - 100	%
834RVA	opening inlet valve of RPV simulator	0 - 100	%

The instrumentation includes a vortex meter measuring the injected water mass flow rate. The injected air mass flow rate was measured and controlled using thermal mass flow meters, the steam flow rate over the pressure drop through a Venturi tube. The temperature of the fluids was measured with thermocouples at various positions in the facility. Furthermore, the water levels in both separators were determined by the measurement of the differential pressure between the top and the bottom of the vessels with differential pressure transducers. The pressure drop over the test section was measured by a differential pressure transducer placed between the SG and RPV separators. These global parameters give important input or output values for the comparison with simulations.

Moreover, as already mentioned, the flow behaviour was recorded with a high-speed video camera placed in the pressure chamber. The camera was operated at frequencies of 60 to 100 Hz and a shutter speed of 1/500 to 1/1000 s during 40 to 180 s. Furthermore, the camera was synchronised with the data

acquisition system of TOPFLOW. The synchronisation method is similar to the clapperboard in film productions: a signal was manually switched on from the control room during the experiment, actuating a LED placed in the field of view of the camera. This signal was recorded simultaneously by the data acquisition system on one hand and in the camera pictures on the other hand. The accuracy of simultaneity depends on the delay of the bus system and of the signal processing components. The time shift is smaller than ±1 s, which is acceptable for our applications.

4.1.3.2. Correction of the air flow meter FIC4-10

Unfortunately, after all the measurement series have been completed, an error in the implementation of the air flow meter FIC4-10 into the test facility was noticed. As a consequence, the raw flow rates recorded by the digital data acquisition system of TOPFLOW with this flow meter (highest measuring range) are wrong. This concerns only the air/water CCFL experiments. In order to correct afterwards the measured flow rates, a calibration curve was recorded with a certified rotameter. This flow meter was mounted in series with the FIC4-10, its outlet being opened to the atmosphere. The scale of the rotameter (*Yokogawa* type *RAMC08*) was established for air at reference conditions of 20.0°C and 1.000 bar. Because the measuring conditions were slightly different, the read values were corrected according to the indications given by the manufacturer as follows:

$$\dot{V}_{N,corr} = \dot{V}_{N,read} \cdot \sqrt{\frac{T_{ref}}{T_{real}} \cdot \frac{p_{real}}{p_{ref}}} \tag{4.1}$$

The actual temperature T_{real} was measured with a thermocouple placed in the flow section at the outlet of the rotameter. The actual pressure p_{real} was obtained from the value at the sea level p_0 published hourly in the internet (site: www.wetter.com / meteorological station of Dresden-Klotzsche), which was converted to the altitude z of HZDR using the barometric formula:

$$p_{real} = p_0 \cdot \exp\left(-\frac{g \cdot M_{air}}{R \cdot T_{real}} \cdot z_{FZD} \right) \tag{4.2}$$

with M_{air} the molar mass of air ($28.96 \cdot 10^{-3}$ kg/mol) and R the universal gas constant ($8.314\ J \cdot mol^{-1} \cdot K^{-1}$). For the calculations, an altitude of 290 m was taken for the HZDR.

After conversion of the volume flow rates (indicated by the meters in norm cubic meter per hour) to mass flow rates, the obtained calibration points could be modelled with a quadratic function as shown in Figure 4.11. The resulting correction function, leading to a good correlation coefficient, is:

$$\dot{m}_{corr} = -2.43822773 \cdot \dot{m}_{raw}^{\ 2} + 2.38124793 \cdot \dot{m}_{raw} - 0.117486184 \tag{4.3}$$

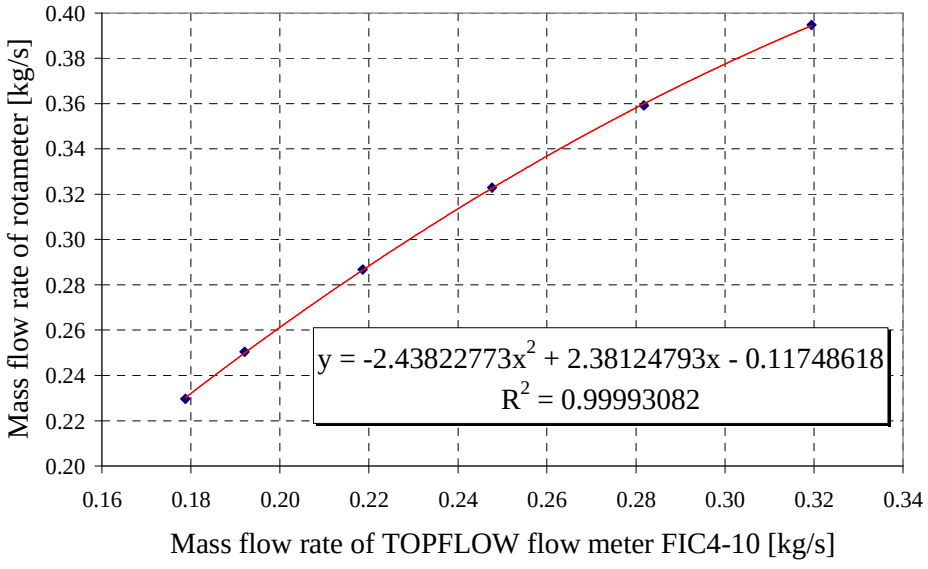

Figure 4.11: Calibration curve of the air flow meter FIC4-10

4.2. Overview of the hot leg experiments

4.2.1. Type of experiments

The following types of experiments were performed with air/water as well as steam/water.

1. Experiments without water circulation for CFD validation purposes:

First of all, the test section is filled with a certain amount of water in order to obtain a stratification in the horizontal part of the hot leg model. During the measurement, a constant gas flow rate is injected, which flows through the test section and entrains the stagnant water, analogical to bubble column experiments. As expected from the Kelvin-Helmholtz instability theory, a minimum gas flow rate is needed to generate water plugs or slugs, which transport the water to the steam generator separator. This gas flow rate was determined empirically before the experiments and only points leading to water entrainment were measured. The experiments were repeated with different gas flow rates and for the air/water tests with 3 different initial water levels.

In order to enable reproducible measurements of the amount of water in the test facility, two reference tests without gas flow rate (i.e. with a stagnant water level) were performed before and after the runs. In this way, the possible variation over time of the water inventory due to droplet entrainment out of the test section or steam condensation inside the setup was captured. This problem was particularly pronounced during the steam/water experiments at high pressure due to the relatively large heat losses and to the time needed to establish the desired gas flow rate. This leads to high condensation rates, and consequently, particular attention is needed for the analysis of the data. The raw measurement data, including a total of 36 runs (cf. test matrix in the appendix), is currently available for comparisons with CFD. However, the data from the experiments without water circulation was not analysed in more details in this thesis.

2. Simulation of the co-current two-phase flow natural convection:

Different combinations of water and gas flow rates are injected in the RPV simulator and flow to the SG separator. The water flow rate to the SG separator can be evaluated from the water level increase in this vessel.

3. Simulation of the reflux condenser mode during mid-loop operation:

Water is injected from the SG side and flows through the test section to the RPV simulator, which is filled. When the water level in the RPV simulator and in the horizontal part of the hot leg is high enough, waves and slugs are generated and inhibit the water to flow to the RPV simulator. Therefore, the injected water accumulates in the SG separator. Theses experiments were repeated with different combinations of water and gas flow rates.

4. Simulation of the reflux condenser mode and counter-current flow limitation:

A constant water flow rate is injected in the SG separator and flows to the test section. The gas is injected in the RPV simulator and flows in counter-current to the water through the test section to the SG separator. The limitation of the water flow rate streaming through the test section (discharge water flow) is evaluated over the increase of the water level in the RPV simulator. Therefore, the water level in this separator is kept below the inlet nozzle of the hot leg. The experiments were repeated with different water mass flow rates.

The CCFL experiments were divided in 2 different subtypes:

1. Flooding experiments: the experiments are began with a low gas flow rate where the counter-current flow is stable. During the run, the air flow rate is stepwise increased up to CCFL conditions, and when possible to zero penetration conditions.
2. Deflooding experiments: first, a high gas flow rate is injected in order to establish flooding conditions. During the run, the gas flow rate is stepwise decreased until the breakdown of the CCFL and the achievement of a stable counter-current flow.

4.2.2. Boundaries and arrangement of the test matrix

The boundaries of the test matrix are limited on one hand by the installed hardware and on the other hand by physical or practical reasons. After the definition of the range of the possible, the test matrix can be arranged in details, leading to the final number of runs. However, the test matrix defines only theoretical goal values that cannot be perfectly achieved during the experiment. Consequently, the measured values may be slightly different. The detailed test matrices for each experiment type are presented in the appendix, while the complete overview of the boundary conditions of each run are documented in the experimental report by Seidel et al. (2010).

First, the pressure levels of the experiments were chosen. The maximum value is limited by the design pressure of the pressure chamber of 50 bar. However, this is only possible for steam/water experiments, because the air supply system of the TOPFLOW test facility only works at pressures up to about 7 bar. Furthermore, for a safe operation of the test facility, and especially in order to treat the large glass windows with care, the occurrence of condensation shocks should be avoided. Therefore, it was chosen not to perform steam/water experiments at low-pressure levels, where condensation shocks may also occur with water subcooling of just a few Kelvin. The lowest pressure level for the steam/water tests was set to 15 bar, in order to enable comparisons with the results obtained at the UPTF test facility, where this value was often chosen for experiments (e.g. CCFL experiments in Test n°11). Moreover, the temperature of the steam/water experiments always corresponds to saturation conditions, whereas the air/water tests were performed at room temperature.

The hot leg experiments were performed at the following pressure and temperature conditions:

- air/water: 1.5 bar (only CCFL experiments) and 3.0 bar / 14-29°C
- steam/water: 15.0 bar / 198°C, 30.0 bar / 234°C, 50.0 bar / 264°C

With the available hardware of the facility, the fluid flow rates can be varied in the following range:

- water: 0.3 … 1.0 kg/s (flow meters FI8-31 and FI8-32)
- air: 0.002 … 0.340 kg/s (flow meters FIC4-10 … 12)
- steam: 0.016 … 1.40 kg/s (flow meter FIC4-04/FIC4-05 and max. heating power)

Since the possible range of water flow rates is narrow, this was completely used (0.3 to 1.0 kg/s) for all types of experiments with water injection. Some CCFL experiments were performed at lower water flow rates. In this case, the flow rate can only be estimated over the water level increase in the separators, because the flow meter gives no indication.

For all types of quasi-stationary experiments (all apart from the CCFL experiments), the test matrix was built in order to be able to match different parameters: points with equal mass flow rate $\dot{m}_i$, equal superficial velocity j_i and equal Wallis parameter J^*_i were chosen. This allows to check the possible similarities involving these parameters at different pressures. The relation between the parameters and the mass flow rate are:

$$j_i = \frac{\dot{m}_i}{\rho_i \cdot A} \tag{4.4}$$

$$J^*_i = j_i \cdot \sqrt{\frac{1}{g \cdot H} \cdot \frac{\rho_i}{\rho_L - \rho_G}} = \frac{\dot{m}_i / A}{\sqrt{g \cdot H \cdot \rho_i \cdot (\rho_L - \rho_G)}} \tag{4.5}$$

Because of the variation of the fluid densities, the three parameters evolve differently with the pressure and temperature conditions, as shown in Table 4.2. As an example, a reference steam/water experiment at 15.0 bar and a steam mass flow rate of 0.150 kg/s is chosen. This corresponds to a superficial velocity in the horizontal part of the test section of 1.58 m/s and a Wallis parameter of 0.095. In order to obtain the same Wallis parameter at 50.0 bar, 0.256 kg/s of steam is necessary. The same gas superficial velocity is achieved at 0.501 kg/s of steam. This important difference in the mass flow rates was used for the arrangement of the test matrix: as shown in Table 4.3 and Figure 4.12, the

intermediate points were chosen near the equivalent parameter values (e.g. 0.250 instead of 0.256 kg/s for the point with equivalent Wallis parameter of the example).
Furthermore, although the variation of the density with the pressure and temperature is not so significant for the water than for the gas, its influence is not negligible. In fact, for a mass flow rate of 0.900 kg/s at 15.0 bar, the same Wallis parameter and liquid superficial velocity are obtained at 50.0 bar with 0.798 and 0.807 kg/s, respectively (cf. Table 4.2). Therefore, the water flow rate has to be chosen according to the same equivalent parameter as for the steam flow rate. This was originally intended but, unfortunately, after the conduction of the experimental series a systematic error in the measurement of the water flow rate during the steam/water experiments was identified. In fact, the measuring device FI8-31 was calibrated for a pressure of 62.0 bar and 260°C. While using it at other conditions, a correction function has to be applied. Because this compensation of the density variations was not known at the moment of the arrangement of the test matrix, the real water flow rate deviates from the intended one. The most important deviations are obtained for the experiments at 15 bar and reach up to about 10% (e.g. 0.993 instead of 0.900 kg/s).

Table 4.2: Equivalences for the steam and water mass flow rates between 15 and 50 bar for the reference experiments with 0.300 and 0.900 kg/s of water as well as 0.075, 0.150 and 0.250 kg/s of steam at 15 bar

	Reference conditions			**Same Wallis parameter J***		**Same superficial velocity j**	
Pressure:	**15.0 bar**			**30.0 bar**	**50.0 bar**	**30.0 bar**	**50.0 bar**
Fluid [-]	**m [kg/s]**	**J* [-]**	**j [m/s]**	**m [kg/s]**	**m [kg/s]**	**m [kg/s]**	**m [kg/s]**
Steam	0.075	0.0474	0.790	0.102	0.128	0.148	0.250
Steam	0.150	0.0949	1.58	0.204	0.256	0.296	0.501
Steam	0.250	0.158	2.63	0.341	0.427	0.494	0.835
Water	0.300	0.0178	0.0277	0.283	0.266	0.285	0.269
Water	0.900	0.0533	0.0831	0.849	0.798	0.854	0.807

Table 4.3: Equivalences between the experimental points of the test matrix

15 bar experiments		**Equivalent 3 bar experiments**		**Equivalent 30 bar experiments**	**Equivalent 50 bar experiments**
Steam mass flow rate	**Equivalent parameter**	**Air flow rate**		**Steam mass flow rate**	**Steam mass flow rate**
[g/s]	**[-]**	**[Nm³/h]**	**[g/s]**	**[g/s]**	**[g/s]**
35	mass flow rate	100	35.9	-	-
	Wallis parameter	60	21.5	-	-
75	mass flow rate	200	71.8	75	75
	Wallis parameter	-	-	100	130
	superficial velocity	100	35.9	150	250
150	mass flow rate	400	143.6	150	150
	Wallis parameter	300	107.7	200	250
	superficial velocity	200	71.8	320	500
250	mass flow rate	-	-	250	250
	Wallis parameter	-	-	320	430
	superficial velocity	300	107.7	500	835

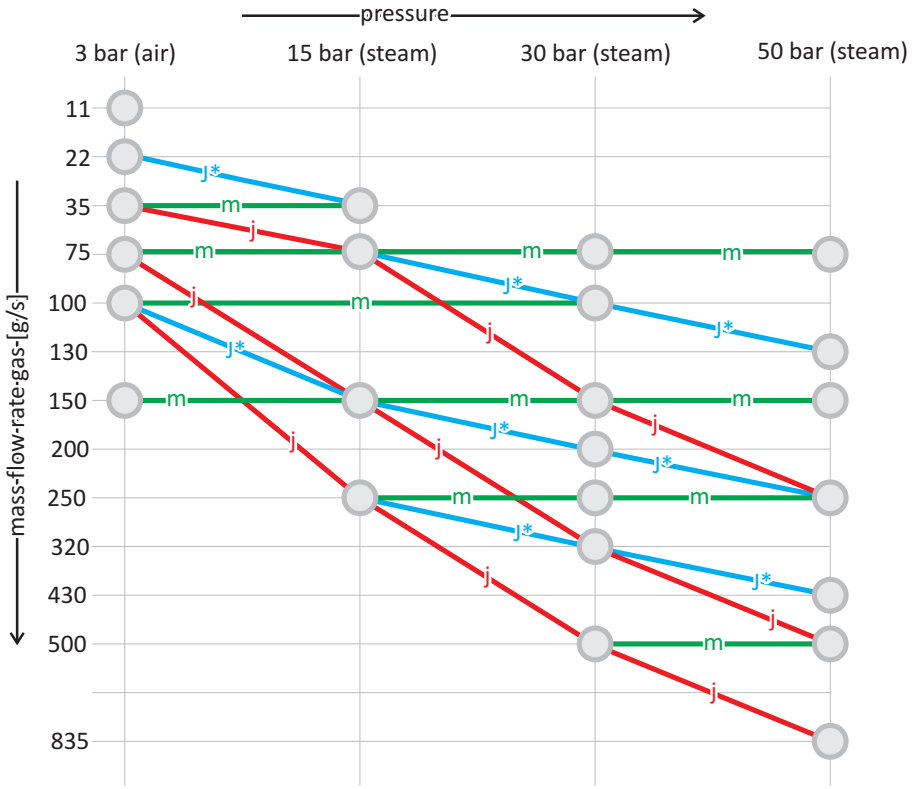

Figure 4.12: Arrangement of the test matrix

4.3. Co-current flow experiments

4.3.1. Experimental procedure and test matrix

During the experiments, a constant flow rate of each fluid was injected in the RPV simulator (see Figure 4.13) and flowed through the test section to the SG separator. In this tank, the liquid phase is separated from the gas, which flows to the condenser unit. The water is stored in the SG separator so that the water level increase can be used to check the mass balance. Because an accumulation of water in the SG separator could influence the two-phase flow in the test section, special attention was paid to the water level in this tank. The experiments were completed as soon as the water in the SG separator reached the level of the steam generator inlet chamber. Table 4.4 shows an overview of the varied boundary conditions. The co-current flow experiments were performed with air and water at 3.0 bar and room temperature as well as with steam and water at pressures up to 50.0 bar and the corresponding saturation temperature. In the experimental series, the water mass flow rate was varied between 0.3 and 0.9 kg/s and the gas mass flow rate between 0.01 and 0.84 kg/s.

Table 4.4: Co-current flow experiments in the hot leg model: overview of the test matrix

Gas [-]	**Pressure level [bar]**	**Temperature [°C]**	**Water flow rate [kg/s]**	**Gas flow rate [g/s]**	**Number of runs [-]**
air	3.0	19 – 25	0.32 – 0.91	11 – 144	12
steam	15.0	198	0.30 – 0.92	35 – 400	18
steam	30.0	233	0.28 – 0.91	75 – 500	15
steam	50.0	263	0.27 – 0.91	76 – 840	16

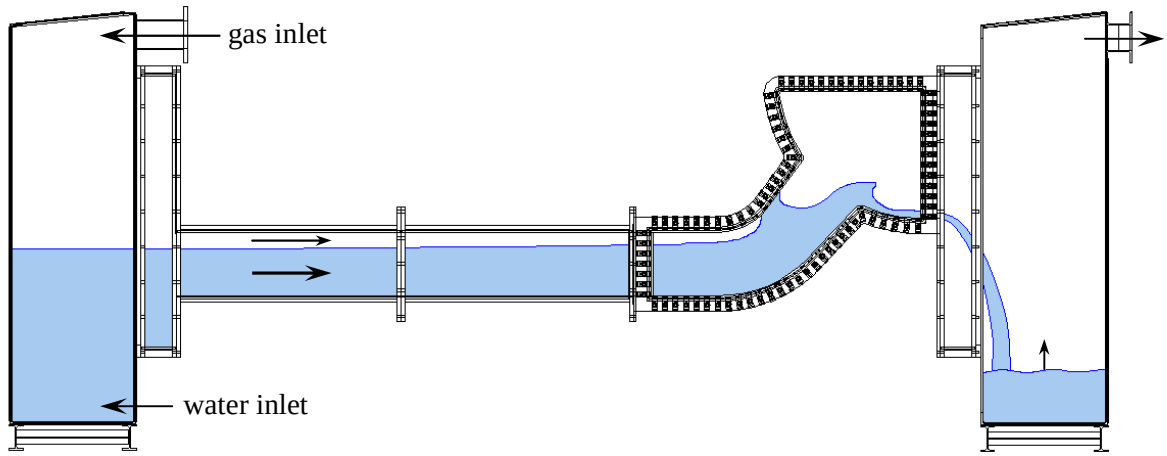

Figure 4.13: Co-current flow experiments

4.3.2. Examples of typical co-current flow experiments

Basically, two different time dependent behaviours were observed during the co-current flow experiments. As an example, one typical experiment of each is presented in the next sections in order to illustrate the observed phenomena.

4.3.2.1. Experiment with continuous behaviour

The chosen run was performed at a system pressure of 30.0 bar and a temperature of about 231°C, which is close to the saturation conditions. The measured mass flow rates were 0.29 kg/s (±6 g/s) for the water and 0.50 kg/s (±5 g/s) for the steam. Figure 4.14 shows the evolution in time of the water level in the separators and of the pressure drop over the test section. At these boundary conditions, the water level in the RPV simulator, and consequently in the horizontal part of the hot leg, is nearly constant at 562 mm ±2 mm. The measured pressure drop over the test section fluctuates between 0.35 and 1.2 kPa all the time, indicating that the flow regime is intermittent. As shown in Figure 4.15, slug flow was observed in the test section: waves generated in the horizontal part of the hot leg (Figure 4.15-a and b) grow to slugs in the bend (Figure 4.15-c). Due to the high gas velocity, droplets detach for the slug front and transport water to the SG inlet chamber (Figure 4.15-d to f). Simultaneously, the next significant wave approaches (Figure 4.15-f) and the process repeats. This fractional water transport mechanism is continuous and leads to an almost linear increase of the water level in the steam generator separator.

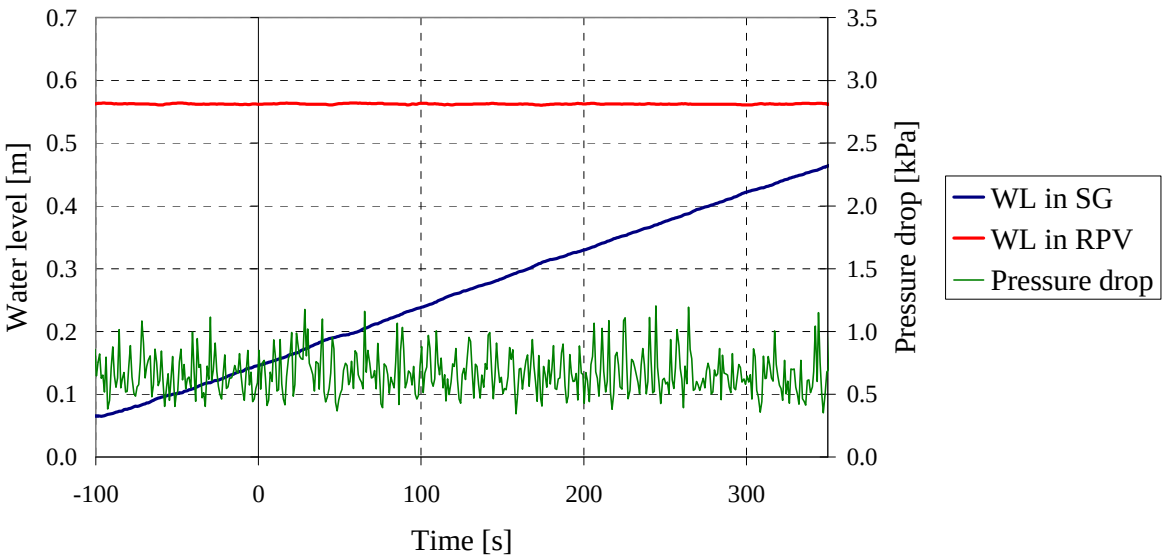

Figure 4.14: Evolution of the water levels and pressure drop in time during a co-current flow experiment at 30.0 bar and 231°C, with $\dot{m}_G$ = 0.50 kg/s and $\dot{m}_L$ = 0.29 kg/s

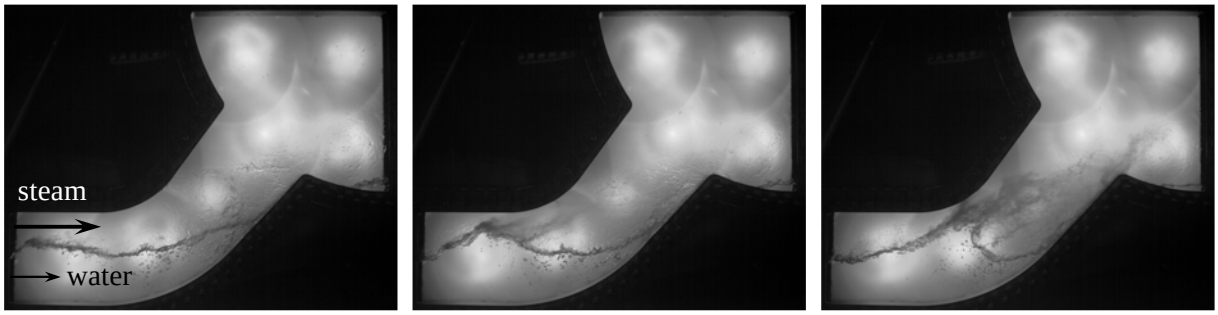

(a) t = 0.75 s (b) t = 0.85 s (c) t = 0.95 s

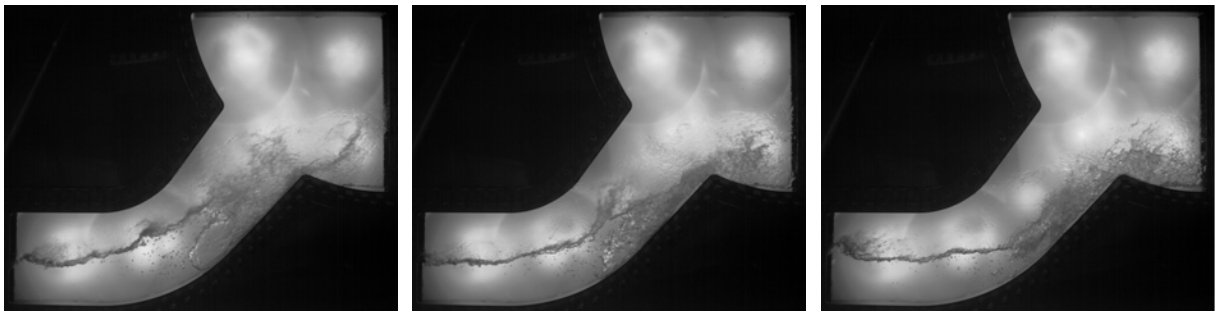

(d) t = 1.05 s (e) t = 1.15 s (f) t = 1.25 s

Figure 4.15: Evolution of the interface structure during a co-current flow experiment at 30.0 bar and 231°C, with $\dot{m}_G$ = 0.50 kg/s and $\dot{m}_L$ = 0.29 kg/s

4.3.2.2. Experiment with periodic behaviour

The presented run was performed at a system pressure of 30.0 bar, a temperature of about 230°C, a mass flow rate of 0.30 kg/s for the water and 0.15 kg/s for the steam. Figure 4.16 shows the evolution in time of the water level in the separators and of the pressure drop over the test section. It is remarkable that the water level in the SG separator increases stepwise. This indicates that despite of the constant inlet flow rates, the water transport to the SG separator is discontinuous. This behaviour explains the periodic variation of the water level in the RPV simulator between 640 and 660 mm as well as the regular increase of the pressure drop over the test section.

According to the flow structures observed with the high-speed camera over one period (cf. Figure 4.17), the following two flow regimes were observed:

1. First, for t < 31.6 s, the flow in the horizontal part of the channel is stratified wavy (Figure 4.17-a) and no water is transported to the SG separator. This flow regime is characterised by a negligible pressure drop over the test section.
2. Afterwards, the water level reached in the horizontal part of the hot leg obstructs the steam flow enough to generate instable wave growth to plugs (Figure 4.17-b and c). Consequently, water is transported to the SG separator and the pressure difference between the separators increases and becomes unstable. For 40 < t < 45 s, the plugs become bigger (Figure 4.17-d) and the amount of water transported is higher than the injected flow rate. Therefore, the water level in the RPV simulator decreases, affecting the plug flow regime which can not be sustained after about 48 s (Figure 4.17-e).

Subsequently, the flow in the horizontal part of the hot leg quiets and comes back to a wavy flow (Figure 4.17-f), before the sequence starts over.

It should be noticed that this intermittent flow behaviour is untypical during natural circulation and basically due to the connection of the hot leg test section to the empty SG separator at the outlet, where the water in drained. In fact, during two-phase natural circulation in the primary circuit of a PWR, the flow in the hot leg is influenced by the downstream conditions in the steam generator. Due to the high elevation, the vertical U-tubes are usually filled with a two-phase mixture which do not allow the flow to quiet in the hot leg. Consequently, due to the particular outlet conditions of our experiments, the results are well suited for generic CFD validation of stratified flows in a reactor

typical geometry. However, the results can probably not be used to reflect the flow conditions in the primary circuit of a PWR.

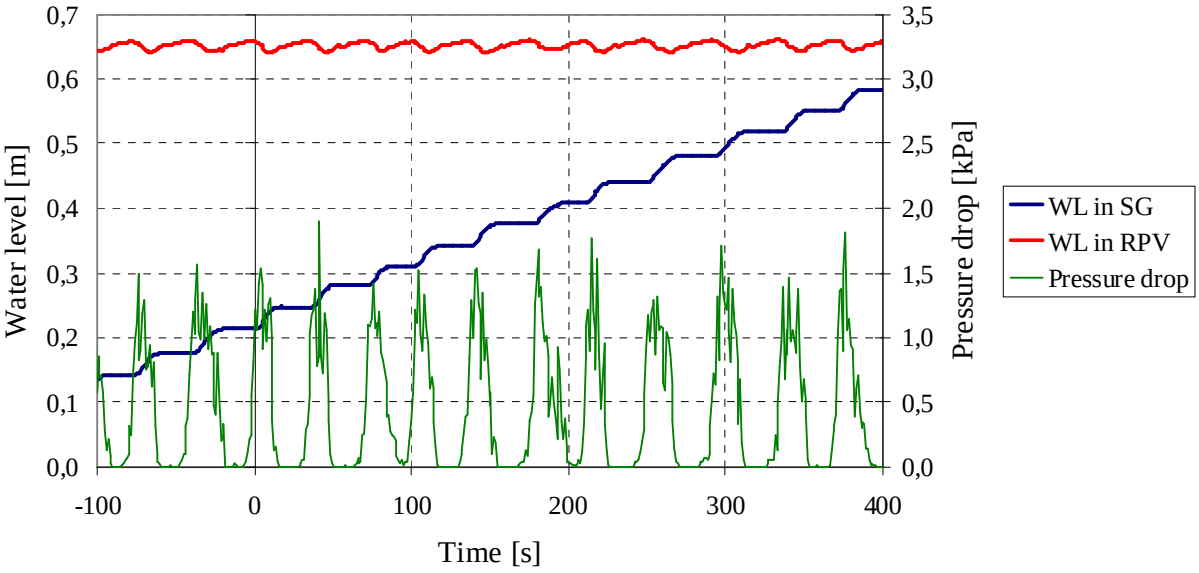

Figure 4.16: Evolution of the water levels and pressure drop in time during a co-current flow experiment at 30.0 bar and 230°C, with $\dot{m}_G$ = 0.15 kg/s and $\dot{m}_L$ = 0.30 kg/s

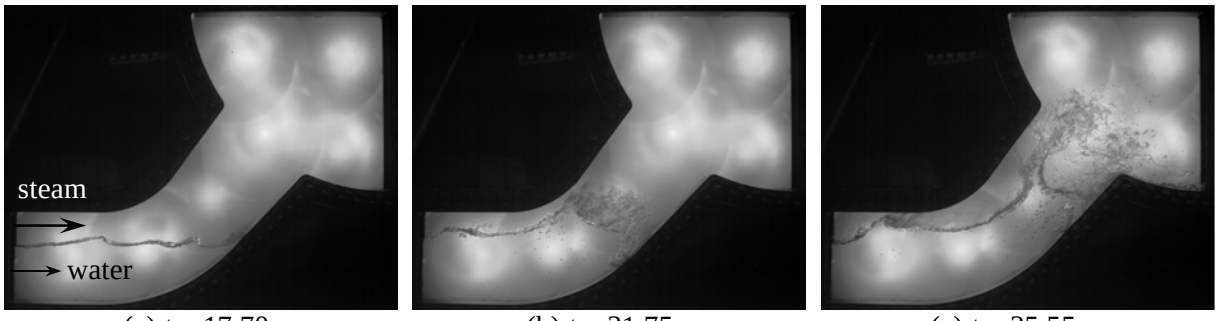

(a) t = 17.70 s (b) t = 31.75 s (c) t = 35.55 s

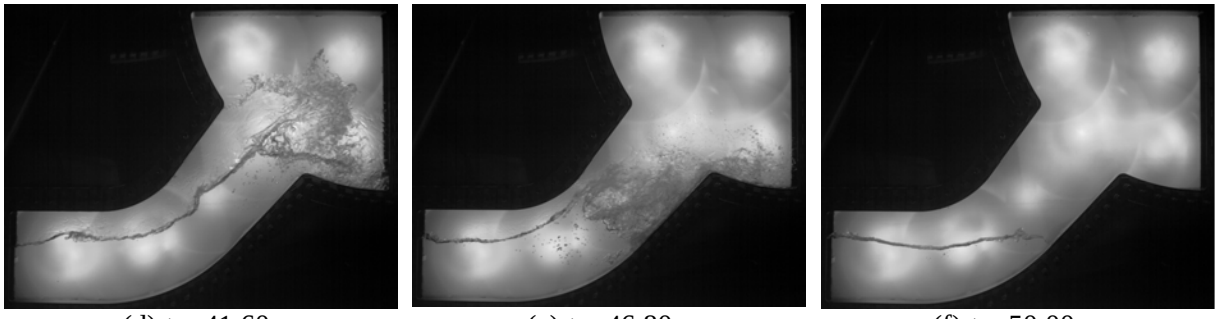

(d) t = 41.60 s (e) t = 46.80 s (f) t = 50.00 s

Figure 4.17: Evolution of the interface structure during a co-current flow experiment at 30.0 bar and 230°C, with $\dot{m}_G$ = 0.15 kg/s and $\dot{m}_L$ = 0.30 kg/s

4.3.3. Evolution of the probability distribution of the water level measured in the RPV simulator

In order to reflect the variation over the time of the water level measured in the RPV simulator as shown in section 4.3.2, a statistical approach is proposed. The probability density distribution of the water level was calculated over the available measuring time (about 250 to 800 s, depending mainly on

the water flow rate). The water level in the RPV simulator l_{RPV} was scaled relatively to the height H of the horizontal part of the hot leg model as follows:

$$L = \frac{l_{RPV} - l_{HL}}{H - l_{HL}} \tag{4.6}$$

with l_{HL} the level of the lower edge of the horizontal part of the hot leg.

The evolution of the probability distribution with the varied boundary conditions (shown in Table 4.4) is presented in Figure 4.18: the row defines the gas and pressure/temperature conditions, the column the water mass flow rate. The exact flow rates measured during each experiment are listed in Table 4.5, where the runs are numbered according to the diagram letter followed by the number of the curve. Figure 4.18 shows that the water level in the RPV simulator, and consequently in the test section, decreases with an increase of the gas flow rate. Furthermore, the form of the distribution varies with the boundary conditions: the air/water experiments at 3.0 bar with a water flow rate of about 0.3 kg/s (Figure 4.18-a) present very large and flat distributions whereas peaked curves were obtained with steam and water at 50.0 bar and a water flow rate of about 0.9 kg/s (Figure 4.18-h). The form of the distribution informs about the stationarity of the water flow to the steam generator: the broader the distribution, the more discontinuous the transport of water over time. In fact, in Figure 4.18-e the peaked distribution 8 corresponds to the exemplary experiment with continuous behaviour shown in section 4.3.2.1, while the flat distribution 3 corresponds to the example with periodic behaviour presented in section 4.3.2.2. In this case, the broad distribution indicates that plug flow transports spontaneously more water to the SG separator than the water flow rate injected in the RPV simulator. This behaviour could mean that the water flow rate naturally entrained by the gas flow can not be reduced below a minimum value. In fact, when the injected water flow rate is lower than this value, the inequality in the input and output mass flow rates leads to an intermittent discharge of the water in the horizontal channel and consequently to a broad probability distribution.

A comparison between the columns of Figure 4.18 shows that at the same pressure and temperature boundary conditions, an increase of the water flow rate tends to sharpen the probability distributions of the water level. According to the theory developed in the previous section, an increase of the water flow rate above the minimum possible discharge water flow rate leads to a continuous water transport and consequently to a peaked distribution. This could be the case between the experiments a-1 and b-1. However, some broad distributions become only slightly sharper with the increase of the water flow rate (e.g. experiments e-3 and f-3). This behaviour could be explained by the resulting reduction of the duration while no water is transported, which corresponds to the time during that waves at the water surface can quiet. Therefore, a higher water flow rate increases the probability for sustaining instabilities at the free surface to lead to an earlier begin of the next plug flow period.

Table 4.5: Mass flow rates of the co-current flow experiments in kg/s (gas/liquid)

	1	**2**	**3**	**4**	**5**	**6**	**7**	**8**
a	0.011/0.32	0.022/0.33	0.036/0.32	0.072/0.33	0.108/0.33	0.144/0.32		
b	0.011/0.90	0.022/0.89	0.036/0.90	0.072/0.89	0.108/0.88	0.144/0.88		
c	0.035/0.34	0.069/0.34	0.15/0.33	0.25/0.34	0.40/0.33	0.59/0.33		
d	0.037/0.98	0.069/0.98	0.15/0.96	0.25/0.97	0.39/0.97	0.61/0.97		
e	0.075/0.32	0.10/0.29	0.15/0.31	0.20/0.30	0.20/0.29	0.25/0.31	0.32/0.29	0.50/0.30
f	0.075/0.93	0.10/0.88	0.15/0.91	0.20/0.88	0.25/0.94	0.32/0.88	0.50/0.87	
g	0.076/0.30	0.14/0.27	0.15/0.29	0.25/0.26	0.25/0.29	0.43/0.27	0.51/0.27	0.83/0.26
h	0.077/0.88	0.13/0.79	0.15/0.89	0.25/0.77	0.25/0.89	0.43/0.78	0.50/0.79	0.84/0.79

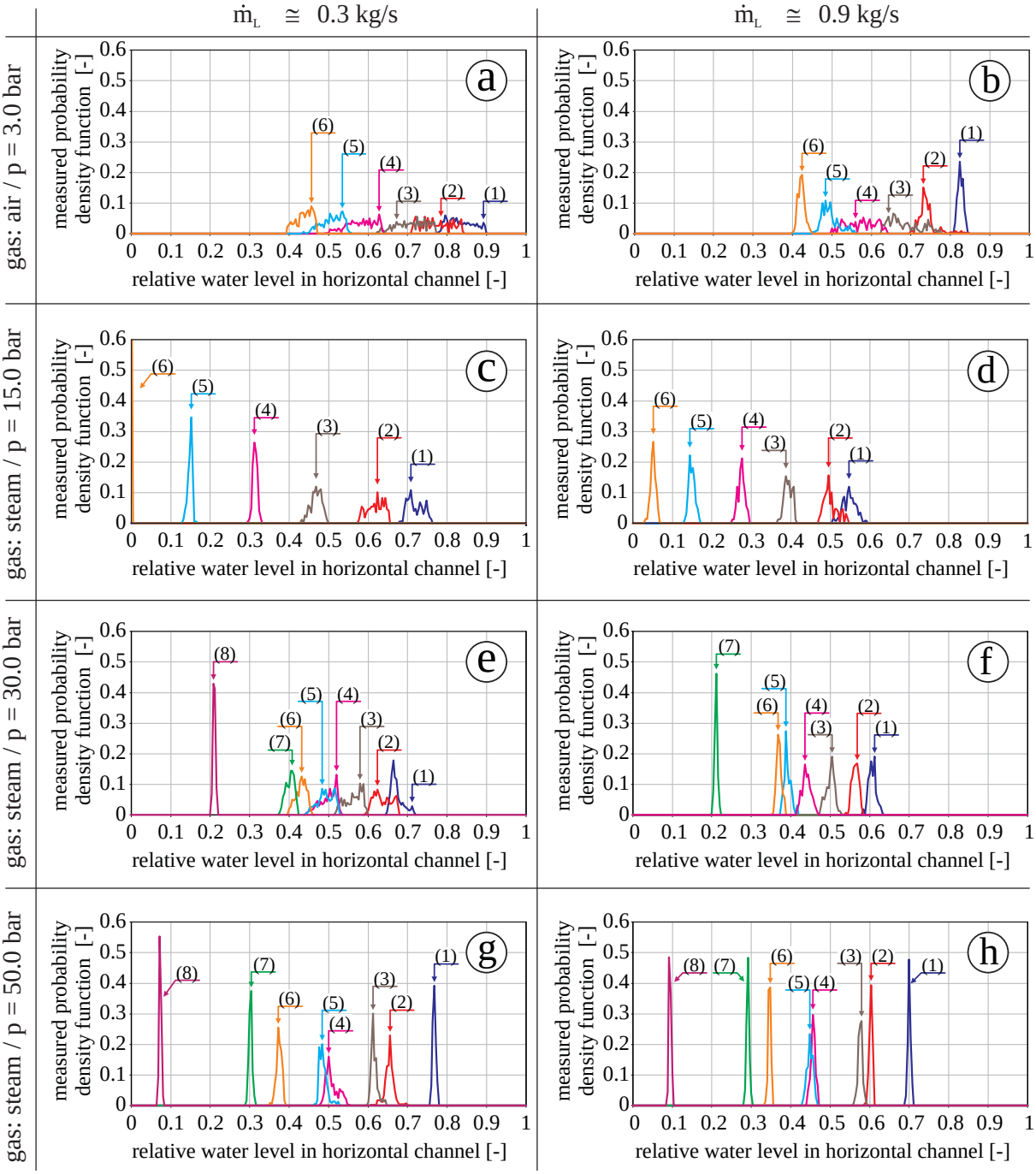

Figure 4.18: Evolution of the frequency distribution of the water level in the RPV simulator during co-current flow experiments under variation of the gas flow rate, for different water flow rates as well as pressure and temperature levels

The left column in Figure 4.18 shows the variation of the distributions with the pressure at a constant water mass flow rate of about 0.3 kg/s. It was observed that the distributions become more peaked and narrow with increasing pressure. However, the temperature was varied with the pressure and therefore the viscosity and the surface tension. Between 20 and 264°C, especially the liquid viscosity as well as the surface tension decrease of a factor of 10 and 3.2, respectively. This substantial variation can explain the more continuous transport of the water to the SG separator by the gas flow at higher pressure and temperature levels. Moreover, this trend is not influenced by an increase of the water flow rate to about 0.9 kg/s (see right column of Figure 4.18).

4.3.4. Comparison with high-speed video observations

In order to interpret the evolution of the form of the distributions shown in Figure 4.18 with the gas flow rate, typical flow pictures taken during different co-current flow experiments are presented in Figure 4.19. As an example, the experiments were chosen at the extrema of the available boundary conditions.

At low gas flow rates, the flow regime was identified as elongated bubble flow (Figure 4.19, left column) and as slug flow at high gas flow rates (Figure 4.19, right column). The probability distributions corresponding to these experiments are peaked. In the case of elongated bubble flow, the transport of water is continuous due to overflow as can be seen in the images. During slug flow, the transport of water occurs with droplets that detach from the wave front, which is also a continuous mechanism. At intermediate gas flow rates (Figure 4.19, middle column), the water transport is periodic and the probability distribution of the water level is flat, like in the experiment presented in section 4.3.2.2. These observations allow to conclude that a change in the form of the probability distribution from peaked over flat to peaked indicates a flow regime transition.

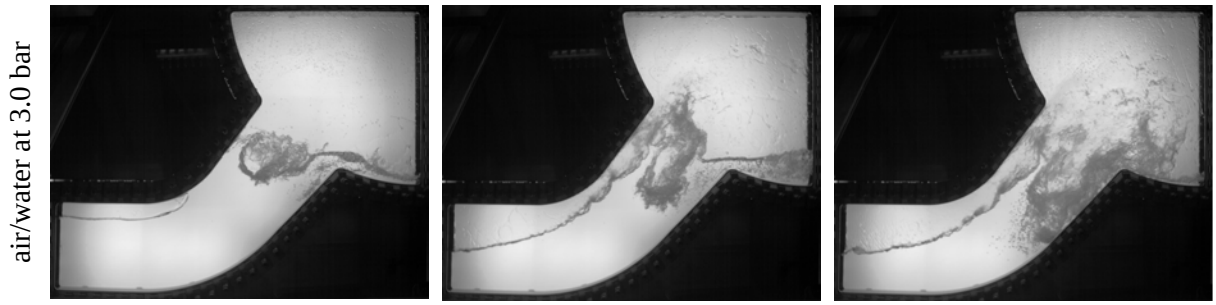

Exp. b-1: $\dot{m}_G$ = 11 g/s | Exp. b-4: $\dot{m}_G$ = 72 g/s | Exp. b-6: $\dot{m}_G$ = 144 g/s

Exp. h-1: $\dot{m}_G$ = 76 g/s | Exp. h-6: $\dot{m}_G$ = 0.43 kg/s | Exp. h-8: $\dot{m}_G$ = 0.84 kg/s

Figure 4.19: Typical flow pictures taken during different co-current flow experiments with $\dot{m}_L \approx 0.90$ kg/s

4.4. Counter-current flow experiments

4.4.1. Experimental procedure

As shown in Figure 4.20, water is injected from the SG side and flows through the test section to the RPV simulator, which is filled. When the water level in the RPV simulator and in the horizontal part of the hot leg is high enough, waves and slugs are generated and inhibit the water to flow to the RPV simulator. Therefore, the injected water accumulates in the SG separator. Theses experiments were repeated with different combinations of water and gas flow rates.

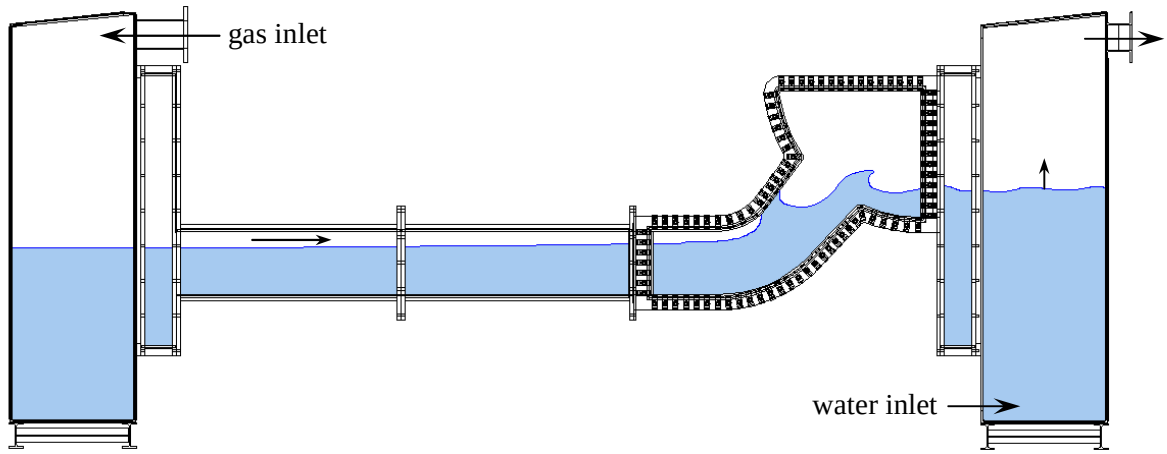

Figure 4.20: Stationary counter-current flow experiments

4.4.2. Example of counter-current flow experiment

As an example, a counter-current flow experiment was chosen to illustrate the available data. This run was performed at a system pressure of 30 bar and a temperature of about 232°C, which is close to the saturation conditions. The mass flow rates were 0.85 kg/s for the water and 0.20 kg/s for the steam. Figure 4.21 shows the evolution of the water level in the separators and of the pressure drop over the test section. Before the beginning of slug flow generation in the test section ($t \leq 20$ s), the water injected in the SG separator flows through the test section to the RPV simulator (Figure 4.22-a). Therefore, the water level in the SG separator is constant at about 0.86 m and the water level in the RPV simulator increases. At about t = 20 s, the water level reached in the horizontal part of the hot leg obstructs the steam flow enough to generate waves at the interface, which finally grow to slugs (Figure 4.22-b). Consequently, the pressure difference between the separators increases and becomes unstable. Afterwards, the gas hindering the water to flow to the RPV, it accumulates in the SG separator. The mean pressure drop over the test section increases with the water level in the SG and the slugs become bigger (Figure 4.22-c).

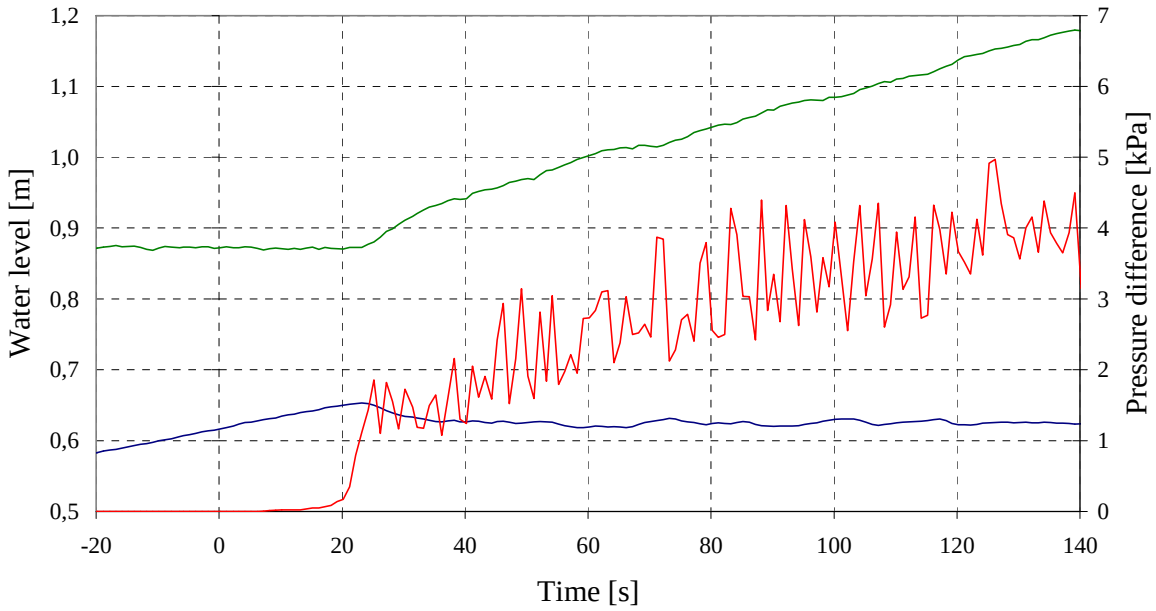

Figure 4.21: Evolution of the water level in the RPV simulator (in blue) and SG separator (in green) and of the pressure difference (in red) during a counter-current flow experiment at 30 bar with $\dot{m}_L$ = 0.85 kg/s and $\dot{m}_G$ = 0.20 kg/s

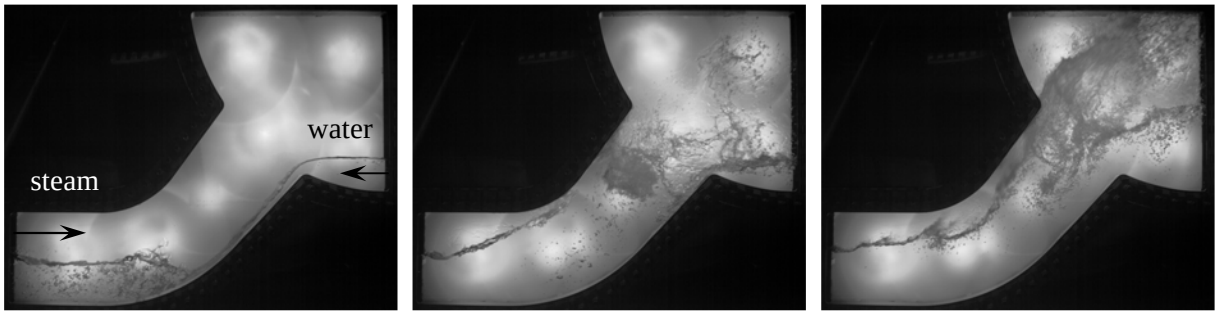

(a) t = 0.00 s (b) t = 23.00 s (c) t = 80.00 s

Figure 4.22: Evolution of the flow during the steam/water counter-current flow experiment performed at 30 bar with $\dot{m}_L$ = 0.85 kg/s and $\dot{m}_G$ = 0.20 kg/s

4.4.3. Qualitative comparison with other counter-current flow experiments

As an example, a series of counter-current flow experiments performed at similar Wallis parameters J^* (cf. definition in equation (2.49), applied with $D = H$ in our case) were compared. The boundary conditions of the compared experiments are given in Table 4.6. The flow rates correspond to a Wallis parameter of about 0.050 for the water and about 0.094 for the gas. Figure 4.23 shows high-speed camera pictures of the flow after an accumulation of water in the SG separator of about 1.0 m (i.e. at t = 60 s for the 30 bar experiment – see Figure 4.21). The aspect of the flow shown at different boundary conditions presents clear qualitative similarities: a well stratified flow in the bend and highly mixed zones in the steam generator inlet chamber (large amount of droplets and bubbles).

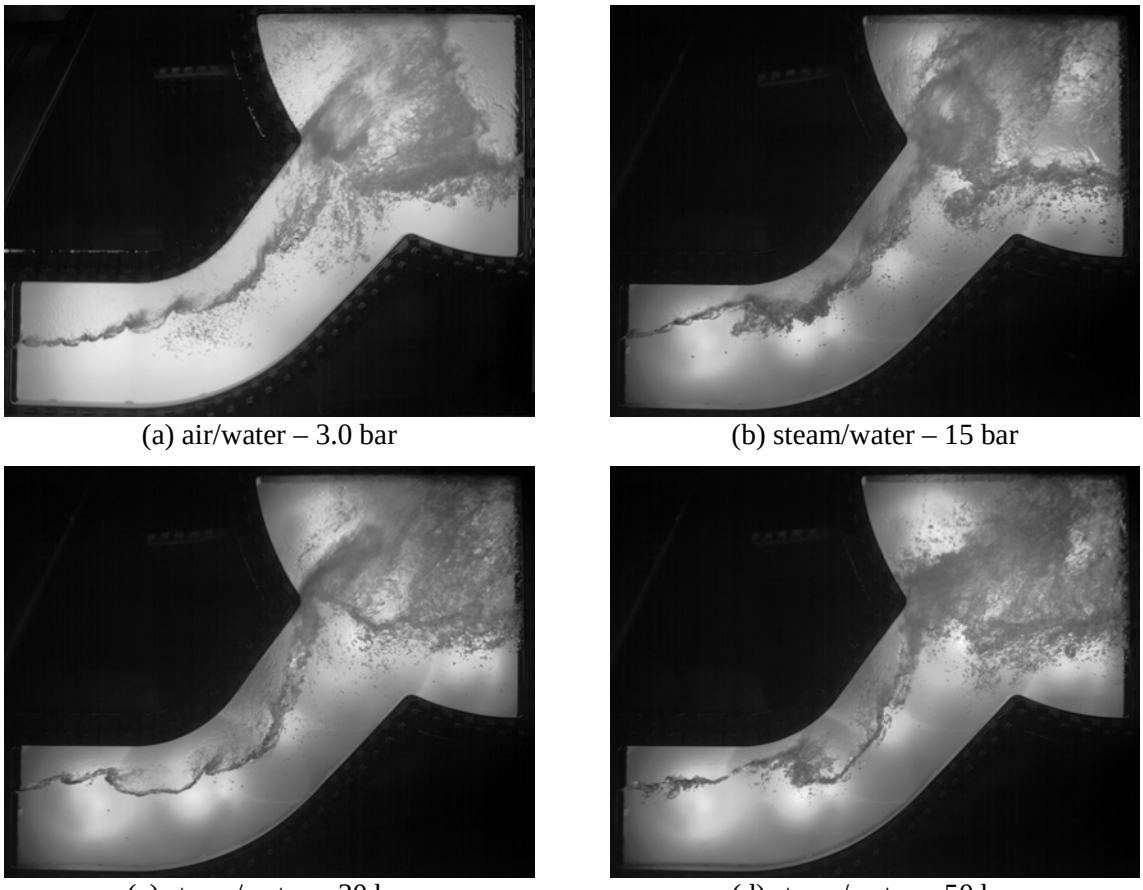

(a) air/water – 3.0 bar (b) steam/water – 15 bar

(c) steam/water – 30 bar (d) steam/water – 50 bar

Figure 4.23: Example of images obtained at different pressures during counter-current flow experiments

Table 4.6: Boundary conditions of the compared counter-current flow experiments

Gas / Run number	Air / 24-12	Steam / 17-13	Steam / 13-08	Steam / 15-15
pressure [bar]	3.0	15	30	50
temperature [°C]	20 - 25	197	232	262
gas flow rate [kg/s]	0.108	0.15	0.20	0.25
water flow rate [kg/s]	0.90	0.90	0.85	0.80

4.5. Counter-current flow limitation experiments

4.5.1. Experimental procedure and test matrix

During the experiments, a constant water flow rate was injected at the bottom of the SG separator (see Figure 4.24), from where it can flow through the test section to the RPV simulator. The gas was injected from the top in the RPV simulator and flowed through the test section in counter-current to the water flow to the SG separator. The increase of the water level in the RPV simulator was used to determine the water flow rate streaming over the test section (discharge flow), which indicates the intensity of the counter-current flow limitation. Therefore, special attention was paid to the water level in this separator, which was always kept below the inlet nozzle of the hot leg. In order to investigate the onset of flooding as well as the recovery of stable counter-current flow conditions after CCFL, two types of transient experiments were performed:

1. flooding experiments: the gas flow rate is stepwise increased with small increments to reach CCFL conditions and, if possible, zero liquid penetration (zero discharge flow).
2. deflooding experiments: at the beginning, a high gas flow rate is injected in order to establish counter-current flow limitation. During the run, the gas flow rate is stepwise decreased until the breakdown of the CCFL and the achievement of a stable counter-current flow.

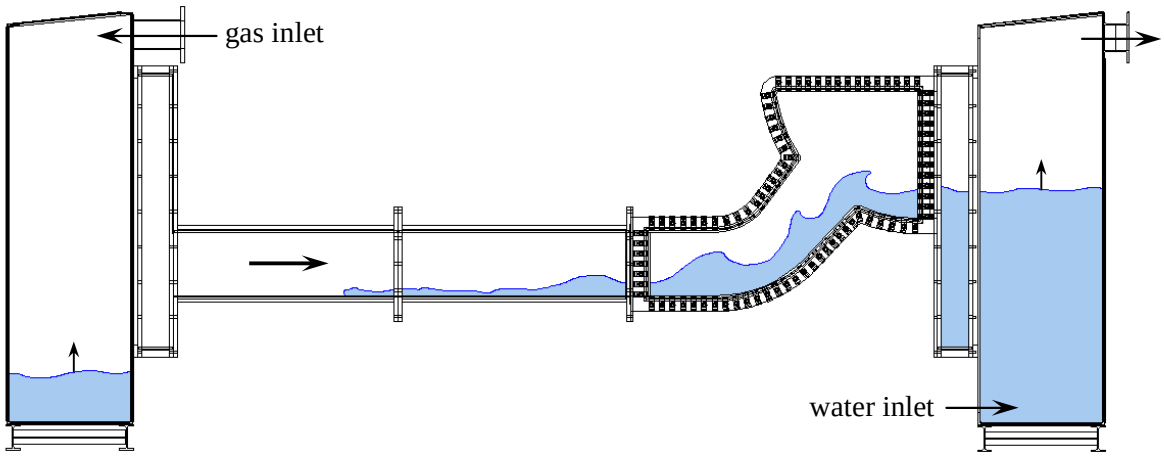

Figure 4.24: Counter-current flow limitation experiments

The boundary conditions varied during the CCFL experiments are detailed in Table 4.7. The test matrix includes 2 pressure levels with the fluid combination air/water and 3 with steam and saturated water. The mass flow rate was varied between 0.1 and 0.9 kg/s for the water, between 0.23 and 0.41 kg/s for the air and between 0.3 and 1.2 kg/s for the steam.

The stepwise increase and decrease of the gas flow rate during the experiments leads to plateaux of constant flow rates. The number and duration of these plateaux as well as the difference between 2 plateaux were changed from run to run. Due to the limited measuring time of the high-speed video camera (internal buffer of 8 GB) as well as the water accumulation in the SG separator, a compromise had to be found in each run between the number and duration of the plateaux of gas flow rate.

Furthermore, due to the difficulties to operate the test facility during the highly transient steam/water experiments, perfect steps could not be realised. In fact, the steam flow rate could not be stabilised perfectly after each increase, because it should be nearly doubled within a few minutes.

Table 4.7: Test matrix of the counter-current flow limitation experiments

Gas	**Pressure**	**Temperature**	**Flow rates [kg/s]**		**Number of runs [-]**	
[-]	**[bar]**	**[°C]**	**water**	**gas**	**flooding**	**deflooding**
air	1.5	18-24	0.1-0.9	0.23-0.41	5	1
air	3.0	18-24	0.1-0.9	0.23-0.41	7	8
steam	15.0	197	0.3-0.9	0.3-0.7	3	3
steam	30.0	232	0.3-0.6	0.35-0.85	2	2
steam	50.0	262	0.3-0.7	0.6-1.2	4	2

4.5.2. Typical counter-current flow limitation experiments

4.5.2.1. Air/water experiment with a water flow rate of 0.3 kg/s

Figure 4.25 shows the water levels measured in the SG and RPV separators, the pressure difference between the two vessels and the injected air mass flow rate. During this flooding experiment performed at a system pressure of 3.0 bar, a constant water mass flow rate of 0.3 kg/s was injected. The water levels inside both separators are shown in the upper graph. The pressure difference between the vessels and the injected air mass flow rate are represented in the lower graph of this figure. From the slopes of the curve of the water level in the RPV simulator shown in Figure 4.25, the experiment can be divided into three regions:

I. In the first region (Figure 4.25: Region I), the water level in the RPV simulator increases with the increase of air mass flow rate, meanwhile the water level in the SG separator is almost constant. This means that all the injected water flows from the SG separator to the RPV simulator. In this region, it is also found that the pressure difference between the vessels is still low, and slightly increases with the air mass flow rate. We defined this region as the stable counter-current flow. The flow behaviour can be described from the high-speed camera images shown in Figure 4.26. It should be noticed that the flow pattern on the inclined plane of the riser is a supercritical stratified flow for $t < 61{,}5$ s. Supercritical flow means that the local Froude number of the liquid film is larger than unity. In the geometry of the hot leg, the supercritical flow condition is due to gravity acceleration. In the horizontal part of the hot leg, the supercritical flow changes to subcritical flow, and a hydraulic jump as a transition from supercritical to subcritical flow is observed near the bended region (Figure 4.26-a). Furthermore, the air/water interface in the inclined riser is stable, indicating that the water flow is not disturbed by the air stream.

II. At an injected air mass flow rate of 0.38 kg/s (Figure 4.25: $t = 61.5$ s), a limitation of the discharged water flow is detected. Here the slope of the curve of water level in the RPV simulator and SG separator begin to decrease and increase, respectively. This means that a part of the water injected in the SG separator does not flow to the side of the RPV simulator. This point is defined as the onset of flooding, and the subsequent region II as the partial delivery region. Around the onset of flooding, the pressure difference between the vessels begins to present higher fluctuations as shown in the lower graph of Figure 4.25. Visual observation indicates that at this point, the air/water interface becomes wavier and a large amplitude wave grows with droplet entrainment from its crest. This phenomenon was captured by the camera and is shown in Figure 4.26-b. Due to the waves, the free cross-section available for the air flow decreases. Therefore the air is accelerated above the wave, this starts to blow up the liquid slug, finally breaking up the slug into small droplets. With further increase of the air mass flow rate, the liquid slugs reduce and sometimes block the whole cross-section for the air flow in the test section. Consequently, the pressure drop over

the test section increases at these flow conditions ($\dot{m}_G$ = 0.395 kg/s), which is revealed by the pressure difference measured between the vessels ($t \geq 74.0$ s in Figure 4.25).

III. With further increasing of the air mass flow rate up to 0.41 kg/s (Figure 4.25: $t \geq 98$ s), the injected water mass flow rate of 0.3 kg/s is hindered to flow to the RPV simulator and the water level measured there shows a plateau (region III). Therefore, the water remains completely in the test section and in the SG separator, where the water level rises. This region corresponds to the zero liquid penetration. The visual observations indicate that large amplitude rolling waves are formed near the bend and block the cross-section of the rectangular duct. Furthermore, large two-phase mixing regions were observed with droplet detachment at the wave crest and bubble entrainment in the bended region due to the rolling flow pattern (see Figure 4.26-c).

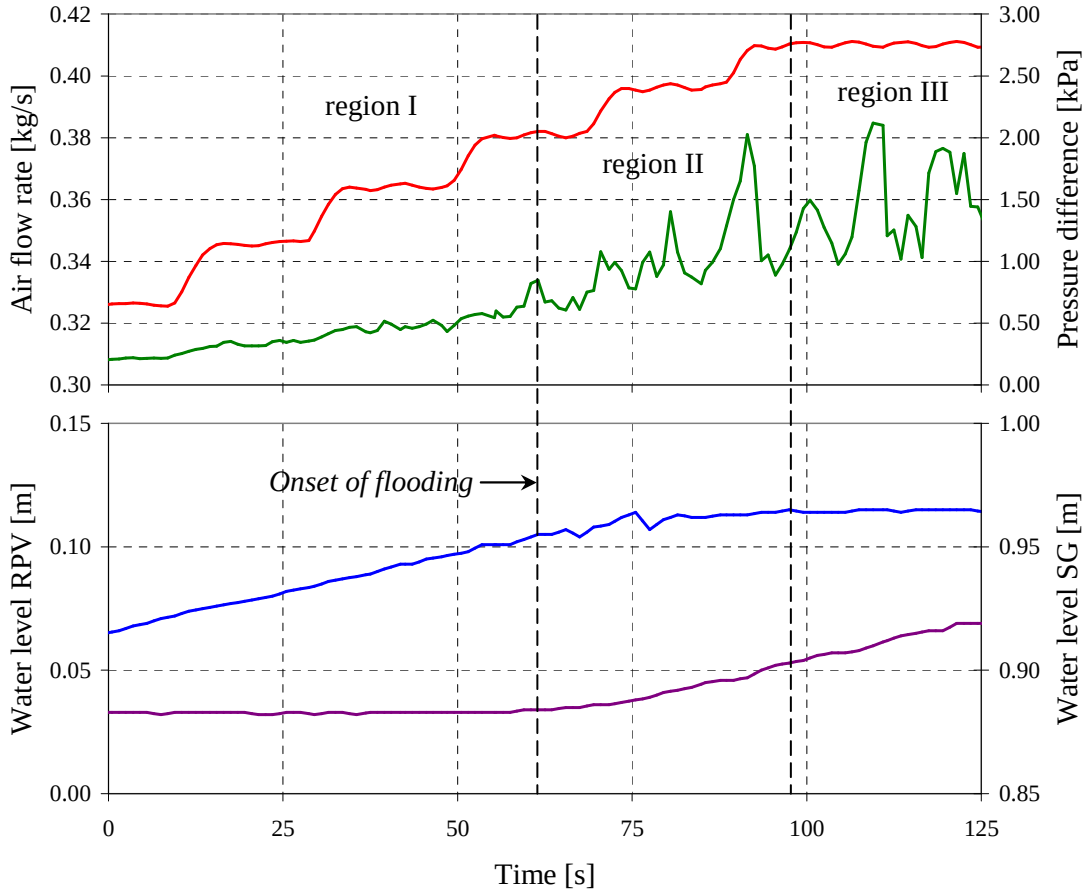

Figure 4.25: Variation of the air mass flow rate (top diagram, red curve) and of the pressure drop over the test section (top diagram, green curve), and of the water levels in the RPV simulator (bottom diagram, blue curve) and in the SG separator (bottom diagram, purple curve) measured at a water mass flow rate of 0.3 kg/s and a pressure of 3.0 bar

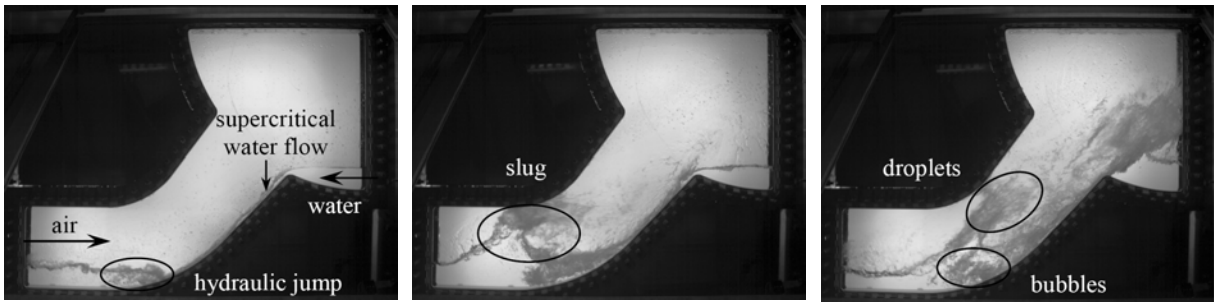

(a) $\dot{m}_G$ = 0.345 kg/s; t = 21.50 s (b) $\dot{m}_G$ = 0.395 kg/s ; t = 76.59 s (c) $\dot{m}_G$ = 0.41 kg/s ; t = 97.92 s

Figure 4.26: Flow behaviour during the counter-current flow of air and water at a water flow rate of 0.3 kg/s and a pressure of 3.0 bar

4.5.2.2. Air/water experiment with a water flow rate of 0.9 kg/s

Another experiment was performed with a higher water mass flow rate of 0.9 kg/s. The measured global parameters are shown in Figure 4.27, which indicate also three main flow behaviours:

I. In Region I of stable counter-current flow, the water level in the SG separator increases and the water level in the RPV simulator keeps constant. The pressure difference between the vessels is low and stable. From visual observations, it is noted that before the inception of flooding (t = 78.3 s), the flow pattern is also a supercritical stratified flow, but no hydraulic jump is detected in the bended region as shown in Figure 4.28-a.

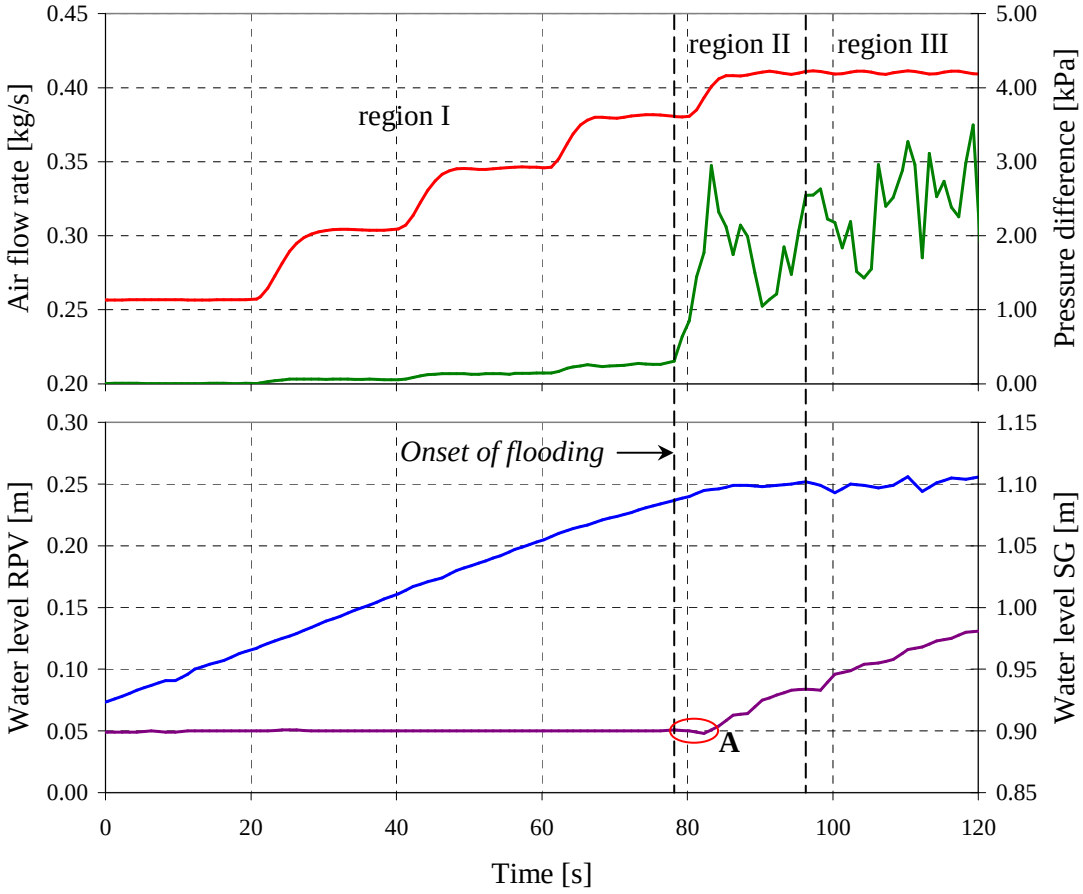

Figure 4.27: Variation of the air mass flow rate (top diagram, red curve) and of the pressure drop over the test section (top diagram, green curve), and of the water levels in the RPV simulator (bottom diagram, blue curve) and in the SG separator (bottom diagram, purple curve) measured at a water mass flow rate of 0.9 kg/s and a pressure of 3.0 bar

II. At an injected air mass flow rate of 0.38 kg/s (Figure 4.27: t > 78.3 s), a limitation of the counter-current flow is detected, as marked as the onset of flooding in Figure 4.27. Close inspection of the figure reveals that the behaviour of water levels changes a little with increasing water mass flow rate. At the initiation of flooding, the slope of water level in the RPV simulator begins to decrease. Meanwhile, the water level in the SG separator remains almost constant for about 5.5 seconds. This phenomenon is marked as *A* in Figure 4.27 and means that a part of the liquid does not flow to either of the tanks. During this period of time, the high-speed camera images indicate that the water flow begins to be partially reversed. Therefore, at the initial stage of flooding the flow in the horizontal part of the hot leg becomes subcritical and bigger waves are observed (Figure 4.28-b to d). This causes an accumulation of water in the test section, which explains the decrease of the slope of water level measured in the RPV simulator. Furthermore, no liquid is transported to the steam generator inlet chamber, neither from waves nor from droplets. Consequently, the water level in the SG separator remains relatively constant. In the region II, the behaviour of the pressure drop in the test section is found to be similar to that at lower water mass flow rate (0.3 kg/s, cf. previous section), while the absolute maximum pressure difference measured increases with higher water flow rate.

III. The zero liquid penetration is reached with further increasing of the air mass flow rate up to 0.41 kg/s (Figure 4.27: t = 97.3 s). The visual observations (Figure 4.28-e and f) indicate that in the region III, the flow behaviour is similar to that at lower water mass flow rate (0.3 kg/s) with highly mixed zones.

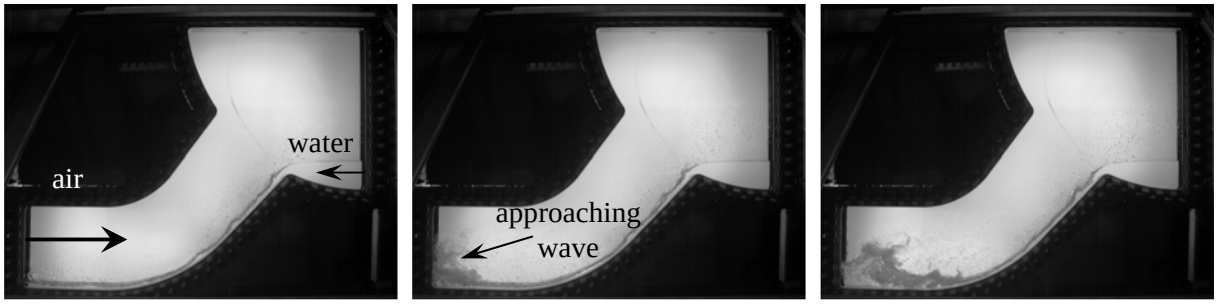

(a) before the onset of flooding t = 60.00 s; $\dot{m}_G$ = 0.345 kg/s

(b) at the onset of flooding t = 78.00 s; $\dot{m}_G$ = 0.38 kg/s

(c) t = 78.60 s; $\dot{m}_G$ = 0.38 kg/s

(d) t = 79.10 s; $\dot{m}_G$ = 0.38 kg/s

(e) t = 96.00 s; $\dot{m}_G$ = 0.41 kg/s

(f) t = 108.90 s; $\dot{m}_G$ = 0.41 kg/s

Figure 4.28: Flow behaviour observed during the counter-current flow experiment at a water flow rate of 0.9 kg/s and pressure of 3.0 bar

4.5.2.3. Flow behaviour observed during a steam/water experiment

As an example, one of the steam/water experiments was chosen to describe the observed phenomena and to explain the methodology used to analyse the measured data. This run was performed at following boundary conditions: a system pressure of 50.0 bar, a temperature of about 262°C and a water flow rate of 0.72 kg/s. An analysis of the evolution of the global parameters over time (Figure 4.29) allows to characterise the flow behaviour. Especially the water levels measured in the separators and the pressure difference between them give indication of the flow regime. Furthermore, the

increase of the water level in the RPV simulator allows to determine the water flow rate streaming over the test section (discharge flow). This indicates the onset of flooding and beyond it the intensity of the counter-current flow limitation. Therefore, linear interpolation lines were added to the measured water level in Figure 4.29. Based on the trend indicated by these lines, the experiment was divided into 4 regions:

I. For a steam flow rate lower than 0.82 kg/s (t < 65 s), the water level in the SG separator is constant and the slope of the water level increase in the RPV simulator corresponds to a water flow rate of 0.71 kg/s, which is very close to the injected mass flow rate. This indicates a stable counter-current flow, confirmed by the camera images (Figure 4.30-a), which is characterised by a constant and very low pressure drop over the test section (< 0.2 kPa).

II. At t = 65 s, the steam flow rate is increased to about 0.94 kg/s (±0.02). Immediately, the pressure difference between the separators increases, indicating the beginning of the counter-current flow limitation. With a delay of about 5 s, the slope of the water level in the RPV simulator decreases to a discharge water flow of 0.23 kg/s. Consequently, the water level in the SG separator increases significantly. Furthermore, the pressure difference between the separators becomes unstable and fluctuates between 1 and 2.5 kPa due to the slugs generated in the hot leg (Figure 4.30-b).

III. For 105 < t < 150 s, the steam flow rate is slowly increased to values up to 0.99 kg/s. This further reduces the discharge water flow to a minimum of 0.08 kg/s and the pressure drop over the test section increases up to values over 4 kPa. The camera pictures (Figure 4.30-c) reveal a highly mixed two-phase flow: big slugs are observed which flow up the riser and transport water into the SG separator, where the water accumulates.

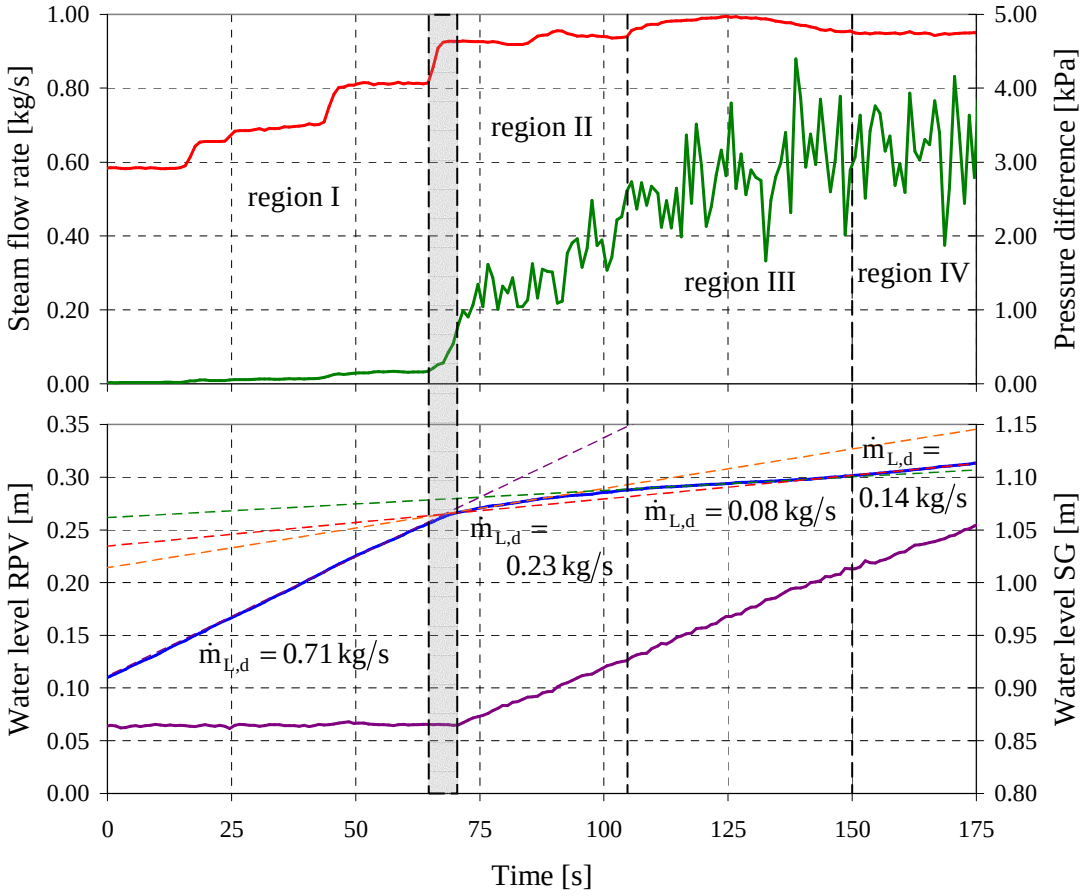

Figure 4.29: Variation of the steam mass flow rate (top diagram, red curve), of the pressure drop over the test section (top diagram, green curve), of the water level in the RPV simulator (bottom diagram, blue curve) and in the SG separator (bottom diagram, purple curve) during the CCFL experiment at 50 bar and a water flow rate of 0.72 kg/s

IV. After t = 150 s, the steam flow rates stabilises to 0.95 kg/s (±0.005) for about 40 s, leading to a discharge water flow rate of 0.14 kg/s. The further increase of the water level in the SG separator occurring during this time seams not to have a significant impact on the discharge water flow. However, the high-speed camera observation shows the additional formation of large slugs in the steam generator inlet chamber (Figure 4.30-d). All the slugs developing in the riser and in the SG inlet chamber obstruct the steam flow, increasing consequently the droplet entrainment significantly.

The slight decrease of the steam flow rate at the end of the experiment leads to a decreasing CCFL intensity after t = 150 s, which is similar to the processes observed during deflooding experiments. The flow conditions described here are similar to those observed during the air/water experiments reported in the previous sections.

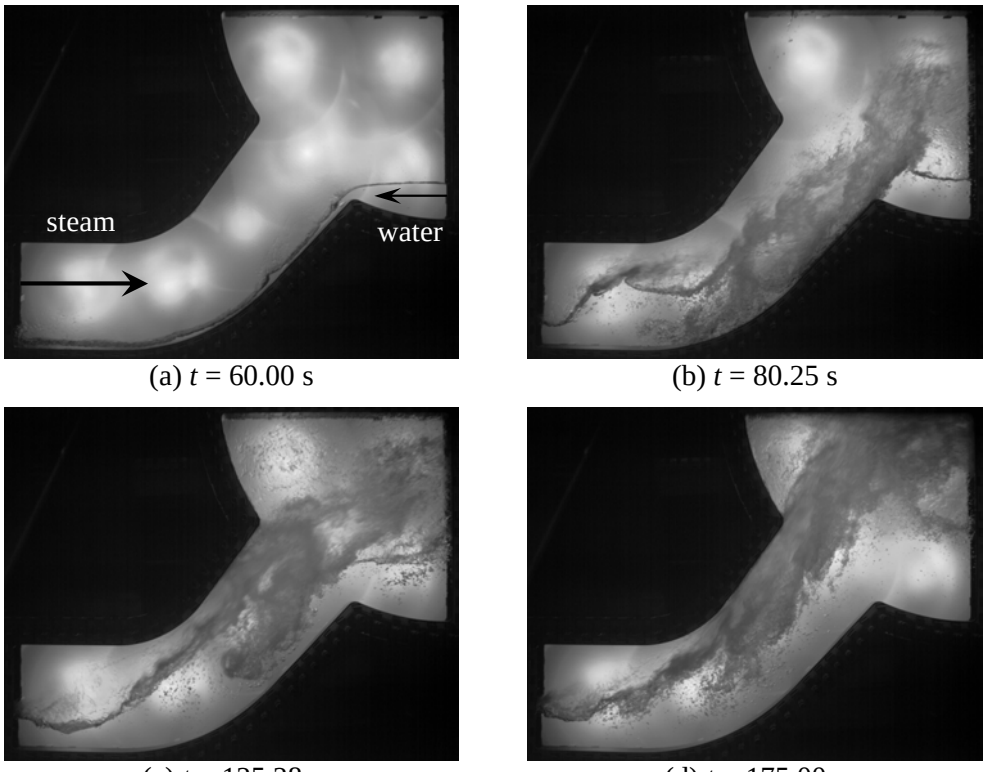

(a) t = 60.00 s (b) t = 80.25 s

(c) t = 125.28 s (d) t = 175.00 s

Figure 4.30: Flow behaviour during steam/water counter-current flow at 50.0 bar and a water flow rate of 0.72 kg/s

4.5.3. Data treatment procedures for the arrangement of the flooding curve of the hot leg model

4.5.3.1. Principle

The plot of the gas flow rate versus the discharge water flow rate during CCFL leads to the flooding characteristic. In order to automate the arrangement of the flooding diagram, a data treatment routine was developed. As an example, the result of the main steps of this procedure is shown in Figure 4.31 for the steam/water experiment presented qualitatively in section 4.5.2.3.

The discharge water flow rate was determined from the time derivative of the water level measured in the RPV simulator at 1 Hz. However, the derivation amplifies each slight fluctuation of the measured signal and induces too large oscillations of the superficial velocity (see “unfiltered” curve in Figure 4.31) for further analysis. In order to damp these fluctuations, the measured water level was first treated with a low-pass filter of Gaussian type with a time constant of 6.0 s. Figure 4.31 shows the result of the time derivation after filtering, which presents a significant reduction of the oscillations in

comparison with the raw measurement data. As the last procedure, selection criteria were applied to the filtered curve in order to consider only the quasi-stationary points obtained after the onset of flooding. Consequently, to be selected for the flooding characteristics, each point (i.e. time step) had to fulfil the following 4 criteria simultaneously:

1. The pressure drop measured over the test section was used to distinguish between stable counter-current flow and CCFL (cf. remarks in the phenomenological analysis of section 4.5.2). In fact, it was considered that only points with a pressure drop higher than 0.5 kPa correspond to counter-current flow limitation and can, therefore, be included in the flooding diagram. This threshold value was chosen on the basis of general observations. As an example of its representativity, please refer to the time plots shown in section 4.5.2 (Figure 4.25, Figure 4.27 and Figure 4.29). At high liquid flow rates, the pressure drop rises rapidly from values lower than 0.2 kPa to 1 kPa during the onset of flooding. The transition is not that distinctive in case of lower water flow rates, nevertheless, the pressure drop is maintained durably above 0.5 kPa after the onset of flooding (cf. Figure 4.25).
2. In order to evaluate the quasi-stationarity of each point, the time derivative of the superficial velocities was calculated. This should not exceed 0.0005 m/s² for the discharge water flow (after filtering) in order to be considered for the flooding characteristics.
3. The second procedure was applied comparably to the gas superficial velocity with a limit fixed at 0.01 m/s².
4. Besides of the sought stable CCFL points, also inflexion points can satisfy the two aforementioned conditions. Therefore, points are only considered to be stable if they additionally are immediately preceded or followed in time by at least another point fulfilling the first 3 criteria.

As an example, the result of the data processing method for the steam/water experiment presented in section 4.5.2.3 is presented in Figure 4.31 (series “selected points”). This shows already the trend of the flooding characteristics with a relatively restrained scatter compared to the raw measurement data.

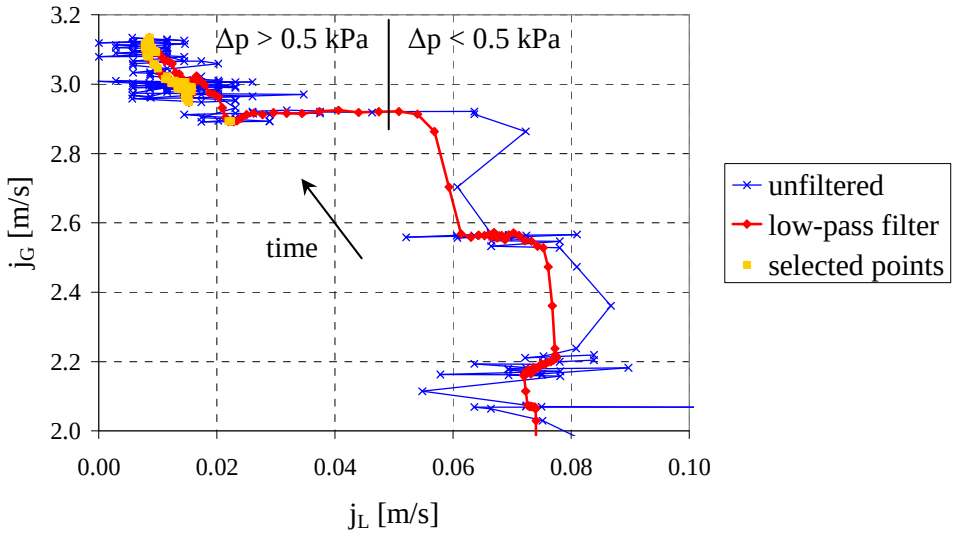

Figure 4.31: Steam vs. discharge liquid superficial velocity during the CCFL experiment at 50.0 bar and a water flow rate of 0.72 kg/s

4.5.3.2. Validation of the processing method

In order to validate the data processing method presented in the previous section, the outcome shown in Figure 4.31 was compared with the results from the linear regression lines of the RPV water level shown in Figure 4.29. The slope of the regression lines was used to calculate the averaged value of the discharge water flow rate over the chosen period of time. However, it is not evident to define a pertinent steam flow rate to associate. In fact, due to the difficulties to operate the test facility during these highly transient steam/water experiments (the steam flow rate was nearly doubled within a few minutes), the steam flow rate could not be stabilised perfectly after each increase. Furthermore,

because the steam flow rate is the main input parameter of the considered thermal-hydraulic system, the reduction of the measured values to a time average is not significant enough. Therefore, it was chosen to bound the average with error bars ranging from the minimum to the maximum measured steam flow rate in the considered region (as defined in section 4.5.2.3).

The comparison between both methods is shown in Figure 4.32. The points delivered by the data processing method accumulate around the quasi-stationary equilibrium states. In Figure 4.32, 3 accumulation zones can be identified, which correspond to the regions defined in section 4.5.2.3, as shown by the comparison with the error bars. This agreement makes clear that the 2 methods are comparable. However, the data processing method allows to reduce the scatter of the flooding characteristics because a couple of actual flow rates is associated at each time step. In fact, using this method, the slight variations of the steam flow rate during the experiments lead to a scan of the flooding characteristics and allows to recognise more clearly its slope. However, some differences can be seen between the results of both methods, in particular in region II. These differences are due to the slightly transient character of the flow in this region caused by the varying steam flow rate. This explains why the data processing method has selected only 2 points for the flooding characteristics. Consequently, the probability that the selected time steps correspond to the averaged value is low. On the contrary, the agreement between both methods is nearly perfect in region IV due to the very stable steam flow rate. This indicates that in spite of the selection method used to treat the data, point accumulation zones should be considered as the most reliable. Altogether, the comparison shows that the developed data processing method allows to determine precisely the flooding characteristics, in spite of the measured flow rate fluctuations.

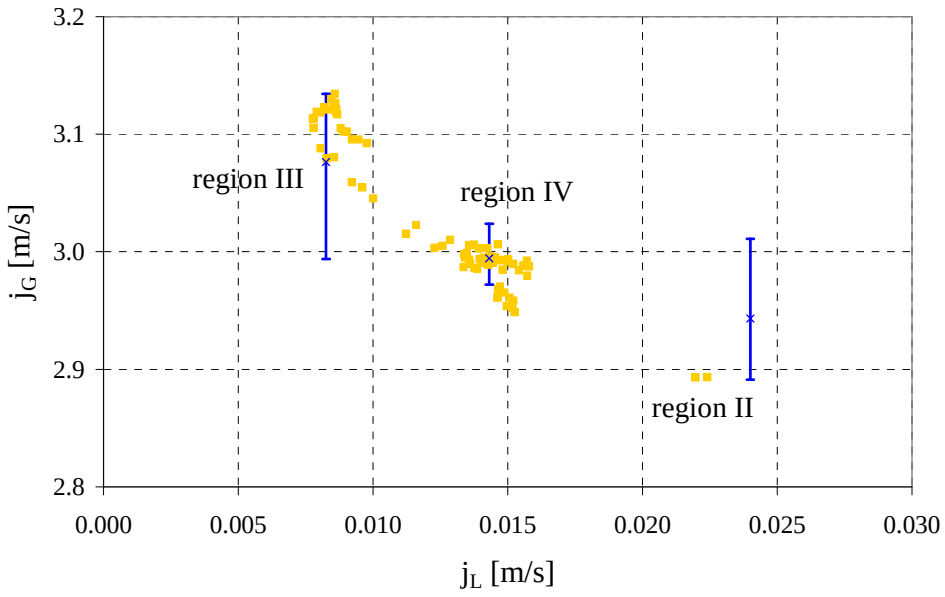

Figure 4.32: Comparison between the points selected with the data processing method and the linear regression lines shown in Figure 4.29

4.5.4. The Wallis parameter for channels with rectangular cross-section

4.5.4.1. Characteristic length for straight channels: indications from the literature

As discussed in section 2.3.2.2, the non-dimensional superficial velocity J_i^* (or *Wallis parameter*) is commonly used to plot the flooding diagram. However, the classical definition of the Wallis parameter as indicated in equation (2.49) contains the pipe diameter D as characteristic length. This was originally defined by Wallis (1969) for counter-current flow limitation in vertical pipes and not in channels with rectangular cross-section. In comparison to the plethora of studies available for CCFL in pipes, the literature concerning flooding in channels is poor. In order to be able to perform comparisons with previous hot leg experiments, the appropriated characteristic length for channels

should be determined. A priori, from the physical point of view, three dimensions should be considered as potential candidate for the characteristic length in the case of CCFL in channels:

1. the hydraulic diameter: for channels with non-circular cross-sections, the hydraulic diameter is the equivalent length used instead of the diameter for the calculation of cross-section dependent parameters. The hydraulic diameter is in particular the characteristic length scale for turbulence and, consequently, is used for the calculation of the Reynolds number.
2. the channel height: due to the predominant effect of gravity in near horizontal channels, the height is one key length in stratified flows. The height of the water head is used for instance for the calculation of the Froude number in open channel flows (cf. equation (2.28)).
3. the Laplace capillary length λ: this leads to the other classical non-dimensional parameter considered in the literature to plot the flooding characteristics: the Kutateladze number (cf. section 2.3.2.3).

Although no specific studies on the suited characteristic length for channels with rectangular cross-sections were found in the literature, some indications could be retrieved. Wallis & Dobson (1973) have investigated the onset of slugging in a horizontal channel with rectangular cross-section. For the analysis of their air/water experiments, they used the non-dimensional group suggested by Wallis for the gaseous phase, while substituting the duct height H for the length term D (equation 4 in their paper). This leads to the following form of the non-dimensional parameter:

$$J^*_G = j_G \cdot \sqrt{\frac{1}{g \cdot H} \cdot \frac{\rho_G}{\rho_L - \rho_G}} \tag{4.7}$$

This way proposed by Wallis & Dobson is supported by the experimental results of Zapke & Kröger (2000-I), who investigated counter-current flows in inclined and vertical rectangular ducts. From experiments in channels with different rectangular cross-sections, they concluded that the flooding gas superficial velocity dependents only on the height of the channel and not on its width (see Figure 7-a in their paper). Finally, for the plot of the flooding characteristics in the Wallis parameter diagram, Zapke & Kröger proposed to use different characteristic lengths for the liquid and for the gaseous phase. In fact, Zapke & Kröger calculated the gaseous Wallis parameter based on the channel height, like Wallis & Dobson, and the liquid Wallis parameter based on the hydraulic diameter. Other approaches, using for example the same characteristic length or a ratio of the duct height and width, were found to fail empirically. However, contrary to the results of the proposed method, this assertion of Zapke & Kröger is not illustrated in the paper.

Finally, probably because the question of the characteristic length for rectangular channels was not the central subject of their paper, the results reported by Zapke & Kröger do not allow to conclude. In fact, the proposition to use different characteristics lengths for each fluid is somewhat difficult to explain. Furthermore, the data obtained in 5 different test sections seem not to have been analysed specifically to clarify this problem, whereas the points plotted in the final diagram (Figure 7-b in their paper) present an overall quite large scatter. Therefore, a new analysis of the data of Zapke & Kröger could give further indications.

In order to exploit the data, a comparison of the results according to the proposition of Zapke & Kröger with those after adequate conversion using only the height as characteristic length was tested. Therefore, only the most significant data of Zapke & Kröger (2000-I) was selected from their experiments in test sections inclined at 60° to the horizontal (Figure 7-a). This includes the data obtained in 2 different rectangular channels with the same height (50 mm) and different widths (10 and 20 mm) as well as in a pipe of 30 mm inner diameter. It should be noted that the hydraulic diameter of the channel with a cross-section of 50 x 20 mm² is 28.6 mm, which is very close to the pipe diameter. These dimensional particularities could make it possible to determine the characteristic length among rectangular channels on one hand as well as in comparison with pipes on the other hand.

The resulting flooding characteristics are presented in Figure 4.33 with the different length terms for the calculation of the Wallis parameter. The differences between the 2 investigated possibilities are small, however, the results tend to indicate that the channel height should be used as the characteristic

length for flooding in channels with rectangular cross-section. In fact, by focussing only at the data from the rectangular channels, the horizontal deviation between the experimental series is clearly reduced by the application of the height as the length term for the calculation of both Wallis parameters. This is also the case for the flooding characteristics obtained in the 50/20 channel compared to the 30 mm pipe, indicating that for stratified flows the height of a channel with rectangular cross-section is equivalent to the diameter of a pipe.

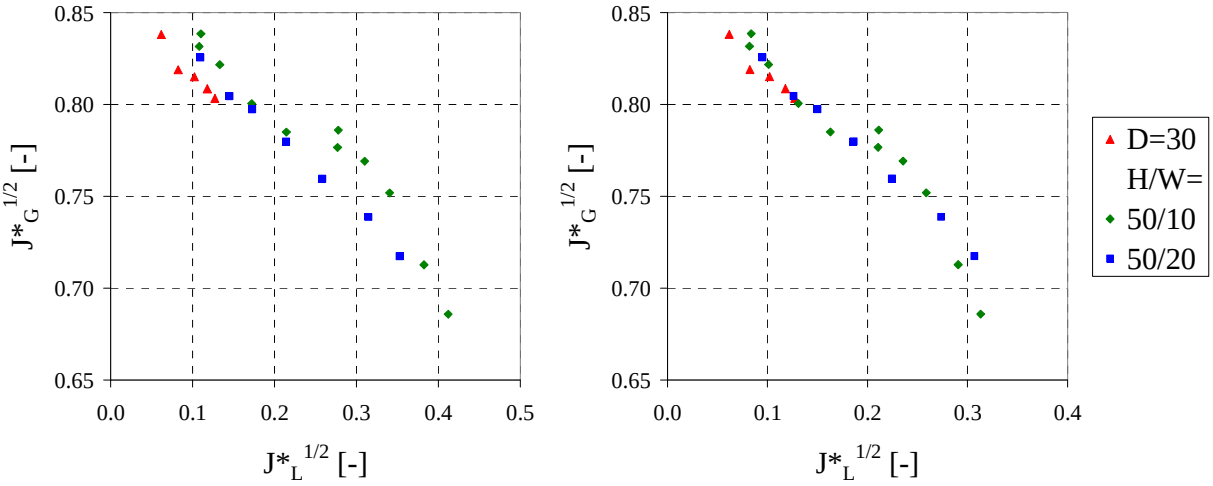

(a) Wallis parameter with $L(J^*_G) = H$ and $L(J^*_L) = D_h$

(b) Wallis parameter with $L = H$

Figure 4.33: Comparison of the flooding characteristics obtained from data by Zapke & Kröger (2000-I) with different characteristic lengths for the calculation of the liquid Wallis parameter (N.B.: for the pipe $L = D = D_h = H$)

4.5.4.2. Characteristic length for hot leg models with rectangular cross-section – comparison of the air/water flooding characteristics with the results of the Kobe University

From the indications found in the literature, the choice of the characteristic length for the calculation of the Wallis parameter seems to be clear in the case of straight channels. In order to verify that the height of the test section H is also adapted to the particular geometry of the hot leg, our results were compared with those obtained independently at the *Kobe University* (Japan). The air/water experiments were conducted in 2008 in a very similar model of the hot leg made of transparent acrylic resin (cf. Minami et al., 2008). In order to focus the comparison on geometrical aspects, the variation of parameters was minimised as far as possible. Therefore, only the results obtained with air and water in the TOPFLOW hot leg model are considered in this section.

a) Comparison of the two test facilities, experimental boundary conditions and procedures

A comparison between both experimental work is shown in details in Figure 4.34 and in Table 4.8. Qualitatively, as shown in Figure 4.34, the profile of both hot leg test sections is very similar and only slight differences can be noticed in the riser and at the connections to the separators. In fact, the riser of the *Kobe University* hot leg model does not expand and the junction to the RPV simulator was realised with larger chamfer compared to TOPFLOW. The main differences between both test facilities are concentrated in auxiliary components: the separators and medium connections. In the Kobe test facility, the steam generator inlet chamber is directly used as a separator, whereas in our case this is part of the test section. Consequently, the TOPFLOW SG inlet chamber is designed with the same width as the hot leg and is connected to an additional separator. Furthermore, thanks to a baffle implemented in the SG separator of the Kobe test facility, an additional water outlet could be realised which allows to perform stationary experiments over a long time. At last, the gas inlet in the RPV simulator is situated in front of the test section in the case of the *Kobe University* test facility (highest injection nozzle in Figure 4.34) and on top of the separator in our case.

Table 4.8 shows the quantitative differences between both hot leg models and experimental boundary conditions. Especially the dimensions of the test section cross-sections are quite different: the profile scale of the Kobe test facility is with 1:5 a factor of 1.67 smaller and the width is with 10 mm 5 times smaller than the dimensions of the TOPFLOW hot leg model. Finally, the essential parts of the two hot leg test sections are very similar with respect to the expected CCFL behaviour, which should allow to perform meaningful comparisons. The major differences concern the dimensions of the cross-section, leading also to very different hydraulic diameters. Consequently, the comparison of the results should allow to point out the appropriate characteristic length for hot leg models with rectangular cross-sections.

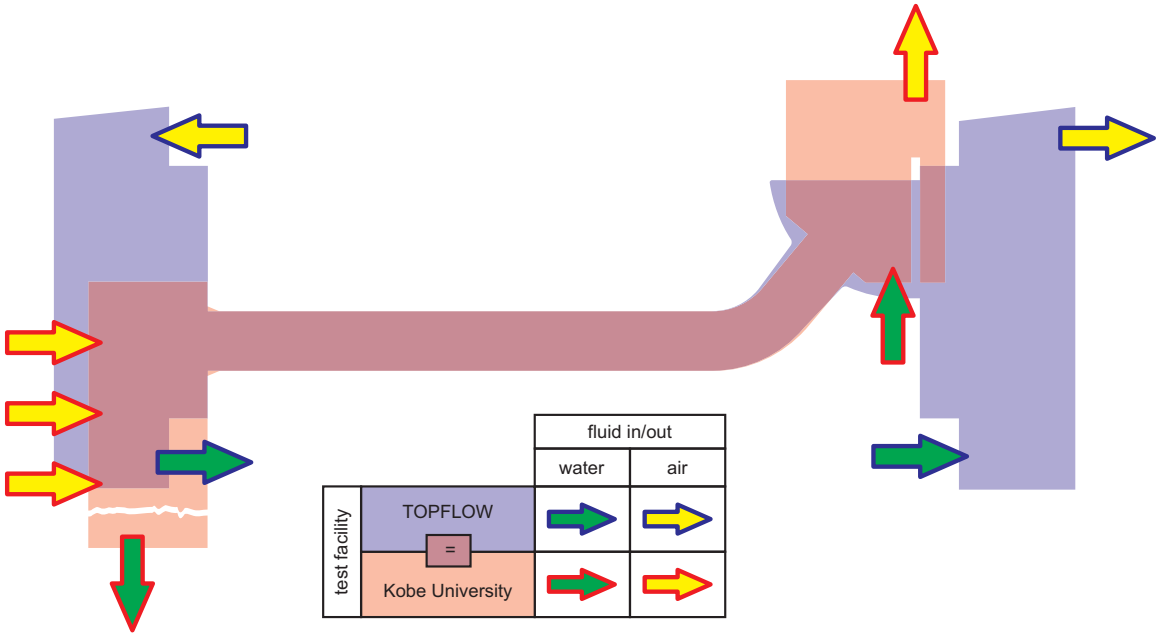

Figure 4.34: Comparison between the test section profiles of the hot leg models at the Kobe University and at TOPFLOW, both represented at the NPP full scale

Table 4.8: Comparison of the test facilities and experimental conditions

	Parameter	**Unit**	**Kobe University**	**TOPFLOW**	**Difference**
Test section	profile scale	[-]	1:5	1:3	x 1.67
	horizontal length	[mm]	1240	2120	x 1.71
	riser length	[mm]	176	230	x 1.31
	riser angle to hor.	[°]	50	50	=
Cross-section	channel height	[mm]	150	250	x 1.67
	channel width	[mm]	10	50	x 5.0
	height/width	[-]	15.0	5.0	x 0.33
	hydraulic diameter	[mm]	18.75	83.3	x 4.44
Experi-ments	fluids	[-]	air/water	air/water	=
	pressures	[bar]	1.0	1.5 ; 3.0	x 1.5 ; x 3.0
	temperatures	[°C]	room temperature	18.0-24.0	=
	experiment type	[-]	flooding	flooding/deflooding	

Moreover, the experiments were performed in both cases with air and water at room temperature, but the pressure was increased in the TOPFLOW pressure chamber up to 3 atmospheres compared to the Kobe tests. Furthermore, both experimental test series included a variation of the fluid flow rates. In Kobe, the liquid and gas flow rates ranged from 0.003 to 0.17 L/s and 6.4 to 14 L/s, respectively. This

is equivalent to the following liquid and gas superficial velocities in the test section: j_L = 0.002-0.11 m/s and j_G = 4.3-9.6 m/s. At TOPFLOW, the water flow rate was varied between 0.1 and 0.9 kg/s (i.e. j_L = 0.008-0.072 m/s) and the air flow rate between 0.23 and 0.41 kg/s (i.e. j_G = 5.1-18 m/s).

In principal, the increase of the water level in the RPV simulator was also used in Kobe to determine the discharge water flow. However, the method used for the analysis of the experimental data is noticeably different to ours. In fact, the Kobe flooding points represent mean values of the discharge water flow over 35 to 320 s, measured after established flow conditions for one combination of the air and water flow rates. In the TOPFLOW test facility, such long measuring time was not possible because of the fast water level increase in the SG separator. Consequently, plateaux of constant air flow rate could be arranged for time intervals of only 15 to 35 s. This difference in the experimental procedures leads to qualitative differences in the results, especially in the scatter of the data.

b) Comparison of the flooding characteristics
In order to verify that the height of the test section H is also adapted to the particular geometry of the hot leg, the flooding characteristics obtained at the *Kobe University* and at the TOPFLOW test facility are plotted in function of different non-dimensional parameters in Figure 4.35.

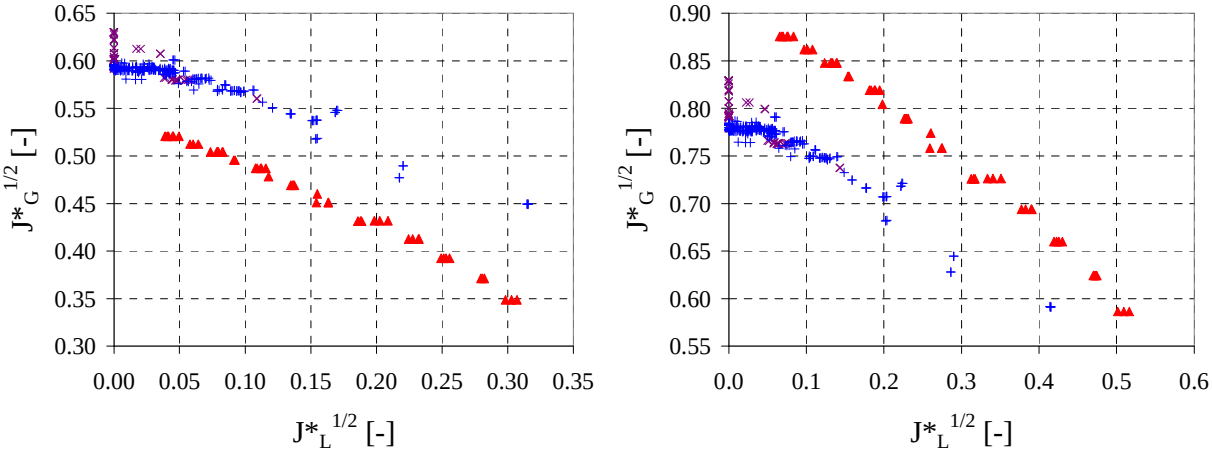

(a) Wallis parameter with $L = H$

(b) Wallis parameter with $L = D_h$

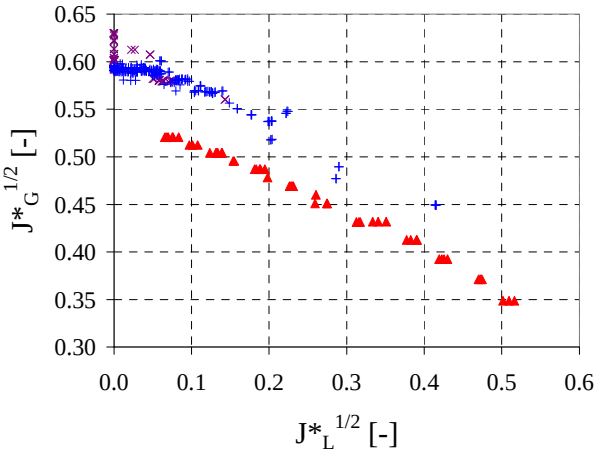

(c) Wallis parameter with $L(J^*_G) = H$ and $L(J^*_L) = D_h$

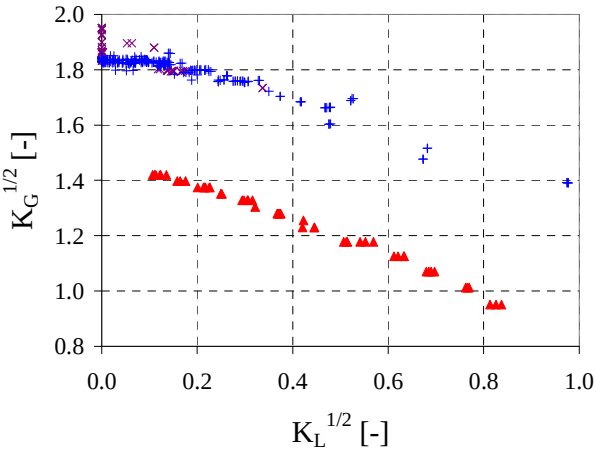

(d) Kutateladze number (i.e. Wallis parameter with $L = \lambda$)

Legend:	Kobe University:	TOPFLOW:
	▲ 1.0 bar	× 1.5 bar + 3.0 bar

Figure 4.35: Comparison of the flooding characteristics plotted in terms of the Wallis parameter with different characteristic length

First, the Wallis parameter was calculated with the channel height H (cf. Figure 4.35-a) and with the hydraulic diameter D_h (cf. Figure 4.35-b) as characteristic length. Furthermore, the Wallis parameter was calculated with H for the gaseous and D_h for the liquid phase in Figure 4.35-c, according to the proposition of Zapke & Kröger (2000-I). At last, the flooding characteristics are compared in the Kutateladze diagram (i.e. Wallis parameter with the Laplace capillary length as a length scale) in Figure 4.35-d.

Figure 4.35 shows that none of the characteristic lengths considered for the Wallis parameter allows a good absolute agreement between the Kobe and TOPFLOW flooding characteristics. However, the large gap between the flooding characteristics in Figure 4.35-d demonstrates clearly that the Kutateladze number is not suited for hot leg models with rectangular cross-section. This result is in agreement with the general observations on the applicability of the Kutateladze number to stratified flows summarised in section 2.3.2.4. Furthermore, it appears that using the channel height as length scale in the Wallis parameter gives better results than with the hydraulic diameter (cf. Figure 4.35-a to Figure 4.35-c). However, the direct comparison of the results itself does not allow to conclude. Due to the sensible quantitative differences of the zero penetration and slope depending on the chosen length scale, a comparison with past experiments in pipes may give more indications.

4.5.4.3. Comparison between the hot leg models with rectangular cross-section and previous investigation in pipes

As shown in section 2.4.3, many investigations were performed in the past on counter-current flow limitation in a hot leg typical geometry. Only some of them are considered in this section, focussing on:

- most comparable experimental data: air/water tests performed in pipes of various diameters but with similar bend angle as well as length to diameter ratios;
- different analytical approaches: experimental database or model.

The selection includes the experimental correlation proposed by Richter et al. (1978) (cf. equation (2.58)) because these results are based on tests in a pipe of large diameter and because it is widespread in the literature for comparisons. The empirical correlation of Ohnuki (1986) was chosen due to its dependence on the hot leg geometry (cf. equation (2.59)). Furthermore, among the data published by Ohnuki et al. (1988), the results obtained in the test section of "*Type A*" are used in the present comparison, because this is the only mock-up without *Hutze* (special ECC nozzle in hot legs of some German PWR's). The experimental points were taken from Figure 4 of their paper. Furthermore, the simple flooding correlation by Lopez-De-Bertodano (1994) for the classical hot leg geometry was selected (cf. equation (2.60)). The experimental data points published by Geffraye et al. (1995) were considered as the test section of large diameter (designated as *R351*) reproduces realistically the shape of a PWR hot leg. Moreover, the flooding correlation proposed by Kim & No (2002) after regression through a total of 356 data points of various authors was chosen. This is a function of the length to diameter ratio of the horizontal part of the hot leg (cf. equation (2.62)) and presents a reasonable prediction error. Navarro (2005) proposed a non-linear experimental correlation to predict the CCFL in the hot leg of a PWR (cf. equation (2.63), noted *a* in this section). Besides this general correlation, the flooding characteristics determined for one of the investigated test sections are also taken into account here as its scaled dimensions are similar to the own (in particular $L_H/D = 9.26$). It concerns the flooding diagram shown in Figure 6 of the paper obtained for a test section with 54 mm inner diameter, which was described with a good accuracy by the following CCFL correlation (noted *b*):

$$\sqrt{J^*_G} + 0.2212 \cdot \sqrt{J^*_L} + 1.1232 \cdot J^*_L = 0.5649 \qquad (4.8)$$

Finally, the experimental points obtained by Minami et al. (2010) are selected for the present comparison. Only the CCFL characteristics obtained by decreasing the air flow rate was found to be independent of the injected liquid flow rate. Consequently, this CCFL characteristics was used here, as it is shown in Figure 12 of the paper.

The above mentioned correlations including geometry dependent parameters were calculated according to the dimensions of the test sections indicated in Table 4.9. In this case, the pipe diameter

D appearing in the equations was substituted either by the hydraulic diameter D_h or by the channel height *H* as possible characteristic lengths for channels with rectangular cross-section. In the case of *L = H*, a noticeable distinction between both test facilities was only necessary for the correlation of Ohnuki (1986) due to the slightly different riser lengths L_R (cf. Figure 4.34).

In order to identify the most comparable experimental data from those found in the literature, the length to diameter ratios were calculated for the selected studies and are presented in Table 4.9. The considered characteristic dimensions are the length of the horizontal part of the hot leg L_H and of the riser *I*. According to the own scaling approach, these ratios should be close to the length to height ratio of the hot leg models with rectangular cross-section. Since this is slightly different at the *Kobe University* and TOPFLOW, average ratios were taken as a reference. Furthermore, as shown in Table 4.9, the reference bend angle α of 50° was observed by all test sections apart from that of Richter et al. (1978) which was 45°. Finally, the experiments performed in test sections with comparable length ratios in a range of ±15% (i.e. $7.12 < L_H/D < 9.63$ and $0.890 < L_R/D < 1.204$) and equal bend angle were marked with *X* in the Table. Only the investigations of Ohnuki et al. (1988) in a pipe of 25.4 mm inner diameter and of Minami et al. (2010) in a 50 mm pipe fulfil all of the three criteria.

Table 4.9: Comparison of the different test section dimensions
(ER: equivalent ratio – i.e. Reference ±15%)

Study: Author (year)	**D [mm]**	**L_H [m]**	**L_H/D [-]**	**ER**	**L_R [m]**	**L_R/D [-]**	**ER**	**α [°]**	**ER**	**All ER**
Richter (1978)	203.2	0.914	4.498	-	0	0.000	-	45	-	-
Ohnuki (1988)	25.4	0.23	9.055	X	0.03	1.181	X	50	X	**X**
Geffraye (1995)	351	2.645	7.536	X	1.06	3.020	-	50	X	-
Navarro (2005)	54	0.5	9.259	X	0.1	1.852	-	50	X	-
Minami (2010)	50	0.43	8.600	X	0.06	1.200	X	50	X	**X**
Rectangular hot leg models:	**H [mm]**	**L_H [m]**	**L_H/H [-]**		**L_R [m]**	**L_R/H [-]**				
Kobe University	150	1.24	8.267	X	0.176	1.173	X	50	X	**X**
TOPFLOW	250	2.12	8.480	X	0.230	0.920	X	50	X	**X**
Ref. (average)			**8.373**			**1.047**		**50**		

As shown in the flooding diagram with the hydraulic diameter as length scale (cf. Figure 4.36), the overall scatter of the previous data and correlations is large. Furthermore, it appears clearly that the own data does not agree with the correlations or data found in the literature. In fact, the data points from the experiments in hot leg models with rectangular cross-section are located at much higher gaseous Wallis parameters than obtained previously in pipes. Moreover, the relative position of the flooding characteristics for the two channels is incorrectly predicted by the correlations of Ohnuki (1986) or Kim & No (2002). Finally, all these observations indicate that the hydraulic diameter is not the suited characteristic length for the Wallis parameter to be used for comparisons between rectangular channels and pipes.

The flooding diagram plotted in terms of the Wallis parameter with the channel height as characteristic length is shown in Figure 4.37 and Figure 4.38 compared with the correlations and experimental data points of other authors, respectively. At first, the overall scatter of the literature data and of the different correlations is much smaller compared to Figure 4.36, although it is still not negligible. Furthermore, in Figure 4.37, the TOPFLOW data fits relatively well in the average trend given by the previous correlations, while flooding was obtained at slightly lower gaseous Wallis parameters in the Kobe test facility. In Figure 4.38, on one hand the TOPFLOW flooding points are in very good agreement with the data of Geffraye et al. (1995) and of Minami et al. (2010). On the other hand, the Kobe experiments agree well with the data points of Ohnuki et al. (1988). With respect to this behaviour, it should be noticed that the experiments of Ohnuki et al. (1988) were performed in pipes of

small diameter (25.4 mm), while those of Minami et al. and Geffraye et al. in pipes of larger diameter (50 and 351 mm, respectively). This result allows to point out the most probable reason for the deviation between the flooding characteristics of the two hot leg models: the height to width ratio of the channels. In fact, the aspect ratio is equal to 5 for the TOPFLOW test section and to 15 for the Kobe test facility, which is indeed very narrow. The large aspect ratio seems to affect the flooding characteristics in the same way as pipes of small diameters: the zero liquid penetration (i.e. $J_L^* = 0$) is obtained at lower values of the gaseous Wallis parameter. Consequently, CCFL is reached basically at slightly lower gas fluxes, which means that the narrow cross-section seems to present a destabilising effect on the flooding behaviour. This trend is probably due to the ratio between the interfacial friction and the wall friction, which is different in narrow conduits compared to wide ones. In fact, the flow surface affected by each frictional effect strongly depends on the water level but also on the cross-sectional geometry.

Finally, we can conclude that the channel height is the characteristic length to apply in the Wallis parameter for channels with rectangular cross-sections, although some limitation appears for very narrow channels. In this case, CCFL is reached at lower gas fluxes, as already observed in small scale hot legs with pipe cross-sections.

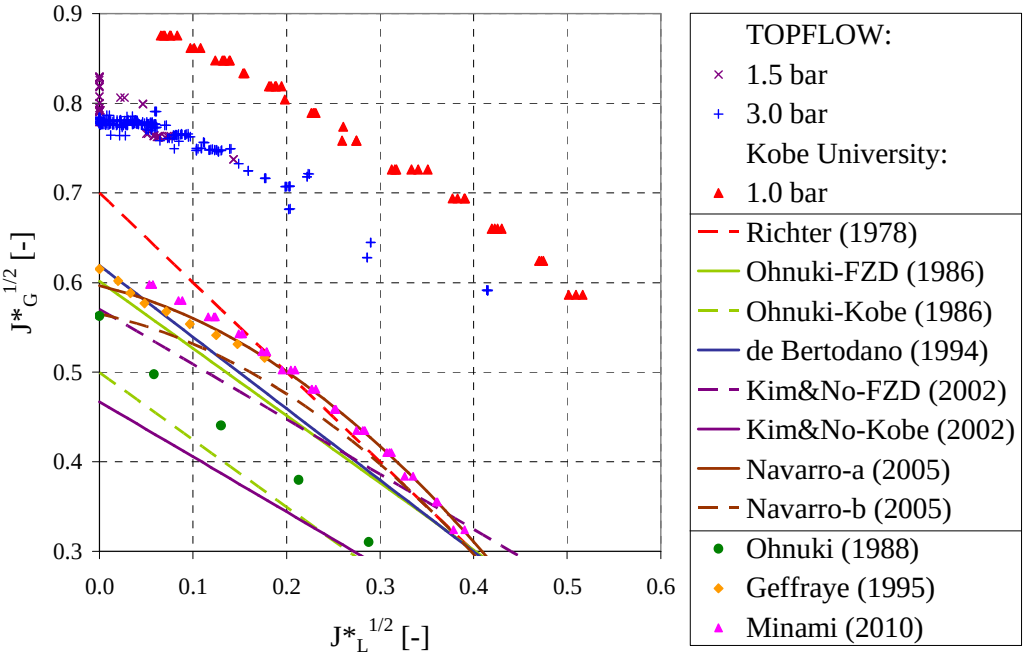

Figure 4.36: Comparison of the present data (plotted in terms of the Wallis parameter with $L = D_h$) with different CCFL correlations and experiments obtained in hot leg typical geometries with pipe cross-section

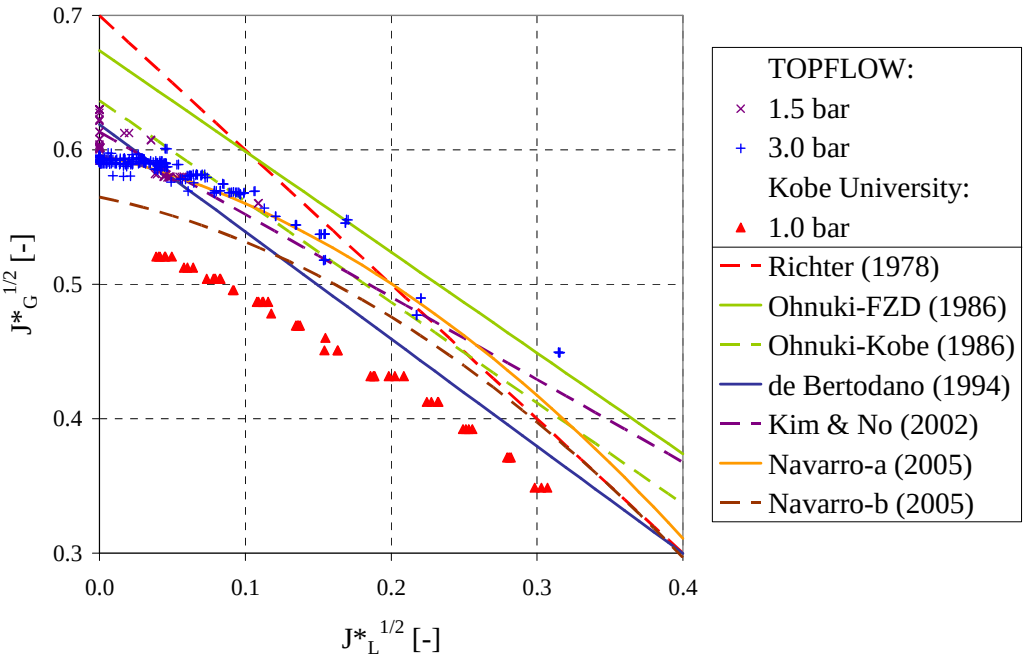

Figure 4.37: Comparison of the present data plotted in terms of the Wallis parameter with $L = H$ with different CCFL correlations obtained for hot leg typical geometries

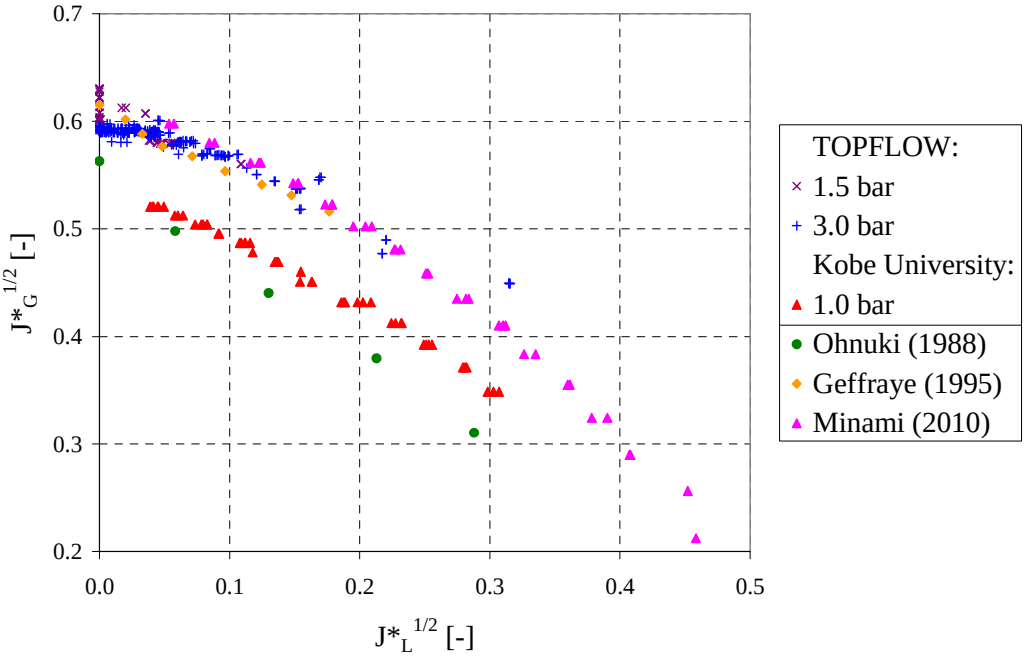

Figure 4.38: Comparison of the present data plotted in terms of the Wallis parameter with $L = H$ with previous CCFL experiments performed in hot leg typical geometries

4.5.5. Flooding characteristics of the hot leg model: comparison between air/water and steam/water experiments

4.5.5.1. Flooding characteristics in the Wallis parameter diagram

For all the experiments (see details in Table 4.7), the points belonging to the flooding curve according to the method explained in section 4.5.3.1. were plotted in terms of the Wallis parameter in Figure 4.39. This diagram reveals a slight segregation between the air/water experiments on one hand and the steam/water experiments on the other hand: mainly due to a higher zero liquid penetration point

(interception of the flooding curve with the ordinate axis), flooding was obtained at higher non-dimensional gas superficial velocities with steam and saturated water.

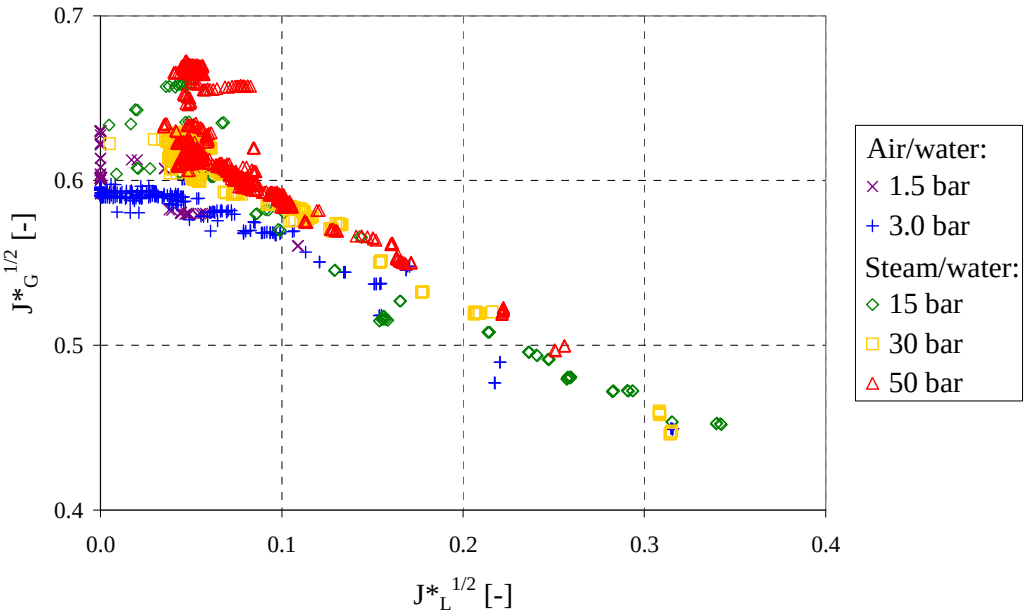

Figure 4.39: Flooding characteristics of the hot leg model plotted in terms of the Wallis parameter

4.5.5.2. Flooding characteristics in the Kutateladze number diagram

Compared to the Wallis parameter, the Kutateladze number (cf. definition in equation (2.50)) includes the surface tension σ and therefore one essential physical property of the fluids which was varied indirectly with the temperature in our experiments. Furthermore, according to Kim & No (2002), this is used with the Wallis parameter as a second possibility to predict counter-current flow limitation in the hot leg in the one dimensional system code *RELAP5*.

As shown in Figure 4.40, the Kutateladze number also fails to correlate our flooding data, in particular the air/water and the steam/water experimental series. Furthermore, the steam/water series at 15, 30 and 50 bar tend to separate in the Kutateladze diagram compared to the Wallis diagram. These results show that the surface tension obviously does not explain the observed discrepancy.

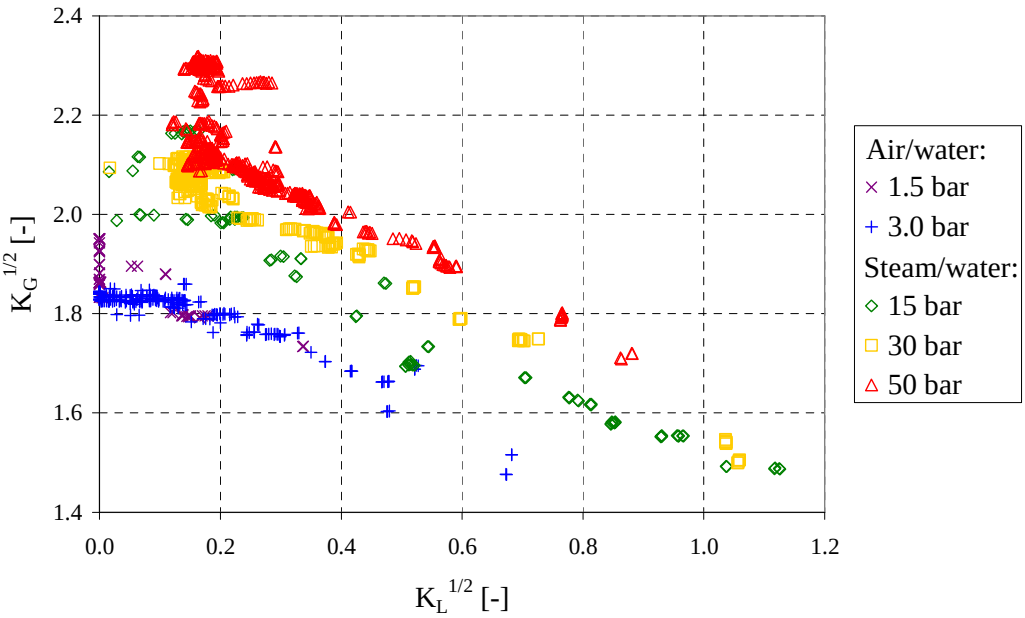

Figure 4.40: Flooding characteristics of the hot leg model plotted in terms of the Kutateladze number

4.5.6. Consideration of steam condensation effects

As shown in the previous sections, the classical Wallis parameter and Kutateladze number both fail to properly correlate our flooding data. Discrepancies were found especially between the experimental series conducted with air/water on the one hand and steam/water on the other hand. One of the main uncertainties arising while conducting steam/water experiments is the steam condensation due to inevitable heat losses in the system. Since these undesirable effects may explain the observed discrepancies, this issue is discussed in the following sections.

4.5.6.1. Qualitative considerations

The steam condensation caused by heat losses in the test facility could affect the effective gas flow rate available for flooding. In fact, the steam flow rate being measured upstream of the test section, an overestimation of the amount effectively streaming through the test section is possible. This explanation matches the fact that the gaseous Wallis parameter needed to reach flooding with steam/water was found to be higher than that with air and water. Unfortunately, no specific instrumentation was available during the experiments which could be used to quantify precisely the heat loss between the steam mass flow meter and the test section. Furthermore, no dedicated test was performed to estimate directly or indirectly the arising amount of condensate.

Nevertheless, in Figure 4.39 and Figure 4.40 it is remarkable that zero liquid penetration was clearly reached during the air/water experiments (especially at 1.5 bar), but apparently not during the steam/water experiments. However, this observation becomes surprising when noticing that the flooding characteristics of the steam experiments present obviously two different parts:

- for $J^*_L{}^{1/2} > 0.05$ or $K_L{}^{1/2} > 0.2$ (in Figure 4.39 and Figure 4.40, respectively), the CCFL characteristics describe a line almost parallel to that of the air/water experiments;
- for smaller parameters, the steam/water flooding points present a nearly vertical trend.

The nearly vertical evolution of the flooding characteristics at low liquid discharge flow rates is particularly pronounced for the 50 bar experiments (cf. diagrams). However, this trend is abnormal in a CCFL diagram plotted in terms of the square root of non-dimensional parameters. In fact, according to the knowledge of the author, such behaviour has never been described in the relatively abundant CCFL literature.

Consequently, we will suppose hereafter that the nearly vertical part of the flooding characteristics is caused by steam condensation. In that case, the condensate formed between the steam flow meter (FIC4-04) and the flooding location in the test section is likely to accumulate in the RPV simulator: due to the large cross-section, this is a place of low gas velocities and, furthermore, the lowest point of the overall experimental apparatus. If this hypothesis is right, the RPV simulator is filled on the one hand by the discharge water, but also by condensate on the other hand. This means that the method used to measure the discharge water flow, which is based on the water level increase in the RPV simulator, includes a disturbance due to steam condensation. Because heat losses always exist, the water level in the RPV simulator further increases also after the zero liquid penetration has been reached due to steam condensation. According to this analysis, the nearly vertical part of the steam/water flooding characteristics in Figure 4.39 and Figure 4.40 should correspond to the zero liquid penetration. However, it has to be mentioned that the plot of the square root of the non-dimensional parameters leads to a distortion of the diagram which enlarges distances close to the zero liquid penetration. This effect emphasises graphically the problem already at small condensation amounts.

4.5.6.2. Methodology and analysis of the results

Following the reasoning of previous section, the flooding characteristics of the steam/water experiments have to be corrected in order to take into account the condensation effects. A determination of the condensation rate in retrospect is only possible over the abscissa of the near vertical part of the CCFL characteristics. In order to improve the statistics, one assumes that the heat losses are only a function of the temperature difference between the saturated steam and the ambient conditions. This means that the arising steam condensation rate is supposed to be constant at a given system pressure. The heat losses being proportional to a mass flow, in order to determine the amount

of condensate, the flooding points were plotted in terms of the mass flow rate separately for each of the three pressure levels. As shown exemplarily for the experiments performed at 30 bar in Figure 4.41, the two regions of this CCFL diagram have been delimited by a line. The coordinates of the line were chosen manually to isolate above the points belonging to the zero liquid penetration. Finally, the condensate mass flow rate was calculated from the average abscissa of the selected points. At 30 bar, 33.7 g/s of condensate were obtained (cf. Figure 4.41), corresponding to heat losses of 60.5 kW. Furthermore, relatively to the steam flow rate of about 0.8 kg/s measured during zero liquid penetration, this represents a condensation ratio of 4.2%.

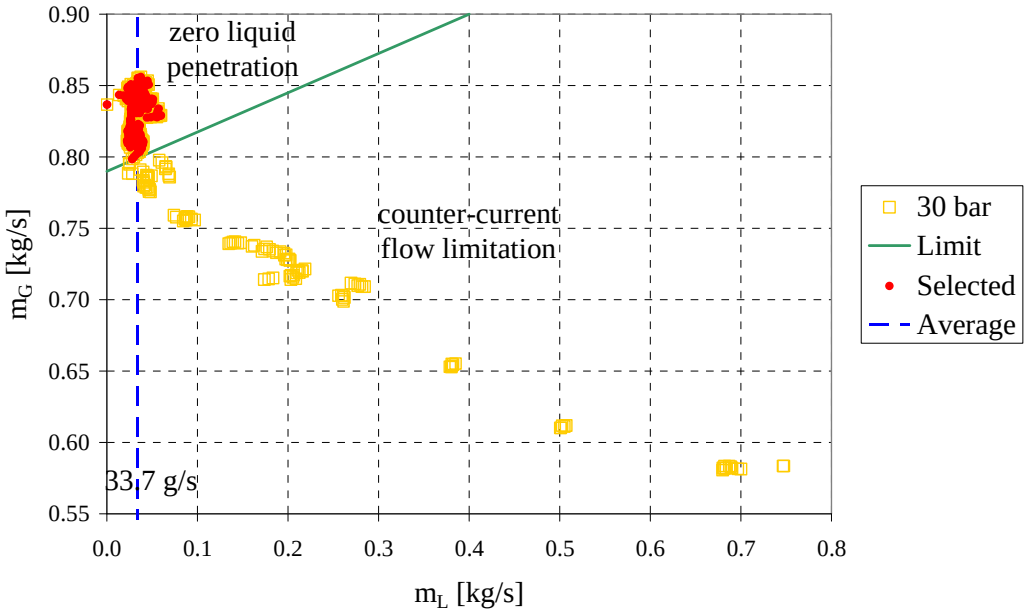

Figure 4.41: Selection of the flooding points belonging to the zero liquid penetration (example for the 30 bar experiments)

For the correction of the flooding characteristics, the obtained condensation rate $\dot{m}_c$ was subtracted from the discharge water flow $\dot{m}_L$ as well as from the measured steam flow rate $\dot{m}_G$ as follows:

$$\dot{m}_{L,\,corr}(t,p) = \dot{m}_L(t) - \dot{m}_c(p) \tag{4.9}$$

$$\dot{m}_{G,\,corr}(t,p) = \dot{m}_G(t) - \dot{m}_c(p) \tag{4.10}$$

The flooding characteristics obtained after application of the correction taking into account the condensation effects is presented in Figure 4.42 and Figure 4.43 in terms of the Kutateladze number and Wallis parameter, respectively. In the Kutateladze diagram, the agreement between the experimental series is not significantly improved by the correction (cf. Figure 4.42). In contrast, the plot in terms of the Wallis parameter shows a reasonable agreement between all the CCFL series, especially considering the scatter of the data (Figure 4.43). Consequently, this result corroborates the hypothesis made in previous section concerning the effect of heat losses and supports the method used to estimate the condensation rate. Furthermore, this shows that the Wallis similarity is appropriate to scale flooding in the hot leg of a PWR over a large range of pressure and temperature conditions. In particular, no significant discrepancy could be observed between the air/water and steam/water series, although the fluid properties vary noteworthy. This confirms the results of Ohnuki (1986) obtained in smaller scale pipes and over a more limited range of boundary conditions (atmospheric pressure). Consequently, the influence of viscosity and surface tension on the flooding characteristics described in the literature for vertical and inclined pipes (cf. section 2.3.3) seems not to be transferable to the hot leg geometry or to the couple of fluids air/water and steam/water. Finally, the flooding characteristics of the hot leg model can be approximated with the following linear regression function:

$$(J^*_G)^{1/2} + 0.533 \cdot (J^*_L)^{1/2} = 0.61 \tag{4.11}$$

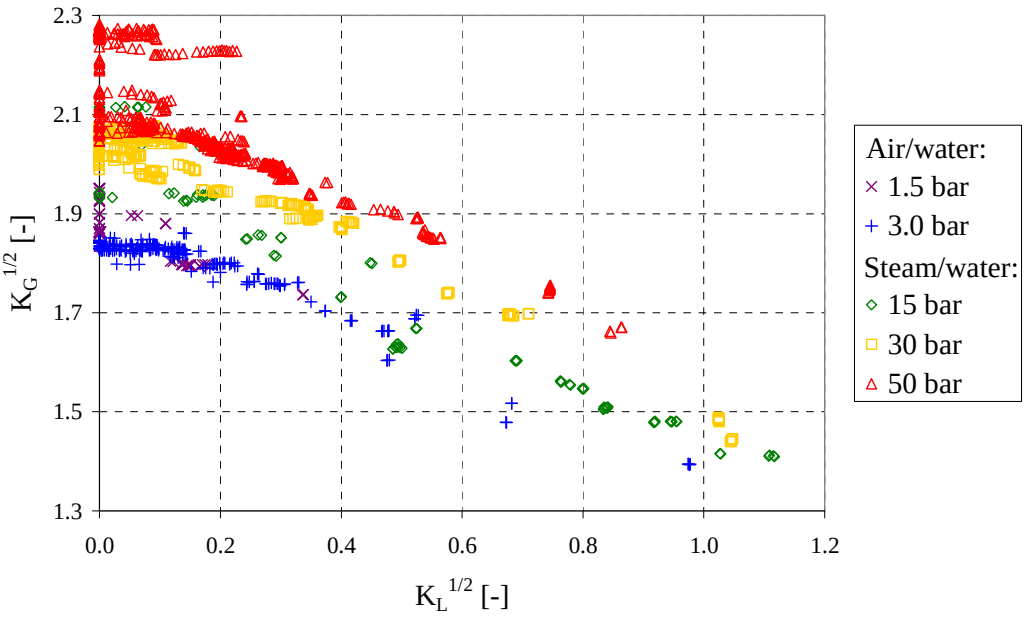

Figure 4.42: Flooding characteristic of the hot leg model plotted in terms of the Kutateladze number after correction of the steam condensation effects

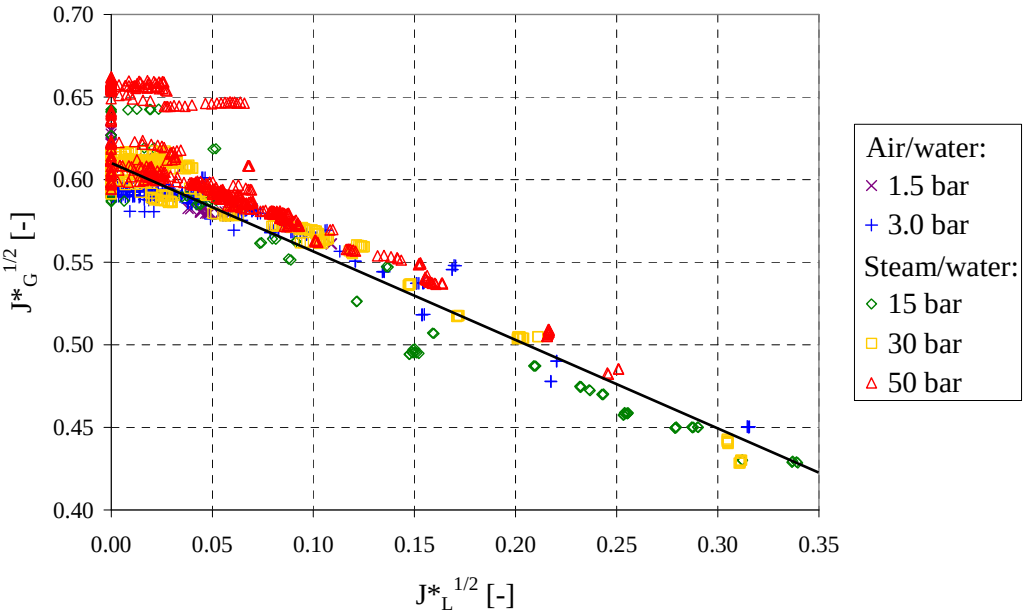

Figure 4.43: Flooding characteristic of the hot leg model plotted in terms of the Wallis parameter after correction of the steam condensation effects

4.5.6.3. Plausibility check on the steam condensation rate

In order to further support or invalidate the hypothesis of steam condensation, a plausibility check was performed. Indirectly it is possible to evaluate approximately the steam condensation amount over three different ways:

1. During other experimental series, steam flow rates down to 0.035 or 0.075 kg/s were injected in the test section. The high-speed camera observations indicate that steam was still flowing through the riser of the hot leg. Therefore, the condensation amount must be significantly lower than 0.075 kg/s.
2. The heat flux released to the atmosphere over the air/air heat exchanger used to cool the inner atmosphere of the pressure chamber (see Figure 4.2) was measured during the experiments. This heat flux was lower than 40 kW, which represents at 50 bar about 0.024 kg/s of steam condensation in the pressure chamber. Although this value only includes the heat losses of the

components inside of the pressure chamber, this is in agreement with the maximisation of the condensation amount performed in the previous point.

3. The condensation rate in the steam line was evaluated with a theoretical model. The empirical correlations recommended by the VDI-Wärmeatlas (1994) were used to calculate the heat flux through the insulation as well as the natural convection around the line. At each pressure level, steam saturation temperature was assumed at the outer wall of this DN100 pipe and the room temperature was supposed to be 20°C. The temperature dependency of the heat conduction of the insulation material was modelled with a polynomial function of the second degree according to the material properties for rock wool indicated in the VDI-Wärmeatlas (1994). Furthermore, the outer diameter of the steam line was set to 260 mm after measurements performed in the test facility and its total length (i.e. from the TOPFLOW separator outlet to the inlet of the pressure vessel, cf. Figure 4.10) was evaluated to 44 m according to isometric drawings. Because of the complicated pipe routing, the natural convection was calculated with the correlations for horizontal pipes on one hand and for vertical pipes on the other hand. The temperature of the outer surface of the insulation material constitutes the interface between both models. Consequently, this was calculated iteratively in order to get convergence between the heat fluxes through the insulation and the heat losses due to natural convection. The correlations for natural convection around horizontal and vertical pipes lead to differences of less than 1%, therefore, the average values were taken. Heat losses of up to 4.4 kW were calculated, representing a maximum condensation rate of 2.6 g/s. Although the insulation conditions of the line are for sure worse compared to the model assumptions, the calculation results are about one order of magnitude lower than the heat losses measured in the pressure vessel. Consequently, the condensation effects along the steam line are probably of second order.

For the different possibilities mentioned previously, the variation of the evaluated amount of condensate in function of the pressure level is shown in Table 4.10. Furthermore, this is illustrated comparatively in Figure 4.44 with base 100 at 50 bar. This comparison points out that the amount of condensate due to heat losses in the pressure chamber (from measurements of the cooling power) or in the steam line (from calculations) depends strongly on the pressure. However, the evolution of the condensate amount measured from the zero liquid penetration (cf. previous section) is significantly less sensitive to the pressure. Besides of the absolute values, these different trends reveal that the water level increase measured in the RPV simulator after reaching zero liquid penetration is probably not only due to heat losses and the resulting steam condensation.

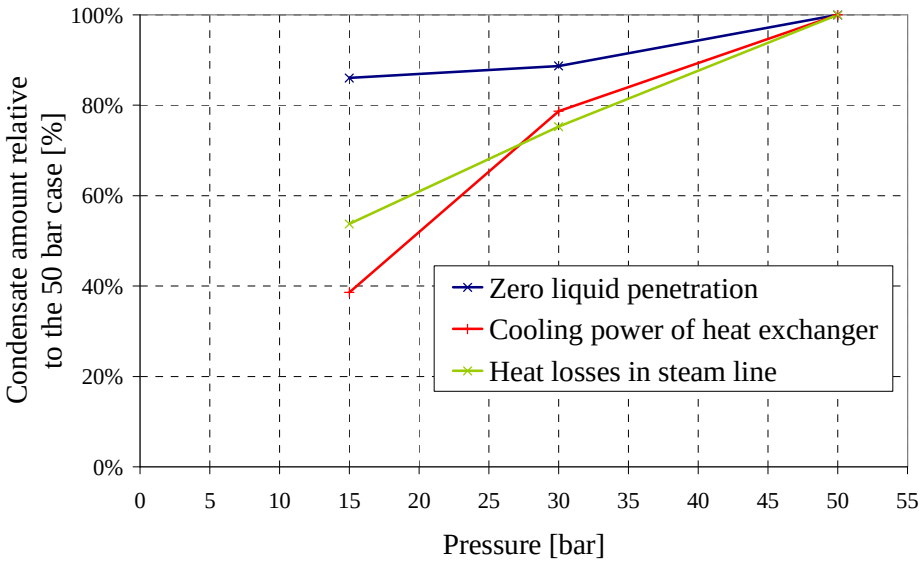

Figure 4.44: Evolution of the relative amount of condensate in function of the system pressure (base 100 at 50 bar)

Table 4.10: Comparison of the steam condensation rate evaluated by different methods

Pressure	Zero liquid penetration	(1) Min. m(steam)	(2) Cooling heat exchanger		(3) Heat losses in steam line	
[bar]	[g/s]	[g/s]	Power [kW]	m(cond) [g/s]	Power [kW]	m(cond) [g/s]
15	32.7	35	16.5	8.5	2.78	1.43
30	33.7	75	31	17	3.59	2.00
50	38.0	75	36	22	4.36	2.66

4.5.6.4. Plausibility check on liquid entrainment from the steam/water separator

Another parasitic source of liquid water in the steam line could be liquid entrainment from the separator of the heater circuit of the TOPFLOW test facility (cf. Figure 4.10). In fact, the steam flow rate needed to reach CCFL, and a fortiori zero liquid penetration, is relatively high and a perfect separation of the two-phase flow in the separator cannot be guarantied. During previous experimental series conducted at the TOPFLOW test facility, liquid entrainment has already been observed with help of conductivity probes installed in the steam line above the separator. Unfortunately, this instrumentation has been removed in the meantime and was not available during the hot leg experiments in order to support this hypothesis.

Therefore, again a dedicated plausibility check was performed. As shown in Table 4.11, the steam superficial velocity in the outlet pipe of the TOPFLOW separator is higher than 10 m/s at zero liquid penetration. In order to have an idea of the flow pattern reached in this section at such gas velocities and high void fractions, the flow regime transition model for vertical pipes proposed by Taitel et al. (1980) was used. According to their analysis, annular flow can only exist if the gas flow rate is sufficient to raise the droplets entrained in the gas core. Consequently, if the developed model predicts annular flow, the steam flow is likely to entrain liquid water out of the separator. The criteria proposed by Taitel et al. (1980) to describe the transition to annular flow is only a function of the fluid properties:

$$j_G = 3.1 \cdot \frac{(\sigma \cdot g \cdot \Delta\rho)^{1/4}}{\sqrt{\rho_G}} \qquad (4.12)$$

The flow transition velocity was calculated accordingly in function of the pressure level as shown in Table 4.11. A comparison with the flow conditions at zero liquid penetration reveals that the superficial velocity is far above the transition, confirming that the steam injected into the hot leg model is probably wet.

Moreover, the liquid entrainment can explain why the parasitic amount of water measured over the zero liquid penetration is almost independent on the pressure. In fact, the superficial velocity at zero liquid penetration decreases with an increase of pressure (cf. Table 4.11). As a result, the amount of entrained water is expected to decrease as well. The dependency of the heat losses to the system pressure being inverse, the superposition of both effects can lead to a mutual compensation.

Table 4.11: Evolution of the steam flow rate at zero liquid penetration in function of the pressure

Pressure level	m(steam) @ zero liquid penetration	j(steam) @ separator outlet	j(steam) @ transition to annular flow
[bar]	[kg/s]	[m/s]	[m/s]
15.0	0.67	24.8	4.76
30.0	0.80	15.0	3.14
50.0	1.05	11.6	2.22

All in all, liquid entrainment from the TOPFLOW separator is probably an important source of the parasitic water accumulating in the RPV simulator during zero liquid penetration. Although this hypothesis does not put into question the qualitative considerations of section 4.5.6.1, this has consequences on the correction of the flow rates. In fact, the assumption that the condensation rate only depends on the pressure level is legitimate, but the amount of entrained liquid should additionally be a function of the steam flow rate. Furthermore, both terms should be considered independently in the correction functions (cf. equations (4.9) and (4.10)) because the liquid entrainment only affects the discharge liquid flow. This means that the contributions of heat losses and liquid entrainment should be determined separately. As this is not possible in retrospect from the available data, dedicated experiments should address these uncertainties in a second experimental campaign.

4.5.7. Comparison with the results obtained at UPTF

The counter-current flow limitation in a hot leg was investigated at the original power plant scale in the Upper Plenum Test Facility (UPTF) during the dedicated test series n°11 reported in Siemens/KWU (1987). The experiments were performed with steam and saturated water at pressures of 3 and 15 bar in order to check the applicability of the Wallis similarity to the original geometry and boundary conditions. Furthermore, investigations were focused on the influence of the several meters long pipe of the *Hutze* (ECC nozzle placed at the bottom of the hot leg) with respect to the flooding behaviour. As a result, it was recommended to calculate the Wallis parameter based on the flow path in the region of the *Hutze*. This concerns in particular the flow cross-section A for the calculation of the superficial velocity and the hydraulic diameter D_h as length scale. Later on, this approach was supported by the small scale experiments of Ohnuki et al. (1988).

The resulting data points (calculated with $A = 0.3974$ m² and $D_h = 0.639$ m) are compared with the own flooding characteristics in Figure 4.45. For clarity reasons, only the experiments performed at the same pressure levels as those of UPTF were plotted (i.e. one air/water and one steam/water series). Figure 4.45 shows an approximate agreement between both experimental works: at UPTF the zero liquid penetration was obtained at higher gas fluxes and the slope of the flooding characteristics is steeper. Consequently, in a second comparison presented in Figure 4.46, the UPTF data points were recalculated with the geometrical parameters in the parts of the hot leg without *Hutze*: $A = 0.4418$ m² and $D_h = 0.750$ m. In that case, the overall agreement with the own results is better, in particular for the zero liquid penetration. This may indicate that flooding does not mainly occur along the *Hutze*. However, close inspection reveals that the slope is again too steep, especially close to zero penetration. Since none of the geometrical considerations gives satisfying agreement, the observed differences may also be due to the rectangular cross-section of the TOPFLOW hot leg model (cf. remarks of section 4.5.4.3). Nevertheless, with respect to the uncertainty of the data, the differences between both experimental series are acceptable and precise explanations would require dedicated investigations.

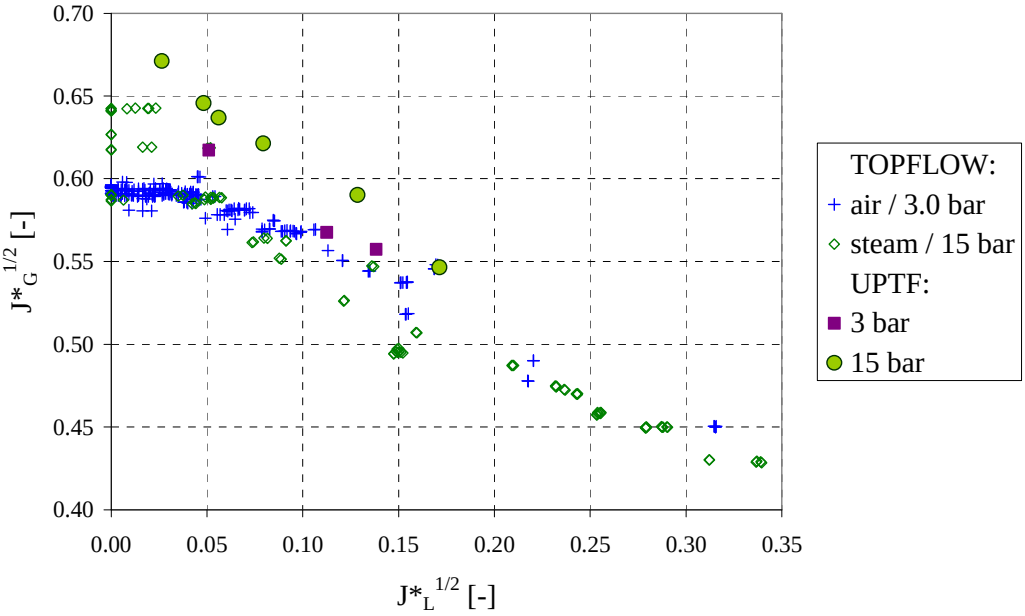

Figure 4.45: Comparison of the present data with the CCFL characteristics of UPTF (Siemens/KWU, 1987) considering the *Hutze* (A = 0.3974 m² / D_h = 0.639 m)

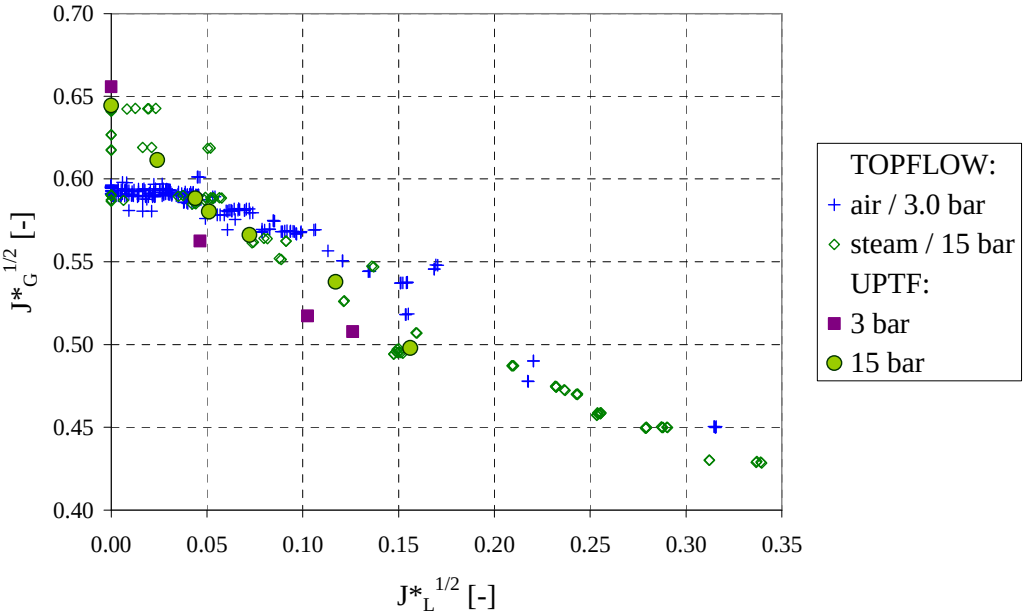

Figure 4.46: Comparison of the present data with the CCFL characteristics of UPTF (Siemens/KWU, 1987) without considering the *Hutze* (A = 0.4418 m² / D_h = 0.750 m)

5. EXAMPLE OF COMPARISONS BETWEEN EXPERIMENTAL RESULTS AND CFD SIMULATIONS

The goal of the present work was to deliver high resolution experimental data suited for the development and validation of CFD codes. Especially the intended use of CFD for nuclear reactor safety issues affords a high level of confidence for these tasks. Consequently, the development of methods for comparisons between experimental results and CFD simulations is considered as integrant part of this process. Although no CFD calculation was done by the author, it appears that it is necessary to bring the experimental data and the simulation results together in order to be able to perform meaningful comparisons. Therefore, data treatment routines have been developed by the author for the CFD simulation results, especially in order to make quantitative comparisons with the experiments possible. As a result, different examples of comparison possibilities offered by the data are presented in this section.

5.1. CFD simulation with time-dependent inlet boundary conditions for slug generation in a short channel

5.1.1. CFD model of the preliminary test channel

The slug flow experiment performed in the preliminary test channel with a water flow rate of 8.68 l/s and an air flow rate of 1650 l/min presented in section 3.1.2.2 was simulated with CFD (cf. Vallée et al., 2007-a). The two fluid model with free surface option implemented in the commercial software package *ANSYS-CFX-5.7* was used. The turbulence was modelled separately for each phase applying the *k-ω* based shear stress transport (SST) turbulence model. Furthermore, a surface capturing method using a compressive advection scheme was applied. Due to the high numerical efforts of transient slug flow simulations, the modelling of the complete test facility as described in section 3.1.1 was not feasible. In order to keep computational time within acceptable limits, only the horizontal test section with its rectangular cross-section was modelled. Consequently, a grid consisting of $4 \cdot 10^5$ hexahedral elements was generated, corresponding to the channel dimensions of 2000 x 250 x 50 mm³ (length x height x width).

In the simulation, the gaseous phase was air and the liquid phase was water, both at 25°C and at a reference pressure of 1 bar. The phases were treated as isothermal and incompressible. Buoyancy effects between the two phases were taken into account by the directed gravity term and a hydrostatic pressure was assumed for the liquid phase. According to the experimental conditions and to the initial water level of 194 mm, the velocities at the inlet (i.e. at an abscissa of the model x_m = 0.0 m) were set to 8.93 m/s for the gaseous phase and to 0.895 m/s for the liquid phase. These velocities were kept constant during the simulation. The turbulent kinetic energy and dissipation rate at the inlet were set to the standard values of *ANSYS-CFX*. The inner surfaces of the channel walls were defined as hydraulically smooth with a non-slip boundary condition applied to both gaseous and liquid phases. At the other end of the horizontal channel (i.e. at x_m = 2.0 m), a pressure controlled outlet boundary condition was applied.

In the CFD simulations, it was not possible to generate slug flow in the channel with constant inlet boundary conditions. This is probably due to the relatively short length of the channel and to the simple inlet conditions chosen, which do not reflect the instabilities of the experimental inlet conditions. In fact, as mentioned in section 3.1.2.2, during the experiment the water level in the channel vary sensibly in time. In Figure 3.6, basically two phenomena influence the variation of the water level: the waves which are responsible for the small and short period variations, and the slugs which generate long period variations with important amplitudes (of about 50 mm). Although the wavy flow can be considered to be only located in the test channel, the water level the inlet separator must also be varying with the time due to the slugs. Therefore, the inlet boundary conditions of the CFD calculation (water level and mass flow rate) should be time-dependent too. Thanks to the interface capture, the water level history of the recalculated experiment is known at a distance from the

inlet of the facility of x_f = 0.75 m (see section 3.1.2.2 and Figure 3.6). At this position a length to height ratio of L/H = 3 is achieved, and therefore, the influence of the duct inlet geometry on the flow is not so prominent anymore. For this reason, the experimental water level history measured at x_f = 0.75 m (see the blue curve in Figure 3.6) was used as time-dependent boundary condition for the CFD calculation at the inlet cross-section (at x_m = 0.0 m) of the modelling domain. For further details concerning the CFD model, the reader is referred to Vallée et al. (2007-a).

5.1.2. Qualitative comparison of the CFD results with optical observations

The picture sequence in Figure 5.1 shows the flow conditions as simulated with CFD in comparison with the observations made during the corresponding experiment. Since the filmed test section length and the modelled part of the channel are different, the last part of the model can not be compared with experimental data. This explains the length difference between the camera frames and the visualisations of calculation results in Figure 5.1. In both cases, a slug is developing. In the CFD calculation, the slug develops approximately at t = 0.90 s due to a high peak of the experimental water level at the inlet cross-section of the model. The tail of the calculated slug and the flow behind it is in good agreement with the experiment. The entrainment of droplets in front of the slug could not be observed in the calculation. However, the rolling over and breaking of the wave, characteristic of a slug, are clearly to be seen in Figure 5.1. These are created by the shear generated by the high air velocity.

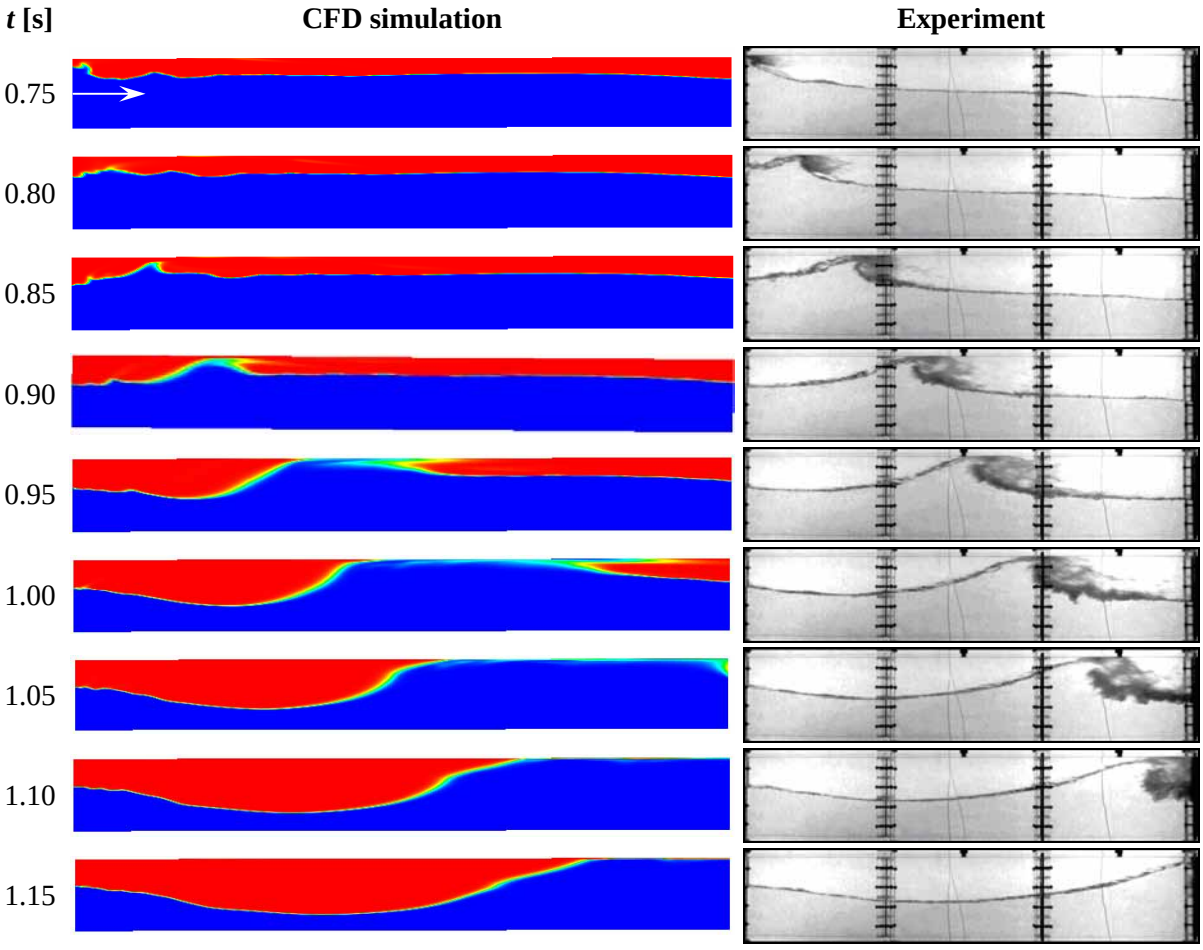

Figure 5.1: Comparison between the measured and calculated image sequences during slug flow

In contrast to the measurement, the slug length is increasing in time in the calculation. This could be a result of the different amount of water in the channel at the beginning of the experiment and the simulation. While in the simulation, the liquid phase covered 78% of the channel, it represented about 70% at the beginning of the experiment. Furthermore, in the experiment, this value was also reduced

by a first slug, which carried a significant amount of water out of the channel. This first slug could not be simulated. This is probably an effect of the simplified initial conditions assumed in the calculation. Because of the constant initial water level, it took quite a long simulation time to establish a wavy flow along the channel, which is necessary for slug formation. Whereas at the beginning of the measurements, the test channel was already in a fully established intermittent slugging regime.

5.1.3. Comparison of quantitative data

5.1.3.1. Slug propagation across the duct

The slug position was extracted from the experimental images after the application of the interface capture algorithm (cf. section 3.1.2.1). Since this method detects only one pixel in each vertical line, the interface function always presents a discontinuity where the slug is rolling over (cf. the yellow box in Figure 5.2). This point was considered as the slug axial position.

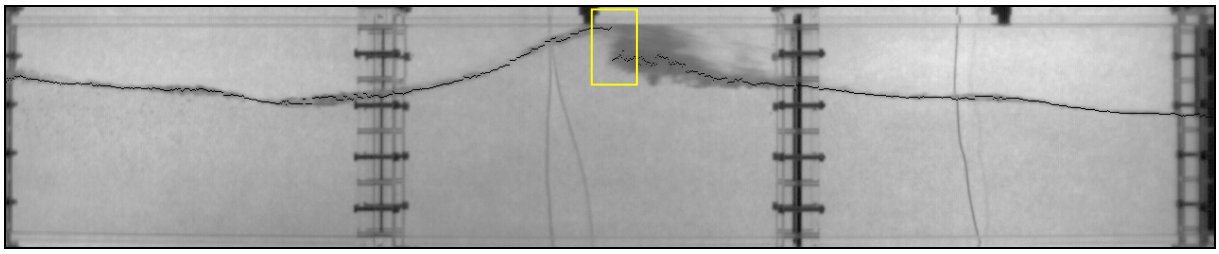

Figure 5.2: Result of the interface detection for a slug and characteristic interface step (yellow)

As remarked in the previous section, the visualised calculation results show that the slug gains length continuously. For this reason, the slug front propagates significantly faster than its tail, which is in a qualitative good agreement with the experiment. Therefore, the slug position was taken as the first axial position (from the left) where the recalculated slug reaches the top of the duct.

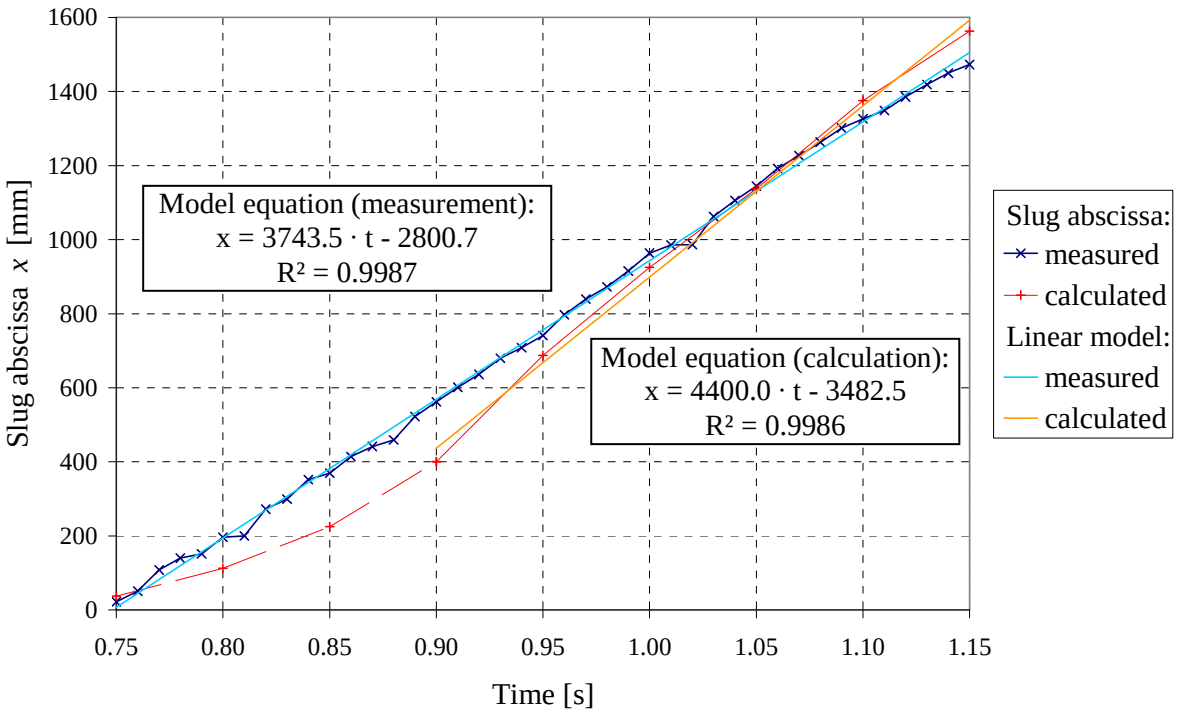

Figure 5.3: Propagation of a slug – comparison between measurement and calculation

The slug axial position obtained in this way was plotted in function of time in Figure 5.3 for both experiment and simulation. This was performed with an accuracy of about ±30 mm. As shown in

Figure 5.3, in the experiment the slug moves along the duct with a constant velocity, in average at 3.7 m/s. The slug propagation of the CFD calculation is divided into two characteristic parts:

- between 0.75 and 0.90 s, as the slug is still in preparation, the wave which is generating the slug is accelerating (dashed part of the red line in Figure 5.3).
- from t = 0.90 s, when the wave blocks the whole cross-section of the channel, the slug propagates with a nearly constant velocity in the calculation, too. The average velocity of the calculated slug is 4.4 m/s, which is 18% higher than in the experiment.

5.1.3.2. Dynamic pressure

Because the slug also closes the channel cross-section in the calculation, an area with high pressure is created after the slug (see Figure 5.4).

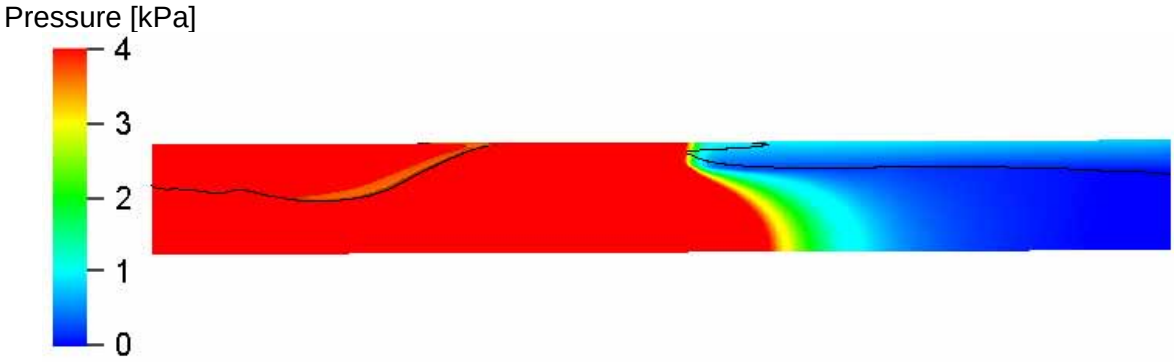

Figure 5.4: Calculated pressure field (colour scale) and interface (black line) at t = 0.95 s

Figure 5.5 shows the comparison of the time-dependent pressure at both sensor positions for the experiment and the CFD calculation. Since it was not possible to simulate the first slug, there is no pressure peak in the calculation that corresponds to the first peak observed experimentally. During the travelling of the second slug, the pressure at the first sensor position increases later in the calculation than in the experiment, which is due to the lower velocities in the acceleration phase. At the second sensor position, the pressure increase is simultaneous. Then, the pressure decreases earlier in the

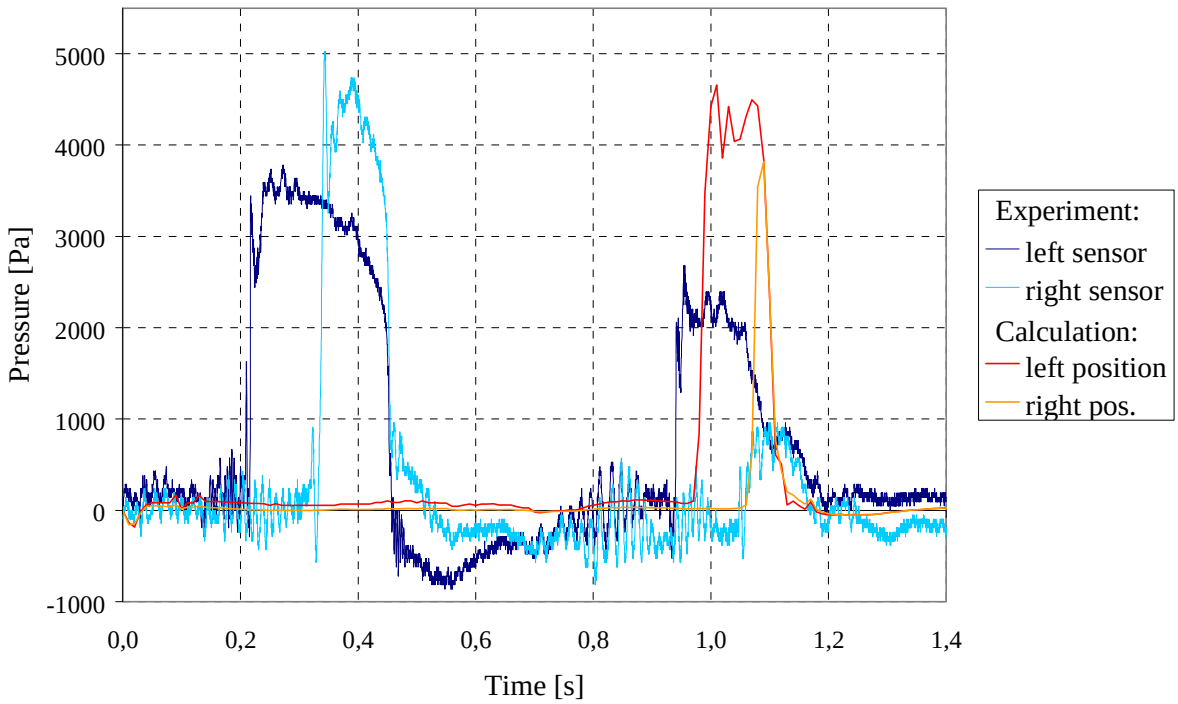

Figure 5.5: Transient pressure at the left and right sensor positions for experiment and *ANSYS-CFX* calculation

calculation than in the experiment, i.e. the calculated slug becomes faster than in reality. This is in agreement with the remarks made on the slug position diagram (see previous section and Figure 5.3).

Furthermore, for the recalculated slug, the pressure peak value is higher in the calculation (4.4 kPa) than in the measurement (2.3 kPa), whereas the peak value of the first slug observed in the experiment reaches between 3.6 and 5.0 kPa (respectively at the first and second sensor positions), which is in much better agreement with the calculated value. This difference of the experimental pressure peak value is due to the fact, that the boundary conditions for the second slug are already influenced by the first slug, which has cleared a certain amount of water from the channel before. The lower pressure peak of the second slug can be explained by the smaller amount of water to be driven by the air pressure. Furthermore, the effective free area on top of the slug where air flows is bigger. This effect is missing in the calculation, since the first slug was not reproduced.

5.1.4. Pertinence of the comparison with the experiment

This preliminary study shows that the slug flow regime can be qualitatively reproduced with CFD. However, the comparison between the simulation results and the available experimental data was not sufficiently pertinent due to the difficulty to model properly the inlet and initial boundary conditions. In fact, in the present test facility, important inlet parameters such as water level and velocity profiles could not be controlled properly and were not stationary because of the separator at the test section inlet. Possible enhancements could be either to implement the inlet separator in the CFD model, or to perform measurements of the inlet boundary conditions, especially the velocity profiles including turbulence, and to take this additional information into account in the simulation. However, both measures are quite expensive, and furthermore, do not allow to separate the effects occurring in the inlet vessel from those in the test channel, which leads to additional uncertainties. Therefore, another approach should be preferred in order to make reasonable quantitative comparisons possible: to care for constant and well defined experimental boundary conditions. Consequently, detailed investigations require an improved channel inlet geometry as realised in the HAWAC test facility described in section 3.2.1.

5.2. CFD model for a self-generation of slug flow

5.2.1. CFD model of the HAWAC

The HAWAC slug flow experiment performed at superficial velocities of 1.0 m/s for the water and 5.0 m/s for the air (cf. section 3.2.4) was simulated with CFD by Höhne & Vallée (2008). Thanks to the constant water level maintained at the inlet by the blade, the Horizontal Air/Water Channel (HAWAC) allows to investigate the generation of waves at the interface as well as their instable growth to slugs. Like in the previous case, in order to reduce the computational costs, only the channel test section was modelled using *ANSYS-CFX*. The three dimensional model dimensions are 8000 x 100 x 30 mm³ (length x height x width). The grid consists of $1.2 \cdot 10^5$ hexahedral elements. According to the experimental boundary conditions (inlet blade in horizontal position), the model inlet was divided into two parts: in the lower 50% of the inlet cross-section, water was injected and in the upper 50% air. Consequently, the simulation begins at the final edge of the inlet blade, which was not implemented into the model. An initial water level of h_0 = 50 mm was assumed for the entire model length.

In the simulation, both phases have been treated as isothermal and incompressible, at 25°C and at a reference pressure of 1 bar. A hydrostatic pressure was assumed for the liquid phase. Buoyancy effects between the two phases are taken into account by the directed gravity term. At the inlet, the turbulence properties were set using the “Medium intensity and Eddy viscosity ratio” option of the flow solver. This is equivalent to a turbulence intensity of 5% in both phases. The inner surface of the channel walls has been defined as hydraulically smooth with a non-slip boundary condition applied to both gaseous and liquid phases. The channel outlet was modelled with a pressure controlled outlet boundary condition. As it was the goal of the CFD calculation to induce surface instabilities, which are later generating waves and slugs, the interfacial momentum exchange as well as the turbulence parameters had to be modelled correctly. Therefore, the damping of turbulence term introduced by Yegorov et al.

(2004) was applied in the simulation for grid cells near the free surface. The used model is described in details in Höhne & Vallée (2008).

The parallel transient calculation of 15.0 s of simulation time on 4 CPU took 20 days. A high-resolution discretisation scheme was used. For time integration, the fully implicit second order backward Euler method was applied with a constant time step of dt = 0.001 s and a maximum of 15 coefficient loops. A convergence in terms of the RMS values of the residuals to be less than 10^{-4} could be assured most of the time.

5.2.2. Qualitative CFD results

In the following picture sequence (Figure 5.6), the calculated phase distribution during slug generation is visualized. The first slug develops spontaneously at approximately t = 16.65 s after the beginning of the simulation, induced by instabilities. The simulated sequence shows that the qualitative behaviour of the creation and propagation of the slug is similar to the experiment (cf. Figure 3.23). The single effects leading to slug flow that can be simulated are:

- Instabilities and small waves are generated by the interfacial momentum transfer randomly. As a result bigger waves are generated.
- Bigger waves roll over and can close the channel cross-section. In this case, an important two phase mixture is produced at the slug front.
- The slug can catch up waves and merge with them.
- A sensible decrease of the water level appears downstream of the region where slugs are generated.

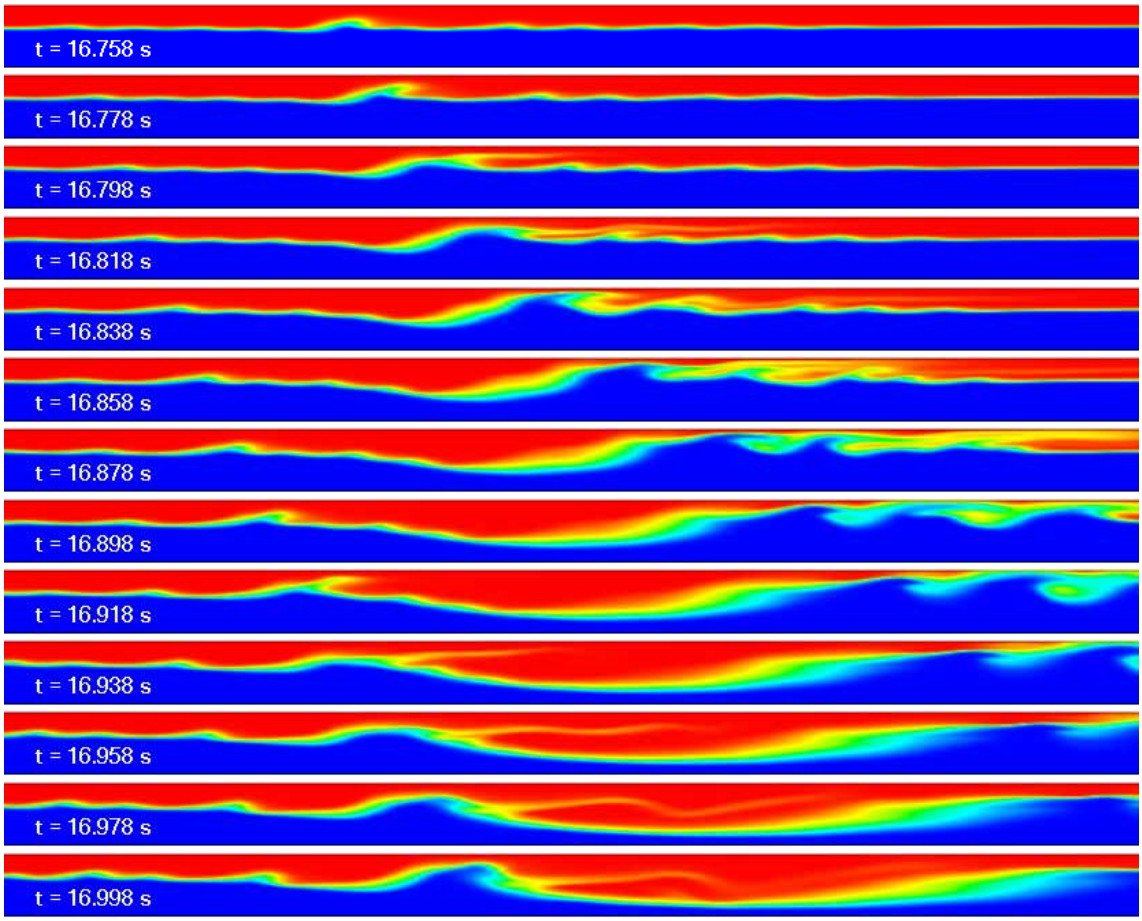

Figure 5.6: Calculated picture sequence at j_L = 1.0 m/s and j_G = 5.0 m/s
(depicted part of the channel: 4.58m to 6.48m after the inlet)

However, a detailed comparison shows quantitative deviations between simulation and measurement. The needed entrance length for slug generation was defined as the length between the inlet and the location nearest the inlet where a wave closes nearly the entire cross-section. This was observed at about 1.5 m in the experiment and 5 m in the calculation. These quantitative differences can be explained with the flow regimes observed at the test section inlet. In fact, the flow pattern has an important influence on the momentum exchange between gas and liquid, especially at high velocity differences between the phases. Small disturbances of the interface provide a more efficient momentum transfer from the air to the water than in a stratified smooth flow. A high momentum transfer induces a rapid wave growth and therefore slug generation. In this case, a smooth interface was obtained over the 3 first meters in the simulation, whereas in the experiment supercritical flow waves were observed from the inlet of the channel. This means that the boundary conditions chosen for the CFD model do not reproduce the small disturbances observed in the experiment. In the end, a quite long channel length is needed before waves appear spontaneously in the simulation, deferring accordingly the instable wave growth to slugs downstream of the 3 m mark. Finally, the quantitative differences noticed between simulation and experiment concern in particular the inlet boundary conditions. Because these have an important influence on the generation of the two-phase flow, future work should focus on the proper modelling of the small instabilities observed at the channel inlet. An implementation of the inlet blade in the model may improve the results.

Other qualitative comparison of the HAWAC slug flow experiment with CFD simulations were performed in the frame of the EU-Project NURESIM (European Platform for NUclear REactor SIMulations). Additionally to the in house calculations with *ANSYS-CFX*, simulations were performed with the commercial code *FLUENT* at the *Université catholique de Louvain* (UCL, Belgium) and with *NEPTUNE_CFD* at *Électricité de France* (EDF). A comparison of the different simulation results with the experiment is given by Bartosiewicz et al. (2010). Not least, the same experiment was selected as a possible benchmark case for primary circuits by the OECD/NEA-CSNI working group on the analysis and management of accidents (cf. OECD report by Smith et al., 2008).

5.2.3. Interface capture method for the CFD simulation results

5.2.3.1. Methodology

Contrary to the interface tracking methods, the two-fluid model does not reproduce a sharp interface between air and water. Nevertheless, for the comparison between CFD calculation and experimental results, a surface similar to the interface observed in the camera pictures should be defined. Therefore, the isosurface with 50% of void fraction was chosen (cf. Figure 5.7) and the coordinates of its intersection with the vertical mid-plane was exported from *ANSYS-CFX*. With this simplification, the three-dimensional shape of the isosurface is not taken into account.

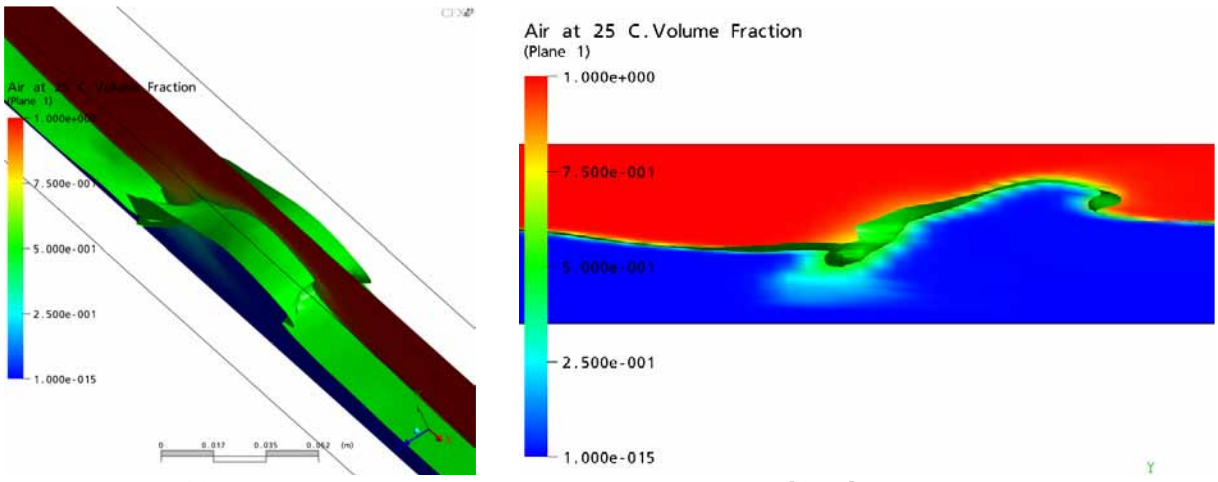

(a) 3D view (b) side view

Figure 5.7: Structure of the calculated void fraction and of the 50% isosurface (in green)

For each time step, the exported data set was treated in order to determine the minimum and maximum water levels in each vertical cross-section. As shown in Figure 5.8, this data set is composed of several domains representing the free surface, bubbles and sometimes droplets. Moreover, the free surface itself is sometimes divided in different domains (discontinuities in the green circles of Figure 5.8). This appears when slugs block the whole cross-section of the channel and consequently the air volume fraction reaches unity on top of the test section.

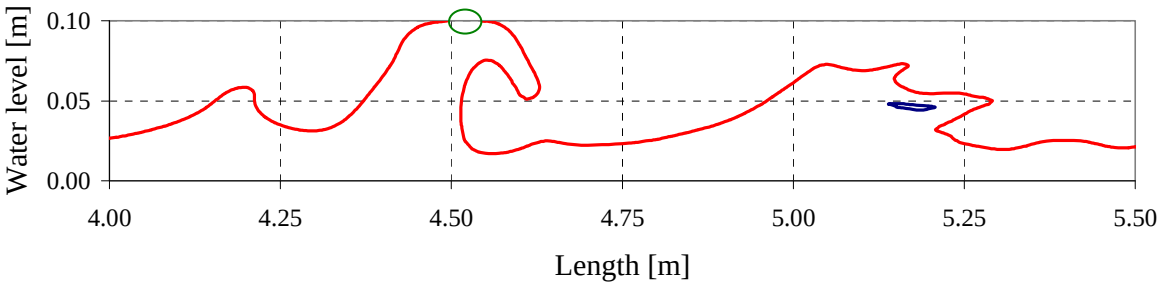

Figure 5.8: Example of data set exported from *ANSYS-CFX*
(in red: domains of the free surface; in blue: a bubble domain)

At first, the free surface has to be recomposed. The domains representing bubbles and droplets are recognised and separated from the domains corresponding to the free surface. Then, free surface domains are unified to a single one by connecting them in the empty spaces left by slugs on top of the channel. In the next step, the droplet and bubble domains are treated. In order to obtain similar results as with the interface capture method used for the experimental data, only the structures with a perimeter exceeding about 20 mm are selected. The small formations are also mostly excluded in the experiment because they do not fit into a continuous interface line (step 4 of the method described in section 3.1.2.1). Furthermore, droplets attached to the top of the channel are not taken into account. Finally, the minimum and maximum water levels are determined from the coordinates of the free surface domain as well as the selected bubble/droplet domains. This is done in each vertical cross-section with a resolution of 1 cm in the horizontal axis (Figure 5.9).

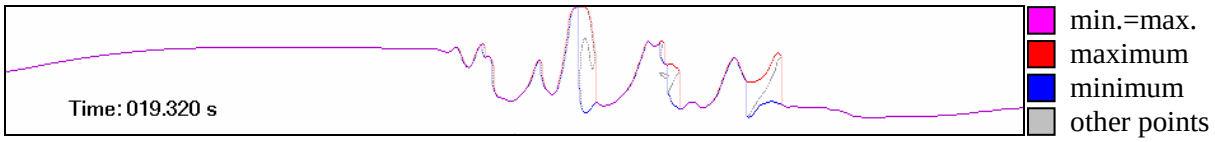

Figure 5.9: Interface profile obtained from the CFD calculation (0.10 x 8.0 m – *H* x *L*)

5.2.3.2. Quantitative results from CFD calculations

The time averaged water level profiles were calculated for the CFD results from the minimum and maximum water levels determined as described previously. These are shown in Figure 5.10 for t = 17,250…20,250 s (i.e. from the passage of the first slug clearing the channel to the end of the calculation time) and are bounded by the standard deviation.

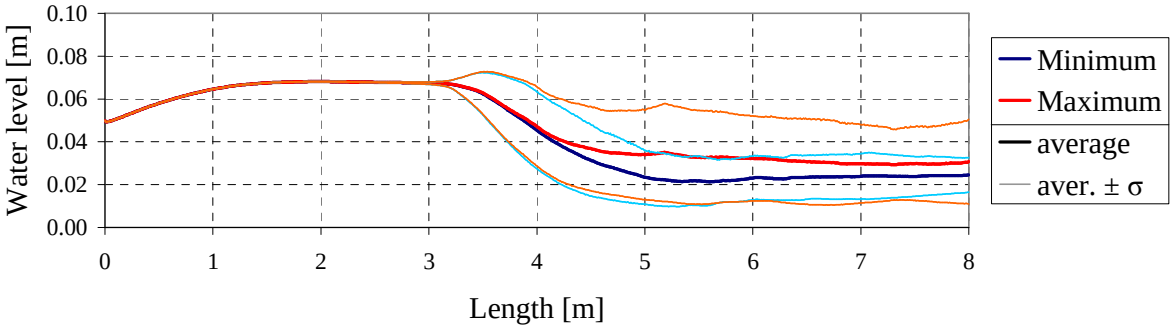

Figure 5.10: Comparison between the mean water level profiles obtained for the minimum and the maximum water levels (*ANSYS-CFX* calculation) for t = 17.250…20.250 s

Qualitatively, Figure 5.10 shows that the trend obtained for the simulation is similar to the measurement (Figure 3.26). Like in the experiment, the mean water level profile increases after being injected over a height of 50 mm at the inlet. Farther, the water levels decrease simultaneously to an increase of the standard deviation. Furthermore, a difference between minimum and maximum appears, which is due to the development of rolling over waves and slugs or the presence of bigger bubbles or droplets structures in the flow. In the last part of the channel, the mean water levels converge slightly together, probably due to collapsing slugs. The water levels tend to about 24 mm and 30 mm for the minimum and maximum water levels respectively.

5.2.4. Quantitative comparison between simulation and experiment

However, a detailed comparison shows quantitative deviations between simulation and measurement (Figure 5.11). With its rising, the water level reaches a maximum of 68 mm, which is 10 mm more than in the experiment, followed by a plateau between 2 and 3 m only observed in the calculation. Furthermore, wave growth starts downstream of the 3 m mark, revealed by a rapid increase of the standard deviation, compared to about 0.9 m in the experiment.

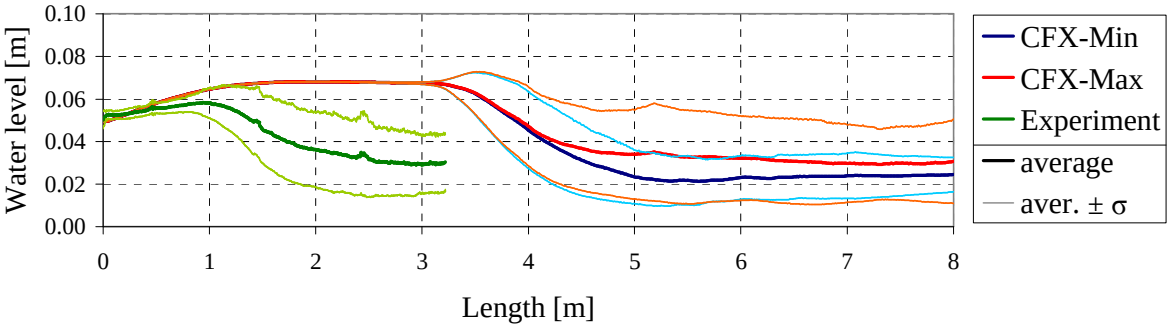

Figure 5.11: Mean water level profiles bounded by the standard deviation: comparison between *ANSYS-CFX* calculation and experiment

These quantitative differences can be explained with the flow regimes observed at the test section inlet. In fact, the flow pattern has an import influence on the momentum exchange between gas and liquid, especially at high velocity differences between the phases. Small disturbances of the interface provide a more efficient momentum transfer from the air to the water than in a stratified smooth flow. A high momentum transfer induces a rapid wave growth and therefore slug generation. In this case, the very low standard deviation ($\sigma \leq 0.5$ mm) observed over the 3 first meters in the simulation reveals a smooth interface, whereas in the experiment the flow is wavy from the inlet of the channel. This means that the boundary conditions chosen for the CFD model do not reproduce the small disturbances observed in the experiment. In the end, a quite long channel length is needed before waves appear spontaneously in the simulation, deferring accordingly the instable wave growth to slugs. This occurs downstream of the 3 m mark, inducing an increase of the standard deviation up to about 18 mm (at 4.00 m) and 23 mm (at 5.20 m) for the minimum and maximum water levels respectively. These values correspond to the order of magnitude measured about 3 m after the inlet.

Finally, the quantitative differences noticed between simulation and experiment concern in particular the inlet boundary conditions. Because these have an important influence on the generation of the two-phase flow, future work should focus on the proper modelling of the small instabilities observed a the channel inlet.

5.3. Simulation of the hot leg experiments

The counter-current flow limitation experiments performed in the hot leg model were simulated with CFD by Deendarlianto et al. (2010) and by Murase et al. (2010). Different model approaches (based on the two-fluid model or volume of fluid method) were tested in order to reflect qualitatively the flow structure observed during the experiments as well as to match quantitatively the flooding

characteristics. As an example, an overview of the calculation results by Deendarlianto et al. (2010) is presented in this section.

5.3.1. CFD model of the hot leg test section

An air/water CCFL experiment was simulated using the two-fluid Euler-Euler model of the commercial CFD code *ANSYS-CFX* (version 12.0). The calculation was carried out in a fully transient manner using a gas/liquid inhomogeneous multiphase flow model coupled with a shear stress transport (SST) turbulence model and an upwind advection scheme. In the simulation, the drag coefficient was approached by the algebraic interfacial area density (AIAD) model by Yegorov et al. (2004) in order to obtain a momentum exchange coefficient depending on the local morphology of the flow. The basic concept of this model can be described as follows:

- The interfacial area density allows the detection of the morphological form of the flow and the corresponding switching for each correlation from one object pair to another.
- The model provides a law for the interfacial area density and for the drag coefficient over the full range of void fractions.
- The interfacial area density in the intermediate range of void fractions is set to the interfacial area density for the free surface.

The fluid domain of the hot leg model, including the test section and both separators, was meshed to a grid consisting of about $2.5 \cdot 10^5$ hexahedral elements and $2.8 \cdot 10^5$ nodes (cf. Figure 5.12).

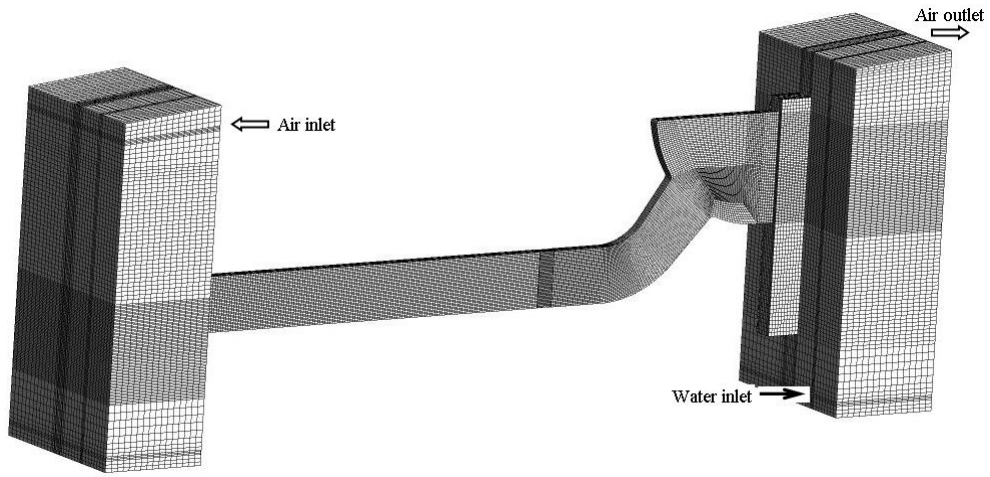

Figure 5.12: Calculation mesh of the hot leg model

The air/water experiment chosen for the CFD calculation (run 30-09) was performed at the following boundary conditions: a system pressure of 1.53 bar, a water mass flow rate of 0.283 kg/s and an air mass flow rate varied in 6 steps from 0.23 to 0.345 kg/s within about 100 s. In the simulation, both phases have been treated as isothermal and incompressible, at 25°C and the measured system pressure. In order to determine the flooding characteristics, a constant water flow rate was injected at the bottom of the SG separator according to the measurements and the air flow rate was varied during the calculation after the experimental course of time. Buoyancy effects between the phases were taken into account by the directed gravity term. The turbulence properties at the inlet of both phases were set to an intensity of 5%. The air outlet was modelled with an opening boundary condition. The inner surface of the channel walls has been defined as hydraulically smooth with a non-slip boundary condition applied to both gas and liquid phases. Further details concerning the CFD model are to be found in Deendarlianto et al. (2010).

A time step of 10^{-4} s and a maximum of 15 coefficient loops were taken for the calculation. A convergence in terms of the RMS values of the residuals to be less than 10^{-4} could be assured most of the time. The transient calculation of 100 s simulation time required four months with 4 parallel processors of the HZDR Linux cluster.

5.3.2. Simulation results and comparison with the experiment

The simulated flow structure before and after the onset of flooding is compared with the experimental observations in Figure 5.13. At low air flow rates, the stratified flow conditions observed during the experiment are well reflected by the CFD calculations: the comparison shows that the thin supercritical water film flowing down the riser and the occurrence of the hydraulic jump in the bend are pretty similar. After reaching the onset of flooding, large slugs are generated in the bend (cf. Figure 5.13), carrying water back to the steam generator. These processes are in qualitative agreement with the experiment, although the phase mixing occurring over droplet detachment and gas entrainment seems to be underpredicted in the simulation.

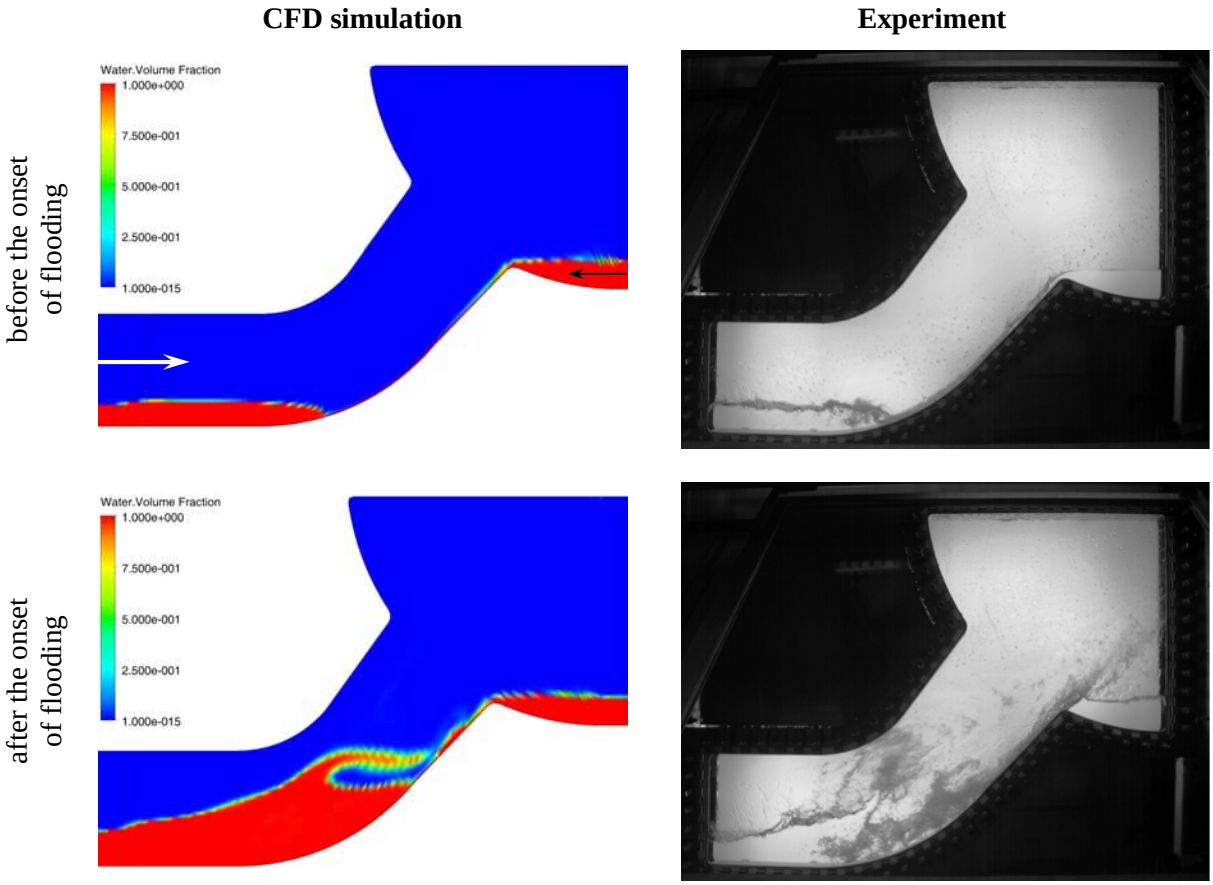

Figure 5.13: Qualitative comparison of the simulation results with the experiment

Finally, Figure 5.14 shows a comparison of the CCFL characteristics obtained from the CFD calculation and the air/water experiments plotted in terms of the Wallis parameter. This quantitative comparison reveals that flooding is predicted at slightly too small gas fluxes in the simulation, pointing out that the applied models lead to a too important momentum transfer between the phases.

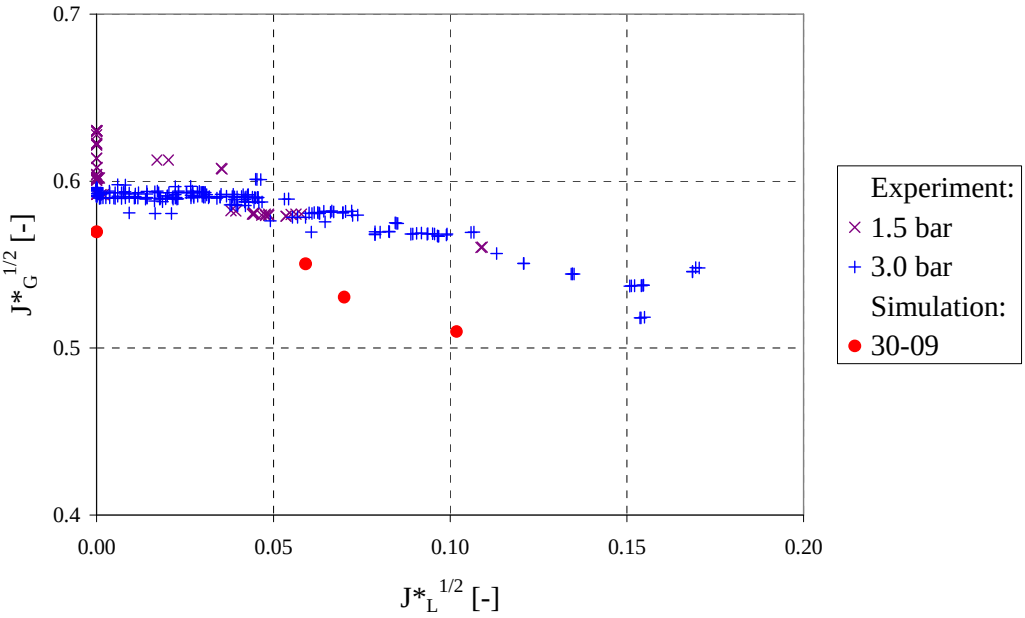

Figure 5.14: Comparison of the flooding characteristics

L'arrivée aux conclusions pratiques
Nécessite aptitude artistique,
L'impressionisme même,
Et les puristes blêmes
Y renoncent en confusion panique.

Pas de deux, G. B. Wallis (1989)

---

6. SUMMARY AND CONCLUSIONS

In order to support the development and validation of computational fluid dynamics (CFD) applied to multiphase flows, dedicated experimental data is needed with high resolution in space and time for pertinent comparison with CFD calculations. Therefore, in the frame of the present thesis, stratified two-phase flows were investigated at different test facilities. For each, a rectangular cross-section design was chosen in order to provide optimal observation possibilities for the application of high-resolution optical measuring techniques.

The first channel, a horizontal test section mounted in between of two separators, was built for preliminary air/water investigations. During slug flow, optical measurements were performed using a high-speed video camera, which were complemented by simultaneous dynamic pressure measurements. An algorithm was developed to recognise the stratified interface in the camera frames, allowing to extract the water level history from the image sequences. The pressure measurements show that the order of magnitude of the pressure behind the slug is about a few kilo-Pascals. The pressure increase is fast (2 to 10 ms) and linked to the slug length. Furthermore, the velocity field of a slug was measured using Particle Image Velocimetry (PIV), revealing its inner flow rotation.

Moreover, a second channel, the **H**orizontal **A**ir/**Wa**ter **C**hannel (HAWAC), was designed for generic co-current flow investigations. A special inlet device provides well defined as well as variable boundary conditions and, consequently, very good CFD code validation possibilities. A flow pattern map was arranged, showing the potential of the HAWAC facility, and compared with indications from the literature. The agreement is reasonable, although the transition from stratified to intermittent flow regimes was observed at slightly higher liquid flow rates. For quantitative analysis of the optical measurements performed in the channel, the developed interface capture algorithm was applied. This allows to make statistical treatments for comparisons of the interface structure with CFD calculation results. The hydraulic jump as the quasi-stationary discontinuous transition between super- and subcritical flow was investigated in this closed channel. The structure of the hydraulic jump over time is revealed by the calculation of the probability density of the water level. A series of experiments shows that the hydraulic jump profile and its position from the inlet vary substantially with the inlet boundary conditions due to the momentum exchange between the phases. Moreover, images of the instable wave growth leading to slug flow are shown from the test section inlet. In order to visualise the evolution of the interface structure along the channel during slug generation, the time averaged water level bounded by the standard deviation was calculated.

Furthermore, the TOPFLOW test facility of HZDR was extended by a new test section representing a flat model of the hot leg of the German *Konvoi* pressurised water reactor scaled at 1:3. The “hot leg model” is installed in a pressure vessel and is operated in pressure equilibrium with the inside atmosphere. This technique allows optical observation of two-phase flows over large windows at pressures up to 50 bar and temperatures of up to 264°C. Therefore, local flow information can be acquired under reactor typical boundary conditions (saturated steam/water flow) for CFD validation purposes. Different types of experiments were performed with air or steam and water in co- and counter-current by variation of the pressure and flow rates. An overview of the experimental methodology and of the recorded data was given. On one hand, the experiments without water circulation are dedicated test cases for CFD development. On the other hand, the counter-current flow limitation experiments represent challenging transient validation cases of a typical nuclear reactor

safety issue. Exemplary pictures of the flow observed in the region of the elbow and of the steam generator inlet chamber were presented.

Co-current flow experiments simulating a two-phase natural circulation in the primary circuit were performed. The frequency distribution of the water level measured in the RPV simulator was used to characterise the flow in the hot leg. It was found that the form of the distribution informs about the stationarity of the water flow to the steam generator: the broader the distribution, the more discontinuous the transport of water over time. Furthermore, the high-speed video observations were used to identify the flow regime. This shows that a change in the form of the probability distribution coincides with a flow regime transition: from elongated bubble flow at low gas flow rates to slug flow at high gas flow rates.

Counter-current flow limitation (CCFL) experiments were performed, simulating the reflux condenser cooling mode appearing in some accident scenarios. As an example, different air/water and steam/water experiments were presented and analysed with the help of detailed high-speed camera pictures of the two-phase flow. Commonly, the macroscopic effects of CCFL are represented in a flooding diagram using the non-dimensional superficial velocity (also known as *Wallis parameter*) as coordinates. Therefore, a numerical data treatment method was developed to plot the flooding characteristics based on the discharge water flow accumulating in the RPV simulator. However, the classical definition of the Wallis parameter contains the pipe diameter as characteristic length and only limited information could be found in the literature about its equivalent for channels with rectangular cross-sections. The CCFL characteristics of the air/water experiments was compared with similar experimental data – especially with the analogue hot leg model of the Kobe University – and with empirical correlations for pipes available in the literature. The hydraulic diameter, the channel height and the Laplace critical wavelength (leading to the Kutateladze number) were tested. The comparison shows that the channel height is the characteristic length to be used in the Wallis parameter for channels with rectangular cross-sections.

Furthermore, a comparison between the air/water and steam/water flooding curves first revealed a difference when plotted in terms of the classical Wallis parameter or Kutateladze number. In fact, condensation effects had to be taken into account to correct the steam measurements. The amount of condensate was evaluated indirectly over the zero liquid penetration noticed in the CCFL diagram. Finally, the experimental results confirm that the Wallis similarity is appropriate to scale flooding in the hot leg of a PWR irrespective of the gas (air or steam) and for pressures ranging from 1.5 to 50 bar and temperatures of 18 to 264°C. However, a plausibility check shows that the evaluated amount of condensate cannot only be explained by heat losses and is probably due to liquid entrainment from the separator of the TOPFLOW heater circuit. Consequently, uncertainties remain in the results, which should be clarified in a second experimental campaign.

Finally, different examples of comparison between experiment and simulation were presented to illustrate the possibilities offered by the data to support the development and validation of CFD codes. Besides the comparison of qualitative aspects of the flow, CFD simulations of slug flow in the horizontal channels show how to enable quantitative comparisons with the experiments. The slug propagation velocity, pressure level and interface structure are examples of parameters to confront. Furthermore, the CCFL experiments in the hot leg model were simulated with CFD as well and quantitative comparisons of the flooding characteristics were performed. In future, the recorded high-speed camera images should be analysed in order to access to quantitative local flow information. However, the existing algorithms for the horizontal channels need to be further developed, in particular due to the bended geometry and to the inhomogeneous illumination conditions.

7. REFERENCES AND CREDITS

Bibliographic references

ABB. “Transient/slugging”. ABB Group, online publication (http://www.abb.com/cawp/seitp161/2cfdabece457886841256f500041089e.aspx), (2004).

A. A. Ahmed, D. A. Ervine, E. J. McKeogh. “The process of aeration in closed conduit hydraulic structures”. Proceedings of the Symposium on Scale Effects in Modelling Hydraulic Structures, Technische Akademie Esslingen, Germany, 3-6 September, article No. 4.13 (1984).

G. B. Airy. “Tides and waves”. Encyclopaedia Metropolitana (1817-1845), Mixed Sciences 3, ed. H. J. Rose et al., London, UK (1841).

F. Ardhuin. “Hydrodynamique côtière – Partie 2 : vagues”. Lecture notes of “Master Mécanique-Physique”, Service Hydrographique et Océanographique de la Marine, Brest, France (2007).

K. H. Ardron, S. Banerjee. “Flooding in an elbow between a vertical and a horizontal or near-horizontal pipe. Part II: theory”. International Journal of Multiphase Flow 12/4, pp. 543-558 (1986).

H. Asaka & Y. Kukita. “Sub- to supercritical flow transition in a horizontally-stratified two-phase flow in PWR hot legs”. Journal of Nuclear Science and Technology 33/9, pp.696-702 (1996).

B. A. Bakhmeteff. “O neravnomernom wwijenii jidkosti v otkrytom rusle (Varied flow in an open channel)”. St Petersburg, Russia (1912).

S. G. Bankoff, R. S. Tankin, M. C. Yuen, C. L. Hsieh. “Countercurrent flow of air/water and steam/water through a horizontal perforated plate”. International Journal of Heat and Mass Transfer, 24/8, pp. 1381-1395 (1981).

S. G. Bankoff & S. C. Lee. “A critical review of the flooding literature”.Multiphase Science and Technology 2, pp. 95-180 (1986).

Y. Bartosiewicz, J.-M. Seynhaeve, C. Vallée, T. Höhne, J. Laviéville. “Modelling free surface flows relevant to a PTS scenario: comparison between experimental data and three RANS based CFD-codes – Comments on the CFD-experiment integration and best practice guideline”. Nuclear Engineering and Design 240/9, pp. 2375-2381 (2010).

J.-B. Bélanger. “Essai sur la solution numérique de quelques problèmes relatifs au mouvement permanent des eaux courantes”. Carilian-Goeury, Paris, France (1828).

T. B. Benjamin. “Shearing flow over a wavy boundary”. Journal of Fluid Mechanics 6/02, pp. 161-205 (1959).

P. A. Berthelsen. “An immersed interface method for two-dimensional modelling of stratified flow in pipes”. Ph.D. thesis, Norges Teknisk-Naturvitenskapelige Universitet (NTNU), Department of energy and process engineering, Trondheim, Norway (2004).

D. Biberg. “Mathematical models for two-phase stratified pipe flow”. Ph.D. thesis, University of Oslo, Faculty of mathematics and natural sciences, Norway (2005).

G. Bidone. “Expériences sur le remou et sur la propagation des ondes”. Memorie della Reale Accademia delle scienze di Torino, Tomo XXV, pp. 21-112. Dalla Stamperia Reale, Torino, Italy (1820).

BP. “Deepwater Horizon accident investigation report”. BP p.l.c., online publication (http://www.bp.com/liveassets/bp_internet/globalbp/globalbp_uk_english/gom_response/STAGING/local_assets/downloads_pdfs/Deepwater_Horizon_Accident_Investigation_Report.pdf), (2010).

G. P. Celata, M. Cumo, G. E. Farello, T. Setaro. “Hysteresis effect in flooding”. International Journal of Multiphase Flow 17/2, pp. 283-289 (1991).

H. Chanson. “Flow characteristics of undular hydraulic jumps - Comparison with near-critical flows”. The University of Queensland, Department of Civil Engineering, Report CH45/95, Brisbane, Australia (1995).

H. Chanson. “Development of the Bélanger equation and backwater equation by Jean-Baptiste Bélanger (1828)”. Journal of hydraulic engineering 135/3, pp. 159-163 (2009).

M. L. Corradini. “Fundamentals of multiphase flow”. University of Wisconsin, Department of Engineering Physics, online publication (http://wins.engr.wisc.edu/teaching/mpfBook/main.html), (1997).

F. D’Auria & M. Frogheri. “Use of a natural circulation map for assessing PWR performance”. Nuclear Engineering and Design 215/1-2, pp. 111-126 (2002).

P. S. Damerell & J. W. Simons. “Reactor safety issues resolved by the 2D/3D program”. International Agreement Report, U.S. Nuclear Regulatory Commission Report No. NUREG/IA-0127, Washington, USA (1993).

H. Darcy & H. Bazin. “Recherches hydrauliques, entreprises par H. Darcy, continuées par H. Bazin”. Dunod, Imprimerie impériale, Paris, France (1865).

Deendarlianto, T. Höhne, D. Lucas, C. Vallée. “Numerical simulation of air-water counter-current two-phase flow in a model of the hot leg of a pressurized water reactor (PWR)”. Proceedings of the International Conference on Multiphase Flow (ICMF-2010), Tampa (FL), USA, May 30 – June 4, Paper No. 10.4.2 (2010).

H. Devold. “Oil and gas production handbook – An introduction to oil and gas production”. ABB AS, Oslo, Norway (2009).

C. Don Fletcher, P. R. McHugh, S. A. Naff, G. W. Johnsen. “Thermal-hydraulic processes involved in loss of residual heat removal during reduced inventory operation”. Idaho National Engineering Laboratory technical report No. EGG-EAST-9337, revision 1, EG&G Idaho, Inc., Idaho Falls, Idaho, USA (1991).

D. Dumont, G. Lavialle, B. Noel, R. Deruaz. “Loss of residual heat removal during mid-loop operation: BETHSY experiments”. Nuclear Engineering and Design 149/1-3, pp. 365-374 (1994).

M. Fermigier. “Hydrodynamique Physique”. Lecture notes, ESPCI - Laboratoire d’Hydrodynamique et Mécanique Physique, Paris, France (2004).

A. Flamant. “Hydraulique”. Seconde édition, Encyclopédie des travaux publiques, Librairie polytechnique, Ch. Béranger, Paris, France (1900).

G. C. Gardner. “Co-current flow of air and water from a reservoir into a short horizontal pipe”. International Journal of Multiphase Flow 14/4, pp. 375-388 (1988).

G. C. Gardner. “Air-water model studies of cocurrent flow into and along a PWR hot leg to the steam generator”. Nuclear Engineering and Design 117/3, pp. 251-261 (1989).

M. Gargallo, T. Schulenberg, L. Meyer, E. Laurien. “Counter-current flow limitations during hot leg injection in pressurized water reactors”. Nuclear Engineering and Design 235/7, pp. 785-804 (2005).

G. Geffraye, P. Bazin, P. Pichon, A. Bengaouer. “CCFL in hot legs and steam generators and its prediction with the CATHARE code”. Proceedings of the 7th International Topical Meeting on Nuclear Reactor Thermal-Hydraulics (NURETH-7), Saratoga Springs (NY), USA, September 10-15, pp. 815-826 (1995).

H. Glaeser. “Downcomer and tie plate countercurrent flow in the Upper Plenum Test Facility (UPTF)”. Nuclear Engineering and Design 133/2, pp. 259-283 (1992).

G. W. Govier & K. Aziz. “The flow of complex mixtures in pipes”. Van Nostrand-Reinhold, New York, USA, p. 503 (1972).

W. H. Hager. “Wassersprung im geschlossenen Kanal”. 3R International, 28/10, pp. 674-679 (1989).

W. H. Hager. “Energy dissipators and hydraulic jump”. Kluwer academic publishers, Dordrecht, Netherlands (1992).

A. Hawighorst, H. Kröning, F. Mayinger. “Fluid dynamic effects in the fuel element top nozzle area during refilling and reflooding”. Nuclear Science and Engineering 88/3, pp. 376-385 (1984).

F. M. Henderson. “Open channel flow”. The Macmillan company, New York, USA (1966).

G. Hetsroni. “The nature of multiphase flows”. Notes of the short courses “Modelling and Computation of Multiphase Flows”, 15-19 February, Zürich, Switzerland (2010).

G. F. Hewitt. “Three-phase gas-liquid-liquid flows in the steady and transient states”. Nuclear Engineering and Design 235/10-12, pp. 1303-1316 (2005).

T. Hibiki & M. Ishii. “Experimental study on hot-leg U-bend two-phase natural circulation in a loop with a large diameter pipe”. Nuclear Engineering and Design 195/1, pp. 69-84 (2000).

T. Höhne & C. Vallée. “Numerical prediction of horizontal stratified flows”. Proceedings of the 6th International Conference on CFD in the Oil & Gas, Metallurgical and Process Industries (CFD2008), June 10-12, Trondheim, Norway, article No. CFD08-12 (2008).

J.-T. Hsu, M. Ishii, T. Hibiki. “Experimental study on two-phase natural circulation and flow termination in a loop”. Nuclear Engineering and Design 186/3, pp. 395-409 (1998).

J. Huhn & J. Wolf. “Zweiphasenströmung – gasförmig/flüssig”. VEB Fachbuchverlag Leipzig, GDR (1975).

H. M. S. Hussein, H. H. El-Ghetany, S. A. Nada. “Performance of wickless heat pipe flat plate solar collectors having different pipes cross sections geometries and filling ratios”. Energy Conversion and Management 47/11-12, pp. 1539-1549 (2006).

H. Jeffreys. “On the formation of water waves by wind”. Proceedings of the Royal Society of London, Series A 107/742, pp. 189-206 (1925).

H. Jeffreys. “On the formation of water waves by wind (second paper)”. Proceedings of the Royal Society of London, Series A 110/754, pp. 241-247 (1926).

H. Y. Jeong. “Prediction of counter-current flow limitation at hot leg pipe during a small-break LOCA”. Annals of Nuclear Energy 29/5, pp. 571-583 (2002).

A. A. Kalinske & P. H. Bliss. “Removal of air from pipe lines by flowing water”. American Society of Civil Engineers, Civil Engineering 13/10, pp. 480-482 (1943).

A. A. Kalinske & J. M. Robertson. “Closed conduit flow”. Transactions of the American Society of Civil Engineers 108, pp. 1435-1447 (1943).

S.-K. Kang, I.-C. Chu, H. C. No, M.-H. Chun, C.-K. Sung. “Air-water countercurrent flow limitation in a horizontal pipe connected to an inclined riser”. Journal of the Korean Nuclear Society 31/6, pp. 548-560 (1999).

H. Y. Kim & H. C. No. “Assessment of RELAP5/MOD3.2.2γ against flooding database in horizontal-to-inclined pipes”. Annals of Nuclear Energy 29/7, pp. 835-850 (2002).

S. M. Krolewski. “Flooding limits in a simulated nuclear reactor hot leg”. Submission for a Bachelor of Science, Massachusetts Institute of Technology, Cambridge (MA), USA (1980).

Y. Kukita, H. Nakamura, Y. Anoda, K. Tasaka. “Hot leg flow characteristics during two-phase natural circulation in pressurized water reactor”. Proceedings of the fourth International Topical Meeting on Nuclear Reactor Thermal Hydraulics (NURETH-4), Karlsruhe, Germany, October 10-13, Vol. 1, pp. 465-470 (1989).

M. J. Landman. “Non-unique holdup and pressure drop in two-phase stratified inclined pipe flow”. International Journal of Multiphase Flow 17/3, pp. 377-394 (1991).

E. W. Lane & C. E. Kindsvater. "Hydraulic jump in enclosed conduits". Engineering News-Record, 29 December, pp. 815-817 (1938).

S. Y. Lee & M. Ishii. “Characteristics of two-phase natural circulation in Freon-113 boiling loop”. Nuclear Engineering and Design 121/1, pp. 69-81 (1990).

C. H. Lee, T. J. Liu, Y. S. Way, D. Y. Hsia. “Investigation of mid-loop operation with loss of RHR at INER integral system test (IIST) facility”. Nuclear Engineering and Design 163/3, pp. 349-358 (1996).

S. Levy. “Two-phase flow in complex systems”. John Wiley & Sons, New York, USA (1999).

T.-J. Liu. “Reflux condensation behavior in a U-tube steam generator with or without noncondensables”. Nuclear Engineering and Design 204/1-3, pp. 221-232 (2001).

M. Lopez-De-Bertodano. “Countercurrent gas-liquid flow in a pressurized water reactor hot leg”. Nuclear Science and Engineering 117/2, 126-133 (1994).

J. M. Mandhane, G. A. Gregory, K. Aziz. “A flow pattern map for gas-liquid flow in horizontal pipes”. International Journal of Multiphase Flow 1/4, pp. 537-553 (1974).

N. Minami, D. Nishiwaki, H. Kataoka, A. Tomiyama, S. Hosokawa, M. Murase. “Experiments on air-water countercurrent flow in a rectangular duct simulating PWR hot leg”. Proceedings of the 16th International Conference on Nuclear Engineering, Orlando (FL), USA, May 11-15, article No. ICONE16-48113 (2008).

N. Minami, D. Nishiwaki, T. Nariai, A. Tomiyama, M. Murase. “Countercurrent gas-liquid flow in a PWR hot leg under reflux cooling – (I) Air-water tests for 1/15-scale model of a PWR hot leg”. Journal of Nuclear Science and Technology 47/2, pp. 142-148 (2010).

M. Murase, I. Kinoshita, Y. Utanohara, D. Lucas, C. Vallée, A. Tomiyama. “Numerical calculations for air-water tests on CCFL in different models of PWR hot legs”. Proceedings of the 18th International Conference on Nuclear Engineering, Xi'an, China, May 17-21, Paper No. ICONE18-29092 (2010).

M. A. Navarro. “Study of countercurrent flow limitation in a horizontal pipe connected to an inclined one”. Nuclear Engineering and Design 235/10-12, pp. 1139-1148 (2005).

H. C. No, K.-W. Lee, C.-H. Song. “An experimental study on air-water countercurrent flow limitation in the upper plenum with a multi-hole plate”. Nuclear Engineering and Technology 37/6, pp. 557-564 (2005).

A. Ohnuki. “Experimental study of counter-current two-phase flow in horizontal tube connected to inclined riser”. Journal of Nuclear Science and Technology 23/3, pp. 219-232 (1986).

A. Ohnuki, H. Adachi, Y. Murao. “Scale effects on countercurrent gas-liquid flow in a horizontal tube connected to an inclined riser”. Nuclear Engineering and Design 107/3, pp. 283-294 (1988).

A. Ousaka, Deendarlianto, A. Kariyasaki, T. Fukano. “Prediction of flooding gas velocity in gas-liquid counter-current two-phase flow in inclined pipes”. Nuclear Engineering and Design 236/12, pp. 1282-1292 (2006).

G. Petritsch & D. Mewes. “Experimentelle Untersuchung der Strömungsform in der heißseitigen Hauptkühlmittelleitung eines Druckwasserreaktors”. Universität Hannover, Institut für Verfahrenstechnik, BMBF Förderkennzeichen 150 1004, Abschlußbericht, Teil 1, Hannover, Germany (1997).

G. Petritsch & D. Mewes. “Experimental investigations of the flow patterns in the hot leg of a pressurized water reactor” Nuclear Engineering and Design 188/1, pp. 75-84 (1999).

O. L. Pushkina & Y. L. Sorokin. “Breakdown of liquid film motion in vertical tubes”. Heat Transfer Soviet Research 1/5, pp. 56-64 (1969).

H. J. Richter. “Flooding in tubes and annuli”. International Journal of Multiphase Flow 7/6, pp. 647-658 (1981).

H. J. Richter, G. B. Wallis, K. H. Carter, S. L. Murphy. “Deentrainment and counter-current air-water flow in a model PWR hot leg”. U.S. Nuclear Regulatory Commission Report No. NRC-0193-9, Hanover (NH), USA (1978).

ROSA-IV Group. “ROSA-IV Large Scale Test Facility (LSTF) system description”. JAERI report JAERI-M 84-237, Japan Atomic Energy Research Institute, Tokai-mura, Naka-gun, Ibaraki-ken, Japan (1985).

H. Schmidt & H. Limprecht. “Versuch PKL III B 3.4”. Siemens/KWU Report No. KWU E312/91/16, Erlangen, Germany (1991).

S. P. Schollenberger, B. Schoen, K. Umminger. “Experimentelle Untersuchungen in der PKL-Versuchsanlage zum Ausfall der Nachkühlung im mitte-loop betrieb”. Proceedings of the Jahrestagung Kerntechnik 2008, Hamburg, Germany, May 27-29, pp. 140-146 (2008).

J. Scott Russell. “Report on waves, made to the fourteenth meeting of the British association for the advancement of science (held at York in September 1844)”. London, UK (1845).

T. Seidel, C. Vallée, D. Lucas, M. Beyer, Deendarlianto. “Two-phase flow experiments in a model of the hot leg of a pressurised water reactor”. FZD report/Wissenschaftlich-Technische Berichte FZD-531, Dresden-Rossendorf, Germany (2010).

H. Siddiqui, S. Banerjee, K. H. Ardron. “Flooding in an elbow between a vertical and a horizontal or near-horizontal pipe”. International Journal of Multiphase Flow 12/4, pp. 531-541 (1986).

Siemens/KWU. “UPTF-Test no. 11: Countercurrent flow in PWR hot leg test”. Siemens/KWU Quick Look Report R 515/87/08, Erlangen, Germany (1987).

Siemens/KWU. “UPTF-TRAM Versuch A2: Ausbildung der Schichtenströmung in der heißseitigen Leitung“. Siemens/KWU Quick Look Report S554/92/012, Erlangen, Germany (1992).

B. L. Smith, U. Bieder, E. Graffard, M. Heitsch, M. Henriksson, T. Höhne, E. Komen, J. Mahaffy, F. Moretti, T. Morii, P. Mühlbauer, U. Rohde, M. Scheuerer, C.-H. Song, G. Zigh. “Assessment of computational fluid dynamics (CFD) for nuclear reactor safety problems”. OECD report NEA/CSNI/R(2007)13, (2008).

B. L. Smith & Y. A. Hassan. “Foreword – Topical issue on CFD4NRS”. Nuclear Engineering and Design 238/3, pp. 443-444 (2008).

Yu. L. Sorokin, A. A. Kirdyashkin, B. G. Pokusaev. “Investigation of the stability of the film flow of liquid in a vertical pipe with an upward flow of gas”. Chemical and Petroleum Engineering 1/5, pp. 401-405 (1965).

H. Stahl & W. H. Hager. “Hydraulic jump in circular pipes”. Canadian Journal of Civil Engineering 26/3, pp. 368-373 (1999).

Y. Taitel, D. Bornea, A. E. Dukler. “Modelling flow pattern transitions for steady upward gas-liquid flow in vertical tubes”. American Institute of Chemical Engineers (AIChE) Journal 26/3, pp. 345-354 (1980).

Y. Taitel & A. E. Dukler. “A model for predicting flow regime transitions in horizontal and near horizontal gas-liquid flow”. American Institute of Chemical Engineers (AIChE) Journal 22/1, pp. 47-55 (1976).

M. J. Tan, G. A. Lambert, M. Ishii. “An experimental study of two-phase natural circulation in an adiabatic flow loop”. Proceedings of the 5. Miami international symposium on multi-phase transport and particulate phenomena, Miami Beach (FL), USA, 12 December (1988).

V. Teschendorff, M. Scheurer, H.-G. Sonnenburg. “Konzertierte Aktion zur Integration von CFD-Codes bzw. deren Module in den Systemcode ATHLET zur physikalisch fundierten und sicher skalierbaren Simulation mehrdimensionaler Zweiphasenströmungen”. 12. Sitzung des Projektkommitees “Transienten und Unfallabläufe”, 22 September, Köln, Germany (1998).

D. L. Tien. “A simple analytical model for counter-current flow limiting phenomena with vapor condensation”. Letters in Heat and Mass Transfer 4, pp. 231-238 (1977).

Total. “Pazflor – Bringing together deep offshore experience and technological boldness”. Total E&P Angola, March (2008).

U.S.NRC. “Loss of vital AC power and the residual heat removal system during mid-loop operations at Vogtle Unit 1 on March 20, 1990”. U.S. Nuclear Regulatory Commission Report No. NUREG 1410, Washington (DC), USA (1990).

U.S.NRC. “Reactor Concepts Manual – 4. Pressurized Water Reactor (PWR) Systems”. USNRC Technical Training Center, report n°0603, online publication (http://www.nrc.gov/reading-rm/basic-ref/teachers/04.pdf), pp. 1-28 (2009).

C. Vallée, T. Höhne, H.-M. Prasser, T. Sühnel. “Experimental investigation and CFD simulation of slug flow in horizontal channels”. FZD report/Wissenschaftlich-Technische Berichte FZD-485, Forschungszentrum Dresden-Rossendorf, Dresden, Germany (2007-a).

C. Vallée, H.-M. Prasser, T. Sühnel. “Experimentelle Untersuchung von geschichteten Luft/Wasser Strömungen in einem horizontalen Kanal”. FZD report/Wissenschaftlich-Technische Berichte FZD-484, Forschungszentrum Dresden-Rossendorf, Dresden, Germany (2007-b).

VDI-Wärmeatlas. “Berechnungsblätter für den Wärmeübergang”. Verein Deutscher Ingenieure, VDI-Gesellschaft Verfahrenstechnik und Chemieingenieurwesen, Siebte erweiterte Auflage, VDI-Verlag, Düsseldorf (1994).

K. Vierow, I. Choutapalli, K. Hogan, Y. Liao, M. Solmos, S. N. Williams. “Countercurrent flow limitation experiments and modeling for improved reactor safety”. Contract research final report, submitted to U.S. Department of Energy (2008).

G. B. Wallis. “Flooding velocities for air and water in vertical tubes”. United Kingdom Atomic Energy Authority, Reactor group, Reactor Development Division, Atomic Energy Establishment, Report AEEW - R 123, Winfrith, Dorchester, Dorset, UK (1961).

G. B. Wallis. “The influence of liquid viscosity on flooding in a vertical tube”. General electric, General Engineering Laboratory, Report n° 62GL132, Schenectady, New York, USA (1962).

G. B. Wallis. “One-dimensional two-phase flow”. Mc Graw-Hill, New York, USA (1969).

G. B. Wallis & J. E. Dobson. “The onset of slugging in horizontal stratified air-water flow”. International Journal of Multiphase Flow 1/1, pp. 173-193 (1973).

P. T. Wan. “Countercurrent steam-water flow in an upright 90° elbow”. Proceeding of the eighth International Heat Transfer Conference, San Francisco (CA), USA, August 17-22, Vol. 5, pp. 2313-2318 (1986).

P. T. Wan & V. S. Krishnan. “Air-water flooding in a 90° elbow with a slightly inclined lower leg”. Proceedings of the seventh Annual Conference of the Canadian Nuclear Society, Toronto, Canada, June 9-10, pp. 273-278 (1986).

M. J. Wang & F. Mayinger. “Simulation and analysis of thermal-hydraulic phenomena in a PWR hot leg related to SBLOCA”. Nuclear Engineering and Design 155/3, pp. 643-652 (1995).

S. Wongwises. “Flooding in a horizontal pipe with bend”. International Journal of Multiphase Flow 22/1, pp. 195-201 (1996-a).

S. Wongwises. “Two-phase countercurrent flow in a model of a pressurized water reactor hot leg”. Nuclear Engineering and Design 166/2, pp. 121-133 (1996-b).

Y. Yegorov, M. Boucker, A. Martin, S. Pigny, M. Scheuerer, S. Willemsen. “Validation of CFD codes with PTS-relevant test cases”. EVOL-ECORA project report, Deliverable D07 (2004).

A. Zapke & D. G. Kröger. “The influence of fluid properties and inlet geometry on flooding in vertical and inclined tubes”. International Journal of Multiphase Flow 22/3, pp. 461-472 (1996).

A. Zapke & D. G. Kröger. “Countercurrent gas-liquid flow in inclined and vertical ducts - I: Flow patterns, pressure drop characteristics and flooding”. International Journal of Multiphase Flow 26/9, pp. 1439-1455 (2000-I).

A. Zapke & D. G. Kröger. “Countercurrent gas-liquid flow in inclined and vertical ducts - II: The validity of the Froude-Ohnesorge number correlation for flooding”. International Journal of Multiphase Flow 26/9, pp. 1457-1468 (2000-II).

Publications of the author

This thesis is in part based on the following publications by the author:

C. Vallée, T. Höhne, H.-M. Prasser, T. Sühnel. “Experimental investigation and CFD simulation of horizontal air/water slug flow”. Kerntechnik 71/3, pp. 95-103 (2006).

C. Vallée. “Experiments on the interface dynamics of stratified air/water flows”. Jahrestagung Kerntechnik 2007, May 22-24, Karlsruhe, Germany. Fachsitzung, Berlin: INFORUM Verlags- und Verwaltungsgesellschaft, pp. 23-26 (2007).

C. Vallée. “Hydraulic jump in a closed horizontal two-phase flow channel”. Proceedings of the International Conference on Multiphase Flow (ICMF 2007), July 9-13, Leipzig, Germany (2007), Paper S5_Fri_A_63 (2007).

C. Vallée, T. Höhne, H.-M. Prasser, T. Sühnel. “Experimental investigation and CFD simulation of slug flow in horizontal channels”. FZD report/Wissenschaftlich-Technische Berichte FZD-485, Forschungszentrum Dresden-Rossendorf, Dresden, Germany (2007).

C. Vallée, H.-M. Prasser, T. Sühnel. “Experimentelle Untersuchung von geschichteten Luft/Wasser Strömungen in einem horizontalen Kanal”. FZD report/Wissenschaftlich-Technische Berichte FZD-484, Forschungszentrum Dresden-Rossendorf, Dresden, Germany (2007).

C. Vallée, T. Höhne, H.-M. Prasser, T. Sühnel. “Experimental investigation and CFD simulation of horizontal stratified two-phase flow phenomena”. Nuclear Engineering and Design 238/3, pp. 637-646 (2008).

Deendarlianto, C. Vallée, D. Lucas, M. Beyer, H. Pietruske, H. Carl. “Experimental study on the air/water counter-current flow limitation in a model of the hot leg of a pressurised water reactor”. Nuclear Engineering and Design 238/12, pp. 3389-3402 (2008).

C. Vallée, Deendarlianto, M. Beyer, D. Lucas, H. Carl. “Air/water counter-current flow experiments in a model of the hot leg of a pressurised water reactor”. Journal of Engineering for Gas Turbines and Power - Transactions of the ASME 131/2, article 022905 (2009).

C. Vallée, T. Seidel, D. Lucas, M. Beyer, H.-M. Prasser, H. Pietruske, P. Schütz, H. Carl. “Influence of the fluid properties on co-current two-phase flows in a horizontal channel connected to a riser”. Proceedings of the 7th World Conference on Experimental Heat Transfer, Fluid Mechanics and Thermodynamics (ExHFT-7), June 28-July 3, Krakow, Poland, pp. 443-452 (2009).

C. Vallée, D. Lucas, M. Beyer, H. Pietruske, P. Schütz, H. Carl. “Experimental CFD grade data for stratified two-phase flows”. Nuclear Engineering and Design 240/9, pp. 2347-2356 (2010).

T. Höhne, C. Vallée. “Experiments and numerical simulations of horizontal two-phase flow regimes using an interfacial area density model”. Journal of Computational Multiphase Flows 2/3, pp. 131-143 (2010).

C. Vallée, T. Seidel, D. Lucas, A. Tomiyama, M. Murase. “Comparison of counter-current flow limitation experiments performed in two different models of the hot leg of a pressurised water reactor with rectangular cross-section”. Journal of Engineering for Gas Turbines and Power – Transactions of the ASME 133/5, article 052917 (2011).

T. Seidel, C. Vallée, D. Lucas, M. Beyer, Deendarlianto. “Two-phase flow experiments in a model of the hot leg of a pressurised water reactor”. HZDR report/Wissenschaftlich-Technische Berichte HZDR-010, Helmholtz-Zentrum Dresden-Rossendorf, Dresden, Germany (2011).

C. Vallée, T. Seidel, D. Lucas, M. Beyer, H.-M. Prasser, H. Pietruske, P. Schütz, H. Carl. “Counter-current flow limitation in a model of the hot leg of a PWR - comparison between air/water and steam/water experiments”. Nuclear Engineering and Design, doi:10.1016/j.nucengdes.2012.01.001 (in press).

Figure credits

The permission to reproduce certain figures was obtained from the copyright holders and is gratefully acknowledged.

Figure 1.1: reprinted from the brochure “Pazflor – Bringing together deep offshore experience and technological boldness”, online publication (http://www.total.com/MEDIAS/MEDIAS_INFOS/2160/EN/Pazflor-VA.pdf), Copyright (2008), with kind permission from *Total S.A.*

Figure 1.2: reprinted from the presentation slides “Deepwater Horizon investigation”, online publication (url: http://www.bp.com/liveassets/bp_internet/globalbp/globalbp_uk_english/gom_response/STAGING/local_assets/downloads_pdfs/Deepwater_Horizon_Accident_Investigation_static_presentation.pdf), Copyright (2010), with kind permission from *BP p.l.c.*

Figure 2.1: adapted from the notes of the short courses *Modelling and Computation of Multiphase Flows*, G. Hetsroni, “The nature of multiphase flows”, 15-19 February, Zürich, Switzerland, Copyright (2010), with kind permission from the author.

Figure 2.2: reprinted from the International Journal of Multiphase Flow 1/4, J. M. Mandhane, G. A. Gregory, K. Aziz, “A flow pattern map for gas-liquid flow in horizontal pipes”, pp. 537-553, Copyright (1974), with kind permission from *Elsevier*.

Figure 2.3 to Figure 2.5: reprinted from the American Institute of Chemical Engineers (AIChE) Journal 22/1, Y. Taitel & A. E. Dukler, “A model for predicting flow regime transitions in horizontal and near horizontal gas-liquid flow”, pp. 47-55, Copyright (1976), with kind permission from *John Wiley & Sons, Inc*.

Figure 2.10: adapted from the International Journal of Multiphase Flow 26/9, A. Zapke & D. G. Kröger, “Countercurrent gas-liquid flow in inclined and vertical ducts - I: Flow patterns, pressure drop characteristics and flooding”, pp. 1439-1455, Copyright (2000), with kind permission from *Elsevier*.

8. NOMENCLATURE

Symbols

Symbol	Denomination	Unit
A	cross-sectional area	m^2
b	coefficient	-
c	propagation velocity	m/s
C	coefficient	-
D	diameter	m
e	specific energy	J/kg
F	force	N
F	modified Froude number	-
Fr	Froude number	-
f	friction factor	-
g	acceleration of gravity	m/s^2
h	(water) level	m
H	channel height	m
j	superficial velocity	m/s
J*	Wallis parameter	-
k	wavenumber	m^{-1}
K	non-dimensional parameter	-
K	Kutateladze number	-
l	level	m
L	length	m
L	non-dimensional water level	-
m	constant	-
$\dot{m}$	mass flow rate	kg/s
M	molar mass	kg/mol
n	coefficient, number	-
N	non-dimensional inverse viscosity parameter	-
N	number of frames	-
Oh	Ohnesorge number	-
p	pressure	Pa
p	probability	-
R	universal gas constant	$J \cdot mol^{-1} \cdot K^{-1}$
Re	Reynolds number	-
s	sheltering coefficient	-
S	part of the conduit perimeter in contact with the phase	m
S	surface	m^2
t	time	s
T	non-dimensional parameter	-
T	temperature	K
u	flow velocity	m/s
v	flow velocity	m/s
$\dot{V}$	volume flow rate	m^3/s
W	channel width	m
x	coordinate in flow direction	m
X	Lockhart-Martinelli parameter	-
y	coordinate perpendicular to the flow direction	m
Y	non-dimensional inclination parameter	-
z	vertical coordinate, altitude	m

Greek symbols

Symbol	Denomination	Unit
α	conduit inclination angle to the horizontal	°
Δ	difference	-
λ	wavelength / critical length	m
μ	dynamic viscosity	Pa·s
ν	kinematic viscosity	m^2/s
ρ	fluid density	kg/m^3
τ	shear stress	Pa
σ	surface tension	N/m
σ	standard deviation	-
ω	angular frequency	rad/s

Subscripts

0	initial, at sea level
air	air
atm	atmospheric
corr	corrected
d	discharge
f	facility
G	gaseous phase
h	hydraulic
H	horizontal part
HL	hot leg
i	interface / index
k	index
L	liquid phase
m	model
N	standard condition for temperature and pressure (0°C / 101.325 kPa)
R	riser
read	read
real	real
ref	reference
RPV	reactor pressure vessel
W	wall

Abbreviations and acronyms

AIAD	algebraic interfacial area density (CFD model)
amb.	ambient
BETHSY	**B**oucle d'**é**tudes **th**ermohydrauliques **sy**steme (test facility)
CCFL	counter-current flow limitation
CAD	computer-aided design
CCFL	counter-current flow limitation
CCTV	closed-circuit television
CFD	computational fluid dynamics
CPU	central processing unit
CSNI	Committee on the Safety of Nuclear Installations of the NEA
DN	nominal diameter
DNS	direct numerical simulations
DWR	**D**ruck**w**asser**r**eaktor (German for PWR)
ECC	emergency core cooling
ER	equivalent ratio
EU	European Union

FPSO	floating production, storage and offloading
HAWAC	**H**orizontal **A**ir/**Wa**ter **C**hannel of the *HZDR*
HZDR	Helmholtz-Zentrum Dresden-Rossendorf
LED	light-emitting diode
LOCA	loss of coolant accident
LSTF	Large Scale Test Facility
NEA	Nuclear Energy Agency of the OECD
NPP	nuclear power plant
OECD	Organisation for Economic Co-operation and Development
PIV	particle image velocimetry
PKL	**P**rimär**k**reis**l**auf (test facility)
PWR	pressurised water reactor
REP	réacteur à eau pressurisée (French for PWR)
RHR	residual heat removal
RMS	root mean square
RPV	reactor pressure vessel
sat.	saturation
SG	steam generator
SST	shear stress transport (turbulence model)
sub	subcooling
TOPFLOW	**T**ransient **T**w**o** **P**hase **Flow** test facility of the *HZDR*
TRAM	**Tr**ansient **a**ccident **m**anagement
UPTF	Upper Plenum Test Facility

APPENDIX: DETAILED TEST MATRIX OF THE HOT LEG EXPERIMENTS

Nomenclature for the numbering of the runs

The runs are numbered with 2 hyphenated double-digits (e.g. “06-15”): the first number (“06”) refers to the day of the experiments, the second (“15”) is a serial number.
If experimental points were repeated the same day, the serial numbers were separated by a slash in the test matrix (e.g. “06-15/16” stands for the two runs “06-15” and “06-16”)

Experiments without water circulation

Pressure: 3 bar								**Water level**
29-21	-	*29-22/23*	*29-24*	-	*29-25*	*29-26*	*29-28*	high
	29-17	*29-16*	*29-15*	-	*29-14*	*29-13*	*29-12*	middle
				30-22/23	*30-24*	*30-25*	*30-26*	low
30	45	60	100	120/150	200	300	400	**Air [Nm³/h]**

Pressure: 15 bar				
17-18	*17-19*	*17-20*	*17-21*	
75	110	150	250	**Steam [g/s]**

Pressure: 30 bar			
18-13	*18-16*	*18-19*	
13-26	*13-27*	*13-28*	
15-02	*15-03*	*15-04*	
150	205	295	**Steam [g/s]**

Pressure: 50 bar			
29-47 *06-02/11*	*06-05*	*06-08*	
150	255	500	**Steam [g/s]**

Co-current flow experiments

Pressure: 3 bar							
Water [kg/s]							
0.90	*23-08*	*23-09*	*24-01*	*24-02*	*24-03*	*24-04*	
0.33	*23-07*	*18-01*	*23-02*	*23-04*	*23-05*	*23-06*	
	30	60	100	200	300	400	**Air [Nm³/h]**

Pressure: 15 bar							
Water [kg/s]							
0.99	*14-12*	*14-13*	*14-14*	*14-15*	*14-16*	*14-18*	
0.66	*14-11*	*14-10*	*14-09*	*14-08*	*14-07*	*14-17*	
0.33	*14-01*	*14-02*	*14-03*	*14-04*	*14-05*	*14-06*	
	35	70	150	250	400	600	**Steam [g/s]**

Pressure: 30 bar								
Water [kg/s]								
ca. 0.9	*13-10*	*13-11*	*13-12*	*13-13*	*13-14*	*13-15*	*13-16*	
ca. 0.3	*13-24*	*13-23*	*13-22*	*13-20/21*	*13-19*	*13-18*	*13-17*	
	75	100	150	200	250	320	500	**Steam [g/s]**

Pressure: 50 bar								
Water [kg/s]								
ca. 0.85	*29-41*	*29-40*	*29-38*	*29-35/36*	*29-42*	*29-43*	*29-44*	
ca. 0.3	*29-31*	*29-32*	*29-33*	*29-34 09-11*	*09-10*	*09-09*	*29-45*	
	75	130	150	250	430	500	835	**Steam [g/s]**

Counter-current flow experiments

Pressure: 3 bar							
Water [kg/s]							
0.90	*24-16*	*24-15*	*24-14*	*24-13*	*24-12*	*24-11*	
0.30	*24-05*	*24-06*	*24-07*	*24-08*	*24-09*	*24-10*	
	30	60	100	200	300	400	**Air [Nm³/h]**

Pressure: 15 bar							
Water [kg/s]							
0.99	*17-11*	*17-12*	*17-13*	*17-14*	*17-16*		
0.66	*17-10*	*17-09*	*17-08*	*17-07*	*17-06*		
0.33	*17-01*	*17-02*	*17-03*	*17-04*	*17-05*		
	35	75	150	250	400	**Steam [g/s]**	

Pressure: 30 bar								
Water [kg/s]								
ca. 0.9	*11-15*	*11-16*	*13-09*	*13-08*	*13-07*	*13-05*	*13-06*	
ca. 0.3	*11-14*	*11-13*	*11-12*	*11-11*	*11-10*	*11-09*	*11-08*	
	75	100	150	200	250	320	500	**Steam [g/s]**

Pressure: 50 bar							
Water [kg/s]							
ca. 0.85	*15-20*	*15-18*	*15-17*	*15-15/16*	*15-14*	*15-13*	
ca. 0.3	*09-03*	*09-02*	*09-01*	*09-04/05/06*	*09-07*	*09-08*	
	75	130	150	250	430	500	**Steam [g/s]**

Counter-current flow limitation: flooding experiments

Gas	**Pressure [bar]**					
Steam	**50**		*06-15/16*	*06-13/14*		
Steam	**30**		*15-07*	*15-10*		
Steam	**23.6**			*11-07*		
Steam	**15**		*11-01*	*11-04*	*11-06*	
Air	**3.0**	*18-08/09*	*30-05*	*30-03/04*	*30-01/02*	
Air	**1.5**	*19-01/02*	*30-09*	*30-06*	*30-07*	
		0.15	**0.3**	**0.6**	**0.9**	**Water [kg/s]**

Counter-current flow limitation: deflooding experiments

Gas	**Pressure [bar]**				
Steam	**50**	*06-17*	*06-18*		
Steam	**30**	*15-08*	*15-12*		
Steam	**15**	*11-03*	*11-05* *13-02*		
Air	**3.0**	*29-02/03/04* *18-03*	*29-06*	*29-05* *18-04/07*	
Air	**1.5**		*30-10*		
		0.3	**0.6**	**0.9**	**Water [kg/s]**